№3, 2026

ISSN 2706-977X

MATERIAL AND MECHANICAL ENGINEERING TECHNOLOGY

Editorial board of the journal

Gulnara Zhetessova (Abylkas Saginov Karaganda Technical University, Kazakhstan)
Alexander Korsunsky (University of Oxford, England)
Olegas Cernasejus (Vilnius Gediminas Technical University, Lithuania)
Jaroslav Jerz (Institute of Materials & Machine Mechanics SAS, Slovakia)
Boris Moyzes (Tomsk Polytechnic University, Russia)
Nikolai Belov (National Research Technological University «Moscow Institute of Steel and Alloys", Russia)
Georgi Popov (Technical University of Sofia, Bulgaria)
Sergiy Antonyuk (University of Kaiserslautern, Germany)
Zharkynay Christian (University of Texas at Dallas Institute of Nanotechnology, USA)
Katica Simunovic (University of Slavonski Brod, Croatia)
Lesley D.Frame (School of Engeneering University of Connecticute, USA)
Łukasz Gierz (Poznan University of Technology, Poland)
Łukasz Warguła (Poznan University of Technology, Poland)
Olga Zharkevich (Abylkas Saginov Karaganda Technical University, Kazakhstan)

Content

Nefelov I.S., Filatov V.V., Taldykin D.S. Comparison of the Accuracy of Measurements of the Geometry of Parts Using Coordinate Measuring Machines in Manual and Programmed Operating Modes …….3
Dalavi A.M., Jadhav A.A. CLT-Based Mechanical Characterization of Hybrid Composites with Carbon/Kevlar/ Steel and Glass/Kevlar/Steel Layers…….….....13
Ganyukov A.A., Akhmediyev S.K., Bogdanova A.A. Statistical Analysis of Long-Term Operating Structures for Various Purposes Based on the Theory of Probabilistic Outliers……..……31
Berg A.S., Nurzhanova O.A., Zhunuspekov D.S., Wargula L., Suleev B.D. Development of High-Perfomance Sand-Polymer Composites from Regenerated Thermoplastics for Structural Applications under Dynamic Loads....43
Moyzes B., Kuvshinov K., Plotnikova I., Vavilova G., Vtorushina A. The Study of the Feasibility of Generating a Combined Sweep Signal……....49
AV Santhana Babu, Duraivelu J. Hybrid Automotive Composites with Artificial Intelligence Based Optimization-Advances, Challenges and Future Directions……....58
Jayaseelan C., Vimalarani C., Karthikeyani Vijayakumari K., Chitra K. Experimental Evaluation of Carbon Nanoparticle Addition on the Mechanical Properties of Banana Fiber Micro Particle Reinforced Epoxy Matrix Composites…….....78
Pirniazova P., Aksutova A., Aidarkul M. Numerical Simulation of Thermal Conductivity in Silicon Wafers of Transistors……..86
Kim A.S., Kadyrov A.S. Influence of Vessel Material on the Effectiveness of Ultrasonic Treatment of Metalworking Fluids……...94
Berkane I., Labed Z. Finite Element Analysis and J-integral of Repair Using Isotropic Bonded Patches on a Cracked Perforated Plate in an Aircraft Wing……105
Fasol Y.O., Riabenko A. Y., Kubich V.I Influence of Yttrium Content and Its Application Methods on the Thermal Coefficient of Linear Expansion of KNA 82 Alloy Sealing Coatings: Experimental Studies and Analytical Modeling……....115
Tolganay Z., Sherov K.T., Zakirov K., Balgynova A Experimental Investigation of Thermofriction Milling with Pulsed Cooling for Improving the Machinability of Hadfield Steel……...122
Zhetessova G.S., Khrustaleva I.A., Zharkevich O.M., Kanatova A., Kozhanov M.G. Trade-off Analysis and Multi-Objective Decision Support for Mechanical Engineering Supply Chains……129
Karsakova N., Mussayev M., Tattimbek G., Dauletova F. Design and Structural Assessment of a Special Boring Tool with an Inclined Clamping Mechanism……141
Kombayev K.K., Azamatov B.N., Kaliyev D.I., Mukhametbek Zh.M., Gabdyssalyk R. Surface Layer Formation of a 12KH18N10T Stainless Steel Toothed Base During Wire Electrical Discharge Machining……149

DOI 10.52209/2706-977X_2026_3_3 IRSTI 55.69.01 UDC 621.1.9

Comparison of the Accuracy of Measurements of the Geometry of Parts Using Coordinate Measuring Machines in Manual and Programmed Operating Modes

Nefelov I.S., Filatov V.V., Taldykin D.S.*
State University of Management, Moscow, Russia
*corresponding author

Abstract. This study compares the accuracy and repeatability of dimensional measurements performed on a coordinate measuring machine in manual and programmed operating modes. A Cummins diesel-engine piston was used as the test object; its diameter was measured in a production-specified section located 119 mm from the piston-skirt end. The experiment comprised part fixturing, establishment of the workpiece coordinate system by the 3-2-1 method, and repeated measurements in both modes. A Mezorix Atlas C 686 Basic CMM equipped with a Renishaw TP20 probe was used. In manual mode, the self-learning function recorded contact-point coordinates and approach vectors. In programmed mode, the RationalDMIS routine refined approach vectors according to nominal geometry and maintained a controlled contact speed. Ten repeated measurements were completed in each mode, and manual-mode reproducibility was additionally evaluated by three operators. The programmed mode produced a mean diameter of 157.7548 mm, a standard deviation of 0.0012 mm, and an uncertainty of ±0.0024 mm. The corresponding manual-mode values were 157.7382 mm, 0.0057 mm, and ±0.0114 mm. Relative to manual control, programmed control reduced the absolute deviation from the nominal diameter by 39.1% and the standard deviation by a factor of 4.75. The results show that automated control improves measurement repeatability by stabilizing probe direction and speed, whereas manual measurement remains dependent on operator skill. Self-learning is recommended for rapid generation of an initial inspection program followed by software-based optimization.

Keywords: coordinate measuring machines, measurement accuracy, programmed control, manual control, probe approach vector, self-learning mode.

Introduction

When performing coordinate measurements, coordinate systems are required. A distinction is made between a machine coordinate system and a workpiece coordinate system. The Machine Coordinate System is fixed relative to the physical coordinate axes of the coordinate measuring machine. It is determined at the design and manufacturing stage of the coordinate measuring machine and is usually located in one of the corners of the machine. The Workpiece Coordinate System is a coordinate system that is fixed relative to the workpiece (Fig. 1). This coordinate system depends on the position of the workpiece and is determined based on its design.

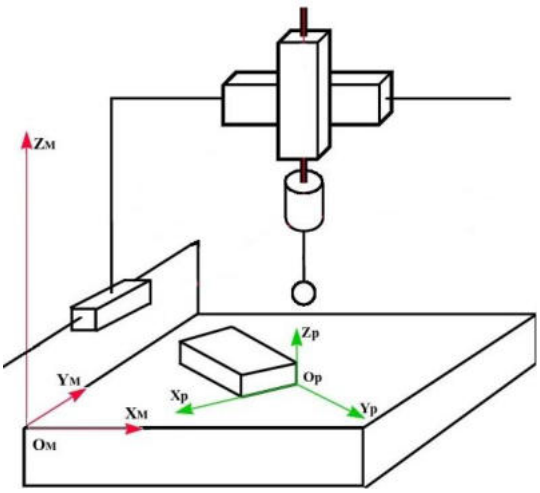

Fig. 1. - Coordinate systems for measurements on a coordinate measuring machine: O_M - origin of the machine coordinate system; X_M, Y_M, Z_M - axes of the machine coordinate system; O_P - origin of the workpiece coordinate system; X_P, Y_P, Z_P - axes of the workpiece coordinate system. Source: compiled by the authors.

The configuration of the measured parts is very diverse, but almost any part consists of at least several surfaces (with the exception of the simplest geometric bodies such as a sphere). It is known that surfaces consist of many points. To determine the position of these points, coordinates along the X, Y, Z axes are used. However, even knowing

the coordinates of all points on the surface, it is difficult to perform correct measurements of this surface on a coordinate measuring machine, since the orientation of the surface in space is unknown. To specify the orientation of the surface in space, normal unit vectors are used, which determine the direction perpendicular to the tangent plane at a given point on the surface (Fig. 2) [1].

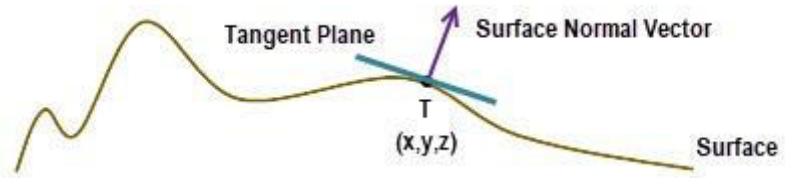

Fig. 2. - Tangent plane to the surface and the unit normal vector. Source: compiled by the authors.

The direction of the unit normal vector $\vec{n}$ to a point on the surface is determined by specifying its components I (1,0,0), J (0,1,0), K (0,0,1), representing the projections of this vector onto the coordinate axes X, Y, Z, respectively. Then the direction of the normal unit vector can be written as follows:

$$\vec{n} = (I, J, K) \tag{1}$$

Normal vectors of surfaces play a huge role in coordinate measurements, as they allow determining the optimal direction of approach of the measuring tip to a surface point during contact measurement (Fig. 3).

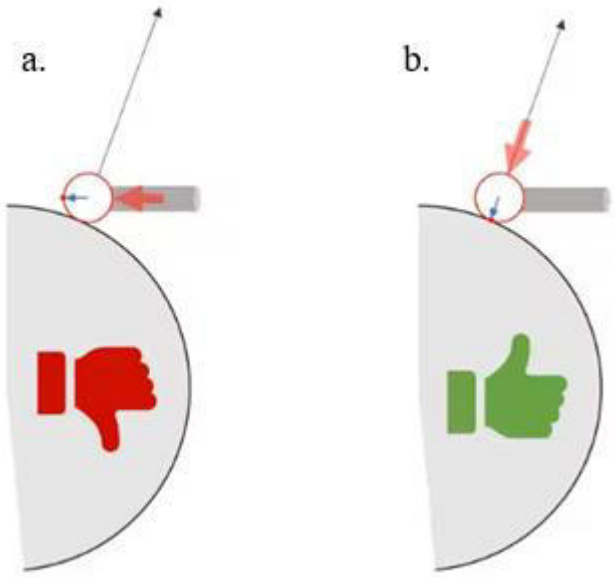

Fig. 3. - Non-optimal (a) and optimal (b) directions of measuring-tip motion at surface contact. Source: [2].

"Sliding" touches significantly reduce the accuracy and repeatability of measurements. Therefore, their use is undesirable when performing high-precision measurements. When performing measurements, it is recommended that the direction of the motion vector of the measuring tip should be in a cone of ±20° relative to the normal vector to the surface point. It is considered ideal when the vector of the tip approaching the surface is perpendicular to the surface [3].

When performing measurements, compensation for the radius of the measuring sphere of the tip is mandatory. At the moment the sphere touches the surface, a mathematical shift in the measured coordinates occurs by the value of the probe radius. The direction of the shift is selected automatically by the software of the coordinate measuring machine.

The accuracy of measurements is greatly affected by the speed of movement of the measuring tip at the moment it touches the surface of the part. For example, according to the recommendations of Renishaw, the optimal speed of movement for most measuring sensors should be in the range from 0.5 mm/s to 40 mm/s. A speed of less than 0.5 mm/s leads to a decrease in accuracy due to malfunctions in the sensor trigger system and the occurrence of false alarms. Speeds above 40 mm/s reduce the measurement performance due to the presence of a shift in the contact point

as a result of the inertial overrun of this point. For the present measurements, a contact-speed range of 2 to 10 mm/s was selected [4]. Considering the possible breadth of the range of controlled parts, which can differ significantly from each other in their configuration, dimensions and requirements for the accuracy of dimensions and relative position of surfaces, modern coordinate measuring machines implement several measurement control modes. Manual and programmed control modes are distinguished [5]. These modes determine the method and level of interaction between the operator and the coordinate measuring machine. It is worth noting that the paper considers coordinate measuring machines equipped with servo drives with numerical control of the axes.

The manual mode of control of the coordinate measuring machine is the simplest. It assumes completely manual control of all movements by the operator. In this case, measurements are carried out sequentially point by point without pre-developed programs [6]. Registration of measurement results is carried out when the measuring tip touches the surface.

The advantages of using the manual mode are:

• no need for programming;

• applicability to individual parts, including those with a complex surface;

• low cost of measurements;

• low labor costs.

The disadvantages of the manual mode of control of the coordinate measuring machine are:

• low measurement productivity;

• increased measurement error due to the human factor (the operator does not always optimally select the speed of movement when touching the measured surface, and the direction of the motion vector of the measuring tip may differ from the normal to the surface by more than ±20°);

• difficulty in maintaining repeatable probe trajectories when measuring complex geometry [7].

Most often, the manual mode is used to measure parts that consist of the simplest geometric elements. In this case, it is easier to determine the correct approach vectors to the surface. It is also possible to use it to control parts with complex geometry for which a solid 3D model is not available.

The main recommendation when using the manual control method is to select the points that are most distant from each other when measuring a specific surface. This minimizes the ambiguity of the position of the geometric element. The main advantage of using coordinate measuring machines equipped with numerical control is the minimization of the human factor by automating the measurement process. Automation is achieved by creating a control program. The programmed control mode of the coordinate measuring machine is characterized by the following advantages:

• automation of the measurement process;

• the ability to use a solid 3D model to create a control program;

• high-precision measurements of complex surfaces;

• high measurement productivity;

• minimization of the human factor.

The disadvantages of the programmed control method are:

• high labor costs for creating a control program;

• complexity of implementing processes for measuring new parts;

• high requirements for operator qualifications.

High qualification requirements for the operator in the context of manual coordinate measuring machine (CMM) operation should be understood as a set of specialized competencies that directly affect measurement accuracy and repeatability.

First, it is critically important to understand the principles of orienting the probe relative to the surface normal. Even slight deviations in the probe approach vector can lead to significant coordinate errors.

Second, the operator must possess precise manual control skills for probe movement speed, especially in the contact zone. Insufficient smoothness or exceeding the allowable speed may result in inertial slipping of the stylus tip and distortion of the measured value.

Third, confident proficiency in fixturing methods based on the 3-2-1 system is required, including knowledge of positional tolerances for base elements and the ability to minimize the influence of residual play or misalignment during part clamping on the machine table.

Finally, the operator must be familiar with the geometry of the inspected component and be able to interpret the measurement results with consideration of potential deformations, form deviations, and applicable technological specifications. The absence of any of these skills significantly reduces the reliability of data obtained in manual mode.

The programmed method of coordinate measuring machine control is used to check serial parts, as well as in cases where high-precision measurements of important individual products are required. Programming is performed in the Dimensional Measuring Interface Standard language, which is a standard control language for coordinate measuring machines.

The structure of the Dimensional Measuring Interface Standard program consists of several key blocks located in a certain regulated sequence.

Definition of the part coordinate system;
Description of geometric elements;
Measurements;
Setting tolerances and checking the conformity of the measured dimensions;
Report generation.

When sequentially measuring several surfaces of one part, the group of blocks 2 - 4 is repeated. The commands that ensure the formation of the report can be specified both after each cycle of surface measurements and at the end of all measurements.

The commands that ensure the performance of surface measurements include a number of process parameters that describe the normals of approach to the surface and the speed of movement of the probe. This allows for high-precision measurements [8].

The software of coordinate measuring machines also has the ability to implement a self-learning mode. In this mode, the probe movement is controlled manually, but there is also the ability to simultaneously record the coordinates of points and commands into the control program. This allows for the optimization of the process of programming measurements of complex products that do not have a 3D model. The machine has the ability to recognize geometric elements and calculate the vectors for bringing the probe to the surface. Also, in the self-learning mode, the number of points for measuring specific surfaces can be set. That is, this process uses predefined algorithms to optimize measurement parameters (trajectories, touch points, speed, number of measurements, normal vector correction, etc.) based on the data obtained as a result of measurements in manual control mode. The purpose of this study is to determine the values of deviations from nominal dimensions when measuring a circle depending on the method of controlling a coordinate measuring machine. The paper examines manual and programmed control methods when measuring.

2. Materials and methods

The measurements were carried out using a coordinate measuring machine (CMM) Mezorix Atlas C 686 Basic, equipped with computer numerical control and servo drives along all axes. The main metrological characteristics of the machine comply with ISO 10360 standards: the maximum permissible error in length measurement (MPE_E) does not exceed $2.6 + L/300$ µm, and the maximum permissible probing error (MPE_P) does not exceed 2.4 µm. The working volume of the machine is limited to coordinates of 600×800×600 mm (X×Y×Z), which meets the dimensional requirements for typical diesel engine components.

A Renishaw TP20 touch-trigger probe with a standard force module was used as the measuring element. The diameter of the stylus ball was 4 mm, and the length of the stylus shaft from the ball center to the mounting point was 40 mm. The probe was mounted on a PH10T motorized indexing head, enabling angular orientation adjustments along axes A and B in 7.5° increments. Two positions were used during measurements: A = +45°; B = +90° and A = +45°; B = –90°, allowing access to opposite sides of the piston's cylindrical surface.

Prior to the measurements, spatial probe calibration was performed in each of the utilized positions in accordance with the CMM manufacturer's recommendations. Additionally, a repeatability check was conducted to confirm the stability of contact points.

Measurements were carried out in a dedicated metrology room with controlled climate conditions. The ambient temperature was maintained at (20 ± 0.5) °C, and the relative humidity did not exceed 50%. Before measurement, the piston underwent thermal stabilization for 4 hours to equilibrate with the laboratory environment, in accordance with GOST 8.563 and ISO 1 standards. This ensured the minimization of thermal expansion and eliminated temperature-induced errors that could affect high-precision measurement results.

The specified parameters of the experimental setup ensured a high level of reproducibility and objectivity of the acquired data, and enabled accurate comparison of results obtained in manual and programmed CMM operating modes.

The object of the study was a piston of a Cummins diesel internal combustion engine. For the study, it is proposed to measure the piston diameter in the measurement zone located at a distance of 119 mm from the end of the piston skirt. The measurement scheme is shown in Fig. 4. The diameter is measured in three sections, the middle of which is parallel to the axis of the hole for the piston pin, and the remaining two sections are at an angle of ±3° to the first section. This measurement scheme is due to the features of the automated control line at the manufacturing plant producing these pistons.

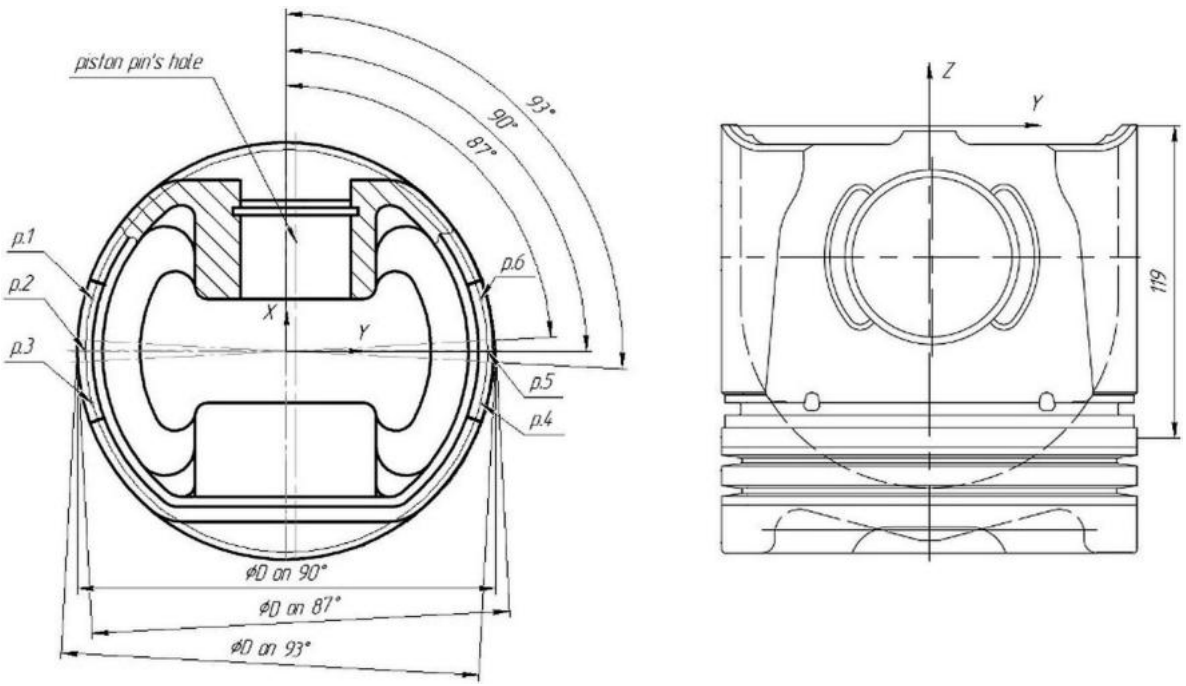

Fig. 4. - Piston-diameter measurement diagram: p.1-p.6 - measurement points in the specified section. Source: compiled by the authors.

The experimental procedure comprised three successive stages. First, the piston was fixtured on the CMM table. Second, the workpiece coordinate system was established. Third, the target diameter was measured first in manual mode and then in programmed mode.

At the basing stage, the piston was installed in the working volume of the coordinate measuring machine so that its axis was directed parallel to the Z axis of the machine, and the axis of the holes for the piston pin was parallel to the X axis. The basing was carried out on three point supports located under the piston bottom and an additional double guide base, ensuring the correct rotation of the piston around the Z axis (Fig. 5). This arrangement of the piston in space provides convenient access to the measured surfaces, and also allows you to set the coordinate system relative to the base surfaces.

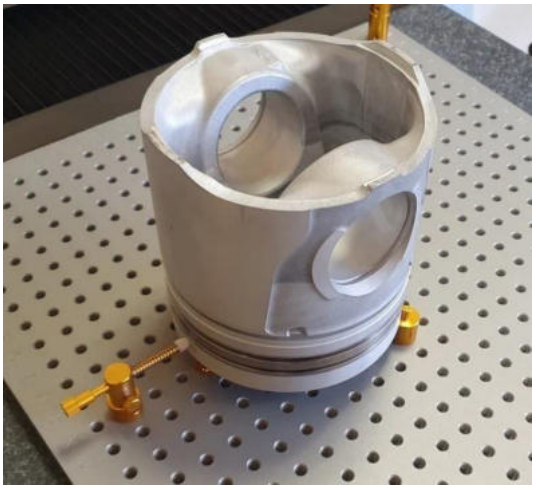

Fig. 5. - Cummins engine piston mounted on the coordinate measuring machine table. Source: compiled by the authors.

The coordinate system at the second stage was set in several successive steps according to the 3-2-1 system (plane, line, point).

Defining the base plane passing through the end surface of the piston skirt. This decision was made due to the specifics of setting the geometric dimensions on the design drawing of the part. The measurement was first carried out in manual mode with self-learning enabled (the software recorded the coordinates of the measured points and the approach vectors to them). Then, after creating a nominal plane passing through six measured points p.1 - p.6, the probe approach vectors and the speed of movement upon contact were adjusted in the software. A repeated

measurement of the base plane was carried out in the programmed mode to improve the accuracy of the measurements.

To set the direction of the X axis of the part coordinate system taking into account the requirements for carrying out measurements, the axis of the hole for the piston pin was measured. The measurements were also preliminarily carried out in manual mode with self-learning of the machine, and then re-measured in the programmed mode according to the calculated approach vectors and speed of movement.

To set the center of coordinates, the circumference was measured in one of the piston belts between the first and second compression rings. The circumference was measured at 6 points located approximately at the same distance from each other on the same diameter. The nominal circumference was determined in the software, and 6 points equally spaced along the circumference were programmed. As a result of the calculation, the approach vectors and the speed of movement were adjusted. Based on the results of repeated measurements in the programmed mode, the point of the center of coordinates of the part was calculated.

At the final step, the coordinate system of the part was combined with the machine coordinate system. This simplified the calculations carried out in the future.

Thus, due to the fact that the part will not be re-based, and the coordinate system is set once for both methods of controlling the coordinate measuring machine, this will not have an additional effect on the differences in the measurement results obtained in the third stage in the manual and programmed measurement modes.

The third stage of measurements was carried out separately in the manual mode, and then in the programmed mode. Let us consider the measurement technique in the manual control mode. Taking into account the performed alignment of the machine coordinate system and the part coordinate system, all movements were set manually via the joystick. For this purpose, the measuring head was initially rotated by an angle of A = +45° B = 90° in order to ensure that the probe tip touched the specified points. It should be noted that before the start of the study, the probe was calibrated in all positions in space required for testing (different angles A and B).

After selecting the required probe position, the measuring probe was moved to the height mark Z = –119 mm, which meets the requirements of the measurement scheme. Measurements were taken at three points. The probe of the coordinate measuring machine was moved to a safe distance, after which the position of the measuring head was changed to angles A = +45° B = -90°. Measurements were taken at the last three control points.

Since the points are located at an extremely small distance from each other when taking measurements according to the scheme shown in Fig. 4, it is not possible to determine and visually correct the approach vector in manual mode. Therefore, all measurements were taken in the direction parallel to the Y axis of the part. The speed control on the joystick was set with a limit of 10 mm/s. Based on the measurement results, the diameter of the circle in the required measurement zone was calculated.

To take measurements in programmed mode, it was initially necessary to create a control program. In the RationalDMIS software, program code can be created in two ways - by manually writing a text file with commands and developing a program based on a preliminary code obtained during self-learning.

In the case of manual code writing, it is necessary to take into account the idle stroke of the measuring head, which is always performed along the shortest path between two points. This prevents the measuring head from colliding with the part or technological equipment. If the operator does not have sufficient experience to write code manually, it is allowed to use the self-learning mode. The advantage of this method is the ability to pre-determine the trajectories of idle movements.

2. Results

Below is a comparison of the code commands obtained as a result of manual mode with self-learning mode enabled and programmed mode, with adjusted normal vectors of approach to measurement points.

Part of the code obtained with manual control with self-learning:

```
UNITS/MM, ANGDMS, MMPS
MODE/MAN
….
F(CIR5_L119)=FEAT/CIRCLE,OUTER,CART, -0.113, 1.038 -119.012,0.000,-0.000,1.000, 157.782
MEAS/CIRCLE, F(CIR5_L119), 6
  SNSLCT/S(D4X40_A45_B90)
  PTMEAS/CART,  -79.172,   4.149, -119.000, -1.000,  0.000, 0.000
  PTMEAS/CART,  -79.281,   0.000, -119.000, -1.000,  0.000, 0.000
  PTMEAS/CART,  -79.172,  -4.149, -119.000, -1.000, -0.000, 0.000
  SNSLCT/S(D4X40_A45_NB90)
….
  PTMEAS/CART,   79.172,  -4.149, -119.000,  1.000, 0.000, 0.000
  PTMEAS/CART,   79.281,   0.000, -119.000,  1.000,  0.000, 0.000
  PTMEAS/CART,   79.172,   4.149, -119.000,  1.000,  0.000, 0.000
```

Code obtained by programming:

```
UNITS/MM, ANGDMS, MMPS
MODE/PROG,MAN
…
```

```
F(CIR5_L119)=FEAT/CIRCLE,OUTER,CART,0.000,0.000,-119.000,0.000,-0.000,1.000, 157.782
MEAS/CIRCLE, F(CIR5_L119), 6
  SNSLCT/S(D4X40_A45_B90)
  PTMEAS/CART,  -79.172,   4.149, -119.000, -0.999,  0.052, 0.000
  PTMEAS/CART,  -79.281,   0.000, -119.000, -1.000,  0.000, 0.000
  PTMEAS/CART,  -79.172,  -4.149, -119.000, -0.999, -0.052, 0.000
  SNSLCT/S(D4X40_A45_NB90)
 …..
  PTMEAS/CART,   79.172,  -4.149, -119.000,  0.999, -0.052, 0.000
  PTMEAS/CART,   79.281,   0.000, -119.000,  1.000,  0.000, 0.000
  PTMEAS/CART,   79.172,   4.149, -119.000,  0.999,  0.052, 0.000
```

The measurement results are shown in Table 1.

Table 1. Results of piston-diameter measurements

Parameter	Manual measurement	Programmed measurement
Nominal diameter according to drawing, mm	157.782	
Maximum deviations according to the drawing, mm	±0.08	
Nominal element	circle	circle
Actual size, mm	157.7377	157.7550
Actual deviation, mm	-0.0443	-0.0270

Source: compiled by the authors.

In addition to the numerical values presented in Table 1, it is important to highlight the nature of the point distribution recorded in each measurement mode. In manual CMM operation mode, a greater dispersion of the measured point coordinates relative to the nominal circle was observed, indicating variability in probe contacts due to the inability to precisely control the approach vector direction and maintain consistent movement speed. In practice, this results in increased ellipticity of the calculated circular profile and a rise in the standard deviation of point coordinates.

In contrast, the programmed mode showed more uniform deviations symmetrically distributed about the center, indicating stable orthogonality of probe contacts and high contact reproducibility. These observations confirm that the trajectory and angular precision of probe approach significantly affect the final diameter measurement value.

To increase the statistical reliability of the conducted study, a series of repeated measurements of the target piston diameter of a Cummins diesel engine was performed using two coordinate measuring machine (CMM) operating modes: manual and programmed. In each mode, 10 measurements of the same diameter were carried out. The measurement results were subjected to statistical analysis, including the calculation of standard deviation (σ), range (R), and measurement uncertainty (U).

The results are presented in Tables 2 and 3.

Table 2. Repeated piston-diameter measurements

Experiment number	Programmed mode, mm	Manual mode, mm
1.	157.7554	157.7356
2.	157.7546	157.7355
3.	157.7556	157.7396
4.	157.7566	157.7273
5.	157.7545	157.7284
6.	157.7545	157.7362
7.	157.7564	157.7415
8.	157.7557	157.7393
9.	157.7543	157.7407
10.	157.7548	157.7377

Source: compiled by the authors.

Table 3. Statistical characteristics of piston-diameter measurements

Measurement mode	Average value, mm	Standard deviation (σ), mm	Range (R), mm	Uncertainty (U), mm
Programmed	157.7548	0.0012	0.0039	±0.0024
Manual	157.7382	0.0057	0.0191	±0.0114

Source: compiled by the authors.

In the programmed mode, the evaluated parameters confirm high repeatability and stability of measurement results, all of which remained within the tolerance limits of ±0.08 mm. In contrast, the significantly higher values of standard deviation (σ) and range (R) observed in the manual mode indicate a pronounced influence of the human factor, primarily associated with inconsistent approach speeds and suboptimal probe approach vectors to the measured surface.

To assess measurement reproducibility, three different operators were involved, each performing a series of five measurements in manual mode. The analysis revealed substantial inter-operator variability: the mean diameter values ranged from 157.7359 mm to 157.7408 mm, while standard deviations varied from 0.0049 mm to 0.0063 mm. In the programmed mode, operator-induced variation was minimal, with mean diameter values ranging from 157.7545 mm to 157.7551 mm and standard deviations between 0.0010 mm and 0.0014 mm. These results underscore the advantage of the automated approach.

Thus, the supplementary experiments confirmed that the programmed CMM operation mode exhibits high repeatability and reproducibility, whereas the manual mode requires a highly skilled operator and results in significant variability in measurement outcomes. The findings of this study provide a well-grounded basis for recommending the programmed CMM mode for serial production and high-precision inspection tasks.

3. Discussion

The analysis of error sources recorded during measurements performed in both manual and programmed modes of coordinate measuring machine (CMM) operation necessitates a comprehensive consideration of the entire set of factors influencing the final deviation from the nominal value. In manual mode, the most significant contribution to the total error arises from the human factor. The key manifestations include deviation of the probe approach vector from the surface normal and instability of approach speed during contact. Even when limiting the speed to 10 mm/s, the operator is not always able to ensure strictly perpendicular contact—particularly in conditions of densely positioned measurement points, where visual vector correction becomes challenging.

An additional source of error is the positioning inaccuracy of the CMM itself, which occurs due to the lack of automatic trajectory error compensation in manual mode. In programmed mode, these errors are substantially minimized thanks to algorithmically calculated probe trajectories based on the nominal geometry of the part.

Thermal effects also impact measurement accuracy—both in terms of thermal expansion of the component and potential thermal drift of the CMM's mechanical elements. However, these factors influence both modes equally and can be considered background variables in the context of this study.

Fixturing error, despite the use of a consistent 3-2-1 method and the absence of reclamping, may result in localized micromovements during manual setup due to contact forces, especially during the initial self-learning phase.

Finally, stylus calibration in various spatial orientations is essential but not absolute. Minor deviations in compensation radius at different angular positions can also affect accuracy, particularly in manual mode, where contact repeatability is lower.

Both measurement results remained within the specified tolerance of ±0.08 mm. The programmed mode yielded an actual deviation of -0.0270 mm, whereas the manual mode yielded -0.0443 mm. Accordingly, programmed control reduced the absolute deviation from the nominal diameter by 39.1%. The programmed result therefore provides a larger tolerance reserve, which is important for serial inspection because it reduces the probability of false rejection and repeated measurement.

The repeated-measurement series supports the same conclusion. The mean values obtained in programmed and manual modes were 157.7548 and 157.7382 mm, corresponding to deviations from the nominal diameter of -0.0272 and -0.0438 mm, respectively. The standard deviation decreased from 0.0057 mm in manual mode to 0.0012 mm in programmed mode, while the uncertainty decreased from ±0.0114 to ±0.0024 mm.

The 4.75-fold reduction in both standard deviation and uncertainty demonstrates the higher repeatability and stability of programmed measurements. These results are consistent with the metrological characteristics of the Mezorix Atlas C 686 Basic CMM and confirm that trajectory control has a stronger effect on result dispersion than on the systematic difference between the measured and nominal diameters.

The programmed measurement routine contains approach vectors (I, J, K) refined according to the nominal geometry. Although the vector values differ only slightly between manual measurement (-1.000, 0.000, 0.000) and programmed measurement (-0.999, 0.052, 0.000), the correction aligns the probe motion more closely with the surface

normal. In manual mode, the proximity of the control points prevents reliable visual correction of the approach direction. The self-learning mode is therefore useful for generating an initial program and recording collision-free intermediate trajectories, after which the approach vectors and contact speed should be optimized in RationalDMIS. Self-learning does not eliminate operator-induced variation during manual probing. The combined procedure preserves the practical advantages of manual trajectory definition while providing the repeatability of programmed control. The unchanged 3-2-1 fixturing scheme and the single workpiece coordinate-system setup excluded re-fixturing error from the comparison.

The novelty of this study lies in the comprehensive evaluation of coordinate measurement accuracy during inspection of the cylindrical surface of a diesel engine piston, specifically in a zone defined by the production process (at a distance of 119 mm from the piston skirt), utilizing both programmed and manual CMM modes, including the self-learning mode. Unlike previously published works, which focused on the measurement of simple geometric elements under laboratory conditions or with complete CAD modeling, the present study implements a hybrid approach: the measurement program is generated programmatically based on trajectories initially obtained in manual mode using the built-in self-learning algorithm.

A distinctive feature of the experiment is the execution of measurements in a zone with limited visualization and densely arranged control points, where visual correction of the probe approach vector in manual mode is virtually impossible. In this context, for the first time, a qualitative comparison has been conducted between the effects of nominal approach vectors calculated via self-learning and those defined manually by the operator. The analysis provides a quantitative assessment of the advantages of the programmed mode with refined approach parameters under conditions of high-precision inspection of a typical precision-manufactured component.

Thus, the contribution of this work extends beyond empirical comparison of the two CMM control modes; it demonstrates the practical significance of self-learning algorithms as an intermediate stage in the development of measurement routines in the absence of a CAD model - an aspect that has not been sufficiently addressed in existing scientific literature.

Conclusions

The use of the programmed control mode of a coordinate measuring machine is preferable when solving problems that require high accuracy and repeatability of results, as well as in the case of use in serial production. The manual control mode with self-learning enabled is proposed to be used to obtain the initial code taking into account the trajectories of the part and technological equipment during the measurement process. It is also possible to use it when checking non-standard parts for which the development of a full-fledged measurement control program is impractical for economic and time reasons. In addition, it can be reliably stated that obtaining accurate measurement results in manual mode requires a highly qualified operator.

Based on the results obtained, the following recommendations are proposed to ensure the most accurate measurement results:

1. Priority selection of the programmed mode.
2. Use of data obtained in the self-learning mode to minimize the time spent on program development.
3. Control of the probe approach speed and the direction of approach to the surface.
4. Training coordinate measuring machine operators in new methods.

The self-learning mode is a convenient tool for obtaining initial data for developing a control program for coordinate measuring machines.

The practical significance of the study lies in the developed recommendations for selecting control modes for a coordinate measuring machine, taking into account the type of production and requirements for measurement accuracy. The results obtained can be applied to real manufacturing enterprises that carry out quality control using CMMs.

Further research can be aimed at optimizing the time spent on measurements and drawing up control programs for CMMs. Also promising is the analysis of the possibility of drawing up control programs using the capabilities of artificial intelligence [9, 10]. These areas of further research will improve the efficiency of using coordinate measuring machines and significantly simplify the implementation of automated solutions in production.

Programmed control increased measurement quality in two complementary respects. The absolute deviation from the nominal diameter decreased from 0.0443 to 0.0270 mm, corresponding to a 39.1% reduction, while the standard deviation decreased from 0.0057 to 0.0012 mm, corresponding to a 4.75-fold improvement in repeatability. These effects provide a larger tolerance reserve and reduce the likelihood of inspection errors in serial production.

The obtained results demonstrate that the application of optimized approach algorithms (in terms of vector direction and speed) can significantly improve measurement quality even in the absence of a complete CAD model. Moreover, the use of self-learning mode proves to be an effective tool for accelerated generation of measurement programs.

Acknowledgements
The article was prepared as part of the research work implemented at the expense of the federal budget (source of funding - the Ministry of Education and Science of Russia) on the topic: "Development of scientific, methodological and practical foundations of reverse engineering for solving complex problems of import substitution in the agro-industrial complex of the Russian Federation" (code of scientific topic FZNW-2024-0026).

References
[1] Pugliese R., Regondi S., Marini R. Machine learning-based approach: global trends, research directions, and regulatory standpoints // Data Science and Management, Vol. 4, 2021. - p. 19-29. DOI: 10.1016/j.dsm.2021.12.002.
[2] Transcat. Calibration of CMM Probe Qualification Sphere. Available at: https://www.transcat.com/calibration-resources/white-papers/qualification-sphere-calibration-quality-assurance-cmm-probe (accessed 25 June 2025).
[3] Cauchick-Miguel P.A., King T.G. Factors which influence CMM touch trigger probe performance. // International Journal of Machine Tools and Manufacture, Vol. 38, Issue 4, 1998. - p. 363-374. DOI: 10.1016/S0890-6955(97)00054-0.
[4] Mian N.S., Fletcher S., Longstaff A.P. Reducing the latency between machining and measurement using FEA to predict thermal transient effects on CMM measurement // Measurement, Vol. 135, 2019. - p. 260-277. DOI: 10.1016/j.measurement.2018.11.034.
[5] Dobosz M., Wozniak A. CMM touch trigger probes testing using a reference axis // Precision Engineering, Vol. 29, Issue 3, 2005. - p. 281-289. DOI: 10.1016/j.precisioneng.2004.11.008.
[6] Weckenmann A., Estler T., Peggs G., McMurtry D. Probing systems in dimensional metrology // CIRP Annals - Manufacturing Technology, Vol. 53, Issue 2, 2004. - p. 657-684. DOI: 10.1016/S0007-8506(07)60034-1.
[7] Watanabe M., Sato O., Matsuzaki K., Kajima M., Watanabe T., Bitou Y., Takatsuji T. Accurate surface profile measurement using CMM without estimating tip correction vectors // Precision Engineering, Vol. 91, 2024. - p. 233-241. DOI: 10.1016/j.precisioneng.2024.09.009.
[8] Urban J., Resl J., Beranek L., Koptis M., Petrasek S. Optimizing coordinate measuring machine measurement plans: economic benefits and environmental impact // Journal of Cleaner Production, Vol. 477, 2024. - 143891. DOI: 10.1016/j.jclepro.2024.143891.
[9] Kugunavar S., Iyer S.V., Sangwan K.S., Bera T.C. Data-driven model for CMM probe calibration to enhance efficiency and sustainability // Procedia CIRP, Vol. 122, 2024. - p. 885-890. DOI: 10.1016/j.procir.2024.01.121.
[10] Cheng Z.-Y., Sun Y., Hu K., Li J., Lu T.-F., Li R.-J. Deep learning-based intelligent measurement methods and system for CMM // Measurement, Vol. 221, 2023. - 113474. DOI: 10.1016/j.measurement.2023.113474.

Information of the authors

Nefelov Ilya, State University of Management
e-mail: nefelov.sum@bk.ru

Filatov Vladimir, State University of Management
e-mail: filatov.isc@bk.ru

Taldykin Dmitriy, State University of Management
e-mail: taldykin.sum@bk.ru

DOI 10.52209/2706-977X_2026_3_13 IRSTI 81.09.07 UDC 678.067.5

CLT-Based Mechanical Characterization of Hybrid Composites with Carbon/Kevlar/Steel and Glass/Kevlar/Steel Layers

Dalavi A.M.[1, 2], Jadhav A.A.[3]
[1]Symbiosis Institute of Technology, Pune, Maharashtra, India
[2]Symbiosis International (Deemed) University, Pune, Maharashtra, India
[3] College of Engineering, Pandharpur, Maharashtra, India

Abstract. The composite materials with hybrid structure with use of metalsare gaining attention nowadays. This article presents a step by step method for performing Classical Laminate Theory (CLT) for calculations on hybrid laminates with different stacking sequences. Hybrid fiber metal laminates (FMLs) provide an effective way to maintain stiffness, strength, and damage resistance for advanced structural applications. This study compare two hybrid laminates: Carbon/Kevlar/Mild Steel Wire Mesh (CKMS) and Glass/Kevlar/Mild Steel Wire Mesh (GKMS), byusing Classical Laminate Theory (CLT).Both laminates were physically fabricated using the hand lay-up technique maintaining the same overall thickness and number of layers, primarily to maintain a constant fiber volume fraction of 50%. The mechanical properties reported were theoretically predicted by means of Classical Laminate Theory by evaluating the extensional (A), coupling (B) and bending (D) stiffness matrices. The CKMS laminate showed good stiffness, with tensile moduli of 148.81 &130.81 GPa in X and Y directions respectively compared with 85.70 &72.30 GPa respectively for GKMS. Its flexural modulus reached to92.75 GPa, more than 200% higher that of GKMS **(**30.24 GPa**),** while the shear modulus varied from 25.79 GPa (GKMS) to 40.22 GPa(CKMS) due to the contribution of carbon fibers and ±45° mild steel mesh. The results highlight the strong influence of carbon-based hybridaz tion and stacking sequence on-extensional, bending, and shear responses, while the glass-based system offers a more compliant and cost-effective alternative. The proposed CLT-based comparison framework supports the design of lightweight, high-stiffness components for aerospace panels, UAV structures, automotive skins, marine components, and impact-resistant engineering applications.

Keywords: Hybrid laminates, Classical Laminate Theory, ABD matrix, Fiber orientation, Structural stiffness.

Nomenclature and Glossary

In order to make the discussion transparent to the audience in any field of engineering, the definitions of the following acronyms, symbols and technical terms will be used in this study:
CLT: Classical Laminate Theory-A theoretical model on which the mechanical behavior of thin composite laminates is predicted using an in-plane forces and moments relative to strains and curvatures.
FML: Hybrid fiber–metal laminates
ABD Matrix: The integrated stiffness matrix of a laminate, consisting of the extensional (A), coupling (B), and bending (D) matrices.
GSM: Grams per Square Meter-A standard measure of the areal density or surface weight of fiber reinforcements.
CKMS: Carbon/Kevlar/Mild Steel-The hybrid laminate configuration investigated as Laminate 1.
GKMS: Glass/Kevlar/Mild Steel-The hybrid laminate configuration investigated as Laminate 2.
E_1, E_2: Youngs longitudinal and transverse Moduli of one ply (lamina).
G_{12}: Shear-in plane modulus of a lamina.
$\boldsymbol{\nu_{12}}$: Ratio of transverse strain to longitudinal strain when axial loaded (major Poisson ratio).
[Q] and $[\bar{Q}]$**:**Simplified and transformed reduced stiffness matrices, which specify the stress strain relation of a single ply in principle and global coordinates.
[A]: Extensional Stiffness Matrix-Relates in-plane forces to mid-plane strains.
[B]: Coupling Stiffness Matrix-Quantifies the interaction between in-plane forces and bending curvatures.
[D]: Bending Stiffness Matrix-Relates bending moments to curvatures, representing out-of-plane rigidity.
Anisotropy: A characteristic of materials where mechanical properties vary depending on the direction of the applied load.
Bending-Extension Coupling: A mechanical phenomenon where axial loading induces bending or twisting in a laminate due to an asymmetric stacking sequence.
Fiber Volume Fraction (v_f): The percentage of the total volume of a composite material occupied by the reinforcing fibers.

Introduction

Hybrid composite materials have been of increasing concern in structural and mechanical engineering practice because of their ability to include several the desired properties, which includes high specific strength, high resistance

to corrosion, energy absorption, and adjustable mechanical [1][2][18]. Such systems take advantage of the special characteristics of various reinforcing phases like carbon, glass, Kevlar fibres, metallic wire meshes and polymeric matrices like epoxy to develop materials that have better performance-to-weight ratios and enhanced multi-functionality [4][5]. The combination of the various fibres enables the hybrid laminates to achieve an optimal balance between stiffness, strength, toughness and cost-efficiency as they are specifically applicable to the aerospace, automotive, marine as well as defence sectors [15][7].

The traditional single-fibre composite is limited mostly by inherent change in the material. An example, for carbon fibres, which have high tensile and flexural stiffness but they are brittle in the impact loading [8][9]. On the other hand, Kevlar fibres are tough and have high impact resistance but with low compressive and transverse strength [10][23]. Glass fibres, while moderately strong and economically viable, may fall short in high-performance environments requiring superior fatigue or thermal resistance [28][17] Integrating mild steel wire mesh into these composites further enhances mechanical performance especially in shear and impact resistance by distributing load more effectively and improving inter-laminar stress transfer when embedded in an epoxy [12][13].

The present work extends Classical Lamination Theory beyond its standard textbook application to homogeneous fibre–polymer laminates by introducing a hybrid fibre–metal–mesh architecture that integrates mild steel wire mesh with carbon, glass, and Kevlar plies. Unlike conventional Fibre Metal Laminate (FML) studies that primarily examine aluminium–fibre systems such as GLARE and CARALL with emphasis on impact or fatigue behavior, this study focuses on stiffness and coupling characteristics using the complete ABD formulation[4][9][17][19][39][41][42]. While CLT has been applied to predict the stiffness behavior of conventional fibre-reinforced polymers and established Fibre Metal Laminates (FMLs) such as GLARE with continuous metallic sheets [4][17][39], most existing analytical and experimental investigations focus on traditional metal–fibre architectures. In addition, a large portion of recent FML research concentrates on impact response and damage mechanisms rather than stiffness modeling using CLT [40]. In this, there is a gap in the application of CLT to **hybrid laminates with mild steel wire mesh as a secondary reinforcement**. The strategic placement of wire mesh to enhance inter-laminar shear and impact resistance which modify the bending–extension coupling behavior in ways that are not captured by conventional laminate models. At present, a controlled, CLT-based comparison between a steel-wire-mesh hybrid laminate and a traditional all-fibre laminate of identical ply count, thickness, and fibre volume fraction is lacking. This study addresses this gap by employing CLT to quantify how the integration of mild steel wire mesh influences the complete ABD stiffness matrix particularly the coupling and bending components thereby providing design guidance for next-generation lightweight and damage-tolerant composite structures.

This paper uses CLT to compare and contrast the behaviour of two hybrid epoxy laminates in regard to stiffness behaviour. The two laminates are similar in the number of ply and the thickness, only that the fibre types and stacking structure vary. Through calculation of the overall ABD stiffness matrices, this paper determines the effects of fibre hybridization on the extensional stiffness, the coupling effect and the bending performance. The findings can be used as a theoretical reference in practice, as well as in designing and optimising fibre metal laminates in the contexts where the reduction of weight, impact resistance, and structural reliability are [8][18][12].

1. Materials and Methods

1.1 Materials Used

These hybrid composite laminates were made by employing four varieties of reinforcements in the form of carbon fiber, Kevlar fiber, glass fiber and mild steel mesh wire incorporated in a thermosetting epoxy resin content of the laminate. Fiber reinforcement was done at a surface weight of 300 grams per square meter (GSM), and a constant weight ratio of 50:50 fiber/resin was used to achieve the best impregnation, even distribution of load, and manufacturability of the structure [3]. Unidirectional carbon fibers were used because they have superior tensile strength and stiffness and because they were purposefully placed at 0^0 and 90^0 in the laminate so that they could carry maximum axial and transverse loads. Kevlar fibers which are the best in toughness and resistance to impact were used at 0^0 orientations in order to promote longitudinal tensile behavior and better damage tolerance when progressing under dynamic loading conditions. A single type of $+\text{-}45^0$ orientations was used with mild steel (MS) wire mesh to add ductility and interlayer toughening in addition to better in-plane shear behaviors. The $+\text{-}45^0$ and 90^0 oriented woven glass fibers were used to provide a more economical way of supporting off-axis and transverse loading without excessive effect on mechanical integrity. The type of matrix system was Araldite LY566 and Aradur 22,962 (hardener) [6], which offered environmental inclusivity, dimensional stability, and effective transfer of stress between dissimilar phases of reinforcement during mechanical loading and curing.

Two hybrid laminate systems were manufactured and analytical compared, including: Carbon/Kevlar/Mild Steel wire mesh and Glass/Kevlar/Mild Steel wire mesh laminates. The high stiffness and load-bearing capability of carbon fibers, moderate cost-effectiveness and stiffness of glass fibers, and toughness and damage resistance of Kevlar fibers were used. M.S. wire mesh was also applied as another reinforcement to enhance the inter-laminar load transfer and shear resistance. All layers were supposed to be parallel in the main direction of the material in accordance to CLT. Both the lamina were treated as orthotropic, linear elastic materials characterized in terms of their elastic

constants. An epoxy resin matrix was also assumed to provide sufficient bonding and load compatibility between the fiber layers and the steel mesh.

The laminate stacking patterns were clearly stipulated in the manuscript and they were utilized in the construction of the laminate stiffness matrices. Analytical homogeneity was applied with uniform thickness of the ply and identical fiber volume fraction. In spite of the fact that the study is mainly analytical, the laminates are associated with configurations that may be produced using traditional techniques like hand lay-up, then compression molding or vacuum bagging, and meaningful comparisons can be made between CLT predictions and experimental flexural performance.

1.2 Material Properties

The reinforcement materials are important in ensuring the required degree of mechanical performance. The main reinforcements were carbon fiber, glass fiber and Kevlar fiber because they had different elasticity properties. Carbon fiber is very stiff with longitudinal modulus of 135Gpa(E_1), transverse modulus of 10Gpa(E_2), shear modulus of 5Gpa(G_{12}) and Poisson ratio of 0.28. At the balance point of mechanical behaviour, glass fiber exhibits balanced behaviour E_1 = 50 GPa, E_2 = 15 GPa, G_{12} = 5 GPa, and ν_{12} = 0.28, while Kevlar fiber provides enhanced toughness with E_1 = 76GPa, E_2 = 5 GPa, G_{12} = 2 GPa, and ν_{12} = 0.34. Each of the fibers was woven in mat form with the areal density of 300 GSM. The secondary reinforcement is done with mild steel wire mesh to increase stiffness and load bearing capacity. The material of the mesh was low-carbon mild steel, the wire diameter is 1 mm, and the isotropic elasticity, which comprises the Youngs modulus and shear modulus is 200 Gpa, and Poisson ratio is 0.30 for solid wire

1.3Laminate Configuration

Two hybrid laminates of different stacking sequences were created and tested. The laminates were developed with each laminate having exploited directional strengths of the constituent and still being balanced and symmetric. Tensile strength, flexural strength and shear strength of fiber hybrid composite laminates is quite different in relation to sequencing of fiber stacking [11].

1.4 Laminate Configuration and Design Logic

The stiffness of the hybrid laminates is mainly determined by stacking arrangement, ply orientations, thickness distribution and addition of mild steel wire mesh layer. Both laminates have the same number of ply and a combined thickness so that a fair comparison can be made of CLT based. The combination of 0^0, 90^0, and $+\text{-}45^0$ orientations can achieve effective multi-axial load transfer with 0deg plies controlling the extensional stiffness A_{11}, 90^0 plies controlling the A_{22} and $+\text{-}45^0$ plies controlling the in-plane shear stiffness A_{66}. The $+\text{-}45^0$oriented mild steel wire mesh enhances shear transfer and inters laminar redistribution stress, alters B matrix behavior, reflected on bending-extension coupling. The stiffness and location of outer plies determine the bending stiffness D matrix, where carbon and Kevlar plies close to the surfaces enhance D_{11} and D_{22}. Therefore, the chosen stacking structure has a direct control on the extensional, coupling and bending responses through the ABD formulation.

Laminate 1 (CKMS): Carbon/Kevlar/Mild Steel Wire Mesh

Stacking Sequence: [0° Carbon / 0° Kevlar / +45° MS / −45° MS / −45° MS / +45° MS / 0° Kevlar / 90° Carbon].The stacking sequence is shown in Figure 1.

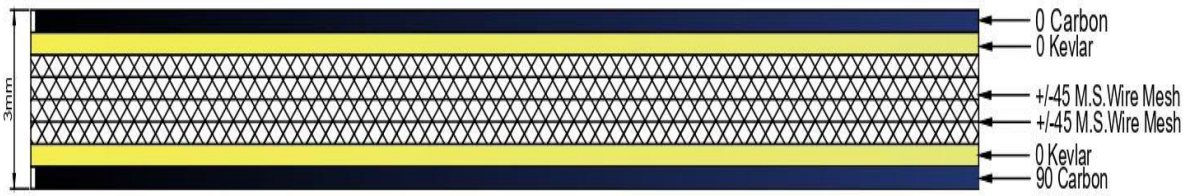

Fig. 1. - Laminate 1- Carbon+Kevlar+M.S.Wire Mesh.

This eight-ply hybrid laminate combines the high stiffness of carbon fiber with the toughness of Kevlar and the ductility of mild steel mesh. The stacking was optimized to enhance tensile performance along the longitudinal axis while preserving transverse and shear strength.

Laminate 2 (GKMS): Glass/Kevlar/Mild Steel Wire Mesh

Stacking Sequence:[+45° Glass / -45° Glass / 0° Kevlar / +45° Mild Steel / -45° Mild Steel / 0° Kevlar / -45° Glass / 90° Glass].The stacking sequence is shown in Figure 2.

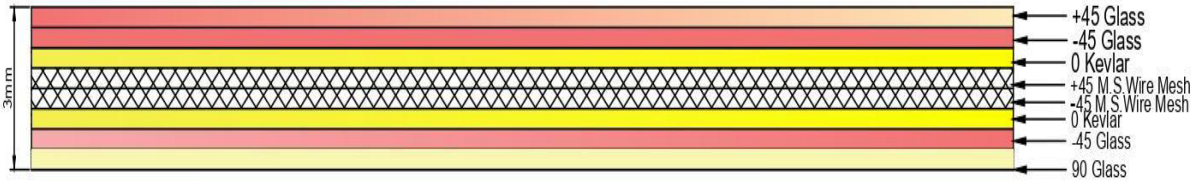

Fig. 2. - Laminate 2 - Glass+Kevlar+M.S.Wire Mesh.

This configuration emphasizes shear and flexural response with fewer layers. The use of woven glass fiber in off-axis and transverse directions helps reduce cost while contributing to a moderate-strength, high-ductility design.

1.5 Fabrication of Hybrid structure Composite Laminates

Overall, composite materials are manufactured with different number of processes. The choice of a specific production method strongly depends on chemical properties of matrix, and also the nature of final product's shape. Hand layup process was selected because it enables precise placement of composite layers and the mild steel wire mesh, ensuring good alignment, uniform resin impregnation and good interfacial bonding.

1.5.1 Setup for laminate manufacturing

After the hand layup process is finished the setup for further process is as shown in Figure 3.

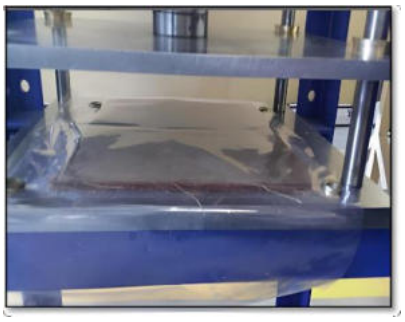

Fig.3.-Setup for laminate manufacturing

1.5.2 Volume fraction Calculation

Fiber volume fraction is the percentage of fiber volume in the entire volume of a fiber-reinforced composite material. The details are listed in Table 1

Table1. Volume fraction calculation

Sr. No	Carbon/Epoxy laminate	Weight of laminates(g)	No. of plies	Weight of fiber(g)	Weight of matrix(g)
1	Laminate1	440	8	250	190
2	Laminate2	440	8	250	190

1.5.3Volume Fraction of Hybrid composite fiber in Hybrid Composite/Epoxy Laminates And (2).

Volume fraction of the Hybrid fibre in the hybrid composite/Epoxylaminatesof440 g, v is given by the following formula.

$$V_{cf} = \frac{(W_{cf}/\rho_{cf})}{(W_m/\rho_m)+(W_{cf}/\rho_{cf})} x100 \quad (1)$$

$$= \frac{250/1.58}{190/1.22+250/1.58} x100 \quad (1.1)$$

$$= 50.39 \cong 50\%$$

where W_{cf}=Weight of Carbon fibre

ρ_{cf}=Density of Carbon fibre

W_m= Weight of matrix

ρ_m=Density of matrix.

1.6 Manufactured Laminates

The manufactured laminate CKMS is represented in Figure 4 and GKMS is represented in Figure 5 respectively.

Fig.4. - Laminate 1 (Carbon+Kevlar+M.SWire) after manufacturing.

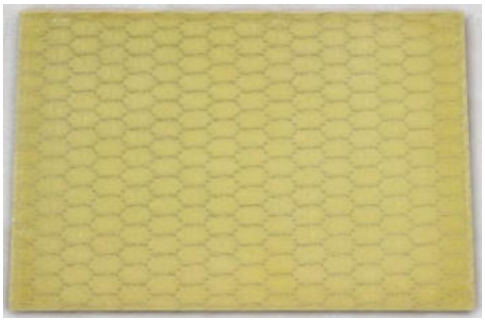

Fig. 5. - Laminate 2 (Glass+Kevlar+M.S. Wire) after manufacturing.

1.7 Simplified Classical Laminate Theory Methodology

The systematic methodology presented in this work consists of a structured sequence involving (i) selection of materials (carbon, glass, Kevlar, and mild steel wire mesh), (ii) stacking sequence design including ±45° mesh layers, (iii) analytical evaluation of laminate stiffness using Classical Lamination Theory (ABD formulation), (iv) fabrication of hybrid laminates via hand lay-up, each step is explicitly defined to ensure repeatability and consistency across laminate configurations.

Moreover, the suggested framework is scalable since the identical CLT-based design analysis validation pipeline can be applied directly to other fiber-metal hybrid laminates by replacing other types of fibers, metal meshes, volume fractions or orientations without changes in the analytical or experimental workflow.

The simplified Classical Laminate Theory methodology, which is shown in figure 6, describes the process starting with the input of material properties through to the development of a stiffness matrix and the effective laminate property assessment.

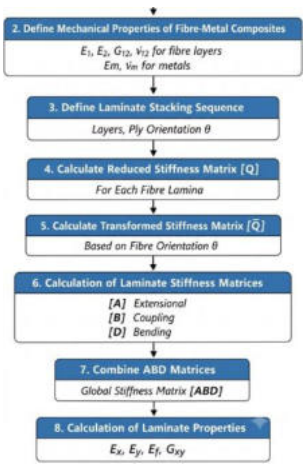

Fig. 6.- Simplified Classical Laminate Theory (CLT) Methodology Flowchart

1.8CLT-Based Theoretical Analysis

Analytical prediction of the mechanical behavior of the hybrid composite laminates under in-plane loading conditions and bending were made by use of Classical Laminate Theory (CLT). CLT assumes linear elastic behavior, ideal bonding between layers, and negligible transverse shear deformation, making it suitable for analyzing thin laminate structures [15]

1.8.1 Reduced Stiffness Matrix [Q]

The constitutive behavior of a single orthotropic lamina in its principal material axes is represented using the reduced stiffness matrix [Q], defined as [26]

$$\begin{bmatrix} \sigma x \\ \sigma y \\ \sigma xy \end{bmatrix} = \begin{bmatrix} Q_{12} & Q_{12} & 0 \\ Q_{12} & Q_{22} & 0 \\ 0 & 0 & Q_{66} \end{bmatrix} . \begin{bmatrix} \varepsilon_x \\ \varepsilon_y \\ \gamma_{xy} \end{bmatrix} \quad (2)$$

The components are as follows:

$$Q_{11}=\frac{E_1}{(1-\nu_{12})}\ ,\ Q_{12}=\frac{\nu_{21}E_1}{(1-\nu_{21}.\nu_{21})}\ ,\ Q_{22}=\frac{E_2}{(1-\nu_{12}\nu_{21})},\ Q_{66}=G_{12},\quad \nu_{21}=\nu_{12}.\frac{E_2}{E_1} \quad (3)$$

where $E_1$is Young's modulus in the longitudinal direction.

E_2 is Young's modulus in the transverse direction.

ν_{12} &$\nu_{21}$are poisons ratio

G_{12}= Modulus of Rigidity

1.8.2 Transformed Stiffness Matrix [$\bar{Q}$]

To account for different ply orientations within the laminate, the reduced stiffness matrix is transformed to the global coordinate system using the following expressions [25].

$$\bar{Q} = \begin{bmatrix} Q_{11} & Q_{12} & Q_{16} \\ Q_{12} & Q_{22} & Q_{26} \\ Q_{16} & Q_{26} & Q_{66} \end{bmatrix} \quad (4)$$

Each component is calculated from the original Q matrix and the ply angle θ

$$\bar{Q}_{11}= Q_{11}m^4+2(Q_{12}+2Q_{66})\ m^2n^2+Q_{22}n^4 \quad (4.1)$$

$$\bar{Q}_{12} = (Q_{11}+Q_{22}-4Q_{66})\ m^2n^2+Q_{12}(m^4+n^4) \quad (4.2)$$

$$\bar{Q}_{22} =Q_{11}n4+2(Q_{12}+2Q_{66})m^2n^2+Q_{22}m^4 \quad (4.3)$$

$$\bar{Q}_{16} = (Q_{11}-Q_{12}-2Q_{66})m^3n-(Q_{22}-Q_{12}-2Q_{66})mn^3 \quad (4.4)$$

$$\bar{Q}_{26}=(Q_{11}-Q_{12}-2Q_{66})mn^3-(Q_{22}-Q_{12}-2Q_{66})m^3 \quad (4.5)$$

$$\bar{Q}_{66}=(Q_{11}+Q_{22}-2Q_{12}-2Q_{66})m^2n^2+Q_{66}(m^4+n^4) \quad (4.6)$$

where m= cosθ & n=sinθ

These transformed matrices are calculated for each ply based on its fiber orientation angle θ.

1.8.3 The ABD matrix has three blocks

A: Extensional stiffness matrix (in MPa.mm)

B: Coupling stiffness matrix (in MPa.mm^2)

D: Bending stiffness matrix (in MPa.mm^3)

A Matrix Structure

This matrix represents the in-plane stiffness of the laminate. It relates in-plane forces (N_x, N_y, N_{xy}) to mid-plane strains (ε_x, ε_y, γ_{xy}) [17]

$$\begin{bmatrix} N_x \\ N_y \\ N_{xy} \end{bmatrix} = \begin{bmatrix} A_{11} & A_{12} & A_{16} \\ A_{12} & A_{22} & A_{26} \\ A_{16} & A_{26} & A_{66} \end{bmatrix} . \begin{bmatrix} \varepsilon_x \\ \varepsilon_y \\ \gamma_{xy} \end{bmatrix} \quad (5)$$

where A_{11}: Stiffness in the x-direction due to strain in the x-direction (analogous to axial stiffness (E_x)

A_{22}: Stiffness in the y-direction due to strain in the y-direction (E_y)

A_{12}: Coupling stiffness between ε_x and N_y or ε_y and N_x (Poisson effect)

A_{66}: Shear stiffness for in-plane shear strain γ_{xy} and in-plane shear force N_{xy} A_{16}: Coupling between axial strain ε_x and in-plane shear force N_{xy} (asymmetry in fiber angle causes this)

A_{26}: Coupling between axial strain ε_y and shear force N_{xy}

1.8.4 Laminate Specifications

The following Combinations were made having 8 layers with total thickness of laminate is 3mm.So thickness will be ply thickness = 3/8= 0.375 mm per ply. The volume fraction calculation presented for the laminate was used to estimate the practical fiber volume fraction achieved during fabrication. The obtained value is 50% fiber volume fraction assumed in the CLT analysis, thereby providing consistency between experimental processing and theoretical modeling.

1.8.5 Laminate Properties

Material properties used in the CLT analysis. Carbon, glass, and Kevlar epoxy ply properties are listed in Table 2.

Table 2. Material properties, [41][42]

Material	E_1(GPa)	E_2 (GPa)	G_{12}(GPa)	ν_{12}
Carbon Fiber	135	10	5	0.28
Glass Fiber	50	15	5	0.28
Kevlar Fiber	76	5	2	0.34
Mild Steel Wire Mesh	200	200	80	0.30

1.9 Fibre Orientation for Hybrid Composite Laminates

The Classical Laminate theory for the laminates will be applied as per fibre orientations and ply thickness and per ply thickness.The values ply orientation and $\bar{Q}$ are given in Table 3 for further calculations.

Table 3. Ply orientation and $\bar{Q}$ values

Ply	Material/Epoxy	θ (deg)	$\bar{Q}_{11}$(MPa)	$\bar{Q}_{12}$ (MPa)	$\bar{Q}_{22}$ (MPa)	$\bar{Q}_{66}$ (MPa)	$\bar{Q}_{16}$ / $\bar{Q}_{26}$ (MPa)
1.	Carbon Fibre	0	135800	2820	10060	5000	0
2.	Kevlar Fibre	0	76580	1710	5040	2000	0
3.	Mild Steel Wire Mesh	+45	222860	62850	222860	76930	0
4.	Mild Steel Wire Mesh	-45	222860	62850	222860	76930	0
5.	Glass	90	15360	4300	51200	5000	0
6.	Mild Steel Wire Mesh	-45	222860	62850	222860	76930	0
7.	Mild Steel Wire Mesh	+45	222860	62850	222860	76930	0
8.	Kevlar Fibre	0	76580	1710	5040	2000	0

Note: $\bar{Q}_{16} = \bar{Q}_{26} = 0$ for all plies (due to symmetry or fiber orientation), so $A_{16} = A_{26} = 0$.
According to above data we will calculate A matrix components.

We compute each component as

1.9.1 Classical Laminate Theory for Laminate1

a. Extensional stiffness Matrix [A]

The equation for A matrix is given as follows:

$$A_{ij} = \sum_{k=1}^{8} Q_{ij}^{k} \cdot (Z_k - Z_{k-1}) \tag{6}$$

So A matrix will be:

$$A = \begin{bmatrix} A_{11} & A_{12} & A_{16} \\ A_{12} & A_{22} & A_{26} \\ A_{16} & A_{26} & A_{66} \end{bmatrix} MPa.mm \tag{7}$$

$$Final\ A\ Matrix = \begin{bmatrix} 446422 & 97800 & 0 \\ 97800 & 392415 & 0 \\ 0 & 0 & 120650 \end{bmatrix} MPa.mm \tag{8}$$

The equation for B matrix is given as follows

b. Coupling Stiffness Matrix [B]

General Equation for B Matrix is given by

$$B_{ij} = \sum_{k=1}^{n} (Q)ij^{(k)} \cdot \frac{1}{2}(z_k^2 - z_{k-1}^2) \tag{9}$$

where $\bar{Q}_{ij}^{(k)}$ is the transformed stiffness matrix component for the k-th ply.

z_k, z_k-1: top and bottom coordinates of the k_{th} ply with respect to the mid-plane

B Matrix (Bending-Extension Coupling Matrix) (MPa.mm^2)

$$B=\begin{bmatrix} B_{11} & B_{12} & B_{16} \\ B_{12} & B_{22} & B_{26} \\ B_{16} & B_{26} & B_{66} \end{bmatrix} = \begin{bmatrix} -61864 & 0 & 0 \\ 16650 & 61684 & 0 \\ 0 & 0 & 0 \end{bmatrix} MPa.mm^2 \tag{10}$$

c. Bending stiffness Matrix [D]

General Equation for D Matrix is given as follows:

$$[D] = \frac{1}{3} \cdot \sum_{k=1}^{n} \bar{Q}_{ij}^{(k)} (z_k^3 - z_{k-1}^3) \tag{11}$$

D Matrix (Bending stiffness Matrix) (MPa.mm^3):

$$D=\begin{bmatrix} D_{11} & D_{12} & D_{16} \\ D_{12} & D_{22} & D_{26} \\ D_{16} & D_{26} & D_{66} \end{bmatrix} = \begin{bmatrix} 208688 & 22484 & 0 \\ 22484 & 160901 & 0 \\ 0 & 0 & 29473 \end{bmatrix} MPa.mm^3 \tag{12}$$

d. Combined ABD Matrix for laminate 1 will be as follows

$$ABD=\begin{bmatrix} A_{11} & A_{12} & A_{16} & B_{11} & B_{12} & B_{16} \\ A_{12} & A_{22} & A_{26} & B_{12} & B_{22} & B_{26} \\ A_{16} & A_{26} & A_{66} & B_{16} & B_{26} & B_{66} \\ B_{11} & B_{12} & B_{16} & D_{11} & D_{12} & D_{16} \\ B_{12} & B_{22} & B_{26} & D_{12} & D_{22} & D_{26} \\ B_{16} & B_{26} & B_{66} & D_{16} & D_{26} & D_{66} \end{bmatrix} \tag{13}$$

$$ABD = \begin{bmatrix} 446422 & 97800 & 0 & -61864 & 0 & 0 \\ 97800 & 392415 & 0 & 16650 & 61684 & 0 \\ 0 & 0 & 120650 & 0 & 0 & 0 \\ -61864 & 0 & 0 & 208688 & 22484 & 0 \\ 16650 & 61684 & 0 & 22484 & 160901 & 0 \\ 0 & 0 & 0 & 0 & 0 & 29473 \end{bmatrix} \tag{14}$$

The mechanical response of Laminate 1 is comprehensively characterized by its ABD stiffness matrices, which quantify the in-plane coupling and bending behaviors respectively. The extensional stiffness matrix (A-matrix) shows significant axial and transverse rigidity with A_{11}=446422 MPa.mm. A_{12}=97800MPa.mm, A_{22}=392415 MPa.mm and moderate in-plane shear stiffness A_{66}=120650 MPa.mm. The laminate is asymmetric as the coupling stiffness matrix (B-matrix) shows with B_{11}=-61864 Mpa.mm2, B_{12}=16650 Mpa.mm^2 and B_{22}=61684 Mpa.mm^2 is not zero, with B_{11},-B_{22} showing a high degree of interaction between the laminate and its constituent materials.

The bending stiffness matrix (D-matrix) reveals the out-of-plane resistance with D_{11}=208688 MPa.mm^3,D_{22}=160901 MPa.mm^3 and shear related D_{66}=29473 MPa.mm^3.D_{12}=22484 MPa.mm^3 off-diagonal bending term also suggests the existence of coupling between orthogonal directional bending. The high in-plane stiffness, large coupling effects, and moderate bending rigidity prove the fact that Laminate 1 is anisotropic and asymmetric in behavior characteristic of the hybrid fiber-metal laminates including carbon, Kevlar and mild steel wire mesh layers.

1.9.2CLT Analysis for Laminate 2(GKMS)

The CLT of laminate 2 is determined based on the following mechanical properties that are displayed in Table 4.

Table 4. Material properties [41][42]

Material/Epoxy	E_1 (GPa)	E_2 (GPa)	G_{12} (GPa)	ν_{12}
Glass Fibre	50	15	5	0.28
Kevlar Fibre	76	5	2	0.34
Mild Steel Wire mesh	200	200	80	0.3

A Matrix for Laminate2 GKMS) (Extensional Stiffness) [MPa.mm]

$$A = \begin{bmatrix} 257103 & 65546 & -3360 \\ 65546 & 216888 & -3360 \\ -3360 & -3360 & 77373 \end{bmatrix} MPa.mm \tag{15}$$

B Matrix (Coupling Stiffness) [MPa.mm^2]

$$B = \begin{bmatrix} -4410 & 1274.9 & -1260 \\ 1274.9 & 18410 & -4410 \\ -1260 & -4410 & -4670.8 \end{bmatrix} MPa.mm^2 \tag{16}$$

D Matrix (Bending Stiffness) [MPa.mm^3]

$$D = \begin{bmatrix} 68030 & 23600 & -160 \\ 23600 & 73680 & -160 \\ -160 & -160 & 25500 \end{bmatrix} MPa.mm^3 \tag{17}$$

Combined ABD Matrix for Laminate2 will be as follows

$$ABD = \begin{bmatrix} A_{11} & A_{12} & A_{16} & B_{11} & B_{12} & B_{16} \\ A_{12} & A_{22} & A_{26} & B_{12} & B_{22} & B_{26} \\ A_{16} & A_{26} & A_{66} & B_{16} & B_{26} & B_{66} \\ B_{11} & B_{12} & B_{16} & D_{11} & D_{12} & D_{16} \\ B_{12} & B_{22} & B_{26} & D_{12} & D_{22} & D_{26} \\ B_{16} & B_{26} & B_{66} & D_{16} & D_{26} & D_{66} \end{bmatrix} \tag{18}$$

$$ABD = \begin{bmatrix} 257103 & 65546 & -3360 & -4410 & 1274.9 & -1260 \\ 65546 & 216888 & -3360 & 1274.9 & 18410 & -4410 \\ -3360 & -3360 & 77373 & -1260 & -4410 & -4670.8 \\ -4410 & 1274.9 & -1260 & 68030 & 23600 & -160 \\ 1274.9 & 18410 & -4410 & 23600 & 73680 & -160 \\ -1260 & -4410 & -4670.8 & -160 & -160 & 25500 \end{bmatrix} \tag{19}$$

Laminate 2 mechanical performance is characterized by the ABD matrices that are the combination of the extensional, bending-extension coupling, and bending stiffness. The A-matrix indicates moderate in-plane stiffness, with A_{11} = 257103 MPa·mm, A_{22} = 216888 MPa·mm, and shear stiffness A_{66}= 77373 MPa·mm. Anisotropy and fiber misalignment of laminates is indicated by the presence of non-zero shear-extension coupling terms like $A_{16} = A_{26}$ = -3360 MPa.mm. The B-matrix further confirms the asymmetry in the laminate's stacking sequence, with non-negligible coupling terms like B_{11} = −4410 MPa·mm², B_{12} = 1274.9 MPa·mm², and B_{22}= 18410 MPa·mm². Additional off-axis coupling, seen in terms such as B_{16} = −1260 MPa·mm² and B_{66} = −4670.8 MPa·mm², indicates strong interactions between in-plane loading and twisting/bending responses. The D-matrix shows the laminate's resistance to bending deformations, with D_{11} = 68030 MPa·mm³, D_{22}= 73680 MPa·mm³, and D_{66} = 25500 MPa·mm³. Off-diagonal entries like D_{12}= 23600 MPa·mm³ and small but non-zero $D_{16} = D_{26}$ = −160 MPa·mm³ reflect orthotropic bending behavior and residual bending-twisting coupling. Taken together, the ABD matrix elements affirm the fact that Laminate 2 behaves anisotopically and asymmetrically structurally, which can be attributed to the fact that the material is a hybrid of glass, Kevlar, and mild steel.

Laminate 2 is anisotropic and asymmetric because of the hybrid building and order. The identified bending-extension coupling and directional stiffness properties show that it can be used in any application that requires control over deformation and customized mechanical behavior.

2. Results

The mechanical analysis of two hybrid laminates Carbon/Kevlar/Mild Steel wire mesh (Laminate 1) and Glass/Kevlar/Mild Steel wire mesh (Laminate 2) was carried out using Classical Laminate Theory with detailed computation of the ABD stiffness matrices. The extensional stiffness (A-matrix) revealed significantly higher values for Laminate 1, including A_{11}=446,422 MPa·mm and A_{22}=392,415 MPa·mm compared to Laminate 2 values of A_{11}=257,103 MPa·mm and A_{22}=216,888MPa·mm. Similarly, shear stiffness $A_{66}$was higher in Laminate 1(120,650 MPa·mm) than in Laminate 2 (77,373 MPa·mm).

The B-matrix analysis showed non zero coupling for Laminate 1 which is asymmetric, whereas Laminate 2 displayed moderate coupling with B_{12}=1274.9 MPa·mm² and notable non-zero B_{16} and B_{26} values. The bending stiffness (D-matrix) further confirmed the best flexural behavior of Laminate 1 with D_{11}=208,688 MPa·mm³ and D_{22} =160,901 MPa·mm³ compared to 68,030 MPa·mm³ and 73,680 MPa·mm³ for Laminate 2.

Modulus derivations from these matrices showed that Laminate 1 achieved tensile moduli of E_f^x =148.81GPa and E_f^y =130.8 Gpa.The flexural moduli of 92.75GPa and 71.51GPa for laminate 1 & 2 respectively and a shear modulus of 40.22GPa. In contrast, Laminate 2 yielded 25.79 GPa. These results demonstrate that Laminate 1 consistently exhibits best mechanical properties, attributed primarily to the incorporation of high-stiffness carbon fibers. Visual comparisons using line graphs further validated this performance distinction, with Laminate 1 displaying greater stiffness anisotropy and higher modulus values in all principal directions. On balance, Laminate 1 is more applicable in the use of large strength to weight ratios, rigidity, and dimensional stability involving complicated loading situations.

2.1 Comparative Evaluation of Laminate 1 and Laminate 2

The analysis is on the basis of three matrices that are A, B& D matrix that are further compared.

2.1.1 Extensional Behavior (A-Matrix)

The extensional stiffness matrix [A] is used to indicate the in-plane mechanical behavior of the laminates. The carbon and Kevlar in the 0^0 and 90^0 orientation give Laminate 1 (CKMS) higher values of axial stiffness, higher values of A12 and A66, higher longitudinal-transverse coupling, and higher in-plane shear strength. Laminate 2 (GKMS), a woven material made of a combination of glass and Kevlar, is more isotropic and balanced in-plane stiffness profile. Although Laminate 2 offers a medium performance on axial, the symmetric orientation of the fibers and the choice of materials helps to achieve the equal distribution of the loads and a less brittle type of failure.

Laminate 1, therefore, has a high in-plane stiffness profile, which is important when using the axial load-dominated constructions. Figure 7 represents the comparison of A matrix.

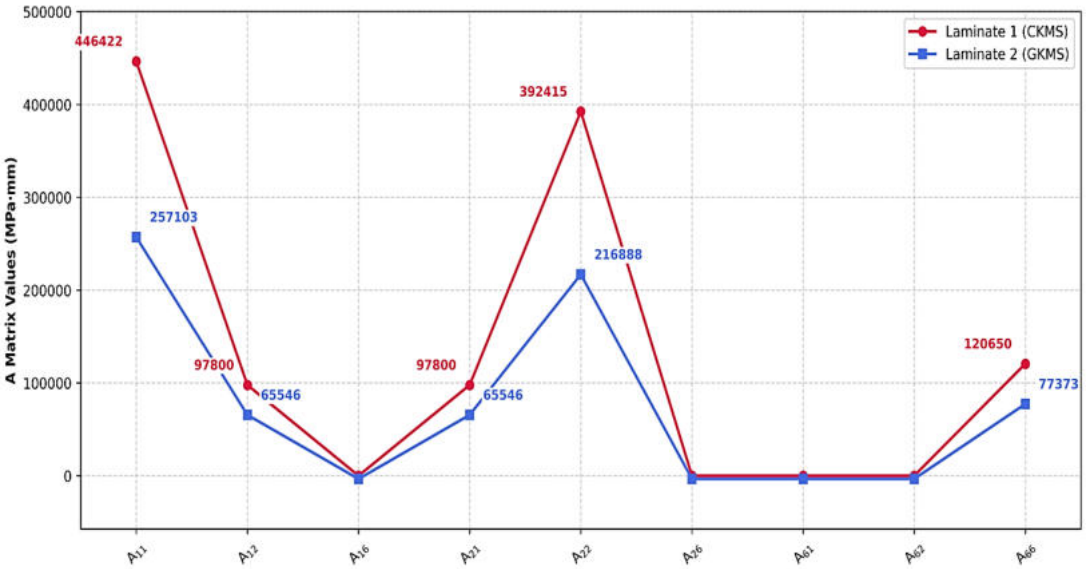

Fig. 7. - In-Plane Stiffness (A matrix) of CKMS and GKMS Laminates.

2.1.2 Coupling Behavior (B-Matrix)

The bending extension coupling characteristic due to laminate asymmetry is given by the [B] matrix. In B_{11}, B_{12}, B_{22} and B_{66}, Laminate 1 has an important value of non-zero numbers, indicating that the Bending interaction of extensions is strong. This is because of the non-symmetric stacking order as well as the heterogeneous distribution of materials. The moderate B_{11}, dominant B_{22}, non-zero B_{16},B_{26} terms refer to the extension bending and extension twisting interactions, especially at the transverse direction. In comparison to Laminate 1, Laminate 2 has lower yet not negligible coupling which offers a trade-off between tailoring of deformation and structural integrity. Thus, though

Laminate 1 is focused on the promotion of the coupling behavior, Laminate 2 provides a relatively controlled coupling with a better load-bearing stability during the multidirectional loading. B matrix values comparison is indicated in Table 8.

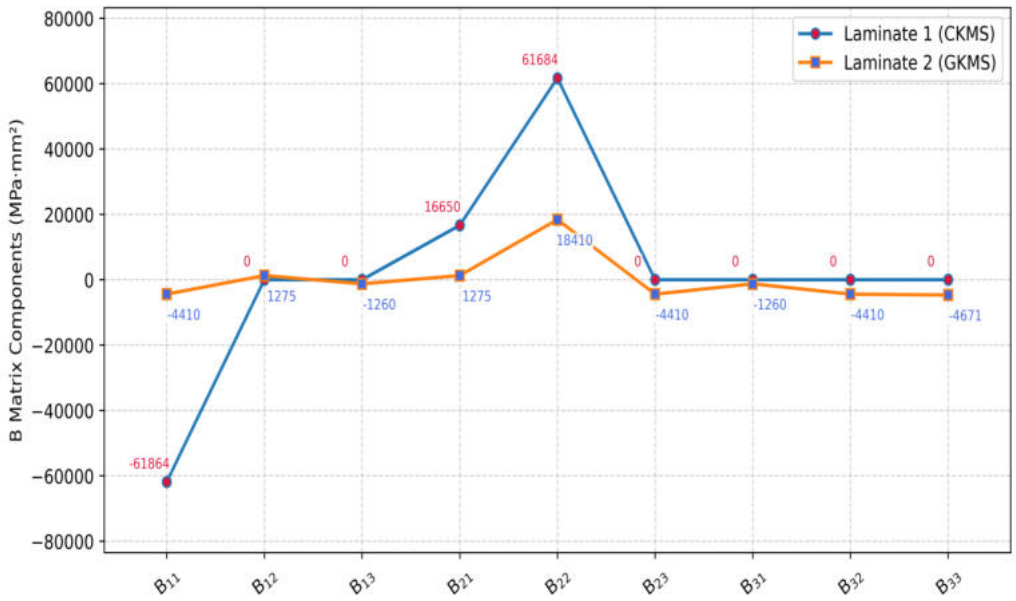

Fig.8. - Distribution of Coupling Stiffness (B- Matrix) Components for CKMS & GKMS Laminates

2.1.3Bending Behavior (D-Matrix)

The out of plane rigidity of the laminates can be determined through bending stiffness (the [D] matrix). Laminate 1 exhibits significantly greater bending stiffness because the outer layers have carbon fibers and therefore are associated with higher values of D_{11} and D_{22}. This causes it to be extremely resistant to flexural deformations. On the one hand, Laminate 2 is less rigid in bending terms, but the performance of the material is average, as the material incorporates +-45^0 mild steel plies and woven glass plies. Its design is also more ductile and damage tolerant to flexural loads, and it is therefore appropriate in areas that demand energy absorption and flexibility.

Therefore, Laminate 1 offers greater flexural rigidity and Laminate 2 is more bend tolerant and ductile. Figure 9 represents the comparison of B matrix values.

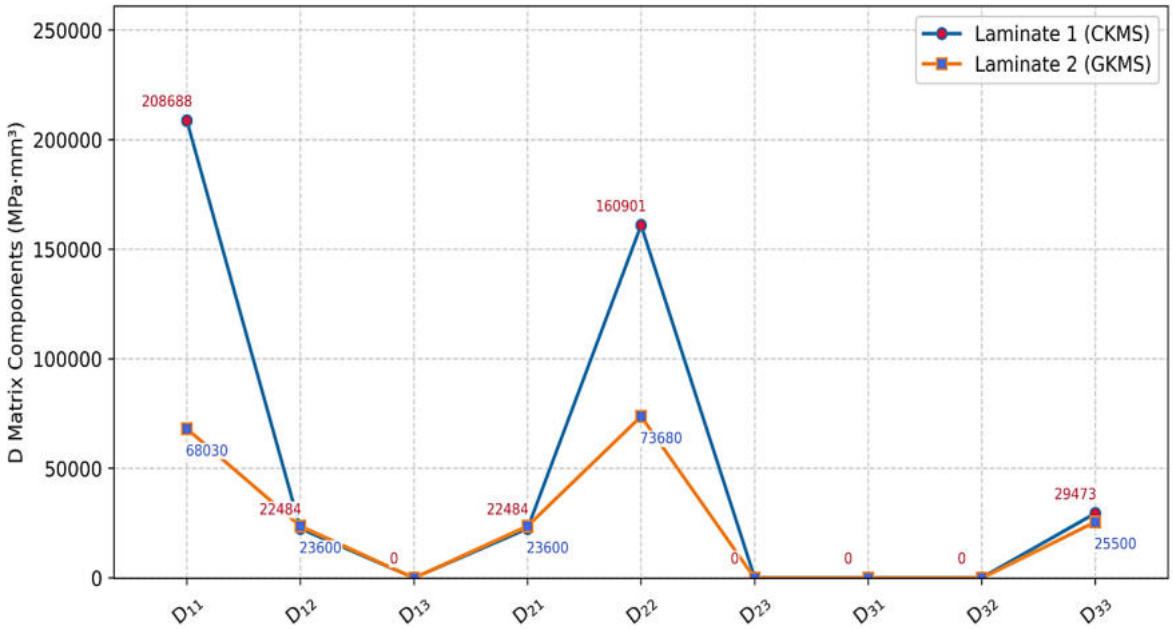

Fig. 9. - Bending Stiffness (D-Matrix) Component Characteristics of CKMS & GKMS Laminates

2.1.4 Overall ABD Comparison for Laminate 1 and Laminate 2

Comparison analysis of the ABD matrices obviously indicates that Laminate 1 is better than Laminate 2 in the fields of extensional, coupling and bending. Laminate 1 has an advantage in high-modulus carbon fibers and asymmetry, which increase the stiffness, coupling properties, and shear resistance. Otherwise, Laminate 2 is less expensive, symmetric, and provides enough in-plane rigidity, low coupling behavior and reasonable bending rigidity. In short, Laminate 1 is designed to be used in high-performance structural applications, whereas Laminate 2 offers performance tradeoff on both cost-sensitive and flexible composite applications. The combined ABD matrix values for laminate 1 & laminate 2 is represented in Figure 10.

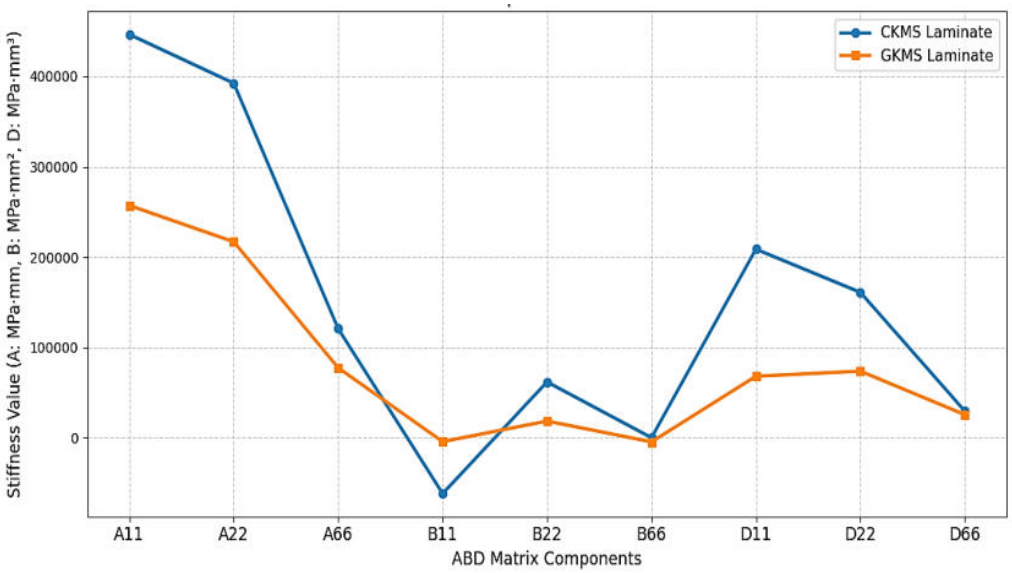

Fig. 10. Variation of ABD Stiffness Components for CKMS & GKMS Laminates

2.2 Flexural Modulus

The calculations for flexural modulus for laminate 1 and 2 are given as follows

2.2.1For Laminate1 (CKMS)

For calculating flexural modulus values of D matrix were utilized which are represented in Table 5.

Table 5. D matrix values for calculation of flexural modulus for Laminate1

Direction	D Value (MPa·mm³)	Flexural Modulus E_f(GPa)
X (D_{11})	208,688	92.75 GPa
Y (D_{22})	160,901	71.51 GPa

The flexural modulus of Laminate 1 was computed from the D matrix using the classical relation

$$E_f^x = \frac{12D11}{h^3} = \frac{12x208688}{3^3} = 92750\ Mpa = 92.75\ GPa \quad (20)$$

$$E_f^y = \frac{12D22}{h^3} = \frac{12x160901}{3^3} = 71511.5\ Mpa = 71.51\ GPa \quad (21)$$

2.2.2 Flexural Modulus for Laminate2 (GKMS)

For calculating flexural modulus we need values of D matrix which are represented in Table 6.

Table 6. D matrix values for calculation of flexural modulus for Laminate 2

Direction	D Value (MPa·mm³)	Flexural Modulus E_f(GPa)
X (D_{11})	68,030	30.24
Y (D_{22})	73,680	32.75

Similarly for laminate2 the modulus in the longitudinal direction was computed as 30.24 GPa, while the transverse modulus was 32.75 GPa.

$$E_f^x = \frac{12D11}{h^3} = \frac{12x68030}{3^3} = 30.24\ GPa \quad (22)$$

$$E_f^y = \frac{12D22}{h^3} = \frac{12x73680}{3^3} = 32.75\ GPa \quad (23)$$

2.2.3 Flexural Modulus Comparison

The flexural modulus comparison for both laminates is given in Table 7.

Table 7. Flexural Modulus Comparison

Laminate	E_f (GPa) X Direction	E_f(GPa) Y Direction
(Carbon/Kevlar/MS)	92.75	71.51
(Glass/Kevlar/MS)	30.24	32.75

The graph for comparison of Flexural modulus is represented in Figure 11.

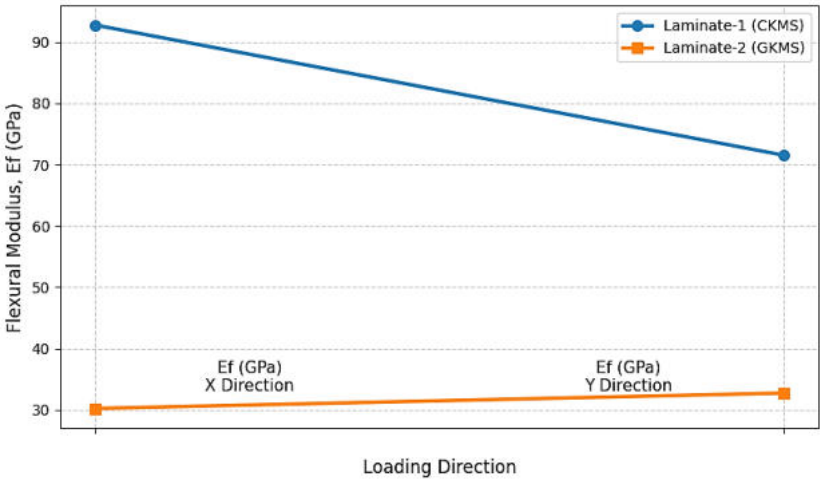

Fig. 11. Flexural Modulus Comparison between CKMS and GKMS

The flexural module of both hybrid laminates were derived from their respective bending stiffness matrices using the Classical Laminate Theory (CLT) (Aklilu et al., 2024) .As shown in the comparative table, Laminate 1 (Carbon/Kevlar/Mild Steel wire mesh) exhibits substantially higher flexural rigidity in both the longitudinal and transverse directions, with values of 92.75 GPa and 71.51 GPa, respectively. These values are more than double those of Laminate 2 (Glass/Kevlar/Mild Steel wire mesh), which recorded 30.24 GPa and 32.75 GPa in the same directions. This pronounced difference is primarily attributed to the higher modulus of carbon fibers and the optimized hybrid stacking sequence used in Laminate 1, which significantly enhances its resistance to out-of-plane bending. On the other hand, Laminate 2 has lower values, which is suggestive of less stiffness provided by glass fibers, hence it is less stiff when it comes to bending loads. This comparative analysis shows clearly the mechanical capability of Laminate 1 over structural usage which requires greater flexural performance which is applied in the aerospace panel, composite shafts and high load carrying components.

2.3Tensile Modulus

The calculations for tensile modulus for laminate 1 and 2 are given as follows

2.3.1Tensile Modulus for Laminate1 (CKMS)

For calculating tensile modulus for laminate 1, we need A matrix values which are represented in Table 8

Table 8. A matrix values for calculation of tensile modulus for laminate 1

Direction	A11/A22 (MPa·mm)	E_f(GPa)
Longitudinal (X)	446,422	148.81
Transverse (Y)	392,415	130.81

The tensile modulus of Laminate 1 was computed from the A matrix using the classical relation

$$E_f^x = \frac{A11}{h} = \frac{446422}{3} = 148.81 \text{ GPa} \quad (24)$$

$$E_f^y = \frac{A22}{h} = \frac{392415}{3} = 130.81 \text{ GPa} \quad (25)$$

2.3.2 Tensile Modulus for Laminate2

For calculating tensile modulus for laminate 2 we need A matrix values which are represented in Table 9

Table 9. A matrix values for calculation of tensile modulus for laminate 2

Direction	A11/A22(MPa·mm)	E_f (GPa)
Longitudinal (X)	257,103	85.70
Transverse (Y)	216,888	72.30

$$E_f^x = \frac{A11}{h} = \frac{257103}{3} = 85.70\ GPa \quad (26)$$

$$E_f^y = \frac{A22}{h} = \frac{216888}{3} = 72.30\ GPa \quad (27)$$

2.3.3Tensile Modulus Comparison

The tensile modulus for laminate 1 and are compared and represented in Figure 12.

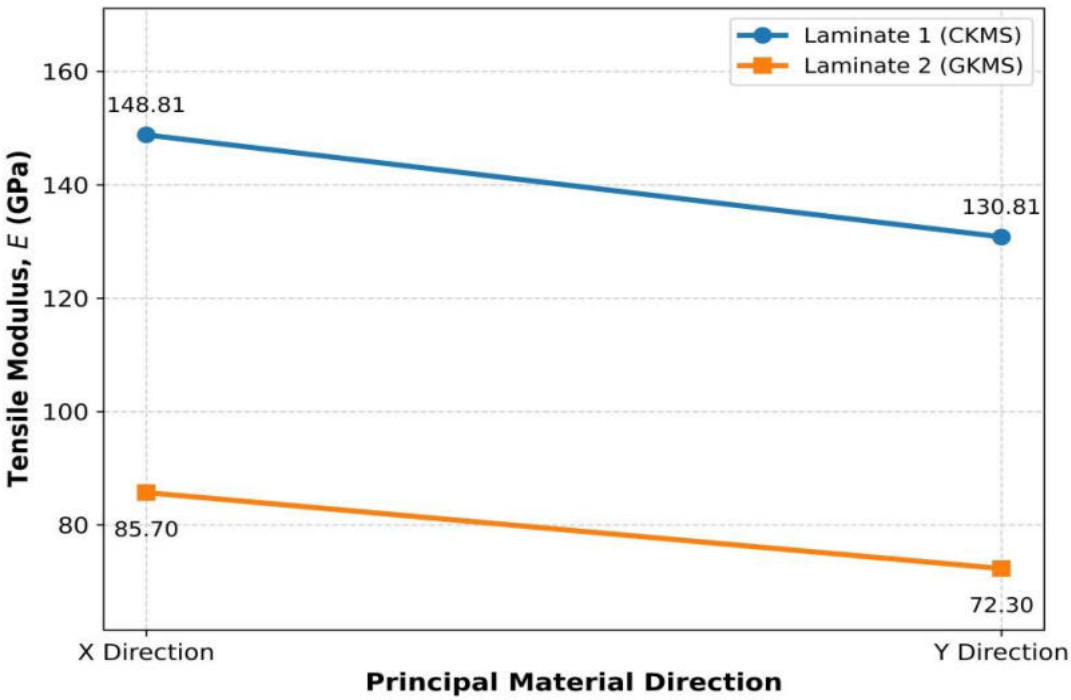

Fig. 12. Directional Tensile Modulus Characteristics of CKMS & GKMS

The in-plane tensile moduli of both laminates were computed from the extensional stiffness (A) matrices using the values A_{11} and A_{22} with thickness of 3mm.Laminate 1 (Carbon/Kevlar/Mild Steel wire mesh) exhibited significantly higher tensile moduli in both principal directions, with values of 148.81 GPa in the longitudinal (X) direction and 130.81 GPa in the transverse (Y) direction. In contrast, Laminate 2 (Glass/Kevlar/Mild Steel wire mesh) showed reduced moduli of 85.70 GPa and 72.30 GPa in the respective directions. These results clearly illustrate the superior in-plane load-carrying capacity and stiffness of Laminate 1, primarily due to the inclusion of high-modulus carbon fibres. The composite Laminate 2 has reduced stiffness because of lower modulus of glass fibres and the high compliance as a result of the greater extensional coupling. In general, the tensile comparison study affirms that Laminate 1 is more structurally efficient when it comes to objects that demand high tensile rigidity e.g. drive shafts, structural skins, and automotive panels.

2.4 Shear Modulus

We obtain the in-plane shear modulus (G_{12}) of the laminate by multiplying the shear stiffness of the A 6 term of the extensional stiffness matrix [A] and the overall laminate thickness h.

2.4.1Shear Modulus for Laminate1

The shear modulus for laminate 1 is calculated by considering values of A matrix listed in Table 10.

Table 10. A matrix values for calculation of shear Modulus

Laminate	A_{66} (MPa·mm)	Thickness h (mm)	G_{12} (GPa)
(Carbon/Kevlar/MS)	120,650	3.0	40.22
(Glass/Kevlar/MS)	77,373	3.0	25.79

$$G_{12} = \frac{A66}{h} = \frac{120650}{3} = 40.22\ GPa \quad (28)$$

Similarly for laminate2

$$G_{12} = \frac{A66}{h} = \frac{77373}{3} = 25.79\ GPa \quad (29)$$

2.4.2Comparison of Shear Modulus

The shear modulus comparison for laminate 1 and 2 is represented in Figure 13.

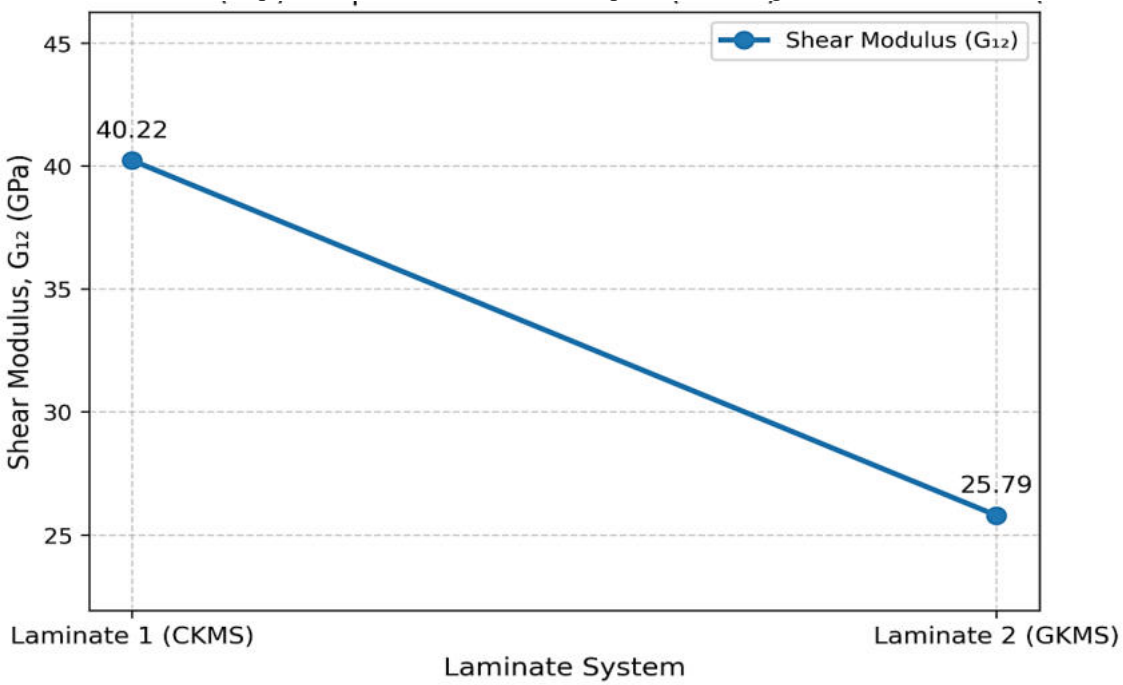

Fig. 13. Shear Modulus (G_{12}) Response of CKMS& GKMS

The in-plane shear modulus $G_{xy}$was calculated for both laminates using the shear stiffness term $A_{66}$from the extensional stiffness matrix. Laminate 1 reinforced with carbon fibers exhibited a significantly higher shear modulus of 40.22 GPa compared to 25.79 GPa for Laminate 2. This reflects the superior resistance of Laminate 1 to in-plane distortion under torsional or shearing loads, owing to the high stiffness characteristics of carbon fibers. The lower shear stiffness in Laminate 2 results from the relatively lower modulus of the glass fibers which, while improving compliance and damping, may limit its use in applications where high shear rigidity is critical.

2.5 Comparison of CLT Predictions

2.5.1 Flexural Modulus

[31] reported that D type composite Carbon/Glass/Kevlar/Carbon/Kevlar/Glass/Carbon [CGKCKGC] flexural strength of 380.96 MPa and Modulus of 36.52GPa respectively. In the present study, the Glass/Kevlar/Mild Steel (GKMS) laminate exhibited flexural moduli in the range of 30.24 & 32.75 GPa, In contrast, the Carbon/Kevlar/Mild Steel (CKMS) laminate demonstrated substantially higher flexural moduli of 71.51 &92.75 GPa. This has been mainly improved by the use of high-modulus carbon fibers and mild steel wire mesh which is much more effective in reducing bending stiffness. By these findings, it is confirmed that the CLT-based predictions are correlated with the reports made of hybrid composite systems previously and it distinctly indicates the increment in stiffness through the optimum hybridization of a fiber-metal composite.

2.5.2 Tensile Modulus

According to [32], tensile modulus values of E-glass/epoxy (GFRP) were 38 Gpa when stacked in order of 159 Gpa when stacked in order of carbon/epoxy (CFRP). The tensile moduli of 72.30 and 85.70 GPA of the GKMS laminate used in the current work are within the range of tensile moduli of glass-dominated hybrid composites. Tensile moduli of CKMS laminate were higher 130.81 &148.81 Gpa, which is near to the upper limits of carbon-based hybrid laminates reported by [32]. This confirms the tensile modulus predictions obtained through Classical Laminate Theory and puts to the fore the usefulness of carbon fiber integration to improve axial stiffness.

2.5.3 Shear Modulus

[30] gave an in-plane shear modulus (0deg/90deg) and (+-45deg) values of 10.3 or 11.5 Gpa (pure carbon-epoxy woven composites). Comparatively, the current hybrid laminates had very high effective shear moduli of 40.22Gpa of the Carbon/ kevlar/ Mild Steel laminate and 25.79 Gpa of the Glass/ kevlar/ Mild Steel laminate, which

were determined using CLT (A 6/ h). This high increment is explained by the fact that it has +-45deg mild steel wire mesh-layers, which is a significant contributor to the laminate shear stiffness. These findings are physically in line with a laminate architecture and theoretical framework, used [30].

3. Limitations of the Current Research

3.1 Assumptions

The current analysis is founded on Classical Laminate Theory (CLT) and presupposes that there will be no interfacial slip, no de-lamination, no de-bonding, and that bonding between the adjacent laminate is perfect. The laminas are assumed to be all homogeneous, orthotropic and linearly elastic. The formulation also assumes that the strains and the deformations are small across the laminate.

3.2 Simplifications

Transverse shear deformation and thickness stretching effects are neglected in accordance with classical laminate assumptions. Material properties are assumed to be uniform within each ply and are adopted from literature sources. Environmental effects such as temperature variation, moisture absorption, and time-dependent behavior are not considered in the present model.

3.3 Potential Sources of Error

Potential sources of error include manufacturing-induced imperfections such as fiber misalignment, voids, and residual stresses, as well as uncertainties in laminate thickness and ply orientation. Experimental measurement inaccuracies and testing-machine compliance may also lead to deviations between analytical predictions and actual structural behavior. However, due to its linear elastic and perfect bonding assumptions, CLT cannot capture interfacial damage between the mild steel wire mesh and the fibers, plasticity of the steel layer under high strain levels, or out-of-plane shear effects in relatively thick hybrid laminates. These behaviors are important for detailed failure and post-elastic analysis and can be addressed in future work using nonlinear and higher-order modeling approaches

4. Discussion

The CLT-based analysis shows that the (CKMS) laminate consistently exhibits higher extensional, bending, tensile, and shear stiffness than the (GKMS) laminate. This improvement is mainly due to the high elastic modulus of carbon fibers and their contribution to load transfer in both in-plane and out-of-plane directions. The non-zero B-matrix terms observed in CKMS indicate extension bending coupling caused by laminate asymmetry& also observed in GKMS asymmetric stacking. Mild steel wire mesh inclusion contributed greatly to the shear stiffness of both laminates resulting in high in-plane shear moduli unlike the traditional fiber-only composites. Also values are validated.

5.Practical Implications

This study gives the results which could be used as a quantitative criterion on informed selection of material as well as laminate structure in high performance engineering. The practical implications are made as a result of the mechanical analysis on the Carbon/Kevlar/Steel (Laminate1) and Glass/Kevlar/Steel (Laminate2).

5.1 Educating Material Choice of Structural Components of Rigidity.

The study proves that Laminate 1 possesses a longitudinal flexural modulus of 92.75 Gpa, more than three times than the one of Laminate 2 of 30.24 Gpa. This brings out the fact that on the aerospace panels, car-chassis, or car load-bearing components, where stiffness-to-weight ratio is extremely important, it is the responsibility of engineers to consider carbon-reinforced hybrid configurations.

5.2 Impact and Damage Tolerance User Design:

Kevlar fibers and mild steel wire mesh through the integration of both laminates helps to provide toughness and shear ductility. In high-dynamic loading/impact scenarios such as defense armor or marine hulls the synergy between high-strength fibers and ductile steel mesh enables a best-case scenario, known as a fail-safe design, where loads are distributed and catastrophic brittle failure is avoided.

5.3 Cost-Effective and Ductile Design Decisions:

Although Laminate 2 is less stiff, the glass-based architecture offers a more balanced in-plane stiffness profile and much reduced material prices. In the industry, where rigidity is not the main consideration because of cost considerations and where energy absorption e.g. general-purpose protective covers Laminate 2 can be used as a replacement of costly all-carbon systems.

5.4 Exploiting Stacking Sequences to Structural Stability:

It is pointed out in the study that stacking sequences directly control the bending-extension coupling with Laminate 1 showing a large value B_{11}=-61,864 MPa.mm^2 and Laminate 2 having asymmetric arrangement with almost zero coupling. On the other hand, the coupling characteristic of Laminate 1 can be deliberately exploited to create smart structures, which would have customized deformation characteristics under the condition of axial loading.

Conclusion

The overall analytical examination of two advanced hybrid composite laminates Carbon/Kevlar/Mild Steel Wire Mesh (Laminate 1) and Glass/Kevlar/Mild Steel Wire Mesh (Laminate 2) showed that the type of fiber and the hybridization strategy impacted greatly on the in-plane and out-of-plane stiffnesss. The Classical Laminate Theory allowed derivation of the ABD stiffness matrices to allow systematic quantification of the extensional, coupling, and bending behaviors. The theoretical values of the moduli of elasticity proved the high quality of mechanical performance of Laminate 1, which has about 74 percent higher tensile and flexural modulus of elasticity in the main directions than Laminate 2.

Besides, the visualizations used in MATLAB were useful in comparative interpretation to give a good graphical framework of design-oriented decision-making. Overall, the findings underscore the critical role of hybridization and stacking sequence optimization in tailoring mechanical performance and establish the present study as a valuable reference for the design of lightweight, high-stiffness structural components in aerospace, automotive, and energy applications.

Conflict of Interest

The authors declare that they have no financial or personal conflicts of interest that could have affected the research presented in this article.

AI Disclosure

During the preparation of this work the author did not use any AI tool for writing the content. The author will take full responsibility for content of the publication.

Acknowledgments

The authors wish to thank Department of Mechanical Engineering, SIT, Pune.

Refrences

[1] Agarwal B. D., Broutman, L. J., Chandrashekhara, K. Analysis and Performance of Fiber Composites, 4th Edition, 2017, https://scholarsmine.mst.edu/mec_aereng_facwork/4412/

[2] Ahmad,F., Choi H. S., Park, M. K. A Review: Natural Fiber Composites Selection in View of Mechanical, Light Weight, and Economic Properties. Macromolecular Materials and Engineering, 2015, 300(1), 10–24. https://doi.org/10.1002/MAME.201400089

[3] Gong, J., Saeed, N., Huang, X., Tian, W., Li, L., Song, J. Influences of Fiber Volume Content on the Mechanical Properties of 2D Plain Carbon-Fiber Woven Composite Materials //Polymers, 2024, 16(1), 108.https://doi.org/10.3390/polym16010108

[4] Asundi, A., Choi, A. Y. N. Fiber metal laminates: An advanced material for future aircraft. Journal of Materials Processing Technology, 1997, 63(1–3), 384–394.https://doi.org/10.1016/S0924-0136(96)02652-0

[5] Barbero E.J. Introductionto Composite Materials Design, 1998, https://www.taylorfrancis.com/books/mono/10.1201/9781439894132/introduction-composite-materials-design-ever-barbero.

[6] Ishtiaq, S., Saleem, M. Q., Naveed, R., Harris, M., & Khan, S. A. (2024). Glass–carbon–Kevlar fiber reinforced hybrid polymer composite (HPC): Part (A) mechanical and thermal characterization for high GSM laminates. Composites Part C: Open Access, 14, 100468. https://doi.org/10.1016/j.jcomc.2024.100468

[7] Gay D., Hoa S.V., Tsai S.W. Composite Materials: Design and Applications (1st ed.), 2002, CRC Press.https://doi.org/10.1201/9781420031683

[8] Monjon A., Santos P. F., Valvez S., Reis P. N. B. Hybridization Effects on Bending and Interlaminar Shear Strength of Composite Laminates.Materials, 2022, 15(4), 1302. https://doi.org/10.3390/ma15041302

[9] Kaw A.K. Mechanics of Composite Materials (2nd ed.), 2005, CRC Press.https://doi.org/10.1201/9781420058291

Murugan R., Narasimhan R. L., Harish A. Effect of Fiber Orientation on Effective Stacking Sequence of Glass/Carbon Hybrid Composite Laminates for Structural Applications, 2018, 204–210.https://doi.org/10.2991/PECTEAM-18.2018.36

[10] Sathyaseelan P., Kumar R. R., Rajesh, D., Raja K., Manivannan J., Munisamy R. Mechanical Characteristics of Kenaf-Glass Fiber Reinforced Hybrid Composites by Varying the Stacking Sequences. PhysicaScripta, 2024 https://doi.org/10.1088/1402-4896/ad79c7

[11] Karthik K., Rajamani D., Balaguru S., Velumayil, R., Bishwakarma, S., Kumara, M. U. N. A. Mechanical Properties of Fiber Metal Laminate Hybrid Composite Materials, 2023, 625–633. Springer Nature. https://doi.org/10.1007/978-981-99-2349-6_56

[12] Mallick P.K. Fiber-Reinforced Composites: Materials, Manufacturing, and Design, Third Edition (3rd ed.), 2007, CRC Press.https://doi.org/10.1201/9781420005981

[13] Bo Madsen, Hans Lilholt, Physical and mechanical properties of unidirectional plant fibre composites - an evaluation of the influence of porosity //Composites Science and Technology,Volume 63, Issue 9, 2003, 1265-1272, https://doi.org/10.1016/S0266-3538(03)00097-6.

[14] Kazemi M. Analysis of laminated composites composed of coupled layers by polar method //Journal of Reinforced Plastics and Composites, 2022, 42(11–12), 537–543. https://doi.org/10.1177/07316844221132717

[15] Malyala H., Mukkoti V. V. Fabrication and Characterization of Hybrid Composite Fibers //NanoWorld Journal, 2023 https://doi.org/10.17756/nwj.2023-s4-050

[16] Koruche U. S., Patil S. F. Application of classical lamination theory and analytical modeling of laminates //International Research Journal of Engineering and Technology (IRJET),2015, 2(2), 958–962.

[17] Rajak D. K., Pagar D. D., Menezes P. L., Linul E. Fiber-Reinforced Polymer Composites: Manufacturing, Properties, and Applications //Polymers, 2019, 11(10), 1667.https://doi.org/10.3390/POLYM11101667
[18] Reddy J. N. Mechanics of Laminated Composite Plates and Shells: Theory and Analysis, Second Edition, 1996 https://www.taylorfrancis.com/books/mono/10.1201/b12409/mechanics-laminated-composite-plates-shells-reddy
[19] Aklilu G., Adali S., Bright, G. Flexural failure properties of fiber-reinforced hybrid laminated beam subject to three-point bending //Dental Science Reports, 2024, 14(1). https://doi.org/10.1038/s41598-024-60078-7
[20] Swolfs Y., Gorbatikh L., Verpoest I. Fibrehybridisation in polymer composites: a review //Composites Part A-Applied Science and Manufacturing, 2014, 67, 181–200. https://doi.org/10.1016/J.COMPOSITESA.2014.08.027
[21] Sethubathi J. (2025). Evaluation of Natural Plant Fibers and their Hybrid Composites to Improve Polymer Strength.813–817. https://doi.org/10.38124/ijisrt/25aug695
[22] Peng B. Advanced Natural/Synthetic Polymer Hybrid Composites //Composites Science and Technology, 2023, 15–29. https://doi.org/10.1007/978-981-99-1583-5_2
[23] Bhardwaj D., Gupta A., Chaudhary V., Gupta S. Hybridization of Natural Fibers to Develop the Polymeric Composite Materials: A Review, 355–363, Springer, Singapore, 2021 https://doi.org/10.1007/978-981-33-6029-7_33
[24] Guo, W., Deng, T., Ding, M., Wang, J., Mi, L., Cheng, X. Matrix Displacement Method for Behavior Analysis of Curved Beam Considering Bending-torsion Coupling. DEStech Transactions on Engineering and Technology Research, 2017
[25] Barulich, N. D., Barulich, N. D., Godoy, L. A., Godoy, L. A., Dardati, P. M. Inter-relationships among stiffness matrix components for general laminates with transverse cracks in oblique plies //Archive of Applied Mechanics, 2019, 89(2), 329–341. https://doi.org/10.1007/S00419-018-1470-Y
[26] Salve A. V., Mache, A. Effect of metallic reinforcement on the mechanical behaviour of a hybrid polymer composite-a review //Materials Today: Proceedings, 2023
[27] Seshaiah, T., Reddy, V. K. Effect of fiber orientation on the mechanical behavior of e-glass fibre reinforced epoxy composite materials. Int. J. Mech. Prod. Eng. Res. Devel //IJMPERD), 2018, 379-396.
[28] Sayyed J., Ramprasad A., Pai Y. Effect of mesh sizes on the mechanical properties of stainless-steel wire mesh/glass fiber reinforced hybrid composite laminates for aerospace applications //Scientific Reports, 2025, 15, 36080.https://doi.org/10.1038/s41598-025-20038-1
[29] Liu F., Grotz L., Cui Y., Kirane K. Experimental dataset on the in-plane tensile, shear, and compressive properties of a carbon-epoxy twill woven composite //Data in Brief, 2022, 45, 108650.https://doi.org/10.1016/j.dib.2022.108650
[30] Rout S. S., Nayak R. K., Patnaik S. C., YazdaniNezhad H. Development of improved flexural and impact performance of Kevlar/carbon/glass fibers reinforced polymer hybrid composites //Journal of Composites Science, 2022, 6(9), 245.https://doi.org/10.3390/jcs6090245
[31] Naito K., Seki Y., Inoue R. Static and fatigue tensile properties of carbon/glass hybrid fiber-reinforced epoxy composite // Scientific Reports, 2022, 12, 6298.https://doi.org/10.1038/s41598-022-10245-5
[32] Gao S., Hou W., Xing J., Sang L. Numerical and experimental investigation of flexural properties and damage behavior of CFRTP/Al laminates. Applied Sciences, 2023, 13(3), 1667.https://doi.org/10.3390/app13031667
[33] Mohammed, A. A. K., Hassan, G. I., Khdir, Y. K. Mechanical behavior of hybrid laminated nanocomposites containing glass and carbon fiber plies //International Journal of Automotive and Mechanical Engineering, 2023, 20(2), 10335–10350. https://doi.org/10.15282/ijame.20.2.2023.01.0799
[34] Zhang Y., Li H., Wang X., Chen Z. Stress evaluation through the layers of a fibre-metal hybrid composite by incremental hole-drilling: Experimental study //Experimental Mechanics, 2024, 64, 487–500. https://doi.org/10.1007/s11340-024-01047-z
[35] Kumar A., Singh R., Patel V. K. Improved mechanical properties of environmentally friendly jute–aluminum fibre- metal laminate sandwich composite //Heliyon, 202410(2), e24345.https://doi.org/10.1016/j.heliyon.2024.e24345
[36] Li J., Zhou P., Wang Y. Flexural properties and optimisation of hybrid composites reinforced by carbon, glass and flax fibres //Hybrid Advances, 2024, 7, 100302. https://doi.org/10.1016/j.hybadv.2024.100302
[37] Hamzat A. K., Adeyemi M. B., Al-Sulaiman F. A. Fiber-reinforced composites for aerospace, energy, and marine applications: Failure mechanisms under chemical, thermal, oxidative, and mechanical loading //Advanced Composites and Hybrid Materials, 2025, 8, 152.https://doi.org/10.1007/s42114-024-01192-y
[38] Cortés P., Cantwell W. J. The prediction of tensile failure in titanium-based thermoplastic fibre-metal laminates. //Composites Science and Technology, 2026, 66(13), 2306–2316. https://doi.org/10.1016/j.compscitech.2006.03.020
[39] Belingardi G., Cavatorta M. P., Paolino D. S. Impact damage characteristics of carbon fibre metal laminates: Experiments and simulation //Applied Composite Materials, 2020, 27, 511–531 https://doi.org/10.1007/s10443-020-09800-y
[40] Kaw A. K. Mechanics of composite materials (2nd ed.), 2006, CRC Press.

Information of the authors

Dalavi Amol, PhD, assistant professor, Symbiosis Institute of Technology, Symbiosis International (Deemed) University
e-mail: amol.dalavi@sitpune.edu.in

Jadhav Amit, M.E., research scholar, College of Engineering
e-mail: amit.jadhav1411@gmail.com

DOI 10.52209/2706-977X_2026_3_31 IRSTI 55.03.05 UDC 621.01:624.04:519.248:519.233

Statistical Analysis of Long-Term Operating Structures for Various Purposes Based on the Theory of Probabilistic Outliers

Ganyukov A.A., Akhmediyev S.K., Bogdanova A.A.*
Abylkas Saginov Karaganda Technical University, Karaganda, Kazakhstan
*corresponding author

Abstract. A probabilistic approach to assessing the reliability of long-term operating mechanical-engineering and building structures based on the theory of probabilistic outliers is considered. The aim of the study was to develop a methodology for determining the probability of failure-free operation of structural elements while accounting for the statistical variability of loads and load-bearing capacity during long-term service. Unlike traditional limit-state calculations, the proposed approach takes into account the statistical parameters of the load-resistance system and actual data from technical inspections of structures. Analytical relationships were obtained for determining the probability of failure-free operation, the safety characteristic, and the strength reserve factor. A probabilistic analysis of a steel beam and a reinforced concrete structure was performed using statistical data from technical inspections. The results showed that the proposed method makes it possible to quantitatively assess operational reliability, predict residual service life, and substantiate engineering decisions on further operation, strengthening, and reconstruction of building structures.

Keywords: reliability of mechanical-engineering and building structures, probability of failure-free operation, theory of probabilistic outliers, statistical analysis, residual service life, operational reliability.

Introduction

The loading processes of mechanical-engineering and building structures, as well as material characteristics and the load-bearing capacity levels of buildings and facilities, are random in nature. The variability of loads, mechanical properties of materials, and geometric parameters of structural elements necessitates the use of probabilistic methods for reliability analysis.

The widely used method for calculating structures for various purposes by limit states has, in fact, a probabilistic interpretation, since the interaction between loads and element resistance is considered in terms of the possibility of reaching limiting states. However, the regulatory approach in most cases provides only an upper estimate of reliability, because it uses normative safety factors and design values of loads and resistances. At the same time, one of the main problems remains the establishment of statistical relationships between random parameters that determine the stress-strain state of a structure [1].

Under real operating conditions, loads, material properties, and geometric parameters of structures change over time and are characterized by a random nature. In this regard, the technical condition of a building object should be considered as a set of random processes describing changes in the parameters of the load-resistance system. The factor parameters of the system may be treated as random variables determined from statistical observations and technical inspections [2].

Estimates of random parameters must satisfy the requirements of consistency, unbiasedness, and efficiency. A consistent estimate is one that tends toward the true value of a parameter as the number of observations increases. An unbiased estimate is one whose mathematical expectation coincides with the true value of the parameter. An efficient estimate is one that has the minimum variance among all possible estimates.

When studying the reliability of mechanical-engineering and building structures, probability theory and mathematical statistics are used to analyze the variability of the parameters of the load-resistance system. One effective approach is the theory of probabilistic outliers, in which structural failure is considered as the event of a random load process exceeding a certain critical level [3].

The theory of probabilistic outliers is one of the areas of probabilistic reliability analysis of mechanical-engineering structures operating under random operational and dynamic effects. The basic idea of this approach is to consider the loading process as a random process in which structural failure is associated with stresses or strains exceeding a dangerous limiting level [4-6].

In mechanical-engineering structures, the random nature of loads is caused by variable operating modes, vibrations, impact effects, wear of elements, and variability in material properties. In this regard, the parameters of the stress-strain state are considered as random functions of time, while structural reliability is determined by the probability that the specified limiting state will not be exceeded [7-9].

The practical value of the theory of probabilistic outliers lies in its ability to assess the probability of failure, predict residual service life, and substantiate engineering decisions regarding further operation, repair, and strengthening of mechanical-engineering and building structures [10-11].

This approach has several advantages [12-14]:

- it directly links structural reliability with the frequency of exceedance of a dangerous load level;
- it accounts for the statistical variability of the load-resistance system parameters;
- it can be used to analyze long-term operating structures based on inspection data.

Existing methods for calculating the reliability of various structures are usually focused on design values of loads and resistances and rarely account for the actual statistical variability of parameters that arises during operation [15-17].

Therefore, it is necessary to develop methods that combine:
- probabilistic reliability theory;
- statistical data from technical inspections of structures;
- stochastic modeling of load-resistance interaction.

The main reliability indicator for building structures is the probability of failure-free operation. It characterizes the probability that a structure will not reach a limiting state within a specified operating period. This study uses a methodology for determining the probability of failure-free operation based on the condition that the load does not exceed a dangerous level.

The scientific novelty of the study is as follows:
- a methodology for the probabilistic assessment of structural reliability based on the number of load crossings of a dangerous level has been developed;
- an approach has been proposed for accounting for statistical inspection data when assessing the reliability of operating structures;
- analytical relationships have been obtained between the safety characteristic, the strength reserve factor, and the statistical parameters of loads and resistance.

The practical usefulness of the study lies in the development of a probabilistic methodology for assessing the operational reliability of building structures while accounting for the statistical variability of loads and load-bearing capacity. The proposed approach makes it possible to assess the probability of failure-free operation, predict residual service life, and substantiate decisions on strengthening and further operation of facilities for various purposes [18-20].

1. Materials and Methods

The main criterion for assessing the reliability of building structures and facilities is the probability of failure-free operation (PFFO). Its value is established on the basis of a number of conditions related to the limitation of the ultimate load, the level of load-bearing capacity, the degree of physical wear, and other operational factors. This paper considers a methodology for calculating the probability of failure-free operation under the condition that the load does not exceed a level dangerous for operation [5, p. 98-105].

It has been established that in this case the realization of the corresponding random process is close to the Poisson distribution law, and the crossing of the dangerous level of external load can be described as a nonstationary Poisson flow. Then the lower estimate of the probability of failure-free operation has the following form (PFFO) [1, p. 68; 2, p. 102]:

$$P_{н.о.}(T) = 1 - b, \tag{1}$$

where T is the operating time of the system, service life, or operating period; b is the average number of load crossings of the dangerous level over time T.

Let the studied factors be denoted as follows: acting load (stress); load-bearing capacity; and the resulting strength reserve parameter.

After transforming the probabilities of crossings of two random processes, the expression for the function b can be written as:

$$\begin{aligned} b &= -T \int_{-\infty}^{0} f\left[\dot{S}_{\Sigma}(t), S_{\Sigma}(t) = 0\right] \cdot \dot{S}_{\Sigma}(t)\, d\dot{S}_{\Sigma}(t) = \\ &= \left\{ T\sigma_S \cdot \exp\left[\left(-\langle S_{\Sigma}\rangle^2 : 2 : \sigma_S^2\right)\right] : (2\pi\sigma_S) \right\}, \end{aligned} \tag{2}$$

where the terms denote the mathematical expectations and standard deviations of the corresponding random processes.

For an ergodic stationary process with a normal distribution law, we obtain [21]:

$$b = T \cdot T_e^{-1} \exp\left[-\left(S_0 - \langle S \rangle\right)^2 : \left(2\sigma_S^2\right)\right], \tag{3}$$

where the effective period of the random process is numerically equal to the average value of the loading-process period; S0 is the dangerous loading level; and the remaining term denotes the average loading level.

The correlation function and mathematical expectation required to determine the average number and average duration of outliers for a normal stationary random process describing structural operation have the following form [22, 23]:

$$K_S(t) = D_н \rho_н(\tau) + D_в \rho_в(\tau) + \left(D_н D_в\right)^{1/2} \rho_{н,в}(\tau), \tag{4}$$

where the subscripts 'l' and 'h' correspond to the low-frequency and high-frequency components of the object loading process.

When the sign of the load is not significant and the load-bearing capacity is a random variable distributed according to a truncated normal law, the following expression can be written instead of equations (2) and (3):

$$b = C_0 \cdot \sigma_S \cdot T \cdot \left[2\pi\left(\sigma_s^2 + \sigma_0^2\right)^{1/2}\right]^{-1} \exp\left[-\left(\langle S_0 \rangle - \langle S \rangle\right)^2 : 2 : \left(\sigma_s^2 + \sigma_0^2\right)\right], \tag{5}$$

where C_1 and C_2 are the normalizing coefficients of the truncated normal distribution for loads and load-bearing capacity, respectively. They are calculated as follows [24]:

$$C_1 = \left[0{,}5\left\{\Phi\left[\left(S_{\max} - \langle S \rangle\right) : \left(\sigma_S \cdot 2^{1/2}\right)\right] - \Phi\left[\left(S_{\min} - \langle S \rangle\right) : \left(\sigma_S \cdot 2^{1/2}\right)\right]\right\}\right], \tag{6}$$

$$C_2 = \left[0{,}5\left\{\Phi\left[\left(S_{0,\max} - \langle S_0 \rangle\right) : \left(\sigma_0 \cdot 2^{1/2}\right)\right] - \Phi\left[\left(S_{0,\min} - \langle S_0 \rangle\right) : \left(\sigma_0 \cdot 2^{1/2}\right)\right]\right\}\right], \tag{7}$$

where Φ is the tabulated Laplace function, $S_{\max}$ and $S_{\min}$ are the maximum and minimum load values, and $S_{0,\max}$ and $S_{0,\min}$ are the corresponding values of the dangerous loading level. In practical calculations, it may be assumed that $C_1=C_2=C_0=1.0$.

In the present study, the normal distributions of the load parameter S and the limiting load-bearing parameter S_0 are truncated over their physically admissible domains, i.e., $S_{\min} = 0$, $S_{\max} \to \infty$, $S_{0,\min} = 0$ and $S_{0,\max} \to \infty$. The lower truncation limit eliminates physically impossible negative values, whereas no artificial upper truncation (e.g., at 3σ) is introduced. These limits are used in determining the normalization coefficients C_1 and C_2 in eqs. (6) and (7). For the statistical parameters considered in this study, the probability mass below zero is negligible; therefore, the normalization coefficients differ only slightly from unity and the approximation $C_1=C_2=C_0\approx1$ is adopted in the subsequent derivation of eqs. (8)–(10).

Then, instead of equation (5), we obtain:

$$b = T \cdot b_c\left(1 + \sigma_0^2 : \sigma_s^2\right)^{-1/2} \exp\left[-\left(\langle S_0 \rangle - \langle S \rangle\right)^2 : 2 : \left(\sigma_s^2 + \sigma_0^2\right)\right], \tag{8}$$

where the parameter denotes the number of outliers per unit time, determined by expert assessment.

Let us further consider the application of the probabilistic calculation method to the case of allowable stresses. Based on expression (8), we obtain the following relationship:

$$\left(\langle S_0 \rangle - \langle S \rangle\right)\left(\sigma_s^2 + \sigma_0^2\right)^{-\frac{1}{2}} = \gamma, \tag{9}$$

where gamma is the safety characteristic, by analogy with [4, p. 146].

This characteristic can be determined using the expression

$$\gamma = \left[\left| -2ln\left\{ -l_p\left[p\right]\left(Tb_c Q\right)^{-1} \right\} \right| \right]^{1/2}, \tag{10}$$

where the parameter denotes the normative probability of failure-free operation (PFFO).

The parameter Q is determined by the expression [24, p.4]:

$$Q = \left(1 + \sigma_0^2 : \sigma_S^2\right)^{-1/2} = \varphi\left(1 + \varphi^2\right)^{-1/2}, \tag{11}$$

where the coefficient determines the ratio related to the standard deviation (SD).

Then, using (9), the required strength reserve factor K can be determined:

$$K = \left\langle S_0 \right\rangle : \left\langle S \right\rangle = \varphi^{-1}\left[\varphi + \gamma \cdot \upsilon_S \left(1 + \varphi^2\right)^{1/2} \right], \tag{12}$$

where

$$\upsilon_S = \sigma_S : \left\langle S \right\rangle \tag{13}$$

is the coefficient of variation of stress.

The value K determined by expression (12) represents the ratio of the average value of load-bearing capacity to the load value.

The condition of probabilistic strength is written as follows [3, p. 87]:

$$\left\langle S_{но} \right\rangle : (R) \geq \left\langle S_H \right\rangle, \tag{14}$$

where $\left\langle S_H \right\rangle$ – the terms denote normal stress in the structure; $\left\langle R \right\rangle$ – the design resistance of the material.

The proposed methodology makes it possible to assess the reliability of building structures from the standpoint of probability theory. The main advantage of this approach is that it accounts for the fact that loads, material strength, and external effects continuously change over time, and these changes are random. Unlike rigid classical calculations, this model makes it possible to calculate the real probability that a structure will operate without failure. It links strength reserve, safety indicators, and load-resistance statistics, which is critically important for objects that have been in service for many years.

This mathematical apparatus can be confidently used to verify the technical condition of buildings based on monitoring results and to accurately predict their residual service life. The probabilistic outlier method captures the real picture: element wear, fluctuations in the stress-strain state, and actual operating conditions of the object. As a result, calculations become much more accurate, allowing engineers to make balanced and justified decisions on whether structures should be strengthened, whether reconstruction is required, or whether the building can continue to be used.

3. Results and Discussion

To illustrate the theoretical provisions of the methodology proposed above, let us consider an example of statistical analysis of the load-bearing capacity of a beam, the design scheme of which is shown in Figure 1 [25-27].

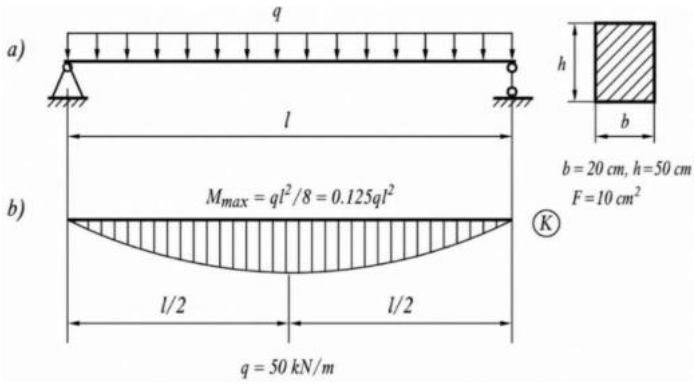

a) initial scheme; b) bending moment diagram.

Fig. 1 – Beam design scheme

Let us introduce the following designations: S_H – normal stress in the structure; $S_{p.c} = S_{н.F} = S_н(b \cdot h)$ – load-bearing capacity of the structure under tension-compression; $S_{iz} = S_н \cdot w = S_н(b \cdot h^3/6)$ – and the same parameter under transverse bending.

For the beam under consideration, the mathematical expectation of the normal stress from the maximum bending moment M_{max} (Figure 1) is assumed, $\langle S_н \rangle = 1 \cdot 10^3\, kgs/cm^2 = 10^4\, kPa$ and the yield strength of the steel material is taken as the specified value $\langle \sigma_T \rangle = \langle \sigma_{но} \rangle = 2{,}7 \cdot 10^3\, kgs/cm^2 = 2{,}7 \cdot 10^4\, kPa$.

For further calculation, the following initial data are adopted: the average number of outliers beyond the average level of normal stress $\langle S_н \rangle$ – $b_c = 5 \cdot 10^{-2}\ \sec^{-1}$; the operating time of the structure under consideration – $T = 7\, years = 2 \cdot 10^8\ \sec$; the normative (specified) probability of failure-free operation (PFFO) – $([p] = 0{,}99)$; $(v_s = \sigma_{но}./\langle S_н \rangle = 0{,}3)$ – the coefficient of variation of normal stresses (conditionally assigned value).

Then the standard deviation (SD) $\sigma_{Sн}$ of normal stresses is determined through the coefficient of variation v_s :

$$\sigma_{Sн} = v_S \cdot \langle S_н \rangle = 0{,}3 \cdot 1 \cdot 10^3\, kgs/cm^2 = 0{,}3 \cdot 10^4\, kPa.$$

The standard deviation of the dangerous-section limiting stress $(\sigma_{н.о})$ is determined through the adopted value $(\varphi = \sigma_{Sн} / \sigma_{но} == 1{,}66)$ as follows:

$$\sigma_{но} = \frac{\sigma_{Sн}}{\varphi} = \frac{0{,}3 \cdot 10^3}{1{,}66} = 0{,}1807 \cdot 10^3 \left(\frac{kgs}{cm^2}\right) = 1{,}807 \cdot 10^3\, kPa\,.$$

We now proceed to solve the probabilistic analysis problem for the structure shown in Figure 1. Using expressions (10) and (11), the safety characteristic is determined [28]:

$$\gamma = -2\ln\left[\frac{-\ln 0{,}99\left(1+1{,}66^2\right)^{1/2}}{1{,}66 \cdot \left(5 \cdot 10^{-2}\right)\left(2 \cdot 10^8\right)}\right]^{1/2} = 6{,}41;\ \boxed{\gamma} \tag{15}$$

$$Q = 1{,}66 + (1+1{,}66^2)^{-1/2}.$$

Using formula (12), the strength reserve factor of the structure is calculated:

$$K = \frac{1{,}66 + 6{,}41 \cdot 0{,}3\left(1 + 1{,}66^2\right)^{1/2}}{1{,}66} = 3{,}24. \tag{16}$$

Using formula (13), the strength condition of the structure is checked with allowance for value (16):

$$\frac{\langle S_{но} \rangle}{R} \geq \langle S_н \rangle, \quad or \quad \left(\frac{2{,}7 \cdot 10^3}{3{,}24} = 0{,}835 \cdot 10^3 \right) < 1 \cdot 10^3 \left(\frac{kgs}{cm^2} \right). \tag{17}$$

The strength check (17) shows that, with the initial cross-section, the reliability condition is not satisfied. This means that further operation requires an increase in the cross-sectional dimensions. Thus, the probabilistic calculation not only records the fact of insufficient strength, but also allows the required level of structural strengthening to be quantitatively assessed.

The required section modulus of the cross-section is determined by the expression:

$$W_{тр} = \langle S \rangle R : \langle S_{но} \rangle, \tag{18}$$

where: $W = bh^2 / 6 \left(b \times h = 2 \times 5cm\right)$; $W = 0{,}167 \cdot Fh$; $F = 10cm^2$; $b = 2cm$; $h = 5cm$.

Let us determine the mathematical expectation of the load-bearing capacity, assuming that the structure operates under transverse bending (Figure 1):

$$\langle S \rangle = \langle S_н \rangle \cdot w = 1 \cdot 10^3 \cdot 0{,}167 \cdot 10 \cdot 5 = 8{,}35 \cdot 10^3 9 \left(kgs \cdot m\right).$$

Let us determine the required value of the cross-sectional section modulus with allowance for (16) and (17):

$$W_{тр} \quad \frac{\langle S \rangle \cdot R}{\langle S_{но} \rangle} = \frac{8{,}35 \cdot 10^3 \cdot 3{,}24}{2{,}7 \cdot 10^3} = 100{,}2\, cm^3. \tag{19}$$

With the previous value b = 2cm, let us determine the new value of the cross-section $W = bh^2 / 6 = 2 \cdot h^2 / 6 = 0{,}333h^2$ height h, taking into account expression (19):

$$h_1 = \sqrt{\frac{100{,}2}{0{,}333}} = 17{,}35\, cm. \tag{20}$$

A newly designed cross-section is assigned in accordance with expression (20) $\left(b \times h\right) = \left(2 \times 18cm\right)$ instead of the previous cross-section $\left(b \times h\right) = \left(2 \times 5cm\right)$ in order to ensure the required load-bearing capacity of the structure considered in Figure 1.

The performed probabilistic calculation showed that the initial beam cross-section does not provide the required reliability and load-bearing capacity under the specified operating conditions. The results indicate that, during long-term operation and at the adopted level of probability of failure-free operation, the existing geometric parameters of the section are insufficient to resist the applied loads. As a result of the probabilistic calculation, the required parameters of the strengthened cross-section were determined, ensuring the necessary strength reserve and reliability of the structure. It was established that increasing the beam height can significantly increase the load-bearing capacity of the element without changing its width. The adopted new section satisfies the strength conditions and may be recommended for further design and operation of the structure under consideration.

Let us apply the theoretical provisions presented above for assessing load-bearing capacity based on the outlier theory to the case of statistical technical-inspection data for a conditional reinforced concrete structure. The use of a probabilistic approach makes it possible to account for the random nature of changes in external actions, material strength characteristics, and geometric parameters of the structure that affect its operational reliability. Unlike deterministic calculation, statistical analysis makes it possible to assess the probability of reaching a limiting state during operation [29-30].

For the calculation, statistical characteristics of the main factor parameters obtained from inspection results and operational-data analysis were used. Data processing was performed by determining mean values, standard deviations, and coefficients of variation, which makes it possible to assess the influence of each parameter on the load-bearing capacity of the structure. Statistical data for the object under consideration are given in Table 1.

Table 1. Statistical characteristics of factor parameters and load-bearing capacity of the reinforced concrete structure

No.	X_1, (MN/m)	X_2, (MPa)	X_3, (MPa)	X_4, (m)	Y, (MPa)
1	0,04	240	15	0,8	10
2	0,05	210	17	0,6	12
3	0,045	220	20	0,7	11
4	0,055	230	22	0,9	9
5	0,06	215	16	1,0	13
Sum	0,25	1115	90	4,0	55
Mean	0,05	223	18	0,8	11
σ	0,006	10,7704	2,6077	0,2289	1,2
v	0,12	0,0483	0,1449	0,28613	0,1091

The use of the probabilistic outlier method makes it possible to assess the degree of dispersion of random variables relative to their mean values and to determine the influence of variable loading factors on the reliability and load-bearing capacity of the structure during a specified operating period. The statistical characteristics were determined on the basis of processed experimental and calculated data, which enables further probabilistic analysis of structural serviceability.

Table 1 presents the factor parameters: X_1 is the variability of external load; X_2 is the design resistance of reinforcement; X_3 is the design resistance of concrete; X_4 is the effective depth of the cross-section; and the resulting parameter Y is the load-bearing capacity of the reinforced concrete structure.

Based on known methods of variance and correlation analysis, probabilistic characteristics of parameter X_1, reflecting the variability of the external load acting on the reinforced concrete structure, were obtained below [6, pp. 134-140]. The standard deviation is indicated accordingly $\sigma(X_1) = 0{,}006 MN/m;\ \sigma(Y) = 1{,}2 MPa$.

Operating time of the structure:

$$T = 40\,years = 40 \cdot 24 \cdot 365 = 1{,}26144 \cdot 10^9 \text{ sec}. \tag{21}$$

Normative (specified) probability of failure-free operation:

$$[p] = 0{,}95. \tag{22}$$

According to Table 1, the mathematical expectations at equal probability $p_i = 0{,}2 = const$ are:

$$M(X_1) = \sum p_i X_{1,i} = 0{,}2(0{,}04 + 0{,}05 + 0{,}045 + 0{,}055 + 0{,}06),\ M(X_1) = 0{,}05 MN/m. \tag{23}$$

$$M(Y) = \sum p_i Y_{1,i} = 0{,}2(10 + 12 + 11 + 9 + 13),\ M(X_1) = 0{,}05 MN/m. \tag{24}$$

Variations of the corresponding parameters:

$$\upsilon_{X1} = \frac{\sigma(X_1)}{M(X_1)} = \frac{0{,}006}{0{,}05} = 0{,}12;\ \upsilon_Y = \frac{\sigma(Y)}{M(Y)} = \frac{1{,}2}{11} = 0{,}1091. \tag{25}$$

The problem was solved with allowance for expressions (21)-(25). The ratios of the standard deviation values $\sigma_{но} = 0{,}8 MPa$ were determined for the adopted conditional value.

$$\varphi = \frac{\sigma(Y)}{\sigma_{но}} = \frac{1{,}2}{0{,}8};\ \varphi = 1{,}5 \tag{26}$$

Using expression (11), the value Q was determined:

$$Q = 1{,}5\left(1+1{,}5^2\right)^{-1/2};\ Q = 4{,}125 \quad (27)$$

Using formula (10), the safety characteristic was determined:

$$\gamma = -2\ln\left(\frac{0{,}0513\cdot 10^{-7}}{26{,}0172}\right)^{1/2};\ \gamma = 4{,}7273 \quad (28)$$

Using expression (12), the values of the strength reserve factor were obtained with allowance for expressions (25), (26), and (28) [31-33]:

$$K = \frac{[1{,}5 + 4{,}7273\cdot 0{,}1091\cdot(1+1{,}5^2)]^{1/2}}{1{,}5} = 1{,}62;\quad K = 1{,}62. \quad (29)$$

Using formula (13), the strength condition $\left([p] = 0{,}95\right)$ was checked with allowance for expressions (23) and (24):

$$\frac{M(y_0)}{R} \geq M(y), \quad (30)$$

where $M(y_0) = 20MPa$ the parameter denotes the mathematical expectation of the dangerous limiting stress.

Using expression (30), it was determined that $\frac{200}{1{,}62} \geq 11$ or 12.346 > 11, therefore, the strength condition is satisfied under the probabilistic calculation method.

Using expressions (1)-(3), the lower estimate of the probability of failure-free operation was determined for the initial data of Example 1 considered in this article:

$$b = 1{,}26144\cdot 10^9\left(5\cdot 10^{-2}\right)\left(1+\frac{0{,}8^2}{1{,}2^2}\right)^{-1/2}\exp\left[\left(20-11\right)^2 : 2 : \left(1{,}2^2+0{,}8^2\right)\right] = 0{,}17862; \quad (31)$$

$$b = 0{,}17862.$$

Using formula (1), and taking into account the value obtained in (31), the following was determined for 40 years of actual operation at the time of inspection:

$$p_{но}(40\ years) = 1 - 0{,}17862 = 0{,}82138;\ p_{н.о} = 0{,}82138. \quad (32)$$

According to value (32), the probability of failure-free operation of the structure under consideration (Figure 2) over 40 years of operation is 82%.

The failure intensity over 40 years of long-term operation, with allowance for (32), was determined as follows [34]:

$$\lambda = \frac{\ln(p_{но}(40))}{-T} = \frac{\ln(0{,}82138)}{-40} = 0{,}00492\ year^{-1}. \quad (33)$$

The time percentage gamma-life was determined considering expression (33):

$$t_{\gamma} = \frac{\ln(p_{но}(40))}{-\lambda} = \frac{\ln(0{,}82138)}{-0{,}00492} = 40\ years. \quad (34)$$

The calculations showed that the proposed probabilistic approach, based on the theory of probabilistic outliers, makes it possible to quantitatively assess the reliability of long-term operating building structures while accounting for the statistical variability of loads and load-bearing capacity. Based on the statistical characteristics of the factor parameters of the reinforced concrete structure, the safety characteristic γ= 4.7273 and the strength reserve factor K=1.62 were determined. The strength check according to expression (30) confirmed satisfaction of the reliability criterion at the specified normative probability of failure-free operation [p] = 0.95.

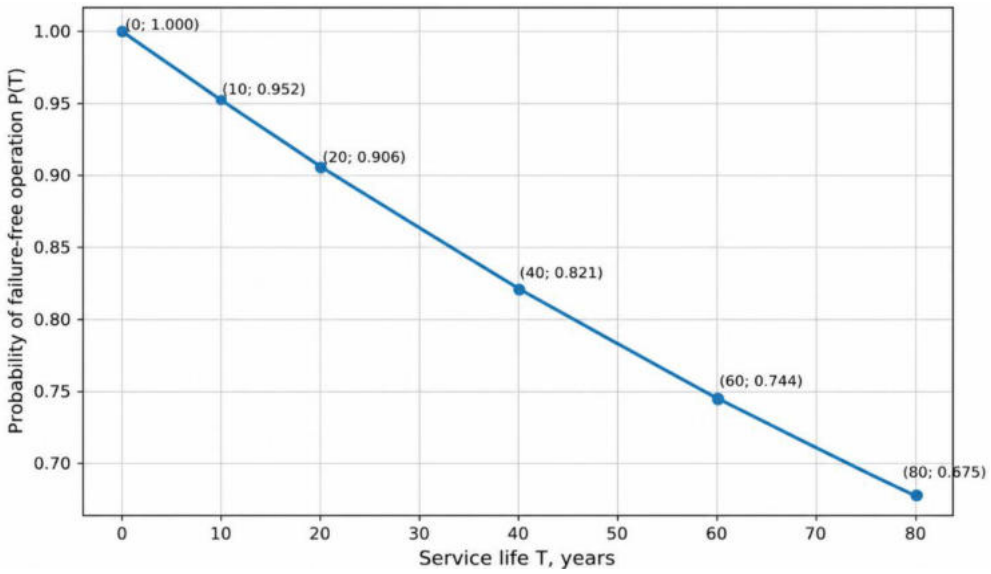

Fig.2. Dependence of the probability of failure-free operation of the structure on service life

In addition, the actual probability of failure-free operation of the structure over 40 years of service was determined as $P_{но}$=0.82138, which corresponds to approximately an 82% probability of failure-free operation. The results confirm that the application of the theory of probabilistic outliers makes it possible to perform a probabilistic assessment of operational reliability and to predict the residual service life of long-term operating building structures.

Based on the results of the probabilistic analysis, a dependence of the probability of failure-free operation of the structure on the service life was obtained (Figure 2). The calculation was performed using the obtained failure intensity λ = 0.00492 year-1 according to expression (33).

The approximating function for the dependence of the probability of failure-free operation shown in Figure 2 has an exponential form [35-36]:

$$P(T) = e^{-\lambda T},$$

where *P(T)* is the probability of failure-free operation of the structure; λ is the failure intensity; *T* is the service life of the structure, years.

Taking into account the failure intensity lambda = 0.00492 year-1 obtained in (33), the approximating function takes the following form (Figure 2):

$$P(T) = e^{-0{,}00492T}. \quad (35)$$

The obtained dependence describes an exponential decrease in the probability of failure-free operation of the structure over time. At *T*=40 years, the value of the function $P(40) = e^{-0{,}0049240} = 0{,}82$ orresponds to the result of the probabilistic calculation performed above. The obtained function can be used to predict residual service life and assess changes in the reliability of building and mechanical-engineering structures during long-term operation.

Analysis of the graph shows that the probability of failure-free operation of the structure decreases according to an exponential law as service life increases. At the initial stage of operation, the decrease in probability is relatively

slow; however, during long-term service, the influence of random loads, damage accumulation, and material degradation gradually reduces the reliability level [37-39].

The characteristic function values are as follows: at a service life of 0 years, the probability of failure-free operation is 1.0; at 10 years, 0.952; at 20 years, 0.906; at 40 years, 0.821; and at 60 years, 0.744.

For the design service life of 40 years, the probability of failure-free operation is about 0.82, which agrees with the results obtained in this study. The constructed dependence confirms the possibility of applying the theory of probabilistic outliers to predict residual service life and assess the operational reliability of building and mechanical-engineering structures [40].

Conclusion

The paper presents a probabilistic method for assessing the reliability of building structures during long-term operation. The method is based on the theory of outliers of random processes and accounts for the actual scatter of loads, strength characteristics of materials, and parameters of the stress-strain state. The proposed algorithm analyzes the frequency with which a random load exceeds a critical level, making it possible to move from standard deterministic strength calculations to a direct quantitative assessment of object reliability.

Analytical relationships were obtained that link the probability of failure-free operation, safety index, reserve factor, and statistical parameters of the load-resistance system. Unlike classical calculations according to building standards, where fixed loads and normative reliability factors are used, this approach accounts for the real statistics of an object accumulated over years of service, including material wear and changes in operating conditions. This is critically important when inspecting old buildings whose actual condition is already far from the original design state.

Using the developed methodology, a steel beam and a reinforced concrete structure were checked. The calculation based on outlier theory helped identify a deficit in load-bearing capacity, determine strengthening parameters, and calculate reliability at the specified normative probability of failure-free operation. For the steel beam, it was established that the original section did not provide the required reliability; therefore, new safe profile dimensions were selected. For the reinforced concrete structure, based on actual inspection data, the probability of failure-free operation over 40 years of service was determined as $P_{но}$ =0.82138, and the failure intensity and gamma-life were calculated.

The analysis showed that the decrease in the probability of failure-free operation of the structure over time follows an exponential law. This confirms the classical nature of the decline in the operational reliability of materials and the accumulation of damage during long-term service. The constructed approximating function clearly illustrates the decline in reliability as service life increases. The obtained dependence makes it possible to forecast the condition of a structure for years ahead, assess its residual service life, and calculate the limiting periods of safe operation while accounting for operational loads.

The results confirm that probabilistic analysis describes the influence of scatter in loads and material properties on structural reliability much more accurately than rigid deterministic calculations. From an engineering standpoint, this makes it possible to make more balanced and economically justified decisions when assessing technical condition, designing strengthening measures, carrying out reconstruction, and predicting the residual service life of objects.

The practical value of the work is that the methodology can be directly applied to the inspection of operating steel structures, reinforced concrete structures, bridges, and industrial buildings subjected to random loads. The transition to a probabilistic approach makes it possible to replace the formal fulfillment of regulatory requirements with an accurate quantitative assessment of the safety of a specific object using field monitoring data.

The developed outlier-theory apparatus can be regarded as a promising tool for the further development of methods for calculating building structures. In the future, these algorithms may form the basis for creating digital systems for structural monitoring, durability prediction, and intelligent models for managing the safety of buildings and facilities.

References

[1] Augusti G., Baratta A., Casciati F. Probabilistic Methods in Structural Engineering // Moscow: Stroyizdat, 2017. – 574 p.
[2] Venttsel E.S. Probability Theory // Moscow: Nauka, 2019. – 564 p.
[3] Bolotin V.V. Application of Probability Theory and Reliability Theory Methods in Structural Calculations // Moscow: Stroyizdat, 2021. – 255 p.
[4] Rzhanitsyn A.R. Theory of Structural Reliability Analysis // Moscow: Stroyizdat, 2016. – 239 p.
[5] Braude V.I. Probabilistic Methods for the Calculation of Lifting Machines // Leningrad: Mashinostroenie, 2023, 232 p.
[6] Lychev A.S. Reliability of Building Structures // Moscow: ASV, 2024. – 188 p.
[7] Dang C., Faes M.G., Valdebenito M.A., Wei P., Beer M. Partially Bayesian active learning cubature for structural reliability analysis with extremely small failure probabilities // Computer Methods in Applied Mechanics and Engineering, 2024, 422, 116828. https://doi.org/10.1016/j.cma.2024.116828
[8] Zhang L., Lu Z., Wang P. Efficient structural reliability analysis method based on advanced Kriging model // Applied Mathematical Modelling, 2015, 39(2), 781-793. https://doi.org/10.1016/j.apm.2014.07.061
[9] Tichy M. Applied Methods of Structural Reliability // Springer Science and Business Media, 1993, 403 p.

[10] Zhang H., Dai H., Beer M., Wang W. Structural reliability analysis on the basis of small samples: an interval quasi-Monte Carlo method // Mechanical Systems and Signal Processing, 2013, 37(1-2), 137-151. https://doi.org/10.1016/j.ymssp.2012.09.008
[11] Zhang H. Interval importance sampling method for finite element-based structural reliability assessment under parameter uncertainties // Structural Safety, 2012, 38, 1-10. https://doi.org/10.1016/j.strusafe.2012.05.002
[12] Der Kiureghian A. Analysis of structural reliability under parameter uncertainties // Probabilistic Engineering Mechanics, 2008, 23(4), 351-358. https://doi.org/10.1016/j.probengmech.2008.05.004
[13] Kang Z., Luo Y. Non-probabilistic reliability-based topology optimization of geometrically nonlinear structures using convex models // Computer Methods in Applied Mechanics and Engineering, 2009, 198(41-44), 3228-3238. https://doi.org/10.1016/j.cma.2009.06.004
[14] Hofer L., Toska K., Zanini M.A. Impact of epistemic and aleatory uncertainties on the seismic reliability assessment of existing structures // Structures, 2023, 57, 105235. https://doi.org/10.1016/j.istruc.2023.105235
[15] Kadyrov A.S., Ganyukov A.A., Amanbayev S.S., Bogdanova A.A. Development of mobile communal overpasses applied during repairing of urban communal networks // Material and Mechanical Engineering Technology, № 3, 2023, 11-14. https://doi.org/10.52209/2706-977X_2023_3_1
[16] Kadyrov A., Sinelnikov K., Sakhapov R., Ganyukov A., Kurmasheva B., Suvunbaev S. Studying the process of transport equipment cooling system ultrasonic cleaning // Communications - Scientific Letters of the University of Zilina, 2022, 24(4), B288-B300. https://doi.org/10.26552/com.C.2022.4.B288-B300
[17] Kadyrov A., Ganyukov A., Pak I., Suleyev B., Balabekova K. Theoretical and experimental study of operation of the tank equipment for ultrasonic purification of the internal combustion engine exhaust gases // Communications - Scientific Letters of the University of Zilina, 2021, 23(3), B219-B226. https://doi.org/10.26552/com.C.2021.3.B219-B226
[18] Kadyrov A., Balabekova K., Ganyukov A., Akhmediyev S. The constructive solution and calculation of elements of the unified module of the mobile bridge overcrossing // Transport Problems, 2017, 12. https://doi.org/10.20858/tp.2017.12.3.6
[19] Kadyrov A., Ganyukov A.A., Balabekova K.G., Zhunusbekova Z.Z., Suleev B.D. Scientific and engineering bases for development of mobile overpasses // Material and Mechanical Engineering Technology, 2020, 2(2), 7-13.
[20] Ganyukov A.A., Sinelnikov K.A., Kabikenov S.Z., Karsakova A.Z. Research and calculation of the deformed state of the roadway mobile overpass // Material and Mechanical Engineering Technology, 2024, 3, 88-95. https://doi.org/10.52209/2706-977X_2024_3_88
[21] Val D.V., Chernin L., Yurchenko D. Updatable probabilistic evaluation of failure rates of mechanical components in power take-off systems of tidal stream turbines // Energies, 2021, 14(20), 6586. https://doi.org/10.3390/en14206586
[22] Li J., Guo X., Zhang X., Wu Z. Time-dependent reliability assessment and optimal design of corroded reinforced concrete beams // Advanced Structural Engineering, 2024, 26(4), 456-472. https://doi.org/10.1177/13694332241247923
[23] Smith J.A., Johnson B.K. Reliability index for steel structure's technical state and residual life assessment // Technical Journal, 2024, 18(si1), 23-35. https://doi.org/10.31803/tg-20230508125238
[24] Development of the procedure for the estimation of reliability of reinforced concrete beams, strengthened by building up the stretched reinforcing bars under load // Eastern-European Journal of Enterprise Technologies, 2018, 5(7(95)), 32-42. https://doi.org/10.15587/1729-4061.2018.142750
[25] Tazhentayeva E., Vighio A.A., Saha K.M., Rakhimov M., Zakaria R., Wen T.J., Rakhimov A., Rakhimova Z., Imanov Y., Maikotova K. A renovation framework for energy efficient dilapidated building retrofitting in Kazakhstan // Chemical Engineering Transactions, 2024, 113, 613-618. https://doi.org/10.3303/CET24113103
[26] Zhangbay N., Oner A., Rakhimov M., Tursunkululy T., Abikerova U. Thermal performance evaluation of a retrofitted building with adaptive composite energy-saving facade systems // Energies, 2025, 18(6), 140. https://doi.org/10.3390/en18061402
[27] Rakhimova G., Aisanova M., Rakhimov M., Abisheva A., Khan M., Maikotova K. The influence of a complex additive on the hydrophysical properties of concrete for road construction // Lindi 2024 6th IEEE International Symposium on Logistics and Industrial Informatics, 2024, 196-172. https://doi.org/10.1109/LINDI63813.2024.10820395
[28] Stanevich V., Rakhimova G., Vyshar O., Bulyga L., Rakhimov M., Kudryshova B., Ibraimbayeva G., Beisenbaev M., Zhakanov A. Overburden coal output rocks as a raw material for making ceramic building materials // Advances in Materials Research South Korea, 2025, 14(2), 63-172. https://doi.org/10.12989/amr.2025.14.2.163
[29] Rakhimov M.A., Abakirova Z.A., Aldungarova A.K., de Navascués I.M.P., Moldamuratov Z.N. Optimization of a sustainable composition of fine-grained concrete for 3D-printing with partial substitution of sand with fly ash and slag waste // Nanotechnologies in Construction, 2025, 17(3), 296-306. https://doi.org/10.15828/2075-8545-2025-17-3-296-306
[30] Bakirbayeva A., Rakhimov M., Aulbikirova Z., Aldungarova A., Menendez I., Mukhambetkaliev K. Impact of pavement quality on improving logistics schemes in the transportation industry // Lindi 2024 6th IEEE International Symposium on Logistics and Industrial Informatics, 2024, 157-161. https://doi.org/10.1109/LINDI63813.2024.10820422
[31] Sherov K.T., Zh N., Karsakova B.N., Absadykov J.B., Toshov M.R., Sikhimbayev. Studying the effect of the boring bar amplitude-frequency characteristics on the accuracy of machining a large-sized part // News of the National Academy of Sciences of the Republic of Kazakhstan. Series of Geology and Technical Sciences, 2024, 2(464), 217-227. https://doi.org/10.32014/2024.2518-170X.405
[32] Sherov K.T., Alikulov D.E. Control ruler for angles between planes of V-shaped guides // Measurement Techniques, 2012, 55(4), 397-399. https://doi.org/10.1007/s11018-012-9971-5
[33] Mardonov B.T., Sherov K.T., Toirov M.S., Makhmudov L.N., Yakhshiev S.N., Kongkybayeva A.N., Shezhau K. Features of engineering methods of research results on butt welding on metal pipelines // Material and Mechanical Engineering Technology, 2024(1), 3. https://doi.org/10.52209/2706-977X_2024_1_3
[34] Kadyrov A., Pak I., Ganyukov A., Imanov M., Balabekova K. Research of operation of equipment for ultrasonic purification of exhaust gases of internal combustion engines // Journal of Engineering Physics and Thermophysics, 2021, 94(6), 1407-1415. https://doi.org/10.1007/s10891-021-02447-x

[35] Jiaqi Liu, Yunwen Feng, Cheng Lu, Chengwei Fei. Operational reliability assessment of complex mechanical systems with multiple failure modes: An adaptive decomposition-synchronous-coordination approach // Reliability Engineering & System Safety, (251) 2024. https://doi.org/10.1016/j.ress.2024.110342
[36] Youbao Jiang, Xuyang Zhang, Michael Beer, Hao Zhou, Yu Leng. An efficient method for reliability-based design optimization of structures under random excitation by mapping between reliability and operator norm // Reliability Engineering & System Safety, 2024. https://doi.org/10.1016/j.ress.2024.110047
[37] Ahmad Baklouti, Khalil Dammak, Abdelkhalak El Hami. Optimum reliable design of rolling element bearings using multi-objective optimization based on C-NSGA-II // Reliability Engineering & System Safety, 2022. https://doi.org/10.1016/j.ress.2022.108567
[38] Bin Xie, Yanzhong Wang, Yunyi Zhu, Peng Liu, Yu Wu, Fengxia Lu. Time-variant reliability analysis of angular contact ball bearing considering the coupled effect of rolling contact fatigue damage and wear // Reliability Engineering & System Safety, 2024. https://doi.org/10.1016/j.ress.2023.109711
[39] Jiashu Yang, Jianbing Chen, Hector Jensen. Structural design optimization under dynamic reliability constraints based on the probability density evolution method and highly-efficient sensitivity analysis // Probabilistic Engineering Mechanics, 2022. https://doi.org/10.1016/j.probengmech.2022.103456
[40] Xintian Liu, Xueguang Yu, Jiachi Tong, Xu Wang, Xiaolan Wang. Mixed uncertainty analysis for dynamic reliability of mechanical structures considering residual strength // Reliability Engineering & System Safety, 021. https://doi.org/10.1016/j.ress.2021.107689

Information of the authors

Ganyukov Alexandr Anatolyevich, PhD, Associate Professor, Abylkas Saginov Karaganda Technical University
e-mail: severchell@gmail.com

Akhmediyev Serik Kabultayevich, Candidate of Technical Sciences, Associate Professor, Abylkas Saginov Karaganda Technical University
e-mail: s.ahmediev@kstu.kz

Bogdanova Anna Alexeevna, Master of Humanities, Senior Lecturer, Abylkas Saginov Karaganda Technical University
e-mail: a.bogdanova@ktu.edu.kz

DOI 10.52209/2706-977X_2026_3_43 IRSTI 81.09.03 UDC 620.17

Development of High-Perfomance Sand-Polymer Composites from Regenerated Thermoplastics for Structural Applications under Dynamic Loads

[1]Berg A.S., [1]Nurzhanova O.A.*, [1]Zhunuspekov D.S., [2]Wargula L., [1]Suleev B.D.
[1]Abylkas Saginov Karaganda Technical University, Karaganda, Kazakhstan
[2]Poznan University of Technology, Poznan, Poland
*corresponding author

Abstract. This study is devoted to the development and scientific and practical substantiation of a technology for producing highly effective sand-polymer composites (SPC) for structural purposes from recycled thermoplastics. The relevance of the work is determined by the need for extensive recycling of polymer waste and a reduction in the carbon footprint in the construction industry by replacing traditional Portland cement. A polymer matrix of a mixture of recycled low-density polyethylene and polypropylene (v-LDPE/v-PP in a ratio of 70:30) was used as a binder. The dispersed filler is quartz sand ($SiO_2 \geq 98.5\%$), the fractional composition of which is optimized according to the Andreasen-Fuller model to reduce the voidage of the framework from 38% to 22%. To eliminate interfacial incompatibility and improve adhesion, the compatibilizer HDPE-g-MA (3 wt.%) and the elastomer modifier SEBS were used. The samples were manufactured using extrusion mixing followed by hot pressing under a pressure of 15–20 MPa. The optimal component ratio was found to be 20% by weight of polymer binder and 80% by weight of sand filler. The introduction of HDPE-g-MA promoted the formation of Si-O-CO chemical bonds at the interface, which changed the nature of material failure from adhesive to cohesive and ensured an increase in flexural strength to 39.1 MPa and compressive strength to 96.2 MPa. The developed PPC is recommended for use in vibration-loaded elements of transport and construction infrastructure (railway sleepers, airfield and road slabs, foundations). The use of recycled raw materials reduces the cost of products by 25–30% and decreases CO emissions by 1.8–2.4 tons per ton of polymer.

Key words: sand-polymer composite; adhesive failure; cohesive rupture; PND-g-MA modifier; scanning electron microscopy (SEM)

Introduction

The growing volume of polymer waste represents one of the key environmental and technological challenges of the 21st century [1]. Hundreds of millions of tons of synthetic polymers are generated annually worldwide, a significant portion of which are widely used thermoplastics – high- and low-density polyethylene (LDPE/HDPE), polypropylene (PP), and polyethylene terephthalate (PET) [2]. Low recycling rates and long periods of environmental degradation require the development of new methods for their advanced recycling [3].

At the same time, the construction industry faces a shortage of high-quality raw materials and stringent requirements to reduce the carbon footprint of traditional binders, particularly Portland cement, the production of which is responsible for nearly 8% of global CO_2 emissions [4].

A promising solution to both problems is the development of sand-polymer composites (SPCs) – materials in which a matrix of recycled thermoplastic melts serves as a binder and sand fractions of varying particle sizes serve as a dispersed filler [5, 6]. Traditional sand-polymer products (paving slabs, manhole elements, curbs) have long proven themselves to be corrosion- and moisture-resistant materials. However, their use is still limited to non-structural or lightly loaded components [7].

When attempting to use standard polymer-sand composites in structures subject to severe operational conditions - cyclic bending, impact loads, vibration, and dynamic abrasion (e.g., road bases, railroad ties, vibration-isolating foundation elements), serious drawbacks emerge [8-10]:

1. The lack of chemical interaction between the non-polar polyolefin matrix and the polar hydrophilic surface of silicon dioxide (sand) leads to rapid delamination of the material under load;
2. Unmodified regenerated polymers accumulate microcracks under repeated alternating stress;
3. High creep of the thermoplastic matrix at temperatures above 40°C reduces the load-bearing capacity of structures.

This study aims to scientifically substantiate, develop the composition, and manufacture technology for high-performance sand-polymer composites based on recycled thermoplastics that exhibit increased crack resistance, damping capacity, and strength under dynamic loads.

1. Research methods

1.1 Components of sand-polymer composites

The following components were used to synthesize sand-polymer composites:

1) Polymer matrix:

- recycled low-density polyethylene (r-HDPE), which is made from crushed waste containers and pipes. MFI = 0.8 g/10 min (190 °C, 2.16 kg), density = 0.952 g/cm³;

- recycled polypropylene (r-PP), which is made from crushed bumper and household plastic. MFI = 3.5 g/10 min (230 °C, 2.16 kg), density = 0.905 g/cm³.

The polymer matrix was formed from a r-HDPE/r-PP blend in a 70:30 (wt.%) ratio, which ensures an optimal balance between impact strength (HDPE) and stiffness (PP).

Modifiers and compatibilizers:

- HDPE-g-MA (polyethylene grafted with maleic anhydride) with a grafting degree of 0.9 wt.% was used as a finishing agent to improve adhesion to sand.

- slope styrene-ethylene-butylene-styrene rubber (SEBS), impregnated into the matrix to increase impact strength at sub-zero temperatures [11].

3) Mineral filler: quartz sand with a SiO_2 content of ≥ 98.5%. Three sand fractions were formed: coarse (1.25–2.5 mm), medium (0.315–0.63 mm), and pulverized quartz flour/filler flour (d_{50} = 15 μm).

To minimize the volume of polymer melt filling the voids between sand grains, the granulometry was optimized using the Andreasen–Fuller model (the equation for optimal particle packing) [12]:

$$P(d) = \left(\frac{d}{d_{max}}\right)^q \cdot 100 \quad (1)$$

where $P(d)$ - total percentage of particles smaller than d;

d_{max} - maximum particle diameter (2.5 mm);

q - packing index (taken equal to 0.35 to ensure maximum packing density of dispersed systems).

1.2 Technological process for obtaining SPC

The experimentally established ratio of fractions was 50:30:20 by weight (coarse:medium:dust), which made it possible to reduce the void content of the sand framework from 38% to 22%. The technological process for obtaining the SPC is shown in Figure 1.

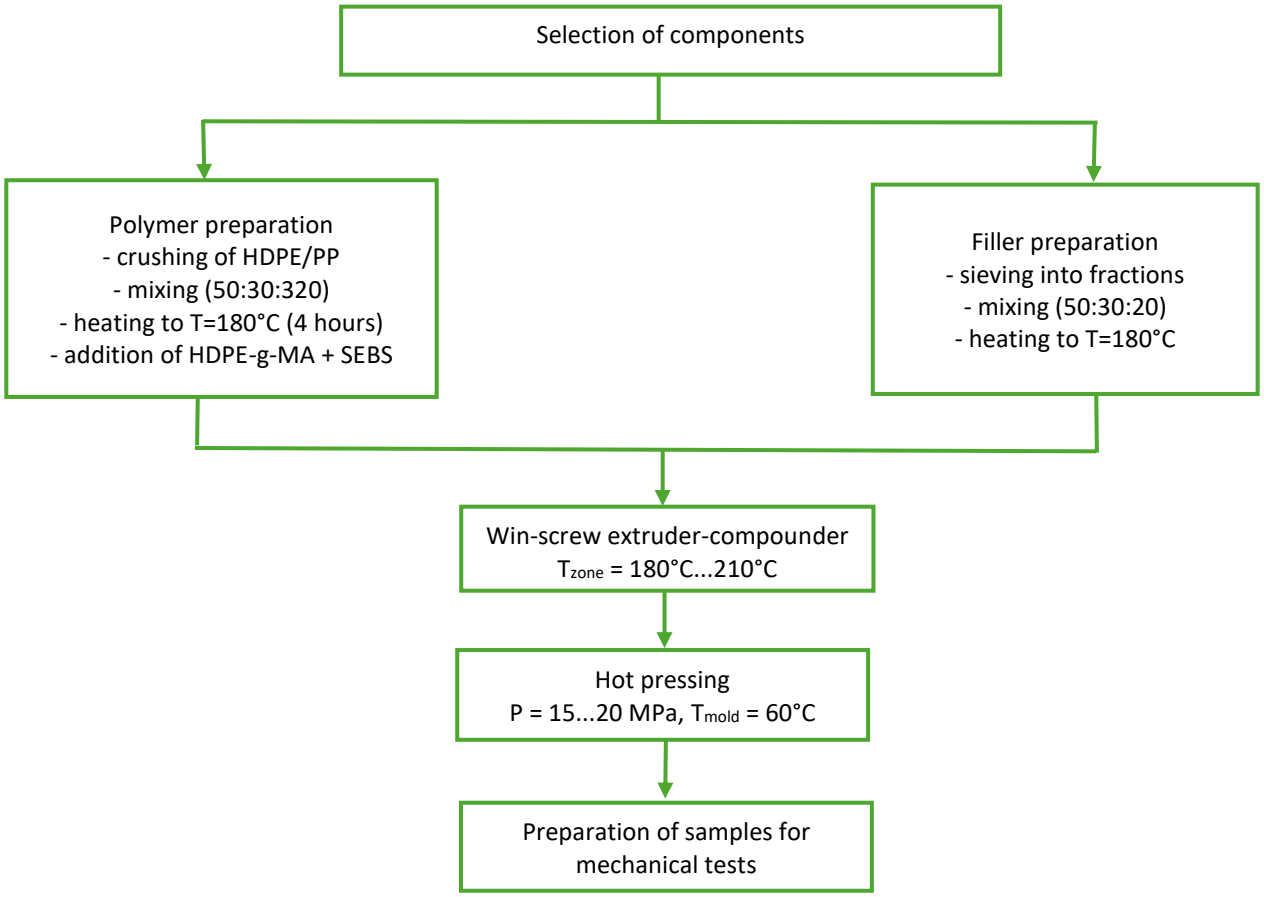

Fig. 1. - Technological process for obtaining SPC

1.3 Preparation of specimens for mechanical tests

Polymer pellets were dried in a vacuum oven at 80°C for 4 hours. The sand was calcined at 150°C to a constant weight. The components were dosed and fed into a co-directional twin-screw extruder (L/D = 40) with a controlled temperature profile in zones from 180°C to 210°C.

The resulting homogenized melt was fed into a heated mold. Compression was performed in a hydraulic press at a pressure of 15–20 MPa, followed by cooling under pressure at a rate of 10°C/min to a temperature of 60°C to prevent shrinkage cavities.

Four series of samples were produced with varying polymer binder content (from 15% to 30% by weight) and modifying system type.

1.4 Test methods

Compressive and flexural strength were determined on a Zwick/Roell Z100 universal testing machine in accordance with GOST 4651-2014 and GOST 4648-2014 at a crosshead speed of 2 mm/min.

Charpy impact strength (unnotched and V-notched) was evaluated on an Instron 9050 pendulum impact tester at temperatures of -40°C, +23°C, and +60°C.

Cyclic bending fatigue testing was performed on a Servopulser servohydraulic testing machine at a frequency of 10 Hz with a cycle asymmetry of R = 0.1. Temperature dependences of the elastic modulus (E') and loss tangent (tanδ) were measured on a DMA 242 E Artemis instrument in three-point bending mode at a frequency of 1 Hz over a temperature range of -80°C to +120°C with a heating rate of 2°C/min.

Surface fracture analysis of the specimens was performed using scanning electron microscopy (SEM) on a TESCAN VEGA3 microscope with microanalysis at an accelerating voltage of 15 kV.

2. Results

2.1 Optimization of the Polymer:Sand ratio and strength indicators

A series of initial tests showed that mechanical properties depend significantly on the degree of filling of the polymer matrix. Average values of the strength characteristics of polyvinylchloride (SPC) are presented below (Table 1) depending on the mass fraction of the polymer binder (a mixture of v-HDPE/v-PP + 3% HDPE-g-MA).

Table 1. Strength characteristics of polyvinylchloride depending on the mass fraction of the polymer binder

Polymer content (wt.%)	Density (ρ, g/cm³)	Compressive strength (σ_c, MPa)	Bending strength (σ_f, MPa)	Flexural modulus of elasticity (E_f, GPa)
12	1.82	42.5	14.2	5.8
16	1.98	78.4	28.6	7.2
20	2.05	96.2	39.1	8.1
25	1.96	82.1	35.4	6.4
30	1.85	67.3	29.0	4.9

At a polymer content of 12%, a binder deficiency is observed: high intergranular porosity remains in the structure, resulting in low strength values.

Maximum strength properties are achieved at 20% polymer by weight (corresponding to 80% optimized sand filler by weight). Increasing the polymer binder content above 25% leads to a decrease in stiffness and compressive strength due to an increase in the volume fraction of the relatively soft polymer phase.

2.2 Effect of interfacial modification on adhesion and failure

The use of the PND-g-MA finishing additive had a decisive impact on the performance of the composites. SEM micrographs of fracture fractures demonstrated a dramatic change in the nature of interaction at the sand-polymer interface.

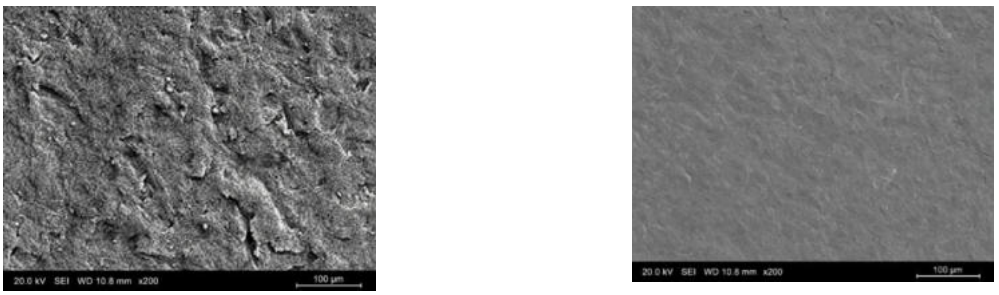

a) b)

Fig. 2. Structure of sand-polymer composites: a) without modifier, b) with the addition of HDPE-g-MA

In unmodified systems, cleavage occurs strictly along the interface: the surfaces of the sand grains remain clean, with traces of complete detachment from the matrix (adhesive failure).

In the modified composite (3% HDPE-g-MA), micrographs reveal the presence of polymer films and plastically deformed filaments remaining on the surface of the sand grains (cohesive failure along the matrix). The anhydride groups of HDPE-g-MA chemically react with silanol groups (Si-OH) on the quartz surface, forming strong Si-O-C(O) bonds.

2.3 Dynamic properties and resistance to cyclic fatigue

The results of cyclic fatigue tests (bending at a frequency of 10 Hz) showed the advantage of the optimized PPC compared to traditional B30 class concrete and unmodified sand-polymer analogues (Figure 3).

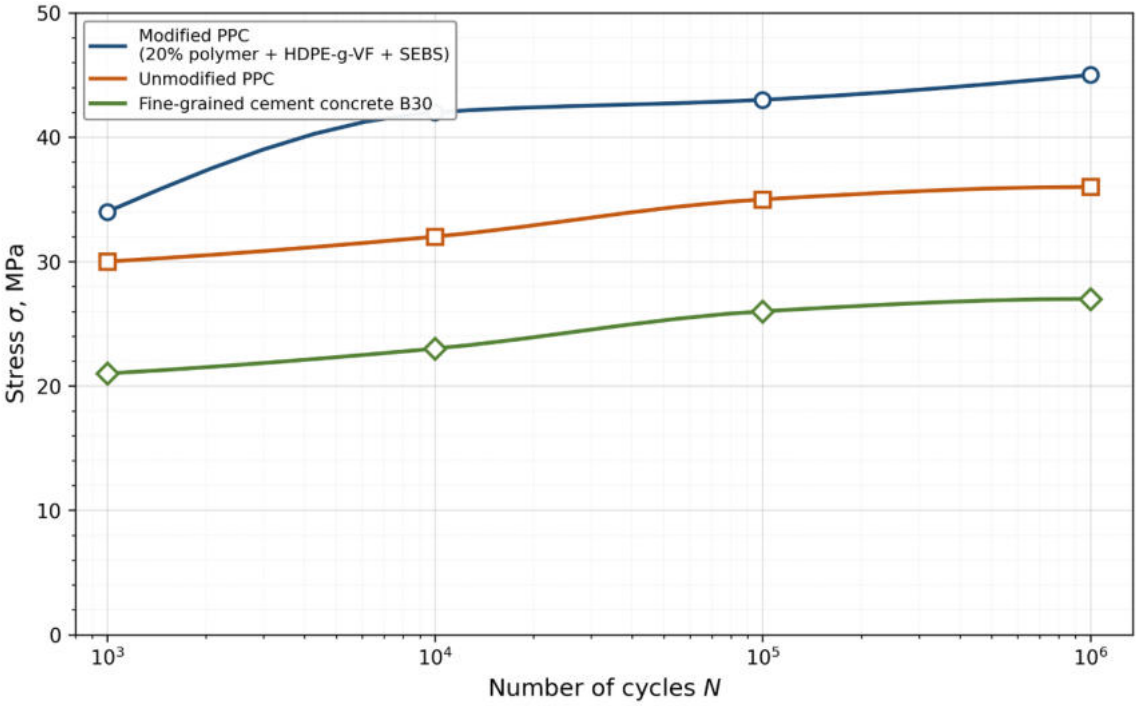

Fig. 3. - Cyclic fatigue of sand-polymer composites

The fatigue strength (N = 10^6 cycles) for the modified PPC was 18.5 MPa, which is almost 47% of its static flexural strength. For the unmodified composite, this value did not exceed 8.2 MPa due to the intensive accumulation of microcracks at the phase boundary.

Cement concrete exhibits rapid strength loss under high-amplitude dynamic loads due to the brittleness of the mineral matrix, whereas the sand-polymer composite dissipates energy more effectively due to the viscoelasticity of the polymer.

2.4 Dynamic mechanical analysis (DMA)

DMA demonstrated the temperature stability range of the developed material.

At -40°C, the modulus is 11.2 GPa, decreasing to 7.5 GPa at +23°C and maintaining a reasonable level of 3.8 GPa at +60°C. Peak damping is observed in the glass transition region of the polymer matrix (approximately -15°C for the elastomeric modifier and +50°C for the amorphous phase of PP). The tanδ value for the modified PPX over the operating temperature range (-20°C to +40°C) is between 0.045 and 0.078, which is 3–5 times higher than that of cement and asphalt concrete. This confirms the material's high vibration absorption.

3.Discussion

The developed composite's high resistance to dynamic and impact loads is due to the synergistic effect of two factors:

1. Multi-level energy dissipation structure:

- at the microlevel, plastic deformation of rubber inclusions (SEBS) initiates localized microsilvering (crazing) of the polymer matrix, preventing crack propagation;

- at the mesolevel, rigid quartz grains force the crack front to deviate from its original direction, increasing the total fracture surface area and the fracture work;

2. Formation of an interfacial trans-crystalline layer:

Sand surface finishing promotes nucleation of the polymer phase on the filler surface during crystallization. This results in the formation of a highly ordered layer with an increased elastic modulus, which transfers mechanical stress from the flexible matrix to the durable filler without stress concentration. To assess the feasibility of using the developed sand-polymer composite in load-bearing and vibration-loaded structures, a comparison of its key characteristics with traditional materials is given (Table 2).

Table 2. Physical characteristics of vibration-loaded structures and PPC and traditional materials

Indicator	Developed by SPC	Cement concrete B30	Asphalt concrete (dense)
Density, kg/m³	2050	2350	2300
Compressive strength, MPa	96.2	40.0	4.5 (at 20 °C)
Bending strength, MPa	39.1	4.5	2.1
Impact strength, kJ/m²	18.4	1.2	-
Water absorption in 28 days, %	0.004	4.5	1.5
Damping coefficient (tan δ)	0.065	0.012	0.035
Frost resistance, cycles	> F500	F200	-

A comparative analysis shows that this development surpasses cement concrete in flexural strength by more than 8 times, and in impact toughness by more than 15 times. Nearly zero water absorption (0.04%) ensures exceptional frost resistance (more than 500 freeze-thaw cycles without loss of mass or strength), as the composite structure lacks the capillary porosity typical of hydrated cement systems.

The use of recycled thermoplastics (HDPE and PP) significantly reduces the cost of finished products. Replacing one ton of traditional polymer raw materials with recycled ones reduces greenhouse gas emissions in CO_2 equivalent by 1.8–2.4 tons. Considering that the composite is 80% made up of readily available mineral filler, the final cost of PPC products is 25–30% lower than that of their primary polymer counterparts and is comparable to high-strength specialized concretes with significantly higher durability in aggressive and dynamic environments.

Conclusions

1.An optimal composition for a structural-grade sand-polymer composite based on a blend of recycled polyolefins (v-HDPE/v-PP 70:30) and particle-balanced quartz sand has been developed. A polymer binder content of 20 wt.% was found to be optimal in terms of physical and mechanical properties.

2.The addition of 3 wt.% of the compatibilizer HDPE-g-MA ensures the formation of stable chemical bonds at the polymer-sand interface. This changes the composite's failure mode from adhesive to cohesive and increases flexural strength by 145% (to 39.1 MPa).

3.Due to matrix modification with an elastomer (SEBS) and high phase adhesion, the cyclic bending fatigue limit based on 10^6 cycles reached 18.5 MPa. The Charpy impact strength was 18.4 kJ/m², allowing the material to be used under intense shock and vibration loads.

4.According to the DMA, the damping coefficient (tanδ) of the developed polymer-sand composite exceeds that of traditional cement concrete by more than five times, making the material effective in reducing vibroacoustic effects.

5.These results open up opportunities for the widespread use of sand-polymer composites made from plastic waste in the production of transport infrastructure components (railway sleepers, interrail decking, airfield and road pavement slabs, and drainage channels) operating under harsh climatic and dynamic conditions.

References

[1] Vanaraj R., Suresh Kumar S.M., Kim S.C., Santhamoorthy M. A Review on Sustainable Upcycling of Plastic Waste Through Depolymerization into High-Value Monomer //Processes 2025, 13, 2431. https://doi.org/10.3390/pr13082431

[2] Dey H, Sheikh Md.R.K, Shuvo A.N. Recent polymer modification strategies for reducing plastic waste and enhancing recyclability //Polymers and Polymer Composites, 2026, 34. doi:10.1177/09673911261441896

[3] Kim H. Advances in Plastic Waste Recycling: Technologies, Environmental Impact, Research Trends, and Policy Perspectives 2025 //International Journal of Environmental Sustainability and Protection, 5(3), 9-19 DOI:10.35745/ijesp2025v05.03.0002

[4] Barbhuiya S., Kanavaris F., Das B.B., Idrees M. Decarbonising cement and concrete production: Strategies, challenges and pathways for sustainable development //Journal of Building Engineering, Volume 86, 2024, 108861, https://doi.org/10.1016/j.jobe.2024.108861.

[5] Yurchenko V., Haiduk V., Skaskevich A., Zharkevich O., Zhetessova G., Reshetnikova O., Smagulov A., Mussayev M. Study of Deformation and Strength Characteristics of Highly Filled Sand–Polymer Composites Based on Regenerated Thermoplastics //J. Compos. Sci. 2025, 9, 206. https:// doi.org/10.3390/jcs9050206

[6] Avdeychik S.V., Antonov A.S., Struk V.A., Prokopchuk N.R., Zhang R. Nanostate Factor in Materials Science of Functional Nanocomposite Materials //Material and Mechanical Engineering Technology, №3, 2024, P.69-75

[7] Barros J.A.O., Soltanzadeh F., de Sousa C., Vera M.O. Development of Sustainable and Innovative Manhole Covers in Fibre-Reinforced Concrete and GFRP Grating // Appl. Sci. 2024, 14, 6903. https://doi.org/10.3390/

app14166903
[8] Liu J., Bai Y. , Li D., Wang Q., Qian W , Wang Y, Kanungo D.P., Wei J. An Experimental Study on the Shear Behaviors of Polymer-Sand Composite Materials after Immersion //Polymers 2018, 10, 924; doi:10.3390/polym10080924Wei
[9] Zhetessova G., Nikonova T., Gierz Ł., Berg A., Yurchenko V., Zharkevich O., Alexey K. A Comparative Analysis of the Dynamic Strength Properties of the Long Guides of Intelligent Machines for a New Method of the Thermal Spraying of Polymer Concrete //Appl. Sci. 2022, 12, 10376. https://doi.org/ 10.3390/app122010376
[10] Milewski H, Leeuw L., Dietz M.S., Diambra A. Shearing resistance of rough polymer-sand interfaces // Conference: ISFOG 2020: 4th International Symposium on Frontiers in Offshore Geotechnics, P.1716-1725
[11] Mashkin N.A., Esirkepova A.B., Sherov K., Rakhimova G.M., Zharkevich O.M., Mussayev M.M. Activation of Cement Binderin Heavy Concrete Technology //Material and mechanical engineering technology, №3, 2020, 8-17
[12] Kravanja G., Mumtaz A.R., Kravanja S. A Comprehensive Review of the Advances, Manufacturing, Properties, Innovations, Environmental Impact and Applications of Ultra-HighPerformance Concrete (UHPC) // Buildings 2024, 14, 382
[13] Zhang T., He J., Xu N., Yin W., Liu D., Liu C., Lang M. Glass fiber-reinforced modified PDCPD composites with improving mode I and mode II interlaminar fracture toughness and impact resistance: Effects of matrix properties //Composites Part B: Engineering 2025, Volume 296, 112225

Funding. The Science Committee of the Ministry of Education and Science of the Republic of Kazakhstan IRN AP 27510559 “Modernization of machine tool equipment of mechanical engineering enterprises using composite materials based on additive technologies”.

Information of the authors

Berg Alexandra Sergeevna, PhD, senior teacher, Abylkas Saginov Karaganda Technical University
e-mail: a.berg@ktu.edu.kz

Nurzhanova Oxana Amangeldyyevna, PhD, associate professor, Abylkas Saginov Karaganda Technical University
e-mail: o.nurzhanova@ktu.edu.kz

Zhunuspekov Darkhan Serikovich, senior teacher, Abylkas Saginov Karaganda Technical University
e-mail: d.zhunuspekov@ktu.edu.kz

Wargula Lukasz, PhD, professor, Poznan University of Technology, Poznan, Poland
e-mail: lukasz.wargula@put.poznan.pl

Suleev Bakhtiyar Daniyarovich, PhD, associate professor, Abylkas Saginov Karaganda Technical University
e-mail: culeev_bahtiyar@mail.ru

DOI 10.52209/2706-977X_2026_3_49 IRSTI 55.29.33 UDC 621.37

The Study of the Feasibility of Generating a Combined Sweep Signal

Moyzes B.*, Kuvshinov K., Plotnikova I., Vavilova G., Vtorushina A.
National Research Tomsk Polytechnic University, Tomsk, Russia
*corresponding author

Abstract. This research is a continuation of a series of studies aimed at developing the shock vibration source of seismic signals with superior parameters compared to existing signal sources. The seismic signal source currently under development will feature compact dimensions and a high capability for extracting useful information against a background of noise. This is achieved through amplitude modulation of the sweep signal and by pressing the base plate down while it is being excited by a force pulse. In this article a schematic diagram, as well as mathematical and physical models of a shock vibration source have been developed. It was conducted a research of the parameters of the amplitude-modulated sweep signal of the shock vibration source of seismic signals and dynamic characteristics of the hydro-volume vibration mechanism. In the article: the results of computer simulations based on a mathematical model are presented; the feasibility of generating an amplitude-modulated sweep signal with a modulation law approximating a harmonic function is proved; the information regarding the experimental design is given.

Keywords: source of seismic signals, sweep signal, amplitude modulation, mathematical model, computer simulations, experimental studies.

Introduction

It's always a current interest to study the vibration parameters during the implementation of various technological processes [1–5].

One of the areas within this field is vibration seismic exploration sweep signal excitation.

One area of focus within this field is seismic exploration involving the generation of sweep signals – ibrational loads produced according to a specific law [6–11].

It was considered in the research works [12-14] a design scheme for a hydro-volume source of seismic oscillations. In the design of a hydrostatic seismic vibrator, where an actuating vibration mechanism based on elastic shells is combined with an impact-based system for pressing the base plate against the ground surface.

A combined signal containing two frequency components will be transmitted to Earth:

- a low-frequency component – the carrier force load;
- a high-frequency component – the informative sweep signal.

In the research [14] it is noted that the oscillatory load generated by a seismic vibration source has a complex, combined form.

The assumption that the force pulse has a nearly sinusoidal shape made it possible to:

- replace the impact assembly with a low-frequency resonant circuit excited by a second generator;
- put forward a hypothesis about the nature of the oscillatory load generated by the source and its physical model (the vibration device) is identical [14].

Thus, the article reviews the operation of a vibration mechanism featuring two oscillation generators:

- a high-frequency generator with oscillation amplitude X_1;
- a low-frequency generator with oscillation amplitude X_2.

The research [14] reviewed the dynamic system of a hydrostatic vibration mechanism, focusing on the influence of the disturbing action of each generator on the displacement amplitude of the moving element.

It was determined in the research the operating resonant frequency of the low-frequency generator and the operating range of the high-frequency generator.

Two generators are involved in the signal generation process, therefore, the low-frequency power-carrying component will be distorted by high frequencies. The first task solved in the research is the theoretical and experimental determination – across various loading conditions – of the high-frequency sweep signal's sweep limit frequencies at which this effect is negligible.

The second task is to determine the excitation parameters at which the useful high-frequency component of the oscillatory load (signal) is maximized relative to the low-frequency force component. Due to the fact that the synchronizing the low- and high-frequency components under laboratory conditions is difficult, the system's operation was analyzed with the generators running at constant frequencies.

The second research part presents the results of computer simulation on the mathematical model of the vibration mechanism (2) [14] with the introduction of nonlinear elements considered in [15]. It is considered the possibility of obtaining a combined oscillatory load with a smooth sinusoidal amplitude envelope [16].

The third part describes the information-measuring system designed for conducting experimental studies.

The results of experimental studies are presented below, and the following issues are considered:

- the influence of the high-frequency generator frequency on the lower resonant frequency to determine the limiting frequencies at which this influence is minimal;
- determining the operating modes at which the ratio of the high-frequency component F_{hf} to the low-frequency component F_{lf} (to the force impulse F_{im}) is the highest (Fig. 1) [13]:
-

$$\left(\frac{F_{hf}}{F_{lf}}\right) \to \max \text{ or } \left(\frac{F_{hf}}{F_{im}}\right) \to \max.$$

It is shown in the research [15] that the generators load the oscillatory system almost identically at the input values of X_2 = 0.603 mm and X_1= 0.701 mm. Thus, after rounding to X_2≈0.6 mm and X_1≈0.7 mm, nominal loading modes were adopted (Table 1).

Table 1. Adopted loading modes

No	Low-frequency generator	High-frequency generator
	Piston stroke, mm	Pistons strokes, mm
1	1.2	1.4
2	1.2	2.8
3	1.2	4.2

The conclusion provides a comparative analysis of computational and experimental data.

1 Theoretical Research

Theoretical studies were conducted using the mathematical model (2) [14] in order to determine the feasibility of obtaining a combined vibration signal.

When modelling the following uniform conditions were adopted:

- an average pressure in the high-pressure hoses: p_0= 0.5 MPa;
- an excitation frequency of the low-frequency generator: f_2=4.2 Hz (close to resonant, as its exact value is not determined (3);
- the loading modes №3 – X_2=1.2 mm and X_1=4.2 mm

The results were obtained from the mathematical model study (Fig. 1 and 2).

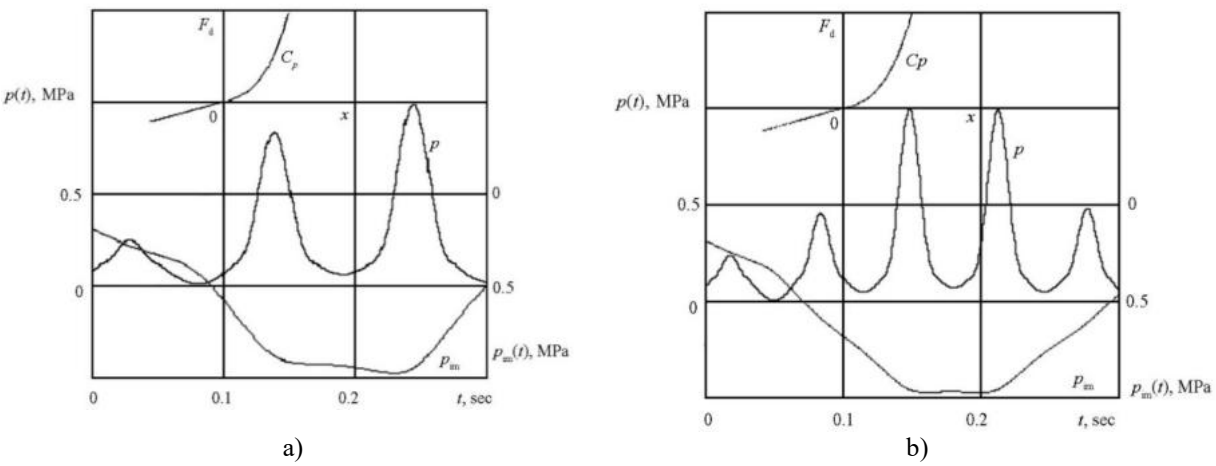

Fig. 1. – Computer simulation results at various frequencies: *a* – f_1=10 Hz; *b* – f_1=15 Hz

F_d are the force transmitted through high pressure hoses (HPH) to the «ground», the driving force;
C_p is the hydraulic stiffness due to volumetric deformation; p_{im} – impulse of force;
p – pressure in HPH when two generators are running (p_2); t – impulse duration

An analysis of the diagrams shows that the influence of the lower (initial) frequencies of the high-frequency generator (f_{1L}) on the impulse decreases as generator operating frequency increases (Fig. 1, 2):

- at initial frequencies of f_{1L}=28Hz – insignificantly,
- at f_{1L}=36Hz – there is no significant influence.

The high frequency limit of the sweep signal for existing generators is in the range of 130÷150 Hz.

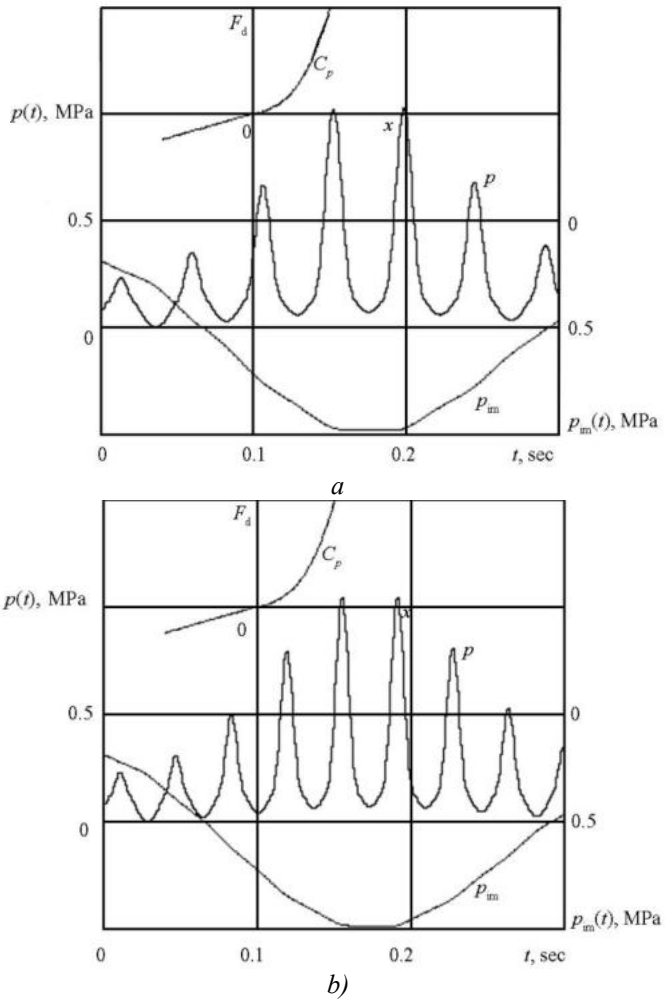

Fig. 2. – Computer modeling results at frequencies: *a* – f_1=25 Hz; *b* – f_1=34 Hz

Given that the determined lower frequency limit under No 3 loading (tabl. 1) [15] is approximately 30–36 Hz (Fig. 1), then for a signal duration of 0.3 sec (Fig. 1), we obtain a signal base of

$$TBWP = \Delta f_0 \cdot T = \left[(130...150) - (30...36)\right] \cdot 0.3 = 28.2...36 \text{ Hz} \cdot \text{sec}.$$

This is discussed in more detail in article [16].

Thus, it is recommended to start the sweep signal at a frequency of 30 Hz.

2 Information and measuring system

Let us consider the schematic diagram of the information-measuring system (Fig. 3), which consists of the actuator [14] and the measuring system.

The measurement system is equipped with five sensors (1–5):

- 1, 2 – pressure sensors in the HPH;
- 3, 4 – displacement sensors for the plungers of the oscillation generators;
- 5 – load displacement sensor.

Sensors transmit information about the actuator parameters to the measurement system. The design of sensors 1–5 is based on using:

- photodiodes as the sensing element;
- LEDs as the luminous flux source.

The measurement principle was based on changing the potential difference across the photodiode by altering the luminous flux incident on it.

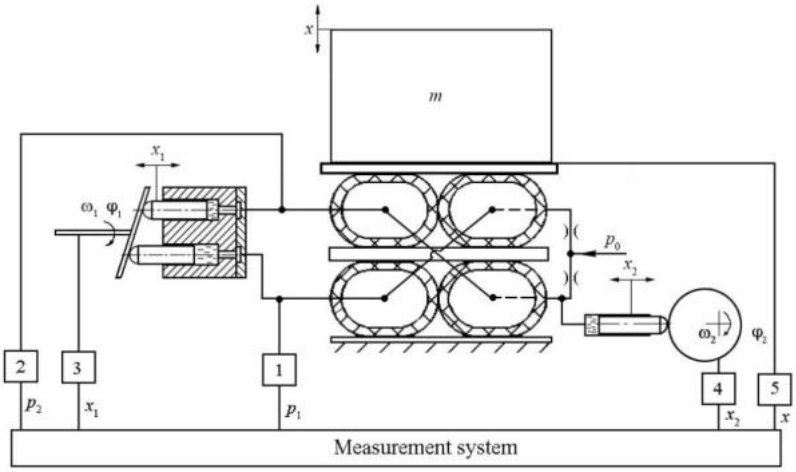

m – load mass; p_0 – average pressure in the high-pressure hose; p_1 and p_2 – pressure in the high-pressure hose generated by the oscillators; x_1, ω_1, φ_1 и x_2, ω_2, φ_2 – parameters of the high-frequency and low-frequency vibration generators (displacement coordinates, angular frequencies, angles of rotation)

Fig. 3. – Information and measurement system

The output signals of generators x_1 and x_2 were measured from the corresponding eccentric 1 rotating on the generators shaft. The phase of signals x and dp was determined by moving the elements of sensor 3 along the curved guide 2 (Fig. 3).

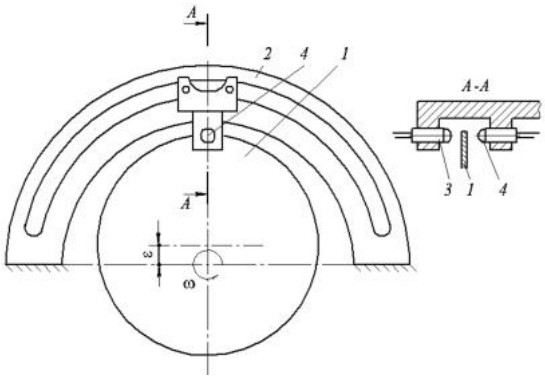

1 – eccentric; 2 – curved guide; 3, 4 – sensor LED and photodiode

Fig. 4. – Sensor installation diagram

The pressures p_1 и p_2 were recorded by blocking the light flux with a shutter attached to the Bourdon tube. Pressure changes in the cavities caused deformation of the tube, resulting in varying degrees of light flux obstruction (Fig. 5).

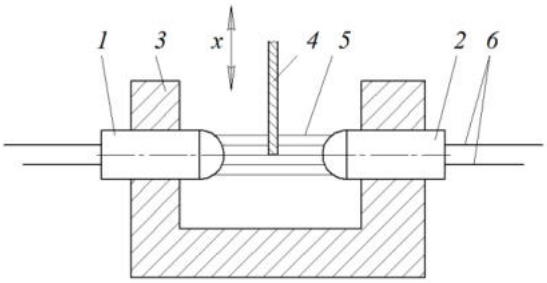

1 – LED; 2 – housing; 3 – light flux; 4 – shutter; 5 – photodiode

Fig. 5. – Sensor operating diagram

The measurement system is shown in Figure 6. For simplicity and cost-effectiveness, it is built using analog instruments:

- C1-91 and C1-93 oscilloscopes;
- Г6-26 signal generator.

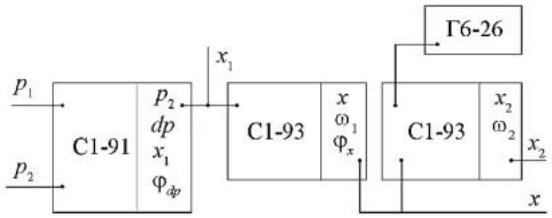

Fig. 6. – The measurement system

The data were digitized after the measurements.

3 Experimental Research

The experimental research methodology in [13] involved separate excitation of the vibromechanism's dynamic system by the generators:

- first, by the high-frequency oscillator;
- then, by the low-frequency oscillator.

As a result, experimental logarithmic amplitude-frequency characteristics (LAFC) were obtained for the following quantities:

- output signal x;
- pressure drop dp;
- phase shift angles $\varphi_{x1/x2}$ and phase shift angle $\varphi_{dp1/dp2}$.

Signal amplitude values were read from the measurement scale on the screens of the C1-91 and C1-93 oscilloscopes, while the phase shift angles were determined by the position of the Lissajous figure on the C1-93 oscilloscope screen. The vibration frequency was determined by comparing the mechanism frequencies with the reference frequency of the Г6-27 signal generator.

An analysis of the LAFC [13] indicates that the dynamic system of the vibromechanism is virtually linear at the average pressure in the high-pressure hose of p_0=2…5 MPa used during the experiments. This is due to the fact that, outside the second resonance zone – which should not occur in an actual signal source, the LAFC exhibits an asymptotic slope of –40 dB/dec, typical for linear systems.

It is known [17–19] that if a linear system is subjected to two disturbing forces, the total effect can be determined by superimposing the effects caused by each force individually. Thus, the disturbing force caused by the operation of both generators will induce complex vibrations

$$x(t) = X_1 \sin(\omega_1 t + \varphi_{01}) + X_2 \sin\left(\omega_2 t + \varphi_{02}\right).$$

If the frequency values ω_1 and ω_2 (f_1 and f_2) are close to each other, the resultant motion takes on a character known as amplitude modulation (Fig. 7).

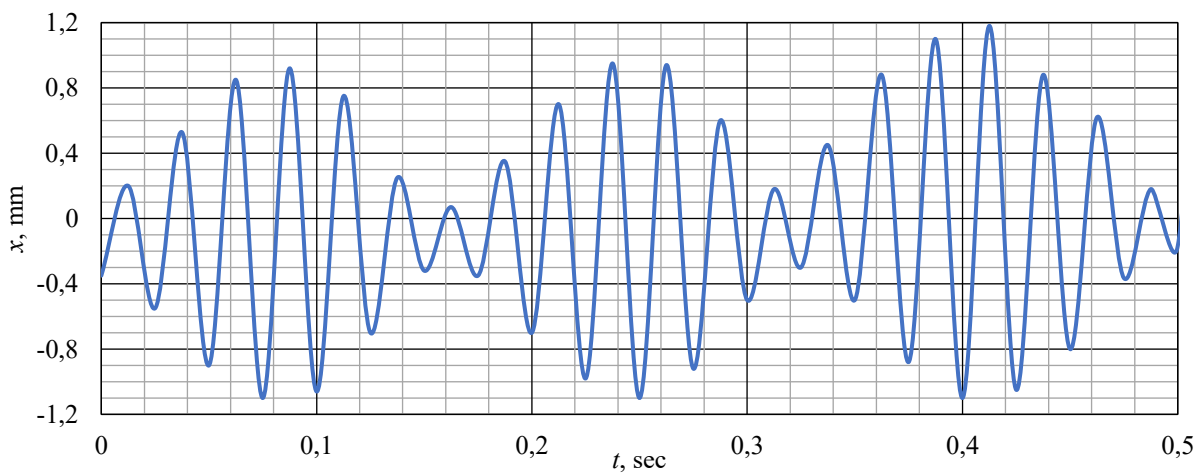

Fig. 7. – Oscillogram of displacement amplitude beats at p_0=2 MPa, f_1=40 Hz and f_2=6,5 Hz

Experimental studies, as well as theoretical ones, demonstrated that as the lower cutoff frequencies of the high-frequency generator increase, the degree of influence of one generator on the other decreases (Fig. 8). There is a threshold frequency at which this influence is virtually unobservable (Fig. 8, *b*).

Experimental studies conducted under various loading conditions of the vibration mechanism confirmed that an increase in the limiting frequency as the degree of loading increased.

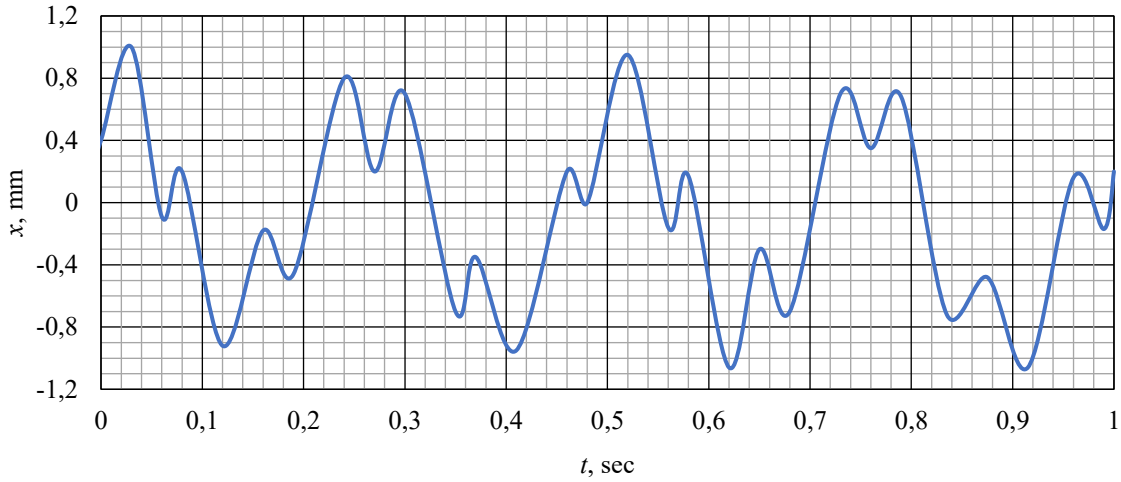

a)

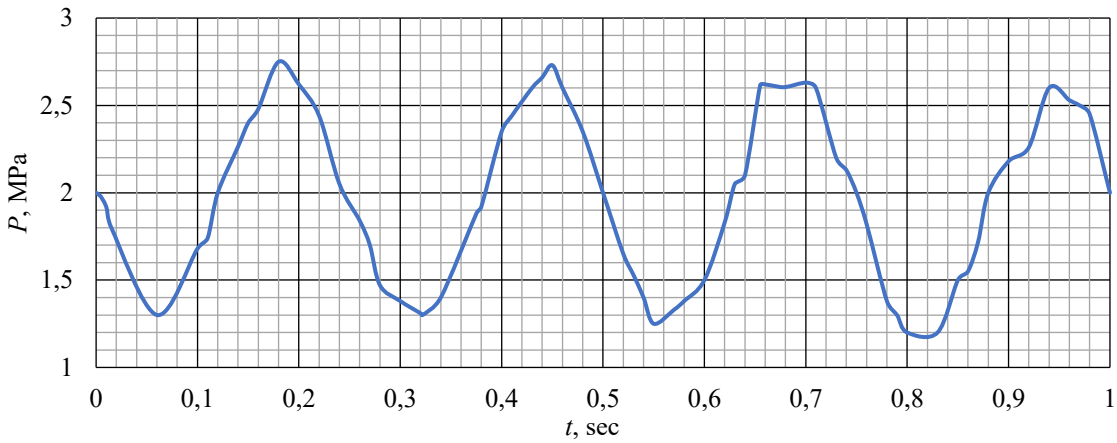

b)

Fig. 8. – Oscillogram of displacement amplitude at p_0=2 MPa at frequencies: *a* – f_1=12 Hz, f_2=4.2 Hz, *b* – f_1=22 Hz, f_2=4.2 Hz

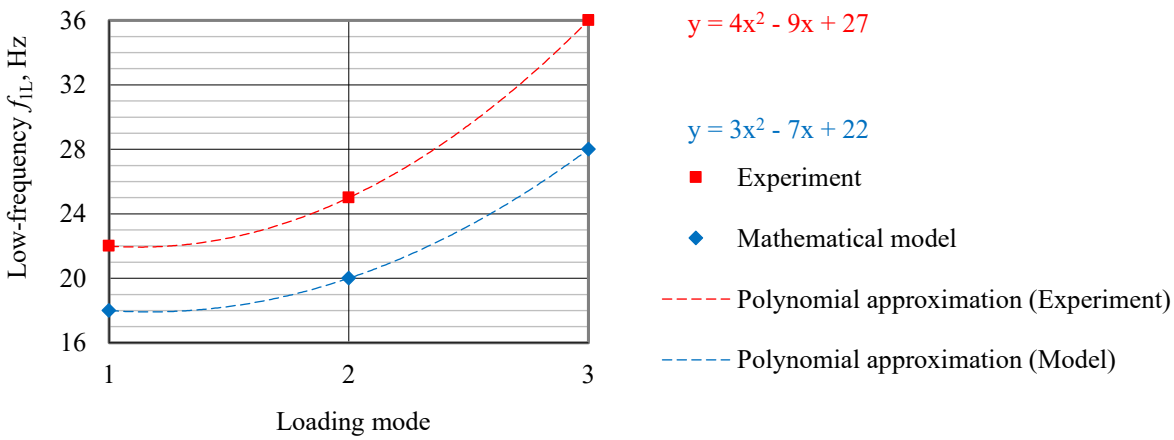

Fig. 9. – Dependence of the limiting frequency on the loading mode: a comparison of the theoretical and experimental research results

The difference between the experimental and theoretical data is due to the presence of an additional resonance [13]. Therefore, for the laboratory prototype of the vibration mechanism, the limiting frequency values were increased during experimental studies.

During the experimental studies, the pressure p (p_2) generated in a single line of the shells by both generators was recorded (Figs. 10–12) under various average pressures p_0 and loading conditions.

The conducted experiments confirmed an increase in the stiffness of the elastic shells with an increase in the average pressure. At the following values:

- at p_0=2 MPa, the system is practically linear (Fig. 10, *b*);
- at p_0=0.5 MPa, the system exhibits significant nonlinearity (Fig. 10, *a*).

Accordingly, the results of studies at an average pressure of p_0=0.5 MPa are presented below, which allows for an increase in the fraction of the high-frequency (informative) component in the sweep signal.

The figures illustrate the change in the ratio of the high-frequency component to the low-frequency component $\frac{F_{hf}}{F_{lf}}$ (Figs. 10–12). The best results were obtained with loading mode No. 3 and an average pressure of p_0= 0.5 MPa (Fig. 12)

$$\frac{F_{hf}}{F_{lf}} \approx 1.$$

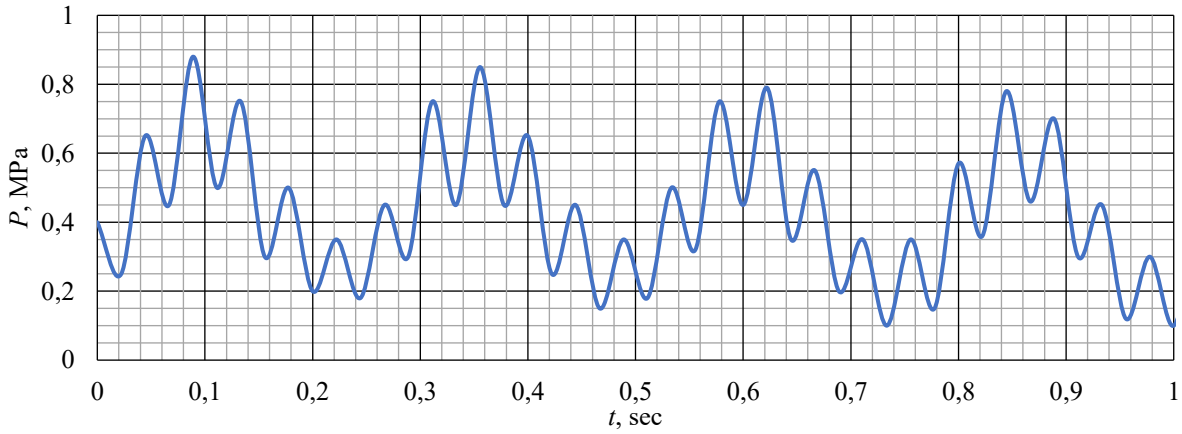

a)

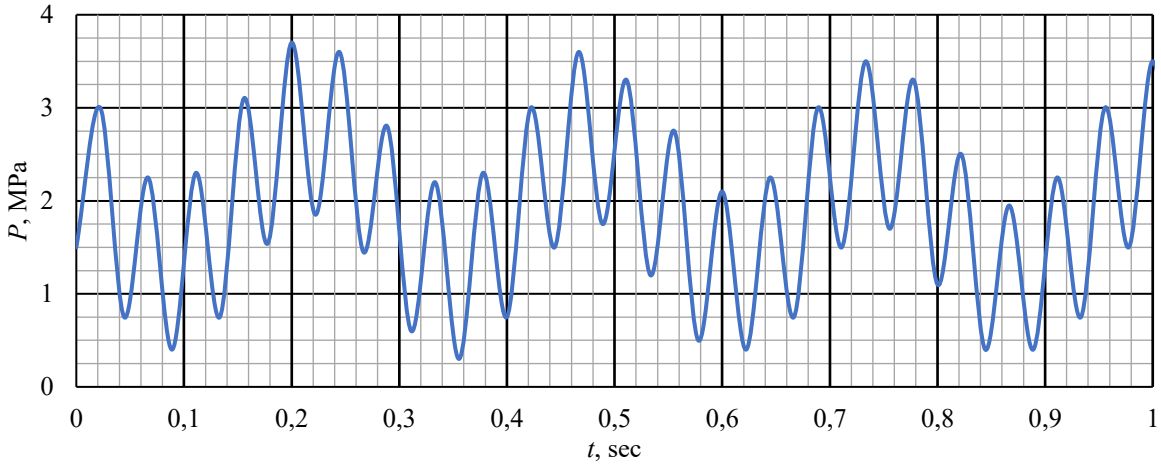

b)

Fig. 10. – Oscillograms of pressure p_2 under loading mode No. 1 at f_1=24 Hz; и f_2=4.2 Hz: *a* – p_0 = 0.5 MPa; *b* – p_0 = 2 MPa

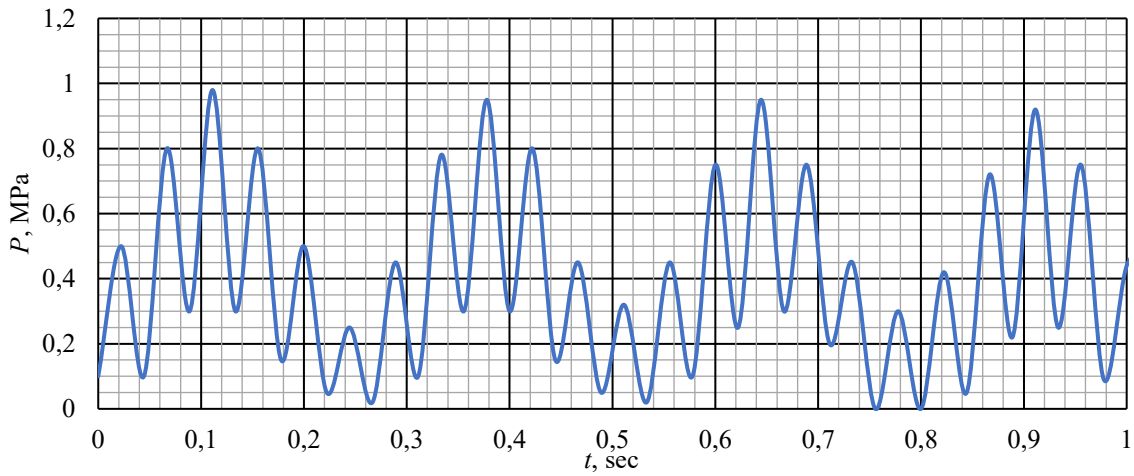

Fig. 11. – Oscillogram of pressure p_2 under loading mode No. 2 and p_0 = 0.5 MPa at f_1=24 Hz; и f_2=4 Hz

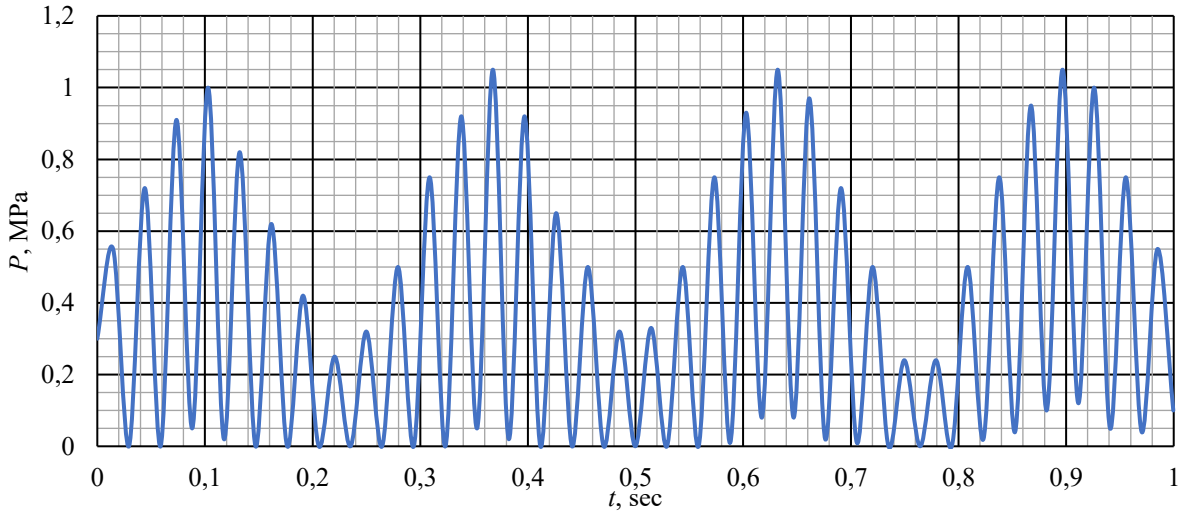

Fig. 12. – Oscillogram of pressure p_2 under loading mode No. 3 and p_0 = 0.5 MPa at f_1=34 Hz; и f_2=4 Hz

Comparing the waveform and amplitude values of the computer-simulated combined signal with those excited by the vibro-mechanism, both qualitative and quantitative agreement of the obtained results can be noted.

Conclusion

This research is a continuation of a series of studies [13–16] addressing to the possibility of exciting an amplitude-modulated sweep signal with a smooth envelope of oscillation peaks.

In the introduction, the authors explain the relevance of the research, highlight the results of previous studies, outline the objectives of the current work, and provide a brief overview of the article's sections.

The research methodology involved a combination of computer modeling and physical experimentation based on the developed information-measuring system.

The chosen approach made it possible to construct and analyze the logarithmic amplitude-frequency characteristics of the system [15] and to plot pressure variations under various loading conditions. At the same time:

- approximate limiting frequencies for the loading modes have been determined (Table 1);
- a decrease in limiting frequency values was recorded as the loading degree of the vibromechanism decreased (Fig. 9).

Experimental studies confirm the conclusion made in [13]: as the mean pressure increases, the system tends toward linear behavior.

By increasing the loading level, it is possible to obtain the maximum possible ratio of the high-frequency sweep component to the dynamic clamping force.

A comparison between the simulated and experimentally formed combined signals shows both quantitative and qualitative agreement (Fig. 1, *b* and Fig. 12).

As a result of the research, it can be concluded that the objectives set in this work have been achieved and that it is physically possible to implement an amplitude-modulated sweep signal with a smooth envelope of oscillation peaks.

References

[1] Akhmediev S.K., Filippova T.S., Oryntayeva G.Zh., Tazhenova G.D., Mikhailov V.F. Free and Forced Vibrations of the Carrier Beam of the Vehicle Chassis // Material and Mechanical Engineering Technology, 2023, №4. – P. 32-41. doi 10.52209/2706-977X_2023_4_32.
[2] Bakirov M.Zh., Mikhailov V.F., Filippova T.S., Oryntayeva G. Zh. Dynamic behaviour analysis in the impact mechanism // Material and Mechanical Engineering Technology, 2022, №4. – 28-35. doi 10.52209/2706-977X_2022_4_28.
[3] Mustafin A., Sadykov N. Reducing Vibration of Elastically Supported Rolling Bearings on a Centrifugal Pump // Material and Mechanical Engineering Technology, 2025, №2. – P. 31-37. doi 10.52209/2706-977X_2025_2_31.
[4] Nikonova T.Yu., Keksel E.Yu., Nurzhanova O.A., Zhukova A.V. Analysis of Effectiveness of Vibrating Screens' Work // Material and Mechanical Engineering Technology, 2020, №1. – P. 17-21.
[5] Zhanibekov T., Nikonova T., Imasheva K.I., Zhukova A.V., Kozhanov M.G., Rakhutin M.G. Studying the Processes that Take Place in Vibroabrasive Machining of Complex-Shaped Parts // Material and Mechanical Engineering Technology, 2022, №3. – P. 42-49. doi 10.52209/2706-977X_2022_3_42.
[6] Nolet G. (Editor). Seismic tomography. With applications in global seismology and exploration geophysics:. – Dordrecht: Reidel, 1987. – 386 pp.
[7] Robert E. Sheriff, Lloyd P. Geldart: Exploration Seismology, 2nd edition. – Cambridge: Cambridge University Press, 1995. – 590 p.
[8] Malischewsky P. Seismic tomography. With applications in global seismology and exploration geophysics: G. Nolet (Editor) // Tectonophysics, Vol. 172, Issues 3–4, 1990. – P. 369-370.
[9] William S.D. Wilcock. Exploration Seismology, 2nd edition: Robert E. Sheriff and Lloyd P. Geldart, Cambridge University Press, 1995 // Continental, Shelf Research, Vol. 17, Issue 5, 1997. – P. 583-584.
[10] Nizhegorodov N., Gavrilin A., Moyzes B., Ditenberg I., Zharkevich O., Zhetessova G., Muravyov O., Mikhail Bets M. Stand for dynamic tests of technical products in the mode of amplitude-frequency modulation with hydrostatic vibratory drive // Journal of Vibroengineering, Volume 18, Issue 6, 2016, 3734-3742
[11] Bizzarri D., Atak O., S. van Ophem, Beriot H. An efficient method for fast frequency sweeps in exterior acoustics using frequency-independent perfectly matched layers // Computer Methods in Applied Mechanics and Engineering, Vol. 451, 2026. – № 118679. doi: 10.1016/j.cma.2025.118679.
[12] Pech D., Prokop G. Optimal frequency sweep synthesis for the identification of low damped systems via a narrow-band method // Signal Processing, Vol. 239, 2026. – № 110283. doi: 10.1016/j.sigpro.2025.110283.
[13] Moyzes B.B., Nizhegorodov A.I. The Study of the Parameters of Amplitude-Modulated Sweep Signal of the Shock Vibration Source of Seismic Signals // Engineering Materials, 2023, Part F1222. – P. 91-128. doi: https://doi.org/10.1007/978-3-031-38964-1_7.
[14] Moyzes B.B., Kuvshinov K.A., Nizhegorodov A.I., Vavilova G.V., Vtorushina A.N. The Study of the Dynamic Characteristics of the Hydro-volume Vibration Mechanism // Material and Mechanical Engineering Technology, 2024, Vol. 4. – P. 120–126. doi 10.52209/2706-977X_2024_4_120
[15] Moyzes B., Kuvshinov K., Plotnikova I., Vavilova G., Vtorushina A. The Influence of Nonlinearity System of the Hydro-volume Vibration Mechanism on its Dynamic Characteristics // Material and Mechanical Engineering Technology, №3, 2025. – P. 8–15. doi 10.52209/2706-977X_2025_3_8.
[16] Moyzes B.B., Gavrilin A.N., Zhetessova G.S. The Selection of Envelope Amplitude of the Sweep Signal Force // Material and Mechanical Engineering Technology, 2019. – P. 16–21.
[17] Gluharev K.K. Rezonans v kolebatel'noj sisteme, vozbuzhdaemyj rotornym gidropul'satorom [Resonance in an oscillatory system excited by a rotary hydraulic pulsator] // Nelinejnye kolebaniya i perekhodnye processy v mashinah [Nonlinear oscillations and transients in machines]. – Moscow: Nauka, 1972. – P. 22-25.
[18] Gluharev K.K., Frolov K.V. Vzaimodejstvie kolebatel'noj sistemy s dvumya istochnikami energii [Interaction of an oscillatory system with two energy sources] // Proceedings of the USSR Academy of Sciences, 1977, №4. – P. 65-71.
[19] Gogonenkov G.N. Izuchenie detal'nogo stroeniya osadochnyh tolshch sejsmorazvedkoj [Study of the detailed structure of sedimentary strata by seismic exploration]. – Moscow: Nedra, 1987. – 221 pp.

Information of the authors

Moyzes Boris Borisovich, c.t.s, associate professor, National Research Tomsk Polytechnic University
e-mail: mbb@tpu.ru

Kuvshinov Kirill Aleksandrovich, senior lector, National Research Tomsk Polytechnic University
e-mail: kuvshinov@tpu.ru

Plotnikova Inna Vasilevna, c.t.s., associate professor, National Research Tomsk Polytechnic University
e-mail: inna@tpu.ru

Vavilova Galina Vasilevna, c.t.s., associate professor, National Research Tomsk Polytechnic University
e-mail: wgw@tpu.ru

Vtorushina Anna Nikolaevna, c.t.s., associate professor, National Research Tomsk Polytechnic University
e-mail: anl@tpu.ru

DOI 10.52209/2706-977X_2026_3_58 IRSTI 81.09.03 UDC 629.331:678.067:004.8

Hybrid Automotive Composites with Artificial Intelligence Based Optimization-Advances, Challenges and Future Directions

AV Santhana Babu[1*], Duraivelu J.[2]
[1]Centre for Excellence-Research, Rajalakshmi Engineering College, Tandalam, Chennai 602105, Tamilnadu, India
[2]Department of Mechanical Engineering, Chennai Institute of Technology, Chennai, India
*corresponding author

Abstract. Modern vehicle designs increasingly employ hybrid automotive composites to reduce weight, enhance performance, and improve sustainability. The growing complexity of hybrid material systems due to multi-reinforcement architectures and process–structure–property linkage has highlighted the limits of classical trial-and-error and physics-based optimization. This review investigates the development of hybrid automotive composites and how Artificial Intelligence (AI)–based optimization is influencing material design, manufacturing, and the service life of composite products and components. These developments include AI aided material selection, hybrid configuration optimization, process parameter tuning, defect prediction, digital twins, and sustainability design frameworks. A systematic assessment is provided of major issues such as performance–recyclability trade-off, data insufficiency, lack of standard datasets, and model interpretability limitations. The review also highlights critical research gaps and future directions towards explainable, lifecycle-aware and autonomous AI-based composite systems. An industrial prospect is also discussed, where proper pathways for scalable, certifiable and sustainable deployment of AI-enabled hybrid composites in the next-generation automotive applications are highlighted.

Keywords: hybrid composite architectures, automotive lightweight materials, digital twins, explainable machine language, sustainable composites, process–structure–property relationships, circular economy design.

Introduction

1.1 Evolution of Automotive Composites

1.1.1 Transition from Monolithic to Hybrid Composites

Automotive materials have evolved from monolithic metals towards increasingly advanced hybrid composite systems to overcome the limitations of individual materials used. The automotive industry initially relied mainly on steels and aluminum alloys for vehicle structures because of their strength, ductility and established processing technologies. However, their relatively high density limits further weight reduction [1, 2]. This was followed by the introduction of fibre-reinforced polymer (FRP) composites, especially glass fibre–reinforced polymers (GFRP), which offered superior specific strength and corrosion resistance, but presented challenges with impact tolerance, recyclability and environmental burden [3, 4]. The emergence of hybrid automotive composites comprising metals combined with FRPs or different fibre types, and multi-reinforcement metal matrix composites to exploit synergistic behavior has been motivated by these limitations [2, 5, 6]. A combined reinforcement of SiC and graphite in a micron-sized hybrid system was found suitable for automotive structural applications [7]. Fibre-metal laminates, natural/synthetic fibre hybrids, and hybrid metal matrix composites are used to tailor stiffness, toughness, durability, and mitigate brittleness or cost penalties associated with monolithic systems [8–10]. This change illustrates a shift to multiple functionalities and balanced performance in the material design of automotive engineering [4, 11].

1.1.2 Lightweighting, Performance, and Sustainability Drivers

The rapid development of hybrid automotive composites has been driven by lightweighting, performance and sustainability requirements. The pressure for stricter fuel economy and emission regulations is compounded by the global trend of electrification. Therefore, the demand for materials that can reduce vehicle mass without losing durability has intensified, despite their relatively high cost, thereby supporting their use in automotive applications [5, 12]. Hybrid composites allow the placement of low-density polymers or natural fibres with high-strength, synthetic fibres or metals to gain stiffness, crashworthiness, fatigue, and energy absorption properties that outperform those of monolithic materials [2, 10, 13]. Natural fibres, recycled reinforcements and agro-waste particulates are increasingly being incorporated in composites so as to reduce embodied energy, cost and life-cycle environmental impact [4, 6, 9]. Advances in processing, interface engineering, and life-cycle assessment further support this transition. This has made hybrid automotive composites important for lightweight, high-performance and sustainable vehicle design [11, 12].

1.2 Need for Artificial Intelligence (AI)-Based Optimization

1.2.1 Complexity of Hybrid Material Systems

Due to the integration of different fibres, matrices, and reinforcements, hybrid automotive composites exhibit complex charecteristics, including pronounced anisotropy, heterogeneous interfaces and strong process-structure-property coupling. Research indicates that multi-reinforcement systems lead to non-linear interactions between the

material composition, process parameters, and functional performances (mechanical strength, wear behavior, and surface integrity) [14]. The situation becomes more complex when considering competing automotive requirements, including lightweighting, crashworthiness, manufacturability, and sustainability, as well as multiphysics effects during processing and service [15-17]. As a result, conventional linear or reductionist approaches cannot effectively navigate the high-dimensional and counterintuitive design space.

1.2.2 Limitations of Trial-and-Error and Conventional Modelling

Conventional techniques such as trial and error experimentation and physics-based modelling approaches cannot capture the complex, non-linear interdependencies between variables and are increasingly inadequate for optimizing hybrid automotive composites. Single-objective optimization often results in sub-optimal trade-offs, such as enhanced wear resistance at the cost of machinability or surface quality [14]. In addition, high-fidelity numerical models are computationally intense and rely on simplifying assumptions that can reduce prediction accuracy under industrially relevant conditions [16, 17]. The combinatorial explosion of design variables makes it impractical to exhaustively experiment, necessitiating the need for AI-driven, data-centric optimization frameworks for robust and efficient composite design. As depicted in Table 1, AI-based analysis can offer advantages over conventional optimization methods [15].

Table 1. Comparative Analysis of AI vs. Traditional Methods

Aspect	Traditional Methods	AI-Driven Methods	Advantage of AI
Computational Cost	High (Iterative Finite Element Analysis (FEA) loops)	Low (Once trained, surrogate models can provide rapid evaluations)	Enables exploration of vast design spaces impracticable with FEA.
Optimality	Often converges to local minima.	Better at finding global optima	Can identify non-intuitive, higher-performance designs within the defined design space.
Handling Uncertainty	Often separate, post hoc analysis (e.g., Monte Carlo).	Integrated directly into the optimization	More efficient and robust reliability-based design.
Manufacturability Integration	Often checked after design, leading to redesign loops.	Can be embedded as constraints within the AI optimization.	Manufacturability can be incorporated as a design constraint, reducing iterations.
Design Interpretation	Based on engineer's intuition from simulation results.	Provides data-driven insights via Explainable AI (XAI) on parameter influence.	Supports faster and more objective decision-making; and can improve user trust.
Knowledge Leverage	Relies on expert experience and documented standards.	Large language models (LLMs) can support cross-disciplinary knowledge synthesis and workflow automation	Can accelerate knowledge transfer and workflow development.

1.3 Scope, Objectives, and Structure of the Review

This review provides an overview of hybrid automotive composites developed using combinations of dissimilar reinforcements, matrices and manufacturing processes aimed at improving mechanical performance, lightweighting potential and sustainability. The main aim of the review is to critically assess how AI-based optimization frameworks are influencing composite materials design, manufacturing, performance prediction and service life. The review synthesizes current knowledge on hybrid composite architectures and processing routes, and state-of-the-art AI and machine-learning (ML) tools being applied across the composite lifecycle. It also highlights contradictions, challenges, and research gaps restricting industrial adoption of hybrid composites. Finally, it outlines near- and long-term research opportunities aligned with automotive sustainability and digitalization goals. The article begins with the fundamentals of hybrid composites and their manufacturing methods, followed by discussions of AI techniques and applications, sustainability issues, industrial case studies, challenges, and future recommendations and concludes with perspectives.

2. Hybrid Automotive Composites: Fundamentals and Classification

2.1 Definition and Design Philosophy of Hybrid Composites

Hybrid automotive composites are defined as advanced engineered material systems consisting of two or more different reinforcements such as natural fibres, synthetic fibres, metals and/or nano-scale fillers purposely incorporated in a polymer matrix or integrated structural assembly to exhibit performance that exceeds that of monolithic materials can offer [1, 18]. Hybrid composites are designed to exploit the complementary mechanical, physical and environmental properties of both fibrous and metallic materials. This combination can improve lightweighting

potential, strength, stiffness, durability, cost effectiveness and sustainability than can be achieved through conventional single-fibre composites or purely metallic structures. The design philosophy is application-driven and system-oriented, and aims to achieve optimal load sharing, tailored stiffness distribution and multifunctionality, rather than maximisation of a single property [19, 20]. In automotive engineering, this philosophy is usually implemented by the combination of natural and synthetic fibres, where carbon or glass fibres are used as the high-performance materials responsible for carrying the primary loads, and natural fibres provide insulation and reduce environmental impacts [1]. Hybridisation may also concern metal–composite systems, where metals ensure impact resistance, torque transmission and joint integrity, while FRPs improve specific stiffness and dynamic response [19]. The emphasis on fibre selection, volume fraction, orientation, stacking sequence and interfacial compatibility in hybrid composites from a materials design perspective serves to efficiently transfer stress, delay damage initiation and improve damage tolerance [20]. Consideration of manufacturability, durability, and lifecycle performance supports the consideration of hybrid automotive composites as smart materials for modern vehicle lightweighting and sustainability designs [18].

2.1 Types of Hybridization

2.1.1 Fibre–Fibre Hybrids

Fibre–fibre hybridization refers to the mixing of two or more fibre types in a common matrix. This is the most studied and widely used type of hybridization in automotive composites to exploit the complementary mechanical and functional properties of different fibres. Standard configurations are carbon-glass, glass-aramid and synthetic-natural fibre hybrids. Here, high-stiffness fibres carry the primary load whereas ductile or sustainable fibres provide toughness, impact resistance and cost efficiency. The stacking sequence, fibre orientation and volume fraction have a strong influence on the hybrid effect and control stress redistribution and gradual damage evolution. Experimental studies show that well-designed fibre-fibre hybrids can suppress brittle failure modes and delay crack propagation, resulting in increased energy absorption under impact loading. Natural-synthetic fibre hybrids also yield weight savings and environmental advantages, particularly for semi-structural components in automobiles. While hybridization can provide significant synergistic benefits, poor architectural design or interfacial incompatibility can reduce their merits [21–23].

2.1.2 Fibre–Matrix Hybrids

Interfacial performance, damage tolerance, and overall composite performance enhancement can be accomplished by hybridization of polymer matrix and fibre reinforcement. In automotive composites, this approach has involved modifying the thermoset or thermoplastic matrix through polymer blending, elastomer toughening or particulate and nano-scale additives while retaining conventional fibre architectures. The matrix plays a key role in governing stress transfer, delamination resistance, and failure mechanisms. Strong fibre-matrix interface adhesion improves stiffness and strength. Controlled interfacial debonding and fibre pull-out promote energy dissipation. Research shows that by optimizing the resin matrix chemistry, it is possible to drastically improve impact resistance and fatigue performance without modifying the fibre content. Poor compatibility between fibres and modified matrices can negate improvements in mechanical properties. Hybridization of fibre and matrix offers an important design control variable for lightweight, crashworthy, and manufacturable automotive composite structures [23-25].

2.1.3 Multi-Scale and Nano-Hybrid Systems

Multi-scale and nano-hybrid composites represent an innovative hybrid approach involving the integration of various scales of reinforcing materials, starting from macro-scale fibres to nano-scale fillers. In general, hybrid composites consist of fibres that serve as the primary source of rigidity and strength, and nano-scaled materials like silica, nanoclay, carbon nanotubes, and graphene that provide toughness and resistance to cracks in the matrix. Adding nano-reinforcements helps to fill in microcracks, limit the growth of even larger cracks, and stabilize the exponential growth of damage. This ultimately leads to improvements in flexural, impact, and fatigue properties. Studies based on morphology show that the properties of the composite benefit from uniform nanoparticle dispersion along with strong interfacial bonding. In the absence of them, performance can degrade due to agglomeration. Multi-scale hybrid composites have the potential to simultaneously improve lightweighting, durability, vibration damping, and environmental resistance of automotive applications. Although promising, barriers to large-scale industrial deployments include processing scalability, control of dispersion, and cost [23-25].

2.2 Common Materials Used in Automotive Applications

2.2.1 Natural, Synthetic, and Recycled Fibres

In automotive composite systems, natural, synthetic and recycled fibres are selected to meet the demands for lightweighting, mechanical performance, cost-effectiveness and sustainability [25, 26]. Natural fibres such as flax, hemp, jute, kenaf, sisal, coir and wood fibres have gained popularity in interior and semi-structural automotive components due to their low density, renewability, biodegradability and relatively favourable specific stiffness and strength [27-29]. Additionally, natural fibres possess beneficial vibration damping and acoustic insulation properties, which are valuable for automotive interior applications [27, 30]. In contrast, synthetic fibres (glass, carbon and aramid

fibres) continue to be widely used in load-bearing and performance-critical automotive components due to their superior absolute strength, stiffness, thermal stability and durability [26, 29, 31]. However, the high energy consumption, non-renewable origin and recycling difficulties associated with synthetic fibres have led to increased research into the use of recycled fibres (reclaimed glass fibres, recycled carbon fibres and recycled polymeric fibres) [32-34]. These recycled fibres support circular economy strategies by minimising material waste and embodied energy while providing adequate mechanical performance in non-critical automotive components [35, 36].

2.2.2 Thermoset versus Thermoplastic Matrices

The polymer matrix plays a decisive role in determining the mechanical performance, processing characteristics, and End-of-Life (EoL) options of automotive composites, with thermoset and thermoplastic systems being the two principal categories [26, 30]. Thermoset matrices such as epoxy, polyester, vinyl ester, phenolic, and polyurethane resins are widely used in automotive applications due to their high stiffness, dimensional stability, chemical resistance, and strong fibre–matrix adhesion resulting from their crosslinked molecular networks [29, 35, 37]. These properties make thermosets suitable for structural and semi-structural components where temperature and mechanical stability are critical. However, the irreversible curing process limits the recyclability and repairability of thermosets posing sustainability concerns [27, 36]. On the other hand, thermoplastics like polypropylene, polyethylene, polyamide, polycarbonate, polyethylene terephthalate, and bio-polymers such as polylactic acid exhibit properties such as reprocessability, high-impact resistance, compatibility with high-volume manufacturing techniques (injection, compression molding, etc.) [28, 32, 38]. Although challenges remain because of higher melt viscosity and fibre–matrix interfacial bonding issues, particularly for natural fibres, thermoplastics are becoming increasingly popular, due to their recyclability as well as vehicle EoL legislations and circular economy [31, 33, 34].

3.Manufacturing Techniques for Hybrid Automotive Composites

3.1Conventional Manufacturing Processes

3.1.1Compression Molding

In the manufacture of hybrid automotive composites, compression molding is one of the most widely used technologies due to its maturity, fast cycle times and suitability for mass production [39-41]. Figure 1 dipicts a schematic of compression molding.

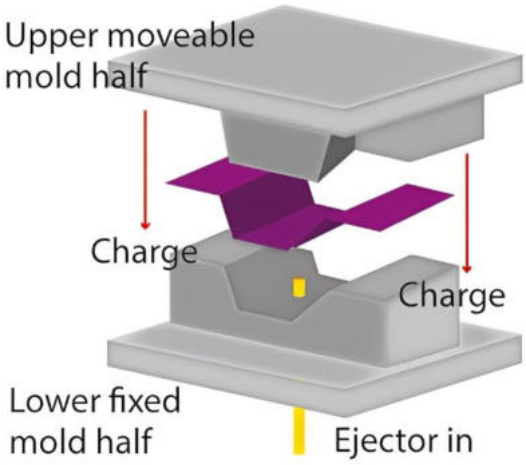

Fig. 1 - Schematic Representation of Compression Molding [42]
(Reproduced Under the Terms of the CC-BY 4.0 License https://creativecommons.org/licenses/by/4.0/.)

Thermoset and thermoplastic hybrid systems may also be used for the process (sheet molding compound, long-fibre thermoplastic, hybrid fibre mat). Different natural and synthetic fibre reinforcements can be combined in a single component [40, 41]. Because compression molding offers good surface finish, dimensional stability, and relatively high fibre volume fractions, it is suitable, for semi-structural and structural automotive components [39, 43]. It is possible to modify hybrid architectures through strategies of charge placement and localized reinforcement to increase stiffness, impact resistance and weight reduction [41, 44]. Nonetheless, fibre reorientation caused by resin flow, non-uniform impregnation, and limited control over complex fibre architectures can cause mechanical anisotropy as well as variations in hybrid laminates [43-45].

3.1.2 Resin Transfer Moulding (RTM)

RTM is an established closed mold technology for high-quality hybrid automotive composites with defined fibre architecture and size precision [39, 40]. Figure 2 shows a schematic of RTM. In RTM, dry hybrid fibre architectures consisting of glass, carbon, and/or natural fibres, among others, are infiltrated with a low-viscosity thermosetting resin with pressure/vacuum assistance [41, 43]. By using this procedure, the fibre wet-out, void content and surface finish are superior to those obtained with open-mold processes [40, 44]. RTM has particular suitability for load-bearing automotive components, especially with fibres placed subject to loading, and high structural integrity [39, 45]. However permeability mismatches between dissimilar fibres, long cycle times, and the need for accurate resin rheology control and injection strategy remain a challenge for high volume automotive applications [43-45].

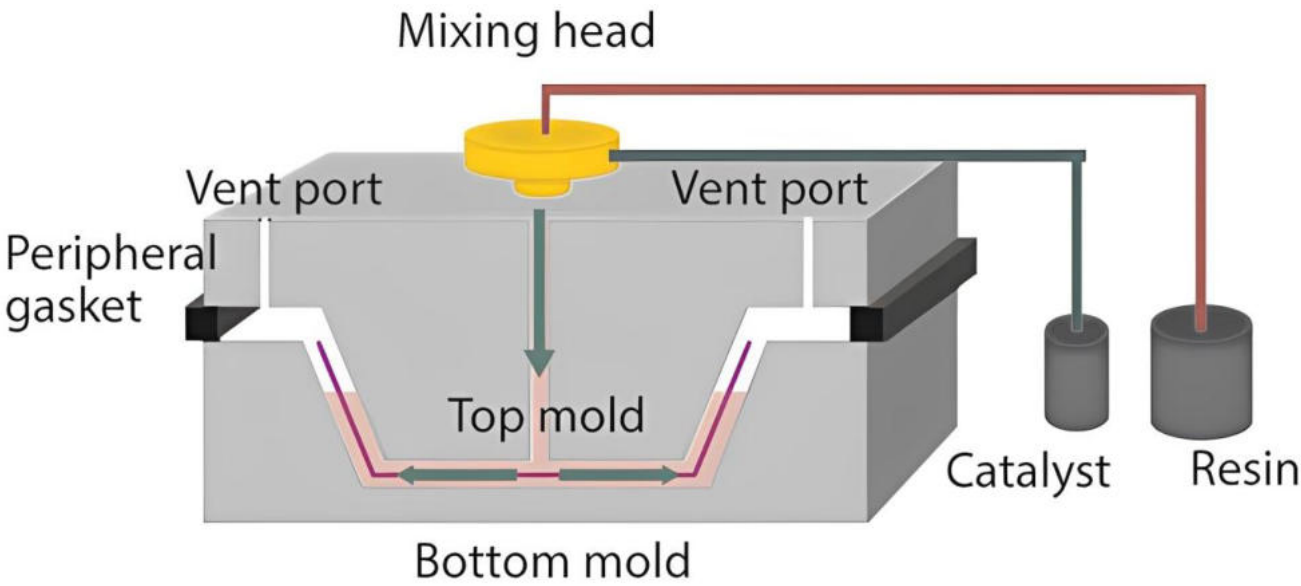

Fig. 2. - Schematic Representation of RTM [42]
(Reproduced Under the Terms of the CC-BY 4.0 License https://creativecommons.org/licenses/by/4.0/.)

3.1.3 Injection Molding and Thermoforming

Injection molding and thermoforming are mainly used in the production of hybrid automotive composites based on thermoplastic materials, where high productivity and recyclability are important requirements [40, 46]. Injection molding is also used in the production of more intricate components through the use of short- or long-fibre-reinforced thermoplastics, enabling high levels of automation, dimensional accuracy, and functional integration [41, 46]. Figure 3 shows a schematic of injection molding. Hybrid structures are typically achieved by overmolding ribs and fastening features onto continuous fibre-reinforced laminates or metallic inserts and provide opportunities for lightweight design and assembly consolidation [44, 47]. Thermoforming shapes pre-consolidated hybrid composite sheets into geometry under controlled heat and pressure while maintaining continuous reinforcement and allowing for rapid cycle times to be achieved [46, 48]. There are, however, significant limitations to the mechanical performance and reliability of injection-molded and thermoformed hybrid components due to fibre breakage, orientation variability, and interfacial bonding quality [46-48].

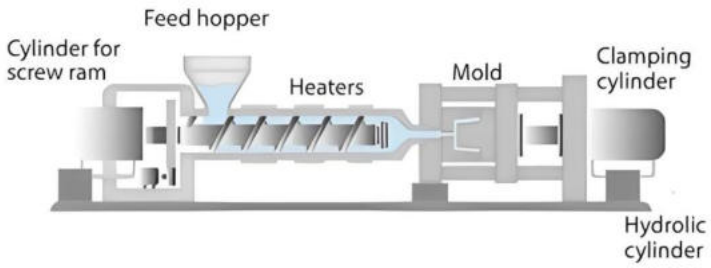

Fig. 3 - Schematic Representation of Injection Molding [42]

(Reproduced Under the Terms of the CC-BY 4.0 License https://creativecommons.org/licenses/by/4.0/.)

3.2 Advanced nd Smart Manufacturing Approaches

3.2.2 Automated Fibre Placement (AFP)

AFP enables precise, programmable placement of continuous fibre tows with controlled orientation and stacking, which is of great value to hybrid composites in automotive parts [43, 44]. AFP makes it possible to hybridize materials at specific localized areas by using high-performance fibres, especially carbon, only in load-carrying areas, while using less expensive fibres, such as glass or natural fibres, in less demanding areas [41, 45]. It is also possible with AFP to optimize material use and maximize structural efficiency while improving stiffness-to-weight ratios [44, 46]. AFP can also reduce labour requirements compared with traditional lay-up methods [43, 47]. However, AFP is relatively expensive, with slower deposition rates, while there is also need for downstream consolidation processes, including RTM and/or compression molding, that can restrict use of AFP in automotive manufacturing [46-48].

3.2.3 Additive Manufacturing (AM) and Hybrid AM

AM is a promising method for the fabrication of hybrid composites to develop tooling, inserts, cores and local reinforcement [46, 47]. AM allows for complex geometries, functional integration, and fast prototyping with less material waste [48]. Hybrid AM approaches combine additive processes with standard composite manufacturing routes. For example, hybrid processes could entail using printed polymer features with RTM or compression molded fibre-reinforced laminates [45, 47]. These strategies improve design freedom and part consolidation, but issues of anisotropy, interfacial bonding and repeatability continue to inhibit large-scale structural automotive applications [46-48].

3.2.4 Digital Twins in Composite Manufacturing

Digital twins connect physical production systems for hybrid composites with virtual process models, offering a promising step towards smart manufacturing of automotive composites [48, 49]. Digital twins that combine sensor information with simulations of resin flow, curing, thermal behavior, and fibre deformation allow process predictions and defect mitigation [45, 47, 49]. In the hybrid composite manufacturing process, these tools are especially useful for optimizing heterogeneous materials, permeability variations and complex interfacial interactions of two or more dissimilar material constituents [44, 48]. Digital twins can reduce the trial and error experimentation, increasing quality assurance and improving process robustness throughout the production life cycle [47, 49]. The performance of these techniques largely depends on reliable material models, dependable in-situ monitoring, and thorough experimental validation [48, 49].

4 AI-Based Optimization Techniques in Hybrid Composite Design

4.1 Overview of AI and ML Methods

4.1.2 Artificial Neural Networks (ANNs)

ANNs are widely used ML methods capable of modelling complex and strongly nonlinear relations, not necessarily relying on physical models of governing equations [50, 51]. Although these methods were inspired by biological neural structures, including layered connections of artificial neurons with input, hidden, and output layers, their learning capability facilitates adaptable structures with weighted connections and nonlinear activation functions [52, 53]. Backpropagation methods of error minimization are generally applied in training ANN models [50, 54]. Due to their flexibility, ANN models are generally well-suited in dealing with complex multivariate, noisy, and multimodal data patterns in many engineering tasks [51, 55]. However, ANN predictions are sensitive to network architecture, learning rate, and training data [53, 56]. Therefore, regularized hyperparameter settings of ANN models are critical in order to obtain statistically reliable and generalizable predictions [55, 57].

4.1.3 Support Vector Machines (SVMs)

SVMs are a type of supervised learning algorithms based on the structural risk minimization principle which enhances generalization capability [50, 53]. The main aim of SVMs is to create an optimal hyperplane in a high dimensional space that maximizes the margin between the data points [52, 54]. SVMs utilize kernel functions for nonlinear problems to implicitly map input data into higher dimensional spaces, thereby modelling complex relationships [51, 55]. By virtue of the margin-based learning framework, SVMs are reasonably robust to overfitting and work well when the number of samples is not too large but the dimensionality is high [53, 56]. SVMs are less susceptible to local-minimum problems than ANNs and their solutions are more stable and repeatable [50, 57]. However, kernel selection and parameter tuning greatly affect their predictive performance, and for large datasets, they have substantial computational complexity, limiting their applicability in big data applications [54, 55].

4.1.4 Decision Trees and Ensemble Models

Decision trees are a rule-based ML method that recursively divides the input feature space into homogeneous sub-groups according to criteria such as information gain or impurity reduction [51, 52]. Due to their sequential nature,

decision trees have clear rules that make them easy to interpret. Therefore, they are suitable for applications where the ability of a model to explain its reasoning is important [53, 57]. Individual decision trees can be unstable and prone to overfitting. This is especially the case if the data used is noisy or complex [50, 54]. To overcome these limitations and improve the predictive accuracy and generalization performance, ensemble learning approaches like random forests, bagging and boosting utilize multiple decision trees [55, 56]. Aggregating the predictions of a number of weak models helps ensemble models reduce the effects of both bias and variance and increase the robustness to the uncertainties associated with the data [51, 57]. In addition, these models allow the calculation of the feature importance and have been shown to outperform standalone models of ANN and SVM in predicting tasks in engineering applications [52, 56].

4.2 Deep Learning and Physics-Informed AI

4.2.2 Convolutional Neural Networks (CNNs) for Microstructure Analysis

Deep learning methods are increasingly applied in microstructure analysis, especially CNNs, which are capable of automatically capturing spatial features from high-dimensional image data [58]. In materials and structural engineering, CNNs enable the analysis of microstructural characteristics such as grain morphology, porosity distribution, crack initiation sites, and damage localization, all of which have crucial effects on macroscopic mechanical and fatigue behavior [59, 60]. Through learning directly from either microscopy images or spatially resolved simulation outputs, CNNs are able to capture complex non-linear correlations between microstructural heterogeneity and material response that are difficult to represent through manually engineered descriptors [60]. By incorporating a stress–strain field, energy dissipation maps, or representative volume element data, CNN-based surrogate models can efficiently establish the microstructure–property link and reduce computational cost, thus complementing traditional physics-based constitutive modelling [58, 61].

4.2.3 Hybrid Data-Driven–Physics-Based Models

Beyond purely data-driven learning, hybrid data-driven-physics based models are a major step towards applying deep learning to engineering and materials problems [58, 61]. ML architectures, training datasets or loss functions can be formulated to incorporate governing physical principles like energy conservation, thermodynamic consistency, damage irreversibility or fatigue evolution laws [59, 62]. This incorporation of physical constraints restricts the solution space of deep neural networks, reduces overfitting, and improves extrapolation to unseen loading or processing conditions [60, 63]. Hybrid methods have shown strong generalisation ability in the literature and also substantial savings in computational cost as compared to fully resolved numerical simulations [58]. By combining mechanistic knowledge with the expressive power of deep learning, physics-informed hybrid models can provide robust, interpretable, and scalable surrogate solutions for multiscale materials modelling, structural analysis, and fatigue life prediction [61-63].

4.3 Optimization Algorithms

4.3.2 Genetic Algorithms (GAs)

GAs are optimization methods based on population evolution. GAs are based on the principle of natural selection. This principle favours the selection of fitter solutions for reproduction. Similarly, this algorithm is based on chromosome-based representations. Genetic and evolution-based algorithms are responsible for generating new offspring [64-70]. The fact that they do not rely on derivatives makes it possible for them to explore complex, nonlinear and multimodal search spaces where gradient information may not be available or uncertain [65, 68]. GAs are readily applied in engineering and ML optimization problems with mixed discrete–continuous variables, complex constraints and multiple local optima [66, 69]. The stochastic nature of GAs provides a stochastic search mechanism which promotes global search and is against to premature convergence, while selection pressure enables gradual exploitation of promising regions [64, 68]. Depending on population size, encoding schemes, and parameters of genetic operators, GA performance depends strongly on these setting, which is often empirical tuning [65, 69]. In addition, the convergence of GAs can be relatively slow for high-dimensional problems, motivating hybridization with swarm-based or probabilistic optimization approaches [66, 70].

4.3.3 Particle Swarm Optimization (PSO)

PSO is a swarm-intelligence-based metaheuristic inspired from social-behavior observed in animal groups such as bird flocks or fish schools [64-70]. Particles in PSO are candidate solutions that move in the search space by updating their velocities and positions through both personal best experience and shared global knowledge [65, 69]. According to [64, 68], this mechanism for information sharing can strike an efficient balance between exploitation and exploration. Moreover, unlike GAs, the mechanism has a relatively simple structure and requires fewer control parameters. PSO usually shows quicker convergence and smaller computational cost, making it appealing for large-scale and real-time optimization problems [65, 70]. Despite this, its performance depends on inertia weights, acceleration coefficients, and swarm topology and insufficient diversity can lead to premature convergence [66, 68].

As a result, numerous studies have investigated on adaptive and hybrid PSO variants to boost reliability and robustness [69, 70].

4.3.4 Bayesian Optimization (BO)

BO is a probabilistic, model-based optimization approach for cases in which objective-function evaluations are costly, noisy, or limited [68-70]. The surrogate model constructed by BO is often based on a Gaussian process, which approximates the objective function and quantifies predictive uncertainty [66, 69]. Thus, acquisition functions guide the sequential selection of new points to evaluate by balancing the exploration of uncertain regions with the exploitation of promising solutions [65, 68]. This strategy, which accounts for predictive uncertainty, allows for high sample efficiency and rapid convergence with far fewer evaluations than population-based heuristics [64, 70]. BO is particularly useful for hyperparameter tuning as well as experimental design in ML and engineering applications [66, 70]. However, the scalability of the approach may be limited in high-dimensional spaces because of the complexity of the surrogate model, which motivates various hybridizations of BO with GA or PSO so as to leverage complementary strengths [67–69].

5 AI Applications Across the Composite Lifecycle

5.1 Material Selection and Hybrid Configuration Optimization

AI has become a key enabler for the material selection and configuration optimization of hybrid automotive composites, where lightweighting, mechanical performance, durability and manufacturability must be considered simultaneously. AI-driven frameworks can efficiently navigate the high-dimensional design space resulting from the complex combinations of matrices, fibres, fillers, geometries, volume fractions, orientations and AM parameters, by learning robust structure–property and process–structure–property relationships from experimental, simulation, and microstructural image data [71, 72]. Predicting the mechanical properties of materials through computational modelling is a common practice in materials science. Supervised ML, deep learning, and hybrid ML–physics models can substantially reduce trial-and-error testing through accelerated screening and ranking of candidate material systems in terms of target metrics such as specific stiffness, strength, energy absorption, and fatigue resistance [71]. Moreover, the implementation of inverse design and optimization strategies, along with ML surrogates, makes it possible to optimize configurations (fibre orientation, stacking sequence, thickness distribution, etc.) autonomously while maintaining their physical plausibility via physics-based validation [71, 72]. Collectively, these approaches will accelerate design iterations, enhance performance trade-offs, and facilitate the design of custom-tailored, high-performance, and sustainable hybrid automotive composite architectures [71, 72].

5.2 Process Parameter Optimization and Defect Prediction

The use of AI has become increasingly important for process parameters optimization and defect prediction of hybrid automotive composite manufacturing due to the coexistence of material heterogeneity, complex processing routes and stringent quality requirements. Surrogate models based on ANNs and ensemble learners are computationally inexpensive alternatives to high-fidelity finite element simulations that can rapidly optimize curing cycles, fibre placement strategies and consolidation parameters while reducing the use of trial-and-error experiments significantly [15]. Table 2 summarizes the prevalent methodologies of the AI-based composite-process optimization. These methodologies mostly consist of ANNs, SVMs and hybrid surrogate frameworks, since they can capture strong nonlinearities between manufacturing variables and quality responses [15].

Table 2. AI Methodologies for Composite Design and Optimization [15]
Reproduced under the terms and conditions of the Creative Commons Attribution (CC BY) license (https://creativecommons.org/licenses/by/4.0/).

Methodology Category	Specific Techniques	Primary Function in Composite Design	Key Advantages	References
Surrogate Modelling & Global Optimization	ANN-GA, ANN-PSO, PSO-ANN	Replaces costly FEA simulations; identifies global or near-global optima for stacking sequences and dimensions.	Can substantially reduce computational cost; effective for high-dimensional, non-linear problems.	[73, 74]
Hybrid & Advanced Predictive Models	Adaptive Neuro-Fuzzy Inference System (ANFIS)-GA, ANFIS-PSO, ANN-Non-Dominated Sorting Genetic Algorithm II (NSGA-II)	Predicts complex behaviors such as buckling and fatigue life while accounting for imperfections.	High accuracy (high R^2 and low root mean squared error); handles uncertainty and multi-objective optimization.	[75, 76]

XAI	SHapley Additive exPlanations (SHAP), Partial Dependence Plots (PDPs), Counterfactual Analysis	Interprets black-box models; identifies critical design parameters and their influence.	Can improve engineering trust; enables informed design adjustments; supports certification.	[77-79]
Uncertainty & Design Allowables	XGBoost, Random Forests, Gaussian Processes	Predicts statistical distribution of material properties (e.g., notched strength, fire-retardant behavior) for reliable design.	Establishes statistical design allowables computationally; manages material and process variability.	[80-84]
LLMs	Generative Pre-trained Transformer 4 (GPT-4) with LangChain, MechGPT, CompCap for Multimodal LLMs (MLLMs)	Automates process planning; integrates cross-disciplinary knowledge; interprets multimodal data.	Automates workflows; enhances knowledge retrieval and synthesis; bridges design and documentation.	[85-87]

Temperature, pressure, resin flow, fibre orientation, and curing time are among the process parameters that can affect the performance of these parts. Robust process windows can be identified by these models minimizing voids and promoting uniform impregnation and the required mechanical properties under loading conditions encountered in automotive applications [88]. At the same time, defect prediction frameworks using AI use deep learning architectures particularly CNNs to identify delamination, porosity, fibre misalignment, and interfacial defects with in-line sensor data, as well as non-destructive evaluation methodologies (e.g. thermography, ultrasonics, X-ray computed tomography) [89, 90]. Integration of XAI further allows identification of dominant process variables responsible for defect formation, supporting closed-loop control and real-time corrective action [15]. AI-enabled approaches equipped with Industry 4.0 and Quality 4.0 paradigms allow a transition from reactive post-process inspection to predictive quality control, scalable, reliable, and sustainable hybrid automotive composite manufacturing [89].

5.3 Mechanical, Thermal, and Impact Property Prediction

AI has proven to be an effective and robust framework for predicting the mechanical, thermal and impact properties of hybrid automotive composites. These materials are complex because of their heterogeneous and multiscale reinforcements with nonlinear damage behavior. A variety of supervised ML models such as ANNs, support vector regression, random forest ensembles, and decision-tree-based algorithms have been widely adopted for the prediction of tensile, flexural, fatigue, and fracture properties by learning their nonlinear correlations with constituent properties, processing conditions, and microstructure features [91, 92]. Data-driven methods can provide improved predictive performance than empirical or physics-based models, particularly in the case of hybrid system models with natural and synthetic fibres, where experimental datasets are scarce or expensive to obtain [91]. AI-based prediction has also been extended from mechanical properties to the prediction of thermophysical properties, namely thermal conductivity, degradation temperature, and thermomechanical stability, using the output from the Thermogravimetric Analysis and Dynamic Mechanical Analysis tests along with the compositional variables [92]. Deep learning models may also allow for the direct extraction of the structure–property relationship from microstructural images. These models can capture of fibre orientation, interfacial quality, and filler dispersion on coupled thermal–mechanical performance [91]. AI-based models have proven to be effective in predicting impact strength, energy absorption, and damage tolerance under dynamic loading. They are useful in crashworthiness design thereby enabling more efficient virtual screening of hybrid composite configurations. [92, 93] When combined, these AI-based predictive tools aid in multi-property assessment in a unified manner, thus expediting material selection, and optimization of performance of next-generation hybrid automotive composites, while diminishing experimental burden and reducing development time significantly [91-93].

5.4 Structural Health Monitoring (SHM) and Damage Detection

AI-enabled SHM is emerging as an integral technique for damage assessment in hybrid automotive composites, thereby supporting a shift towards continuous monitoring instead of periodic inspection. The integration of multi-source information, including vibration response, acoustic emission, strain, ultrasonic, and thermographic data, with ML and deep learning algorithms, respectively, can enable AI-based SHM systems to identify, locate, and categorize complex damage states of matrix cracking, delamination, fibre failure, and barely visible impact damage with high accuracy [90, 94-96]. The use of vibration- and strain-based monitoring with supervised and unsupervised learning can help in identifying the stiffness degradation by looking at the changes in modal parameters under noisy operational conditions [90, 96]. Deep learning architectures such as CNNs, recurrent neural networks (RNNs), long short-term

memory (LSTM) networks, and autoencoders can enhance SHM capability through automated feature extraction, temporal damage tracking, and anomaly detection with reduced dependence on labeled data [94]. Furthermore, AI-driven data fusion systems that blend different types of non-destructive testing improve diagnostic robustness and reduce false positives associated with single-sensor strategies [90, 96]. The scalable and adaptable solutions from these AI-empowered SHM systems improve safety, enable predictive maintenance, and support improved design decision-making of lightweight structures with self-learning capabilities, for hybrid automotive composites with various loading and environmental conditions [94-96].

6 Sustainability, Circular Economy, and Environmental Impact

6.1 AI-Driven Eco-Design of Hybrid Composites

Eco-design for hybrid automotive composites involves incorporating environmental objectives at the material thereby reducing the need for modifications at later design stages. In contrast to traditional design frameworks focusing on mechanical performance, AI-based design frameworks can optimize stiffness, strength and weight along with other environmental parameters, such as embodied energy, recyclability, etc. Utilization of ML and evolutionary algorithms assists in the exploration of large design spaces made of fibre type, stacking sequence, matrix and hybridization ratio, ultimately leading to the identification of eco-efficient solutions that would be difficult to identify through trial-and-error experimentation.

The ability of AI to jointly optimise the natural and synthetic fibres or thermoplastic and thermoset matrices in a hybrid architecture can reduce material use and life-cycle emissions [97]. The pairing of generative design tools with surrogate models also enables the mass-reducing topology optimization of the composite components while maintaining structural performance and avoiding energy intensive mass production. The key implication is that AI-based eco-design promotes principles of circular economy. This can be achieved by introducing design-for-disassembly (DfD), recyclability constraints at an early stage. This happens during the design workflow as opposed to post-design stage. Nonetheless, the success of these techniques mostly depends on the availability of dependable sustainability data and well-defined environmental indicators, which remain fragmented across the automotive composites domain.

6.2 Life Cycle Assessment (LCA) and Carbon Footprint Optimization

LCA evaluates the environmental impact of hybrid automotive composites in the extraction of raw material, manufacturing, use, and end of life. Hybrid composites may produce lower emissions during use-phase due to vehicle lightweighting; however, their production stages can be energy-intensive, especially with the use of carbon or glass fibre [98]. AI-based approaches address this problem by allowing for the quick analysis of scenarios and optimization of carbon footprints over various design and process parameters [99].

The ML models based on LCA database can make predictions about the environmental impact without the high computational cost associated with traditional process-based LCA. This enables real-time feedback during material selection and structural optimization. These techniques let designers weigh trade-offs between savings in manufacturing energy, durability and operational emissions. Alongside this, AI-enhanced optimization has also been used to minimize carbon hotspots in composite manufacturing, such as during autoclave curing or resin infusion, through smart process control and energy-aware scheduling [100]. Carbon-footprint optimization is significantly hindered by uncertainties related to the LCA data of newer hybrid composites, especially those consisting of bio-based or recycled contents. Recognizing these uncertainties and addressing them through hybrid data-driven and physics-based LCA models is a priority research direction.

6.3 Recycling, Reuse, and EoL Challenges for Hybrid Composites

The most critical hurdle to the large-scale adoption of hybrid automotive composites is their recycling and EoL management. The inherent diversity of hybrid systems, which contain various fibres, matrices and interfaces, hampers conventional recycling routes, such as mechanical grinding or thermal recovery. The utilization of AI in the technologies associated with material identification and sorting is increasingly being implemented and investigated. New computer vision and spectroscopy-based techniques are developed for the automatic disassembly of composite parts and their waste segregation. AI-driven damage detection and remaining-life prediction models can support the reuse of composite parts for remanufacturing of components and secondary structural applications. It will also enable safe re-deployment of composite parts. Nonetheless, high-performance hybrid composites may exhibit degraded material properties upon recycling and which may limit their suitability for some automotive applications. The environmental and economic viability of chemical recycling and solvolysis for fibre recovery is still debated [101]. In the context of the circular economy, there is increasing emphasis on AI-supported design-for-recycling approaches to alleviate EoL issues. However, regulatory uncertainty and lack of standardized recycling infrastructure still constrain the implementation of circular hybrid composite systems in practice.

7 Advances and State-of-the-Art Developments

7.1 Recent Research Trends and Breakthroughs

Recent research in hybrid automotive composites is increasingly shifting towards multifunctional and data-driven material systems that combine structural performance with sustainability and smartness. Improvements in fibre hybridization techniques, such as carbon-basalt or natural fibre mixing, have shown enhanced damage tolerance and economic performance [102]. Thermoplastic-based hybrid composites have also attracted attention due to their recyclability and suitability for high-rate manufacturing processes [103]. Advances in AI and digital twin technologies have made it feasible to predict the behavior of composite materials at different scales, from microstructural damage evolution to the performance of components. These tools can reduce the burden of experimentation while speeding up material qualification cycles. The freedom of design has further increased with the introduction of AFP and AM. Furthermore, hybrid composites embedded with sensors can also monitor the health of structures, as the focus on intelligent and connected vehicles intensifies. The world is moving away from simple performance-driven composite design based primarily on conventional objectives to smarter integration of sustainable materials and digitally driven systems.

7.2 Case Studies from the Automotive Industries

7.2.2 Safety-Critical Structural Components: Bumper Beams and Crash Energy Management

Hybrid automotive composites have been widely explored for safety components in automotive structures, especially in impact energy absorption and in the design of bumper beams, where weight reduction should not compromise crashworthiness. In previous automotive research on the application of hybrid composite structures, the primary concept discussed is the ability to offer enhanced specific impact energy absorption and controlled deformation characteristics by laminating natural and synthetic fibres or metal layers [104]. Tests on the effects of jute and kenaf combined with glass fibre in a cost-effective configuration in the production of hybrid bumper beams [105] clearly indicated enhanced hardness, tensile strength, and flexibility than single-fibre structures at relatively cheaper costs, with maximum weight savings up to 33% in the optimized composite structure as opposed to conventional glass fibre-reinforced structures [106-108]. Numerical studies using finite element modelling and classical lamina theory confirmed the ability to control stiffness and impact absorption in optimized glass/carbon hybrid laminates and explored the general advantage and practicability of hybrid composites in the design and production of pedestrian-safe bumpers [104, 109].

7.2.3 Hybrid Composites for Brake and Friction Materials

Brake pads are one of the critical automotive subsystems where hybrid composites formulations have been investigated as alternatives to asbestos-based friction materials due to health and environmental hazards [110]. Previous automotive composite frameworks have pointed out that hybridization entails the synergistic balancing of reinforcement, binder, and filler contributions toward improved thermal stability in tribological applications and under wear conditions [104]. Experimental studies on natural fibre-reinforced hybrid friction composites, based on nettle, sisal, jute, and agricultural by-products embedded in a polymer matrix, demonstrated improved friction stability, reduced fade, and enhanced wear characteristics under SAE standardized testing conditions [111-113]. Full-scale dynamometer assessments further established the acceptability of eco-friendly hybrid brake pads in terms of brake effectiveness, recovery behavior, and thermal endurance for use in light motor vehicles and two-wheelers [1, 112].

7.2.4 Suspension and Chassis Systems: Anti-Roll Bars

Hybrid composites have further been identified for use in suspension parts like anti-roll bars, where resilience, durability, and load-bearing capability are critical. Automotive design work on composites suggests that hybrid composites made from natural and synthetic fibres could potentially replace metallic anti-roll bars if their design and material arrangement were optimized [104]. The design works conducted on kenaf and sugar palm hybrid composites using analytic hierarchy processes and life-cycle assessments showed a decrease in their carbon and energy footprints compared with their steel counterparts [114]. Design work further optimized using quality deployment and inventive problem-solving techniques made it clear that hybrid composites could successfully minimize stress concentration effects and support requirements while providing added emphasis on environmental and customer demands, thereby reaffirming their use in sustainable design applications related to chassis parts like anti-roll bars [115]. In extreme loading and turns, an anti-roll bar is capable of supporting about 30-40% of the collective weight of the suspension parts and thus plays a vital role in controlling roll and ride movements, which emphasizes material resilience, fatigue life, and efficient weight transfer as critical design requirements for their selection [116].

7.2.5 Interior and Exterior Automotive Applications

Market analysis indicates that one of the most common market applications of hybrid composites is for the interior and semi-structural parts of the car. This was attributed to the demand for clean processing, economy, and their ability to provide acoustic insulation. Automotive manufacturers, including Mercedes-Benz, Audi, BMW, Toyota, Ford, and Mitsubishi, have applied hybrid flax, sisal, kenaf, and bamboo. These manufacturers have also used

agricultural-waste-reinforced composites in door panels, dashboards, seat backs, floor mats, and storage bins [117-119]. The assessment and evaluation of all the composites used in the automotive industry show hybridization of the composites, emphasizing the improvement of the stiffness-to-weight ratio of the composites and the noticeable recyclability of the composites, especially the interior parts [104]. Further, the tests and experiments conducted have shown the mechanical requirements of the natural fibre hybrid composites for the interior parts of the car have been attained [120]. Moreover, the laminates made of hybrid glass-carbon and natural and synthetic fibres display an improvement of the flexural and compression strength of the exterior parts [121-123]. However, limitations include moisture and impact resistance [124-126].

7.2.6 Critical Insights and Industrial Relevance

When considered together, the different case studies demonstrate that hybrid composites offer a strong material solution for structural, safety-critical and non-structural automotive components through an integrated approach combining lightweighting, performance, and sustainability [1, 104]. The literature points out that impact robustness, moisture resistance, scalability and EoL recyclability issues remain, especially in natural fibre-dominated hybrids [104]. Addressing these limitations while maintaining the performance advantages of hybrid automotive composites requires integrated material design, advanced processing routes, and life-cycle-oriented optimization frameworks for wider uptake in future vehicle architectures [104].

7.3 Comparison with Conventional Optimization Approaches

Standard optimization strategies applied to hybrid automotive composites are often deterministic, rely on parametric studies or expert-based heuristics. These approaches can face difficulties in addressing complex high-dimensional designs. Methods of this type typically optimize a single objective, e.g., stiffness or weight, while treating sustainability and manufacturability as secondary constraints [127]. In comparison, optimization frameworks that utilize AI can take multiple objectives, which are often conflicting, into consideration at the same time. These objectives include mechanical performance, cost, carbon footprint, and recyclability.

Using ML surrogate models, computational speed can be improved significantly compared to finite-element based iterative optimization to quickly evaluate other hybrid designs. Moreover, as experimental and production-scale data become available, the adaptability of AI-based methods is established. Although AI-driven optimization methods work quite efficiently, there are certain issues associated with data quality, explainability, and generalizability with respect to material systems compared to traditional methods. Even though traditional methods may continue to be acceptable to the authorities for their early-stage validation, it is apparent that the trend is shifting towards hybrid optimization methodologies that blend a physics-informed model with AI capabilities that offers superior performance and sustainability along with design flexibility.

8 Challenges, Contradictions, and Research Gaps

8.1 Manufacturing Challenges and Process–Property Relationships

The production of hybrid automotive composites faces notable challenges due to the interaction of dissimilar fibres, matrices, and processing conditions [39-41]. Differences in the chemical characteristics of fibre interfaces can lead to non-uniform resin distribution during manufacturing and incomplete wetting of fibres which can cause material degradation and reduce strength of the composite [43-45]. Manufacturing defects can affect on mechanical properties, such as stiffness, strength, impact resistance, and fatigue performance, which are important for automotives [44, 46]. Process parameters such as temperature, pressure, resin viscosity, and consolidation time govern fibre orientation, voids formation, and the development of residual stress thereby establishing strong process–property relationships for hybrids [46-48]. Injection molding is a high-shear process that leads to fibre length degradation and greater anisotropy, while compression molding and RTM offer a greater fibre volume fraction and better surface quality [40, 46]. In addition, thermal gradients and differential shrinkage between the hybrid constituents can induce residual stresses that would compromise dimensional stability and long-term durability [44, 47]. Resolving all the aforementioned challenges would require integrated process design coupled with advanced monitoring and predictive modelling frameworks to reliably map the manufacturing parameters to automotive performance [48, 49].

8.2 Performance versus Recyclability Trade-offs

A key conflict concern in AI-aided optimization techniques for hybrid automotive composites is related to performance and recyclability. It has been observed that the majority of existing AI algorithms target the optimization of stiffness, strength, impact resistance, and durability while favoring hybrid topologies, fibre mixes, and thermoset-based materials that impede recyclability and the reuse of car components. Many AI models focus primarily on component performance, while explicit optimization of recyclability and sustainability remains comparatively limited and the use of single materials has not been fully pursued. A clear research gap remains regarding the optimization of recyclability and sustainability together with mechanical performance [15-17].

8.3 Data Scarcity and Lack of Standardized Datasets

Data scarcity and the lack of standardized datasets are among the critical challenges to robust deployment of AI in hybrid automotive composites. High-fidelity experimental datasets, such as X-ray micro-computed tomography-derived fibre orientation fields, process-structure-property relationships, and damage evolution data, are expensive, geometry-specific, and often proprietary. For these reasons, most AI models are based on simulation-generated data. This creates a high risk of overfitting and can limit generalization across materials, processes, and component scales. Meaningful comparison among studies and reproducibility is difficult because of the lack of openly available benchmark-quality datasets. Even though synthetic data generation and physics-informed surrogates alleviate this challenge to an extent, there is a strong need for shared data protocols, standardized testing frameworks, and collaborative data ecosystems that will enable transferable, data-efficient AI models, as reflected in the literature [15-17].

8.4 Model Interpretability and Reliability Issues

Despite reported gains in predictive accuracy, model interpretability and reliability are still concerns that remain unresolved, especially for safety-critical automotive components. Many deep neural networks and reinforcement learning models operate as black-box systems that provide limited physical insight into the governing mechanisms of fibre orientation evolution, defect formation, or failure initiation. This opacity can conflict with the traceability and explainability requirements associated with automotive certification, whose requirements place traceability, conservative design margins, and explainable decision pathways in focus. Moreover, a lack of robustness and industrial trust is brought about by the poor extrapolation shown by models trained within narrow parameter spaces under unseen processing conditions or at novel hybrid configurations. While XAI and physics-informed learning are highly recommended, their adoption has remained fragmented and lacks common validation metrics and reporting protocols suitable for regulatory acceptance [16, 17, 88].

8.5 Scalability and Industrial Implementation Barriers

Scalability and industrial implementation present additional challenges hampering translational readiness. Numerous AI-driven optimization frameworks have been validated at coupon or subcomponent levels but are not connected to full-scale automotive production settings. The challenges associated with their intensive computational requirements, complex sensor integration, latency of acquired data, and poor compatibility with existing Computer Aided Design – Computer Aided Engineering - Product Lifecycle Management infrastructures hinder their real-time or near-real-time deployment. Moreover, scaling up AI-optimized microstructural designs or architectural designs may prove impractical due to manufacturing constraints, quality variability, cost sensitivity, and robustness of the process. A substantial gap remains between the sophistication of current methods and their practical functionality in industrial environments. System-level integration and manufacturing-aware AI remain under-explored [15, 17, 88].

9 Future Directions and Research Opportunities

Future research in hybrid automotive composites is increasingly shaped by advances in AI, digitalization, and sustainability imperatives. In the near term, AI is foreseen to augment existing workflows in composite design and manufacturing by data-driven optimization, predictive analytics, and decision-support systems. In the longer term, on the other hand, point towards autonomous and self-adaptive composite systems capable to optimize performance over the full material life cycle. Critical research opportunities exist concerning the integration of digital twins with generative AI, autonomous materials discovery, and alignment of AI frameworks with policy, standards, and sustainability roadmaps. If AI is to mature to an industry-ready and certifiable technology for automotive composites, these dimensions need to be addressed holistically and not in isolation [16, 17, 88].

9.1 Integration of Digital Twins and Generative AI

In the near term, the integration of digital twins with generative AI expected to focus towards advanced process optimization and predictive analyses in hybrid auto composites. Digital twins, updated through AI, will enable adaptive process control, defect detection, and predictive repair. When implemented with generative intelligence, such as a variational auto-encoder or diffusion models, the technology would be able to test alternative textile architectures, fibre–matrix combinations, and process times, which would be impossible through traditional design methods [15, 17, 88]. Presently, the technology largely uses small data sets, along with simplifications of physics, that limit their use in critical auto applications.

In the long run, digital twins integrated with generative AI and LLMs will likely mature along the vision of holistic and lifecycle-conscious digital twins for hybrid composite systems. The digital twin would thus be capable of performing holistic optimization over the design, production, and operational cycles through the dynamic adjustment of material architectures with the aid of real-world performance and degradation data. The application challenges would lie in keeping pace with model fidelity, uncertainty quantification, and explainability with the increasing

centrality of generative AI in design decision-making. The potential would lie in self-adaptive hybrid composite systems that would support optimal performance during prolonged service lives [15, 17, 88].

9.2 Autonomous Materials Discovery and Self-Optimizing Systems

In the short term, surrogate-based modelling along with evolutionary algorithms or reinforcement learning methods are expected to become important driver in autonomous material innovation for hybrid composites in the automotive sector. These AI-based methodologies are adept at handling large design spaces and can consider manufacturability and performance constraints. Closed-loop simulation infrastructures along with selective validation activities have already illustrated the potential to identify improved trade-offs between mechanical property requirements, mass, and cost and overcome the long-standing contradictions in the current composite designs [17, 88]. Nonetheless, human involvement will continue to be required owing to data unavailability and the absence of complete information regarding practical limitations.

The long-term roadmap would entail the use of fully autonomous and self-optimizing platforms where the AI agents could eventually support the automated suggestion, production, testing, and optimization of hybrid composite materials. The roadmap would ensure the conversion of the hypothesis-driven approach of materials development to a learning and AI-driven approach. The main research void would entail the integration of physics-driven constraints, lifecycle assessment, and recyclability aspects within the autonomous platforms that would avoid the search for materials with high performance but unsustainable and infeasible characteristics [15-17].

9.3 Policy, Standardization, and Industry–Academia Collaboration

In the short term, trust in AI-driven composite design tools will need to be established through standardized benchmarks, validation protocols, and reproducibility criteria. This includes measures required for regulatory acceptance of AI-enabled methodologies in the automotive sector. Collaboration between industry and academia can speed up technology transfer by comparing academic AI models to manufacturing realities, certification requirements, and industrial constraints [17, 88].

Long-term certification of AI-assisted composite design and manufacturing processes will require coordinated policy frameworks and international standards. This encompasses rules for XAI, standardized reporting of uncertainty, and strong validation protocols for automotive regulation-compliant digital twins. Sustained partnerships among industry, academia, and public innovation ecosystems will be essential to assure AI-enabled composite innovation pipelines embed sustainability, safety, and regulatory compliance by design [15, 16, 88].

9.4 Roadmap for AI-Enabled Sustainable Automotive Composites

In the short term, the roadmap for AI-enabled sustainable automotive composites should focus on multi-object optimization frameworks, that simultaneously consider various aspects of sustainability, including performance, costs, manufacturability, and recyclability. However, there is also evidence of many available short-term roadmaps regarding sustainability, treating it as an additional aspect, which may limit their effectiveness for long-term sustainability [16, 17].

In the long run, the developmental approach must be based on a systems level that encompasses lifecycle, circular economy, and EoL into AI-optimization methods. The amalgamation of digital twins, generative AI, and autonomous discovery platforms into an integrated system level approach could support scalable implementation and improvement. The developed AI-roadmaps shall shift the role of AI from marginal performance improvement towards a revolutionary tool for sustainable, intelligent, and resilient automotive composite design [15, 16, 88].

9.5 Explainable, Lifecycle-Aware, and Human-Centric AI Frameworks

Near term research should focus on the development of trustworthy AI approaches that are either explainable or human-centric to improve trust among engineering professionals for the design of hybrid composites. The combination of explainable approaches, sensitivity analysis, and input-level uncertainty estimation can be very effective in developing trustworthy AI approaches for adoption in a risk-sensitive automotive industry [15, 17].

In the long run, explainable and lifecycle-conscious AI and systematic worker upskilling could successfully reshape human-AI collaboration in composite engineering. Rather than replacing engineers, AI systems should augment expert knowledge by providing interpretable insights across design, manufacturing, and sustainability dimensions. This balance is essential for the successful application of hybrid automotive composites in future mobility applications through AI-integrated human-AI collaborations [16, 88].

9.6 Manufacturing-Aware and Sustainable AI Frameworks

Despite this progress, there is a key research gap: AI-based optimization remains largely decoupled from manufacturing realities and sustainability constraints. Process variability, defect tolerance, workforce readiness, and lifecycle issues have been largely ignored in the current literature. Future hybrid AI frameworks should integrate physics-based constraints, uncertainty quantification, and real-time process feedback, where sustainability and recyclability objectives are explicitly embedded. Complementing this technical perspective, manufacturers will also need to overcome organizational hurdles associated with skill shortages, resistance to data-driven decision-making, and cybersecurity. Both technical and systemic gaps must be addressed as part of bridging the gap between laboratory demonstrators and certified large-scale automotive production [16, 88].

Conclusions

This review demonstrates that the field of hybrid automotive composites offers an integrated material strategy that can match diverse demands for lighter, high-performance, cost-effective and more sustainable automobiles. By merging different types of reinforcements and matrices, hybrid materials can provide tailored mechanical properties, crash resistance, and functional components that go beyond traditional materials. AI can play an enabling role in the design and optimization of such materials by providing efficient computational tools for exploring complex design spaces, accelerated optimization, precise prediction, and effective quality control for composites. However, the review identifies ongoing problems that include the trade-off between performance and recyclability, data scarcity, lack of standardized data sets, difficulties in interpreting models, and scaling problems. These problems currently inhibit the implementation of AI-based optimization from lab experiments to automotive application. Nonetheless, to move towards developing authentic, reliable, and green materials through AI technology-based optimization for automotive composites, transparent and informative AI-based models on digital twins and lifecycle assessments, as well as manufacturing-driven constraints, are crucial. The future of AI-enabled hybrid composite development lies in the ability of this technology to reshape the process of material development for vehicles in accordance with future mobility needs and regulations.

References

[1] Chandgude S., and Salunkhe S. In state of art: Mechanical behavior of natural fiber-based hybrid polymeric composites for application of automobile components. Polymer Composites, Vol. 42, Issue 6, 2021, p. 2678-2703. DOI: 10.1002/pc.26045

[2] Xiao H., Sultan M. T. H., Shahar F. S., Gaff M., and Hui D. (2023). Recent developments in the mechanical properties of hybrid fiber metal laminates in the automotive industry: A review. Reviews on Advanced Materials Science, Vol. 62, Issue 1, 2023, 20220328. DOI: 10.1515/rams-2022-0328

[3] Sanjay M. R., and Yogesha B. Studies on natural/glass fiber reinforced polymer hybrid composites: An evolution. Materials today: proceedings, Vol. 4, Issue 2, 2017, p. 2739-2747. DOI: 10.1016/j.matpr.2017.02.151

[4] Skosana, S. J., Khoathane C., and Malwela T. Driving towards sustainability: A review of natural fiber reinforced polymer composites for eco-friendly automotive light-weighting. Journal of Thermoplastic Composite Materials, Vol. 38, Issue 2, 2025, p. 754-780. DOI: 10.1177/08927057241254324

[5] Wang D., Sun H., Xu W., Dong J., Lian F., and Huo H. Research Progress on Fiber Reinforced Polymer/Metal Hybrid Structures for Automotive Applications. Polymer Composites. Vol. 47, Issue 9, 2025, p. 7777-7799, DOI: 10.1002/pc.70706

[6] Chandel R., Sharma N., and Bansal S. A. A review on recent developments of aluminum-based hybrid composites for automotive applications. Emergent Materials, Vol. 4, Issue 5, 2021, p. 1243-1257. DOI: 10.1007/s42247-021-00186-6

[7] Chawla D., Mittal P., Nayak M., Thakur O. P., and Gupta, P. Development and performance evaluation of AA6061-SiC-graphite hybrid composites for lightweight automotive structural applications. Next Materials, Vol. 9, 2025, 101158. DOI: 10.1016/j.nxmate.2025.101158

[8] Olhan S., Antil B., and Behera B. K. Synergistic effect of different high-performance fibers on the microstructural evolution and mechanical performance of novel hybrid metal matrix composites produced via friction stir processing for automotive applications. Proceedings of the Institution of Mechanical Engineers, Part B: Journal of Engineering Manufacture, Vol. 239, Issue 1-2, 2025, p. 236-249. DOI: 10.1177/09544054241229469

[9] Arora G., and Sharma S. (2017). A review on monolithic and hybrid metal–matrix composites reinforced with industrial-agro wastes. Journal of the Brazilian Society of Mechanical Sciences and Engineering, Vol. 39, Issue 11, 2017, p. 4819-4835. DOI 10.1007/s40430-017-0910-x

[10] Isa M. T., Ahmed A. S., Aderemi B. O., Taib R. M., and Mohammed-Dabo I. A. Effect of fiber type and combinations on the mechanical, physical and thermal stability properties of polyester hybrid composites. Composites Part B: Engineering, Vol. 52, 2013, p. 217-223. DOI: 10.1016/j.compositesb.2013.04.018

[11] Faruk, O., Tjong, J., & Sain, M. (Eds.). Lightweight and sustainable materials for automotive applications. Boca Raton: CRC Press. Taylor & Francis Group, LLC, 2017. International Standard Book Number-13: 978-1-4987-5687-7 DOI: 10.1201/9781315152967

[12] Delogu M., Zanchi L., Dattilo C. A., and Pierini M. Innovative composites and hybrid materials for electric vehicles lightweight design in a sustainability perspective. Materials Today Communications, Vol. 13, 2017, p. 192-209. DOI: 10.1016/j.mtcomm.2017.09.012

[13] Ravishankar B., Nayak S. K., and Kader M. A. Hybrid composites for automotive applications–A review. Journal of Reinforced Plastics and Composites, Vol. 38, Issue 18, 2019, p. 835-845. DOI: 10.1177/0731684419849708

[14] Karthick K.N., and Bharathiraja M. AI-Optimized Al6061-T6 Hybrid Metal Matrix Composites Reinforced with Al_2O_3, Graphite, and Bauxite Residue (SiO_2) for Advanced Brake Hub Applications: Tribological and Machining Performance. 2025, *SSRN Electronic Journal*. https://doi.org/10.2139/ssrn.5261637
[15] Elsisi A., Abdel-Monsef S., and Salim H. Artificial Intelligence in the Design and Optimization of Laminated FRP Composites: A Review of Methodologies and Applications. Journal of Composites Science, Vol. 9, Issue 12, 2025, 654. DOI: 10.3390/jcs9120654
[16] Hsu M. K., Huang B. Y., and Yu C. H. AI-driven optimization of woven composite via integrated deep and reinforcement learning. Materials & Design, Vol. 259, 2025, 114798. DOI: 10.1016/j.matdes.2025.114798
[17] Jena S. R., Agarwal S., Sivanandam S., Gamini S., and Rohini, D. AI-driven multiphysics modelling for optimizing fiber dispersion in thermoplastic and thermosetting polymer composites for additive manufacturing. Thermal Science and Engineering Progress, Vol. 59, 2025, 103304. DOI: 10.1016/j.tsep.2025.103304
[18] Lee D.G., Kim H. S., Kim J. W., and Kim J. K. Design and manufacture of an automotive hybrid aluminum/composite drive shaft. Composite structures, Vol. 63, Issue 1, 2004, p. 87-99. DOI: 10.1016/S0263-8223(03)00136-3
[19] Wilson A. The development of hybrid nanoreinforced polymer composites for applications in automotive structures, Master Thesis, Kaunas University of Technology, Lithuania, 2020, DOI: Not Available.
[20] Swolfs Y., Verpoest I., and Gorbatikh L. Recent advances in fibre-hybrid composites: materials selection, opportunities and applications. International Materials Reviews, Vol. 64, Issue 4, 2019, p. 181-215. DOI: 10.1080/09506608.2018.1467365
[21] Kumar K. D., Shantharaja M., Kumar N., and Manjunatha, G. Morphological and mechanical properties of short fibres reinforced hybrid composites for automotive applications. Materials Today: Proceedings, Vol. 52, 2022, p. 957-962. DOI: 10.1016/j.matpr.2021.10.401
[22] Arunachalam S. J., Thanikodi S., and Saravanan R. Effect of nano-hybridization on flexural and impact behavior of jute/kenaf/glass fiber-epoxy composites for automotive application. Results in Engineering, Vol. 25, 2025, 104571.DOI: 10.1016/j.rineng.2025.104571
[23] Ikbal H., Wang Q., Azzam A., and Li W. GF/CF hybrid laminates made through intra-tow hybridization for automobile applications. Fibers and Polymers, Vol. 17, Issue 9, 2016, p. 1505-1521. DOI 10.1007/s12221-016-5953-6
[24] Karikalan L., Chandrasekran M., Ramasubramanian S., and Baskar S. Hybridization of composites using natural and synthetic fibers for automotive application. International Journal of Scientific Research in Science and Technology, Vol. 3, Issue 7, 2017, p. 916-920. DOI: Not Available
[25] Stojanović B., and Ivanović L. Application of aluminium hybrid composites in automotive industry. Tehnički vjesnik, Vol. 22, Issue 1, 2015, p. 247-251. DOI: 10.17559/TV-20130905094303
[26] Mallick P. K. Thermoplastics and thermoplastic–matrix composites for lightweight automotive structures. In Materials, design and manufacturing for lightweight vehicles, Woodhead Publishing, 2021, p. 187-228. DOI: 10.1016/B978-0-12-818712-8.00005-7
[27] Puglia D., Biagiotti J., and Kenny J. M. A review on natural fibre-based composites—Part II: Application of natural reinforcements in composite materials for automotive industry. Journal of natural fibers, Vol. 1, Issue 3, 2005, p. 23-65. DOI: 10.1300/J395v01n03_03
[28] Islam S., Hasan M. B., Karim F. E., Kodrić M., Islam M. R., Khatun M. M., and Motaleb K. A. Thermoset and thermoplastic polymer composites reinforced with flax fiber: Properties and application—A review. SPE polymers, Vol. 6, Issue 1, 2025, e10172. DOI: 10.1002/pls2.10172
[29] Olhan S., Khatkar V., and Behera B. K. Review: Textile-based natural fibre-reinforced polymeric composites in automotive lightweighting. Journal of Materials Science, Vol. 56, Issue 34, 2021, p. 18867-18910. DOI: 10.1007/s10853-021-06509-6
[30] Islam S., Hasan M. B., Kodrić M., Motaleb K. A., Karim F. E., and Islam M. R. Mechanical properties of hemp fiber-reinforced thermoset and thermoplastic polymer composites: A comprehensive review. SPE polymers, Vol. 6, Issue 1, 2025, e10173. DOI: 10.1002/pls2.10173
[31] Oladele I. O., Okoro C. J., Taiwo A. S., Onuh L. N., Agbeboh N. I., Balogun O. P., Olubambi P.A. and Lephuthing S. S. Modern trends in recycling waste thermoplastics and their prospective applications: a review. Journal of Composites Science, Vol. 7, Issue 5, 2023, 198. DOI: 10.3390/jcs7050198
[32] Huda M. K. and Widiastuti I. Natural fiber reinforced polymer in automotive application: a systematic literature review. In Journal of physics: conference series, Vol. 1808, No. 1, 2021, p. 012015. IOP Publishing. DOI:10.1088/1742-6596/1808/1/012015
[33] Devarshi S., Pndhare A., Lokh P. E., and Mooney J. P. Natural fibre reinforced thermoplastic composite synthesis methods and potential applications. ES Materials & Manufacturing, Vol. 21, Issue 5, 2023, 827. DOI: 10.30919/esmm5f827
[34] Begum S., Fawzia S., and Hashmi M. S. J. Polymer matrix composite with natural and synthetic fibres. Advances in Materials and Processing Technologies, Vol. 6, Issue 3, 2020, p. 547-564. DOI: 10.1080/2374068X.2020.1728645
[35] Patel R. V., Yadav A., and Winczek J. Physical, mechanical, and thermal properties of natural fiber-reinforced epoxy composites for construction and automotive applications. Applied Sciences, Vol. 13, Issue 8, 2023, 5126. DOI: 10.3390/app13085126
[36] Kim Y. K., and Chalivendra V. Natural fibre composites (NFCs) for construction and automotive industries. In Handbook of natural fibres, Woodhead Publishing, 2020, p. 469-498. DOI: 10.1016/B978-0-12-818782-1.00014-6
[37] Mahmud S., Konlan J., Deicaza J., Schmidt R. A., and Li G. Thermoset polymer composites with gradient natural and synthetic fiber reinforcement: Self-healing, shape-memory, and fiber recyclability. Materials Today Communications, Vol. 35, 2023, 105950. DOI: 10.1016/j.mtcomm.2023.105950
[38] Jeyanthi S., and Rani J. J. Influence of natural long fiber in mechanical, thermal and recycling properties of thermoplastic composites in automotive components. International Journal of Physical Sciences, Vol. 7, Issue 43, 2012, p. 5765-5771. DOI: 10.5897/IJPS12.521

[39] Giusti R. Development of an Innovative Process Technology for the Manufacture of Structural Hybrid Components, Made by Forming and Overmolding of Thermoplastic Matrix Composites, Doctoral Dissertation, University of Padova, 2017. https://hdl.handle.net/11577/3424899 DOI: Not Available

[40] Aldhahri K. S., and Klosterman D. A. Additively manufactured resin transfer molding (RTM) plastic tooling for producing composite T-joint structures. Progress in Additive Manufacturing, Vol. 10, Issue 4, 2025, p. 2283-2301. DOI: 10.1007/s40964-024-00750-6

[41] Ziegmann G., Oehl G., and Hefft L. T. Recent trends in "conventional" manufacturing of composites. In Additive Manufacturing of Polymer-Based Composite Materials, Woodhead Publishing, 2024, p 1-36. DOI: https://doi.org/10.1016/B978-0-443-15917-6.00001-3

[42] Maiti S., Islam M. R., Uddin M. A., Afroj S., Eichhorn S. J., and Karim N. Sustainable fiber-reinforced composites: a review. Advanced Sustainable Systems, Vol. 6, Issue 11, 2022, 2200258. DOI: 10.1002/adsu.202200258

[43] Mitschang P., and Hildebrandt K. Polymer and composite moulding technologies for automotive applications. In Advanced materials in automotive engineering, Woodhead Publishing, 2012, p. 210-229. 10.1533/9780857095466.210

[44] Rutt M. Aspects of material and process optimisation for automotive composite production using resin transfer moulding, Thesis for EngD in MiNMaT, University of Surrey, McLaren Automotive, EPSRC, 2020. DOI: 10.15126/thesis.00853144

[45] Chaudhari R. Characterization of high-pressure resin transfer molding process variants for manufacturing high-performance composites, Vol. 28. 2014, Doctoral Dissertation, Karlsruhe Institute of Technology, Pfinztal: Fraunhofer Verlag. DOI: 10.24406/publica-fhg-280078

[46] Phillips D.M. Effect of Material and Manufacturing Parameters on Compression Resin Transfer Moulding of Graphene-Based Multi-Scale Composites. Master Thesis, McGill University, Montreal, Canada, 2021. DOI: Not Available.

[47] Lagarinhos J. N. Thermoplastic Matrices for Autoparts By T-RTM Processing, Doctoral dissertation, Universidade de Aveiro Portugal, 2024. DOI: Not Available

[48] Karaduman N. S., and Karaduman Y. Various fabrication methods employed in fiber reinforced composites. In Fiber Reinforced Composites, Woodhead Publishing, 2021, p. 25-45. DOI: 1 0.1016/B978-0-12-821090-1.00016-8

[49] Islam T., Chaion M. H., Jalil M. A., Rafi A. S., Mushtari F., Dhar A. K., and Hossain S. Advancements and challenges in natural fiber-reinforced hybrid composites: a comprehensive review. SPE Polymers, Vol. 5, Issue 4, 2024, p. 481-506. DOI: 10.1002/pls2.10145

[50] Ahmad M. W., Mourshed M., and Rezgui Y. Tree-based ensemble methods for predicting PV power generation and their comparison with support vector regression. Energy, Vol. 164, 2018, p. 465-474. DOI: 10.1016/j.energy.2018.08.207

[51] Chhajer P., Shah M., and Kshirsagar, A. The applications of artificial neural networks, support vector machines, and long–short term memory for stock market prediction. Decision Analytics Journal, Vol. 2, 2022, 100015. DOI: 10.1016/j.dajour.2021.100015

[52] Nhu V. H., Shirzadi A., Shahabi H., Singh S. K., Al-Ansari N., Clague J. J. Jaafari A., Chen W., Miraki S., Dou J., Luu C., Górski K., Pham B.T., Nguyen, H.D., and Ahmad B. B. Shallow landslide susceptibility mapping: A comparison between logistic model tree, logistic regression, naïve bayes tree, artificial neural network, and support vector machine algorithms. International journal of environmental research and public health, Vol. 17, Issue 8, 2020, 2749. DOI: 10.3390/ijerph17082749

[53] Khorshid M., Abou-El-Enien T. H., and Soliman G. M. A comparison among support vector machine and other machine learning classification algorithms. IPASJ International Journal of Computer Science (IIJCS), Vol. 3, Issue 5, 2015, p. 25-35. DOI: Not Available

[54] Jozdani S. E., Johnson B. A., and Chen D. Comparing deep neural networks, ensemble classifiers, and support vector machine algorithms for object-based urban land use/land cover classification. Remote Sensing, Vol. 11, Issue 14, 2019, 1713.DOI: 10.3390/rs11141713

[55] Yaghoubi E., Yaghoubi E., Khamees A., and Vakili A. H. A systematic review and meta-analysis of artificial neural network, machine learning, deep learning, and ensemble learning approaches in field of geotechnical engineering. Neural Computing and Applications, Vol. 36, Issue 21, 2024, p. 12655-12699. DOI: 10.1007/s00521-024-09893-

[56] Rodriguez-Galiano V., Sanchez-Castillo M., Chica-Olmo M., and Chica-Rivas M. J. O. G. R. Machine learning predictive models for mineral prospectivity: An evaluation of neural networks, random forest, regression trees and support vector machines. Ore geology reviews, Vol. 71, 2015, p. 804-818. DOI: 10.1016/j.oregeorev.2015.01.001

[57] Tanveer H., Adam M. A., Khan M. A., Ali M. A., and Shakoor A. Analyzing the performance and efficiency of machine learning algorithms, such as deep learning, decision trees, or support vector machines, on various datasets and applications. The Asian bulletin of big data management, Vol. 3, Issue 2, 2023, p. 126-136. DOI: 10.62019/abbdm.v3i2.83

[58] Rana H., and Ibrahimbegovic A. A hybrid physics-informed and data-driven approach for predicting the fatigue life of concrete using an energy-based fatigue model and machine learning. Computation, Vol. 13, Issue 3, 2025, 61. DOI: 10.3390/computation13030061

[59] Wang J., Li Y., Gao R. X., and Zhang F. Hybrid physics-based and data-driven models for smart manufacturing: Modelling, simulation, and explainability. Journal of Manufacturing Systems, Vol. 63, 2022, p. 381-391. DOI: 10.1016/j.jmsy.2022.04.004

[60] Deng S., Hosseinmardi S., Wang L., Apelian D., and Bostanabad R. Data-driven physics-constrained recurrent neural networks for multiscale damage modeling of metallic alloys with process-induced porosity. Computational Mechanics, Vol. 74, Issue 1, 2024, p. 191-221. DOI: 10.1007/s00466-023-02429-1

[61] Rai R., and Sahu C. K. Driven by data or derived through physics? a review of hybrid physics guided machine learning techniques with cyber-physical system (CPS) focus. IEEE Access, Vol. 8, 2020, 71050-71073. DOI: *10.1109/ACCESS.2020.2987324*

[62] Patel D., Sharma R., and Guo Y. B. Computational, Data-Driven, and Physics-Informed Machine Learning Approaches for Microstructure Modeling in Metal Additive Manufacturing. 2025, p. 339-378, **DOI:** 10.1615/AnnualRevHeatTransfer.2025059621

[63] Zhou K., Sun H., Enos R., Zhang D., and Tang J. Harnessing deep learning for physics-informed prediction of composite strength with microstructural uncertainties. Computational Materials Science, Vol. 197, 2021, 110663. DOI: 10.1016/j.commatsci.2021.110663
[64] Soares R. C., Silva J. C., de Lucena Junior J. A., Lima Filho A. C., de Souza Ramos J. G. G., and Brito A. V. Integration of Bayesian optimization into hyperparameter tuning of the particle swarm optimization algorithm to enhance neural networks in bearing failure classification. Measurement, Vol. 242, 2025, 115829. DOI: 10.1016/j.measurement.2024.115829
[65] Panda S., and Padhy N. P. Comparison of particle swarm optimization and genetic algorithm for FACTS-based controller design. Applied soft computing, Vol. 8, Issue 4, 2008, p. 1418-1427. DOI: 10.1016/j.asoc.2007.10.009
[66] Monson C. K., and Seppi K. D. Bayesian optimization models for particle swarms. In Proceedings of the 7th annual conference on Genetic and evolutionary computation, 2005, p. 193-200. DOI: 10.1145/1068009.1068039
[67] Lan G., Tomczak J. M., Roijers D. M., and Eiben A. E. Time efficiency in optimization with a bayesian-evolutionary algorithm. Swarm and Evolutionary Computation, Vol. 69, 2022, 100970. DOI: 10.1016/j.swevo.2021.100970
[68] Papazoglou G., and Biskas P. Review and comparison of genetic algorithm and particle swarm optimization in the optimal power flow problem. Energies, Vol. 16, Issue 3, 2023, 1152. DOI: 10.3390/en16031152
[69] Zhang Y., Wang S., and Ji G. A comprehensive survey on particle swarm optimization algorithm and its applications. Mathematical problems in engineering, 2015(1), 931256. DOI: 10.1155/2015/931256
[70] Dada B. A., Nwulu N. I., and Olukanmi S. O. Bayesian Optimization with Optuna for Enhanced Soil Nutrient Prediction: A Comparative Study with Genetic Algorithm and Particle Swarm Optimization. Smart Agricultural Technology, Vol. 12, 2025, 101136, DOI: 10.1016/j.atech.2025.101136.
[71] Ferdousi S. Additive Manufacturing and Design of Mechanically Tailor-Made Hybrid Composites With Artificial Intelligence, Doctoral dissertation, University of Oklahoma–Graduate College, 2024. https://hdl.handle.net/11244/341244 DOI: Not Available
[72] Karuppusamy M., Thirumalaisamy R., Palanisamy S., Nagamalai S., Massoud E. E. S., and Ayrilmis N. A review of machine learning applications in polymer composites: advancements, challenges, and future prospects. Journal of Materials Chemistry A., Vol. 13, 2025, p. 16290–16308, DOI: 10.1039/d5ta00982k
[73] Sahib M. M., and Kovács G. Multi-objective optimization of composite sandwich structures using Artificial Neural Networks and Genetic Algorithm. Results in Engineering, Vol. 21, 2024, 101937. DOI: 10.1016/j.rineng.2024.101937
[74] Ho N. X., Le T. T., Dinh T. H., and Nguyen V. H. Prediction of buckling damage of steel equal angle structural members using hybrid machine learning techniques. Scientific Reports, Vol. 15, Issue 1, 2025, 4696. DOI: 10.1038/s41598-025-87869-w
[75] Le L. M., Ly H. B., Pham B. T., Le V. M., Pham T. A., Nguyen D. H., Tran X.T., Le, T. T. Hybrid artificial intelligence approaches for predicting buckling damage of steel columns under axial compression. Materials, Vol. 12, Issue 10, 2019, 1670. DOI: 10.3390/ma12101670
[76] Mirzaei A. H., Haghi P., and Shokrieh M. M. Prediction of fatigue life of laminated composites by integrating artificial neural network model and non-dominated sorting genetic algorithm. International Journal of Fatigue, Vol. 188, 2024, 108528. DOI: 10.1016/j.ijfatigue.2024.108528
[77] Yossef M., Noureldin M., and Alqabbany A. Explainable artificial intelligence framework for FRP composites design. Composite Structures, Vol. 341, 2024, 118190. DOI: 10.1016/j.compstruct.2024.118190
[78] Saberi S., Nasiri H., Ghorbani O., Friswell M. I., and Castro S. G. Explainable artificial intelligence to investigate the contribution of design variables to the static characteristics of bistable composite laminates. Materials, Vol. 16, Issue 15, 2023, 5381. DOI: 10.3390/ma16155381
[79] Azad M. M., and Kim H. S. An explainable artificial intelligence-based approach for reliable damage detection in polymer composite structures using deep learning. Polymer Composites, Vol. 46, Issue 2, 2025, p. 1536-1551. DOI: 10.1002/pc.29055
[80] Furtado C., Pereira L. F., Tavares R. P., Salgado M., Otero F., Catalanotti G., Arteiro A., Bessa M.A. and Camanho P. P. A methodology to generate design allowables of composite laminates using machine learning. International Journal of Solids and Structures, Vol. 233, 2021, 111095. DOI: 10.1016/j.ijsolstr.2021.111095
[81] Cumbo R., Baroni A., Ricciardi A., and Corvaglia S. Design allowables of composite laminates: A review. Journal of Composite Materials, Vol. 56, Issue 23, 2022, p. 3617-3634. DOI: 10.1177/00219983221117216
[82] Nguyen H. T., Nguyen K. T., Le T. C., and Zhang G. Review on the use of artificial intelligence to predict fire performance of construction materials and their flame retardancy. Molecules, Vol. 26, Issue 4, 2021, 1022. DOI: 10.3390/molecules26041022
[83] Chen T., and Guestrin C. Xgboost: A scalable tree boosting system. In Proceedings of the 22nd acm sigkdd international conference on knowledge discovery and data mining 2016, p. 785-794, DOI: 10.1145/2939672.2939785
[84] Osa-Uwagboe N., Udu A. G., Ghalati M. K., Silberschmidt V. V., Aremu A., Dong H., and Demirci E. A machine learning-enabled prediction of damage properties for fiber-reinforced polymer composites under out-of-plane loading. Engineering Structures, Vol. 308, 2024, 117970. DOI: 10.1016/j.engstruct.2024.117970
[85] Holland M., and Chaudhari K. Large language model based agent for process planning of fiber composite structures. Manufacturing Letters, Vol. 40, 2024, p. 100-103. DOI: 10.1016/j.mfglet.2024.03.010
[86] Buehler M. J. MechGPT, a language-based strategy for mechanics and materials modeling that connects knowledge across scales, disciplines, and modalities. Applied Mechanics Reviews, Vol. 76, Issue 2, 2024, 021001 DOI: 10.1115/1.4063843
[87] Chen X., Shukla S. N., Azab M., Singh A., Wang Q., Yang D., Peng S.Y., Yu H., Yan S., Zhang X. and He B. Compcap: Improving multimodal large language models with composite captions. In Proceedings of the IEEE/CVF International Conference on Computer Vision 2025, p. 23582-23592. DOI: 10.1109/ICCV51701.2025.02189
[88] Malashin I., Martysyuk D., Tynchenko V., Gantimurov A., Nelyub V., & Borodulin A. Data-driven optimization of discontinuous and continuous fiber composite processes using machine learning: a review. Polymers, Vol. 17, Issue 18, 2025, 2557. DOI: 10.3390/polym17182557
[89] Morales Matamoros O., Takeo Nava J. G., Moreno Escobar J. J., and Ceballos Chávez B. A. Artificial intelligence for quality defects in the automotive industry: A systemic review. Sensors, Vol. 25, Issue 5, 2025, 1288. DOI: 10.3390/s25051288

[90] Ouabdou M., Benbouras Y., Diar F. Z., El Fahime B., and Radouani M. Innovations in Defect Detection: Integrating AI and NDT Techniques in Composite Materials. Revue des Composites et des Materiaux Avances, Vol. 35, Issue 1, 2025, 165. DOI: 10.18280/rcma.350119
[91] Kibrete F., Trzepieciński T., Gebremedhen H. S., and Woldemichael D. E. Artificial intelligence in predicting mechanical properties of composite materials. Journal of Composites Science, Vol. 7, Issue 9, 2023, 364. DOI: 10.3390/jcs7090364
[92] Kumar S. S., Shyamala P., Pati P. R., Mishra D. K., Sharma V., Tank G., and Kanan M. Investigation and machine learning-based prediction of mechanical properties in hybrid natural fiber composites. Scientific Reports, Vol. 15, Issue 1, 2025, 33700. DOI: 10.1038/s41598-025-18944-5
[93] Arunachalam S. J., Saravanan R., Othman N. A., Thanikodi S., Giri J., Azizi M., and Saidani T. Artificial Intelligence-Driven Prediction and Optimization of Tensile and Impact Strength in Natural Fiber/Aluminum Oxide Polymer Nanocomposites. Engineering Reports, Vol. 7, Issue 4, 2025, e70093. DOI: 10.1002/eng2.70093
[94] Azimi M., Eslamlou A. D., and Pekcan G. Data-driven structural health monitoring and damage detection through deep learning: State-of-the-art review. Sensors, Vol. 20, Issue 10, 2020, 2778. DOI: 10.3390/s20102778
[95] Das M., Sahu S., and Parhi D. R. Composite materials and their damage detection using AI techniques for aerospace application: A brief review. Materials Today: Proceedings, Vol. 44, 2021, p. 955-960. DOI: 10.1016/j.matpr.2020.11.005
[96] Das M., Sahu S., and Parhi D. R. A review of application of composite materials for aerospace structures and its damage detection using artificial intelligence techniques. In International Conference on Artificial Intelligence in Manufacturing & Renewable Energy (ICAIMRE), 2019. DOI: 10.2139/ssrn.3714181
[97] Pickering K. L., Efendy M. A., and Le T. M. A review of recent developments in natural fibre composites and their mechanical performance. Composites Part A: Applied Science and Manufacturing, Vol. 83, 2016, p. 98-112. DOI: 10.1016/j.compositesa.2015.08.038
[98] Das S. Life cycle assessment of carbon fiber-reinforced polymer composites. The International Journal of Life Cycle Assessment, Vol. 16, Issue 3, 2011, p. 268-282. DOI 10.1007/s11367-011-0264-z
[99] Witik R. A., Teuscher R., Michaud V., Ludwig C., and Månson J. A. E. Carbon fibre reinforced composite waste: An environmental assessment of recycling, energy recovery and landfilling. Composites Part A: Applied Science and Manufacturing, Vol. 49, 2013, p. 89-99. DOI: 10.1016/j.compositesa.2013.02.009
[100] Duflou J. R., Sutherland J. W., Dornfeld D., Herrmann C., Jeswiet J., Kara S., Hauschild M., and Kellens K. Towards energy and resource efficient manufacturing: A processes and systems approach. CIRP annals, Vol. 61, Issue 2, 2012, p. 587-609. DOI: 10.1016/j.cirp.2012.05.002
[101] Pimenta S., and Pinho S. T. Recycling carbon fibre reinforced polymers for structural applications: Technology review and market outlook. Waste management, Vol. 31, Issue 2, 2011, p. 378-392. DOI:10.1016/j.wasman.2010.09.019
[102] Swolfs Y., McMeeking R. M., Verpoest I., and Gorbatikh L. The effect of fibre dispersion on initial failure strain and cluster development in unidirectional carbon/glass hybrid composites. Composites Part A: Applied Science and Manufacturing, Vol. 69, 2015, p. 279-287. DOI: 10.1016/j.compositesa.2014.12.001
[103] Friedrich K., and Almajid A. A. Manufacturing aspects of advanced polymer composites for automotive applications. Applied Composite Materials, Vol. 20, Issue 2, 2013, p. 107-128. DOI 10.1007/s10443-012-9258-7
[104] Varatharajulu M., Jagadeesh B., and Hariharasakthisudhan P. Performance of hybrid composites in automotives: Case studies on side intrusion beams and other automobile components. In Sustainable Composites for Automotive Engineering, Woodhead Publishing, 2026, p. 573-600. DOI: 10.1016/B978-0-443-23669-3.00025-7
[105] Belingardi G., Beyene A. T., Koricho E. G., and Martorana B. Alternative lightweight materials and component manufacturing technologies for vehicle frontal bumper beam. Composite Structures, Vol. 120, 2015, p. 483-495. DOI: 10.1016/j.compstruct.2014.10.007
[106] Kulkarni A., Vora R., and Ravi K. Study design and analysis of automobile bumper for pedestrian safety. In IOP Conference Series: Materials Science and Engineering, IOP Publishing, Vol. 263, Issue. 6, 2017, 062060, DOI: 10.1088/1757-899X/263/6/062060
[107] Olorunnishola A. A. G., Adubi E. G. A comparative analysis of a blend of natural jute and glass fibers with synthetic glass fibers composites as car bumper materials. IOSR J. Mech. Civ. Eng, Vol. 15, 2018, p. 67-71. DOI: 10.9790/1684-1503016771
[108] Davoodi M. M., Sapuan S. M., Ahmad D., Ali A., Khalina A., Jonoobi M. Mechanical properties of hybrid kenaf/glass reinforced epoxy composite for passenger car bumper beam. Materials & Design, Vol. 31, Issue 10, 2010, p. 4927-4932. DOI: 10.1002/pls2.10173
[109] Kim D. H., Kim H. G., and Kim H. S. Design optimization and manufacture of hybrid glass/carbon fiber reinforced composite bumper beam for automobile vehicle. Composite structures, Vol. 131, 2015, p. 742-752. DOI: 10.1016/j.compstruct.2015.06.028
[110] Blau P. J. Compositions, functions, and testing of friction brake materials and their additives (No. ORNL/TM-2001/64). Oak Ridge National Lab.(ORNL), Oak Ridge, TN (United States), 2001. DOI: 10.2172/788356
[111] Bajpai P. K., Singh I., and Madaan J. Tribological behavior of natural fiber reinforced PLA composites. Wear, Vol. 297, Issue 1-2, 2013, p. 829-840. DOI: 10.1016/j.wear.2012.10.019
[112] Yun R., Filip P., Lu Y. Performance and evaluation of eco-friendly brake friction materials. Tribology International, Vol. 43, Issue 11, 2010. P. 2010-2019, DOI: 10.1016/j.triboint.2010.05.001
[113] Matějka V., Fu Z., Kukutschová J., Qi S., Jiang S., Zhang X., Yun R., Vaculik M., Heliova M., Lu Y. Jute fibers and powderized hazelnut shells as natural fillers in non-asbestos organic non-metallic friction composites. Materials & Design, Vol. 51, 2013, p. 847-853. DOI: 10.1016/j.matdes.2013.04.079
[114] Mastura M. T., Sapuan S. M., Mansor M. R., Nuraini A. A. Environmentally conscious hybrid bio-composite material selection for automotive anti-roll bar. The International Journal of Advanced Manufacturing Technology, Vol. 89, Issue 5, 2017, p. 2203-2219. DOI: 10.1007/s00170-016-9217-9

[115] Mastura M. T., Sapuan S. M., Mansor M. R., Nuraini A. A. Conceptual design of a natural fibre-reinforced composite automotive anti-roll bar using a hybrid approach. The International Journal of Advanced Manufacturing Technology, Vol. 91, Issue 5, 2017, p. 2031-2048. DOI: 10.1007/s00170-016-9882-8
[116] Bayrakceken H., Tasgetiren S., Aslantas K. Fracture of an automobile anti-roll bar. Engineering Failure Analysis, Vol. 13, Issue 5, 2006, p. 732-738. DOI: 10.1016/j.engfailanal.2005.04.002
[117] Koronis G., Silva A., Fontul M. Green composites: A review of adequate materials for automotive applications. Composites Part B: Engineering, Vol. 44, Issue 1, 2013, p. 120-127. DOI: 10.1016/j.compositesb.2012.07.004
[118] Stewart R. Automotive composites offer lighter solutions. Reinforced Plastics, Vol. 54, Issue 2, 2010, p. 22-28. DOI: 10.1016/S0034-3617(10)70061-8
[119] Motors M. Mitsubishi Motors develops plant-based green plastic floor mat, 2006, DOI: Not Available.
[120] Rwawiire S., Tomkova B., Militky J., Jabbar A., Kale B. M. Development of a biocomposite based on green epoxy polymer and natural cellulose fabric (bark cloth) for automotive instrument panel applications. Composites Part B: Engineering, Vol. 81, 2015, p. 149-157. DOI: 10.1016/j.compositesb.2015.06.021
[121] Suddell B. C., Evans W. J. Natural fiber composites in automotive applications. In Natural fibers, biopolymers, and biocomposites, CRC press, 2005, p 253-282. DOI: 10.1201/9780203508206
[122] Zhang J., Chaisombat K., He S., Wang C. H. Glass/carbon fibre hybrid composite laminates for structural applications in automotive vehicles. In Sustainable Automotive Technologies 2012: Proceedings of the 4th International Conference, Berlin, Heidelberg: Springer Berlin Heidelberg, 2012, p. 69-74. DOI: 10.1007/978-3-642-24145-1_10
[123] Müssig J., Schmehl M., Von Buttlar H. B., Schönfeld U., Arndt K. Exterior components based on renewable resources produced with SMC technology - considering a bus component as example. Industrial Crops and Products, Vol, 24, Issue 2, 2006, p. 132-145. DOI: 10.1016/j.indcrop.2006.03.006
[124] Birat K. C., Panthapulakkal S., Kronka A., Agnelli J. A. M., Tjong J., Sain M. Hybrid biocomposites with enhanced thermal and mechanical properties for structural applications. Journal of Applied Polymer Science, Vol. 132, Issue 34, 2015. DOI: 10.1002/app.42452
[125] Panthapulakkal S., Law S., Sain M. Performance of injection molded natural fiber-hybrid thermoplastic composites for automotive structural applications. SAE Transactions, 2006, p. 27-32. DOI: 10.4271/2006-01-0004
[126] Khondker O. A., Ishiaku U. S., Nakai A., Hamada H. Fabrication mechanical properties of unidirectional jute/PP composites using jute yarns by film stacking method. Journal of Polymers and the Environment, Vol. 13, Issue 2, 2005, p. 115-126. DOI: 10.1007/s10924-005-2943-y
[127] Jones R. M. Mechanics of composite materials. CRC Press, 2018. DOI: 10.1201/9781498711067

Information of the authors

Amur Venugopal Santhana Babu, Professor, Centre for Excellence – Research, Rajalakshmi Engineering College
e-mail: santhanababu.av@rajalakshmi.edu.in

Duraivelu Jayabalakrishnan, Professor, Department of Mechanical Engineering, Chennai Institute of Technology
e-mail: jayabalakrishnand@citchennai.net

DOI 10.52209/2706-977X_2026_3_78 IRSTI 81.09.07 UDC 678.686

Experimental Evaluation of Carbon Nanoparticle Addition on the Mechanical Properties of Banana Fiber Micro Particle Reinforced Epoxy Matrix Composites

Jayaseelan C.[1*], Vimalarani C.[2], Karthikeyani Vijayakumari K.[3], Chitra K.[4]

[1]Department of Mechanical Engineering, J. P. College of Engineering, Tenkasi-627 852,Tamil Nadu, India

[2]Department of Electrical and Electronic Engineering, SRM Madurai College for Engineering and Technology, Sivagangai-630 612 Tamil Nadu, India

[3]Department of Physics, Kalaignar Karunanidhi Government Arts College for Women, Pudukkottai-622 001, Tamil Nadu, India

[4]Department of Plant Pathology, Tamil Nadu Agricultural University, Coimbatore -641 003, Tamil Nadu, India.

*corresponding author

Abstract. In this experiment we evaluated the mechanical characteristics on the carbon nanoparticle addition of banana fiber micro particle reinforced epoxy matrix composites. The composite are manufactured in the compression moulding machine. The 0.5,1 and 1.5 wt% of carbon nanoparticles added with the 30wt% composites. The tensile, flexural, impact and hardness properties are tested on the composites. The test result shows that the maximum tensile, flexural, impact and hardness strength values are identified in the 1.5wt% nano particle addition composites. The values are 55.53 MPa, 51.76 MPa 0.27J and 71.5 N. The morphology studied exposed the distribution of nano particle and manifest the interfacial strength between the particles and the matrix in the composites.

Keywords: carbon nanoparticles, banana fiber micro particles, epoxy resin, mechanical properties, morphological study.

Introduction

The nano science is the multidisciplinary area of research that escalates in the materials development areas. In recent days the technology development is based on the specific properties of nanoparticles like chemical, thermal and mechanical. These properties are investigated by arranging the particles on the nano size into macro size. The different types of nanoparticles are metal, ceramic, and polymeric. The nanoparticles have distinctive physical properties due to their high surface contact area. The tensile, flexural and impact strength of the materials dependent on their size, shape and structure [1]. The study evaluates the tensile, flexuraland hardness properties and shows significant improvement in the polymer composites because of nanoparticle addition [2]. The mechanical properties have improved by the addition of alumina nanoparticles of the short Glass/Carbon fiber reinforced epoxy composites. The result proved that the dispersion of particles in the resin enhances the impact, flexural strength and modulus values [3]. The author investigates that the mechanical properties have been enhanced due to the effect of nanotechnology [4]. The author investigates the nanoparticle addition with polymer filled composites on the mechanical and tribological behaviors. The results shows that the mechanical and wear properties are found to increase with increasing filler materials [5]. The addition of Al_2O_3 nano particle with the pandanus, coconut bunch fiber reinforced composites were prepared and studied. The result shows that the increase in nano particle content with natural fiber composites gives the better result than the without addition of nanoparticle reinforced composites [6]. This study evaluates the tensile, flexural and thermogravimetric characteristics of flax fiber reinforced epoxy composite with the addition of nano TiO_2. The maximum weight percentage was maintained at 28wt%. The Tio2 nanoparticle added to the fiber such as 0%, 0.5%, 0.7% and 0.9% by weight. The experimental result shows that the mechanical properties has improved by adding (0.7%) nanoparticles percentage in the composites [7]. The effects of nano-silica (NS) particle (3 wt%) on the mechanical properties of intraply and woven fiber reinforced carbon/Kevlar/epoxy hybrid composites shows the significant improvement in the composites [8]. The author studied the effect of natural fillers such as rice husk, wheat husk and coconut coir on the mechanical properties of glass fiber reinforced epoxy and polyester composites. The result identifies the natural fillers provided better improvement in the polyester based composites than epoxy resin matrix composites [9]. This research evaluates the influence of nano-Titania loading (0, 0.5, 1.0, and 2.0 % of volume fraction) on the mechanical and water absorption characteristics of jute fiber reinforced epoxy matrix composites. The nano-Titania notably gives the better result in the jute fiber reinforced epoxy composite [10]. The alumina filler reinforced epoxy composites were investigated on the dynamic mechanical behavior which increases significantly because of the addition of nanoparticle [11]. The jute fiber hybrid with hemp fiber reinforced composites and nano titanium oxide are studied. It proved that increased infiller content (6wt %) has been given the highest mechanical strength [12]. In this study used carbon nanoparticle and banana fiber micro particles used as the reinforcement material and the epoxyis the resin to prepare the composites. Then the mechanical properties have been analyzed in the various percentages of nanoparticle

composites. The improvement in results is keenly watched andfinds the reasons for the improvement.

1. Experimental details

1.1 Materials

The materials used in this experiment are resin (LY556) and hardener (HY951) for the composite preparation. The banana plant is the source of fibers which is collected from the banana sheath. The collected fibers are cut into chopped fiber. After that the chopped fibers are crushedinto particles by using a mixer grinder machine and are sieved manually at an average size of 1-10 microns. The resin and the hardener are purchased through Seenu & Company, Coimbatore, Tamil Nadu, India. The carbon nanoparticles are collected from the LMP R&D Laboratory, Pallipalayam, Coimbatore. Tamil Nadu, India.

1.2 Preparation of composites

Fig. 1(a) The mixing of carbon nano particles, acetone solution and epoxy resin. (b) Shows the sonicator used to stirrer the mixer. (c) Shows the oven used to heat the mixer for evaporating the acetone solution. (d) Shows the three different types of composites (i) 0.5wt % addition of nano particle composites, (ii) 1.0 wt % addition of nano particle composites (iii) 1.5 wt % addition of nano particle composites.

Table 1. Composites

30wt % Composites (Particle + Resin+Hardener)	
Banana fiber micro particle	90 grams
Resin	220 ml
Hardener	22 ml
Carbon nano particle wt%	
0.5 wt%	1.5 grams
1.0 wt%	3 grams
1.5 wt%	4.5grams

1. Mechanical testing

2.1Tensile test

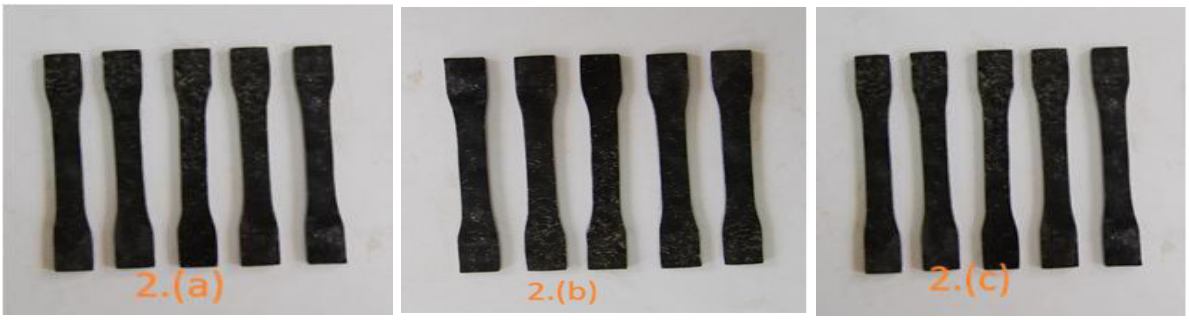

Fig. 2. - (a) The tensile test specimen composites of 0.5wt% carbon nano particle addition (b) Shows the tensile test specimen composites of 1.0wt% carbon nano particle addition (c) Shows the tensile test specimen composites of 1.5wt% carbon nano particle addition

Fig. 2 shows the nano particle addition 0.5,1.0 and 1.5wt% of composite specimen for tensile test. The material subjected to tensile force in the longitudinal direction for measuring tensile strength. The specimen is in the gripper at both ends in the tensile tester. The tensile force is applied on each end of the specimen until it fractures. The graph is plotted against the load vs. length. The ASTM standard (ASTM D 638) is followed during the tests conducted on the universal tensile tester model DTRX-30KN DEEPAK POLY PLAST PVT LTD.

2.2 Flexural tests

Fig. 3. - The flexural test specimen of (a) 0.5 wt % addition of carbon nanoparticle composites (b) 1.0 wt % addition of carbon nanoparticle composites (c) 1.5 wt % addition of carbon nanoparticle composites.

Fig. 3 shows the addition of nano particle composite such as 0.5,1.0 and 1.5wt%. Flexural test determines the force required to bend the specimen. The specimen is placedhorizontally over the lower support of two points of contact. Then a force is applied over the specimen through single point of contact until the specimen fails. Flexural modulus is calculated from the slope of the stress vs strain curve. The flexural tests were carried out in the universal tensile tester (DTRX-30KN DEEPAK POLY PLAST PVT LTD). The ASTM D790 standard has been implemented in the test.

2.3 Impact test

Fig. 4. - The impact test specimen of (a) 0.5 wt % addition of carbon nanoparticle composites (b) 1.0 wt % addition of carbon nanoparticle composites (c) 1.5 wt % addition of carbon nanoparticle composites

Fig. 4 shows the nano particle addition (0.5, 1.0 and 1.5wt%) of composites for impact test. Impact tests conducted to determine the toughness in the material. It is the energy received by the material in the plastic state. The specimen is laid vertically on the grippers, whichhold the specimen tightly, and the pendulum is blown from one side which strikes it with kinetic energy. The energy absorbed by the specimen before the fractures are recorded on the scale for calculations. The test is performed using Izod-Charpy Impact tester machine (Deepak Poly Plast Pvt Ltd) followed by ASTM D256 standard. The experiments were conducted at room temperature.

9.7 Hardness test

The hardness values (HS) measured by shore D test method. The needle shaped indenter tip forced over the composite specimen. The depth of indentation denotes the hardness. The indentation was taken at five different places on the composites and average values were noted. The tests are performed with ASTM D2240 standard.

2.5Morphology study using SEM

The morphology study was carried out by Scanning Electron Microscope. It identifies the distribution of particles and the interfacial strength of the particles and resin matrix. The voltage used in this experiment is 10 KV.

2. Result and Discussions

3.1 Tensile test

Fig. 5 shows the tensile strength value of three different types of composites (0.5wt%, 1.0wt% and 1.5wt% carbon nano particle addition)

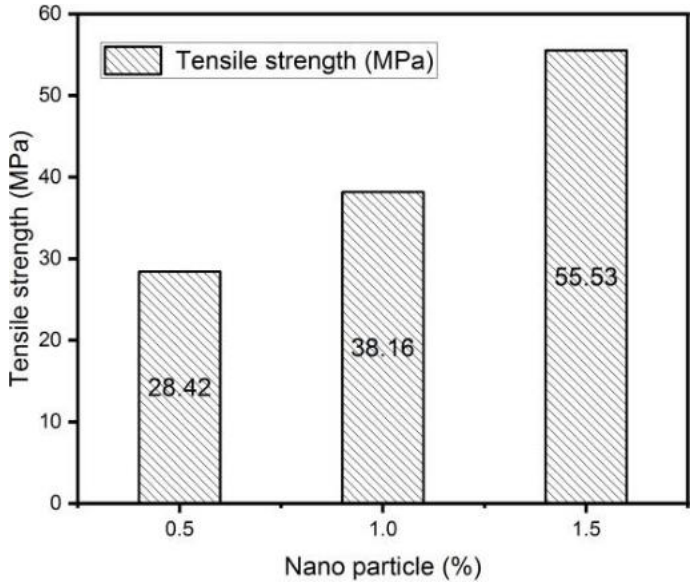

Fig. 5. - The tensile strength value of three different types of composites (0.5wt%, 1.0wt% and 1.5wt% carbon nano particle addition)

The Fig. 5, shows the tensile test result of carbon nanoparticle addition with banana fiber micro particle reinforced epoxy composites. The higher tensile strength identified in the 1.5% addition of nanoparticle composites (55.53 MPa). It is 48.82% higher than the 0.5% addition of nanoparticle composites. The increase in nanoparticle content increases the strength of the composites. The adhesion between the particles and the resin are high is the reason for the high strength. The nanoparticles act as a filler to distribute evenly throughout the composites [13]. So stress transfers from the particles and the resin are good enough also the reason for the maximum tensile strength [14]. The surface contact area of the nanoparticle is more; this is the cause for better strength. The minimum tensile strength value points out in the 0.5% addition of nanoparticle composites due to the reason that the distribution of particle content is not even and the agglomeration of the particle decreases bonding strength of the particle with the resin [15].

Fig. 6 shows the tensile modulus value of three different types of composites (0.5wt%, 1.0wt% and 1.5wt% carbon nano particle addition)

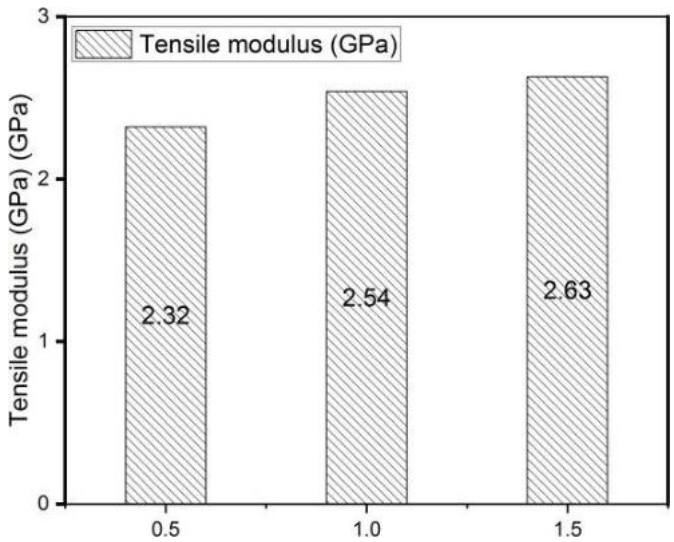

Fig. 6. - The tensile modulus value of three different types of composites (0.5wt%, 1.0wt% and 1.5wt% carbon nano particle addition)

The modulus value of the various percentages of nanoparticle composite are shown in Fig. 6. It shows that the maximum modulus values are in 1.5% addition of composites. That is 3.4% and 11.79% higher than the 1.0% and 0.5% addition of nano particle composites. Here thestress value gradually increases the strain values.

3.2 Flexural strength

Fig. 7 shows the flexural strength value of three different types of composites (0.5wt%, 1.0wt% and 1.5wt% carbon nano particle addition).

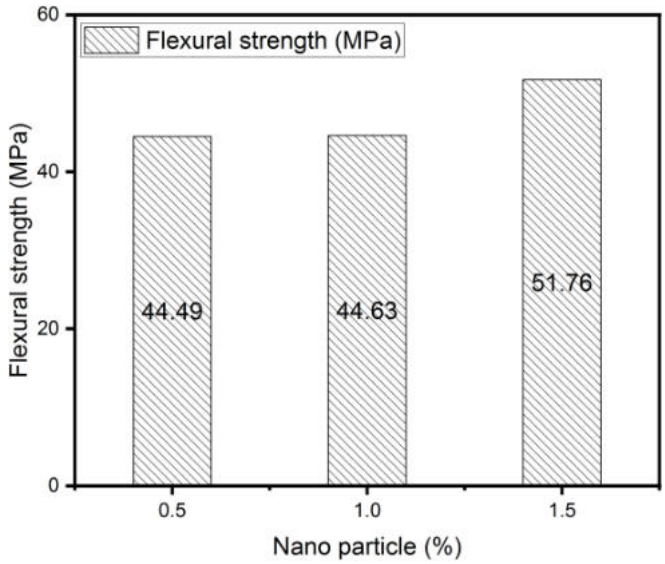

Fig. 7. - The flexural strength value of three different types of composites (0.5wt%, 1.0wt% and 1.5wt% carbon nano particle addition)

The flexural strength values of the composites are shown in Fig. 7. The nanoparticle mixed with the epoxy matrix enhances the interface area more rigidly is the cause for better flexural strength [16]. The load carried from the particle to the resin is high because the better interface between the particle and the matrix is rich. Due to the reason that the composites absorb more loads and bending of composite is limited. The maximum flexural strength marked in the addition of nanoparticles 1.5% in the composites (51.76MPa) which is 14.05 % higher than the composites addition of 0.5% nanoparticle content and 13.76% higher than the 1% addition of nanoparticle composite. The addition of nanoparticles dispersed evenly and created the strong interfacial strength between the particles. The presence of nanoparticles restricts the motion of polymer molecules to enhance the interlocking properties is the reason for higher strength.

Fig. 8 shows the flexural modulus value the composites.

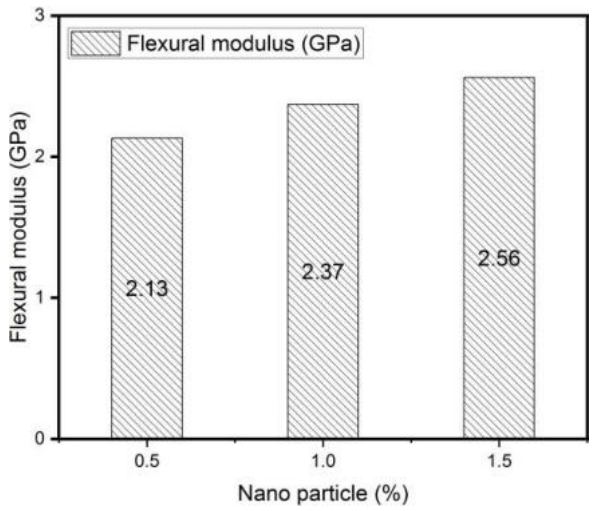

Fig. 8. - The flexural modulus value of three different types of composites (0.5wt%, 1.0wt% and 1.5wt% carbon nanoparticle addition)

The 1.5% addition of nano particle composites shows higher modulus value than the other two nanoparticle additions of composites. This is 7.42 and 16.80 % higher than the 1.0 and 0.5% in addition of nano particle composites.

3.3 Impact test

Fig. 9 shows the impact strength value of three different types of composites (0.5wt%, 1.0wt% and 1.5wt% carbon nano particle addition).

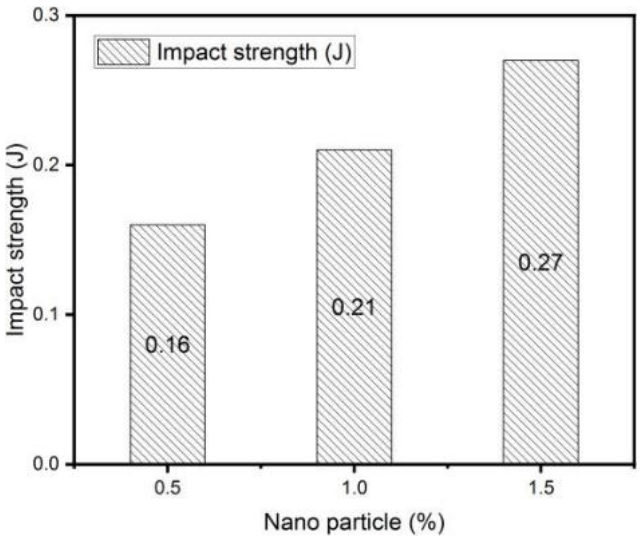

Fig. 9. - The impact strength value of three different types of composites (0.5wt%, 1.0wt% and 1.5wt% carbon nano particle addition)

Fig. 9 shows the impact energy absorbed by the nanoparticle addition of banana fibermicro particle reinforced composites which showed maximum value (0.27J) in the 1.5% nanoparticle addition of composites that is 40.74% higher than the 0.5% nanoparticle addition of composites and 22.22% higher than the 1% nanoparticle addition of composites. This is due tothe dispersion of nanoparticles with the banana fiber micro particle in the matrix.

3.4 Hardness test

Hardness test is the test for identifying the materials properties to use for specific purposes.

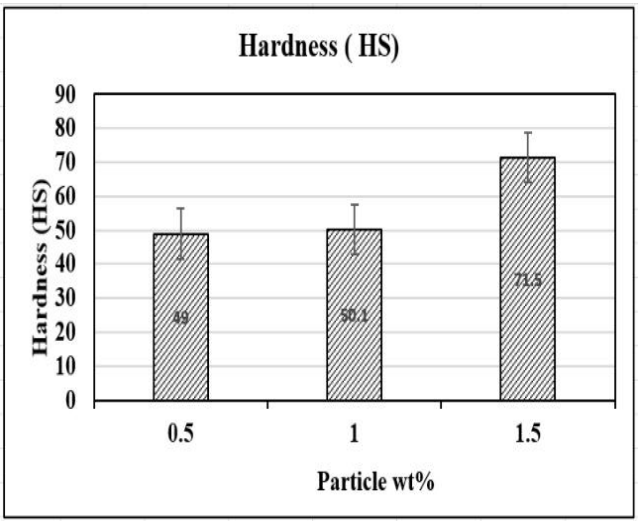

Fig. 10. - The hardness value of three different types of composites (0.5wt%, 1.0wt% and 1.5wt% carbon nano particle addition)

Fig. 10 shows the hardness of various percentage carbon nanoparticles (0.5%, 1% and1.5%) in the polymer composites. The highest hardness value (71.5) is predicted in the addition of 1.5% carbon nanoparticle composites. That is 31.46% higher than the 0.5% added nanoparticlecomposites and 29.93% higher than the 1% addition of nanoparticle composites. The hardness values are increased by adding the particle content in the composites. The

addition of particles increases the resistance force in the material.

3.5 Morphology study using SEM

Fig. 11 shows the surface morphology of (a) 0.5 % nanoparticle addition composites, (b) 1.0 % nanoparticle addition composites, (c) 1.5 % nanoparticle addition composite.

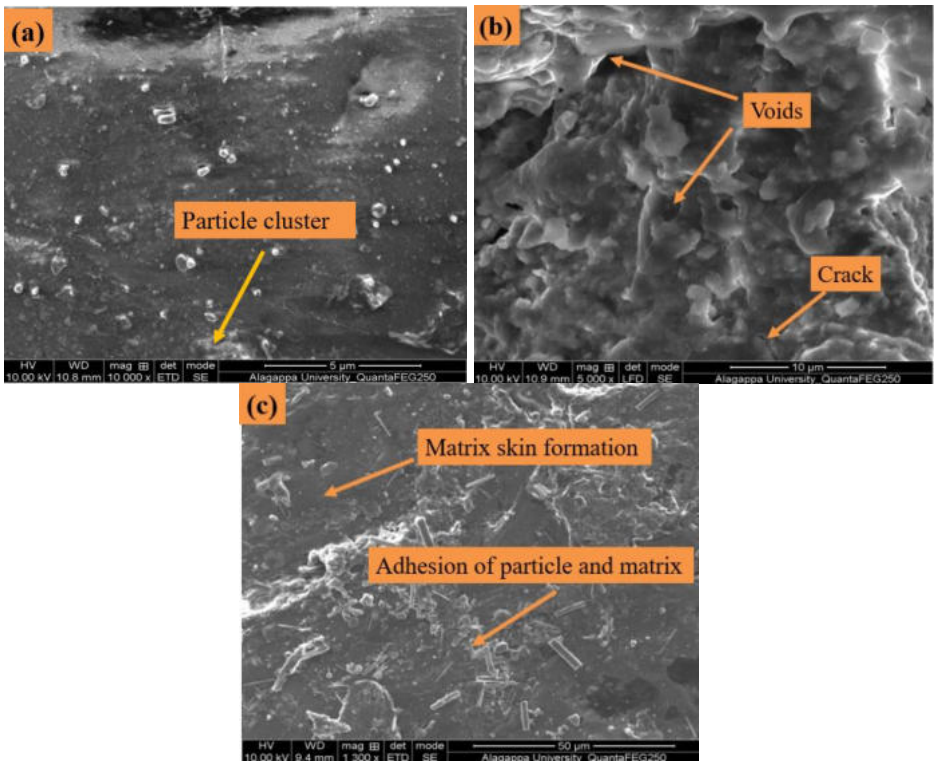

Fig. 11. - The surface morphology of (a) 0.5 % nanoparticle addition composites, (b) 1.0 % nanoparticle addition composites, (c) 1.5 % nanoparticle addition composite.

Fig.11 (a) shows the addition of 0.5% nanoparticle with banana fiber micro particle reinforced epoxy matrix composites. It shows the particle clusters in some places which is the evidence of improper distribution of nanoparticles in the matrix. This is the main reason for the less strength. Fig.11 (b) exhibits the addition of 1% nanoparticle with banana fiber micro particle reinforced epoxy matrix composites. The voids and cracks identified in some locations are the reason for the minimum strength. Fig.11 (c) shows the addition of nanoparticles 1.5% with banana fiber micro particle reinforced epoxy matrix composites. It shows the matrix skin formation in some areas and also the interfacial adhesion between the particles is the cause for the higher strength in the composites.

Conclusion

In this experimental research investigated the effect of carbon nano particle addition of banana fiber micro particle reinforced epoxy matrix composites on the mechanical properties. The research revealed several core findings regarding the performance of the composites. Particularly the 1.5 wt% carbon particle addition of banana fiber micro particle reinforced epoxy matrix composites exhibit superior tensile, flexural, impact and hardness strength compared to 0.5, 1.0 wt% addition of carbon nano particle composites. enhanced performance can be obtained to the 1.5wt% carbon nano particle composites, the uniform distribution of nano particles and the compatibility of the particle and the matrix. which enhances the interfacial strength between the reinforcement and the matrix, thereby increasing the strength and hardness of the composites. Scanning electron microscopy (SEM) analysis strengthen these results, showing that the adhesion between the addition of carbon nano particle (1.5wt%) of the banana fiber micro particle and epoxy matrix is significantly effective. The carbon nano particle acts as a interlocking substance enhances the bonding between the particle and the matrix, contributing to the improved mechanical properties observed.

Overall, the experimental results of this research underscore the potential of 1.5wt% addition of carbon nano particle as a viable reinforcement and act as a filler material in epoxy composites. These materials contributed the combination of high tensile, flexural, impact and hardness strength.

Reference

[1] Qian ZHANG, Lv Si XU, Xiaoyan GUO. Improvement of mechanical properties, microscopic structures, and antibacterial activity by Ag/ZnO nano composite powder for glaze-decorated ceramic. //Journal of Advanced Ceramics, Vol 6, Issue 3, 2017, -

p.269-278.
[2] Hayder Abbas Sallal, Alaa A. Abdul-Hamead, Farhad Mohammad Othman. Effect of nano powder (Al_2O_3-CaO) addition on the mechanical properties of the polymer blend matrix composite. //Defense Technology, V 16, Issue 2, 2020, -p.425-431.
[3] Akash Mohanty, Srivastava V.K. Effect of Alumina Nanoparticles on the Enhancement of Impact and Flexural Properties of the Short Glass/Carbon Fiber Reinforced Epoxy Based Composites. //Fibers and Polymers, Vol. 16, Issue 1, 2015, -p. 188-195.
[4] Ramachandran M, Rishabh Bhargava, Raichurkar P.P. Effect of Nanotechnology in Enhancing Mechanical Properties of Composite Materials. //International Journal on Textile Engineering and Processes, Vol 2, Issue 1, 2016, -p.59-63.
[5] Ibrahim Khan, Khalid Saeed, Idrees Khan. Nanoparticles: Properties, applications and toxicities. //Arabian Journal of Chemistry, Vol 12, 2019, -p.908-931.
[6] Ayman A. Al, El-Shafei B. Zeidan, AbdAllah A. Alshennawy, Aly A. El-Masry, Wahid A. Wasel. Friction and Wear of Polymer Composites Filled by Nano-Particles: A Review. //World Journal of Nano Science and Engineering, Vol 2, 2012, -p. 32-39.
[7] Babu K, Gnanavel babu A. Investigation on the Mechanical Properties of Natural Fiber Composites Reinforced Epoxy with Al_2O_3 Nano Particles, //International Journal of Current Engineering and Scientific Research, Vol.4, issue 9, 2017-p. 44-51.
[8] Vishnu Prasad, Joseph M A, Sekar K. Investigation of mechanical, thermal and water absorption properties of flax fibre reinforced epoxy composite with nano TiO_2 addition. // Composites Part A: Applied Science and Manufacturing, Vol 115, 2018-p.360-370.
[9] Mohamad Alsaadi, Mehmet Bulut, Ahmet Erklig, Arkan Jabbar. Nano-silica inclusion effects on mechanical and dynamic behavior of fiber reinforced carbon/Kevlar with epoxy resin hybrid composites, //Composites Part B: Engineering, Vol 152, 2018, -p.169-179.
[10] MohanGift M.D., Raghuram K.S., SuryanarayanaRaju J.N.S., Ravi D., Venkata Rao M., Ram Subbiah, Makendran Chandrakasu. Study on influence of nano-filler content on the performance of natural fiber reinforced epoxy composites. // materialstoday: PROCEEDINGS, Vol 56, Issue 3, 2022-p. 1562-1566.
[11] Raj KishorDas, Biswajit Nayak, Ganeshan P., Satyam ShivamGautam, Kajal Kumar Mandal. Dynamic mechanical behavior of a nano sized alumina fiber reinforced epoxy hybrid composites. materials today: PROCEEDINGS, Vol76, Issue 3, 2023-p. 524-527.
[12] Mahesha C.R., Suprabha R., Mahesh S. Harne, Sachin G. Galme, Sandeep G. Thorat. Nanotitanium Oxide Particles and Jute-Hemp Fiber Hybrid Composites: Evaluate the Mechanical, Water Absorptions, and Morphological Behaviors. //Journal of Nanomaterials, 2022, -p. 1-7.
[13] Ilyas R.A., Sapuan S.M., Ishak M.R., Zainudin E.S. Development and characterization of sugar palm nanocrystalline cellulose reinforced sugar palm starch bionano composites. //Carbohydrate Polymers, Vol 202, 2018, -p. 186-202.
[14] Akash Mohanty and Srivastava V.K. Effect of Alumina Nanoparticles on the Enhancement of Impact and Flexural Properties of the Short Glass/Carbon Fiber Reinforced Epoxy Based Composites. //Fibers and Polymers, Vol 16, Issue 1, 2015, -p. 188-195.
[15] M.Omar M., Mohamed H., Abdel I., Ghada B. Effect of Al_2O_3 Nanoparticles on the Mechanical and Physical Properties of Epoxy Composite. //Arabian Journal of Science and Engineering. Springer, Vol 43, Issue 1-3, 2017, -p.1-7.
[16] Vishnu Prasad, Joseph M.A., Sekar K. Investigation of mechanical, thermal and water absorption properties of flax fibre reinforced epoxy composite with nano TiO_2 addition. //Composites Part A: Applied Science and Manufacturing, Vol 115, 2018, -p. 360-370.
[17] Jayaseelan C, Padmanabhan P, Athijayamani A, Ramanathan K. Comparative investigation of mechanical properties of epoxy composites reinforced with short fibers, macro particles, and micro particles. // BioResources, Vol 12, Issue 2, 2017, p.- 2864-2871.

Information of the authors

Jayaseelan C., Dr, professor, J.P.College of Engineering
e-mail: cjseelan1@gmail.com

Vimalarani C., Dr, associate professor, SRM Madurai College for Engineering and Technology
e-mail: jaysanjayvim@gmail.com

Karthikeyani Vijayakumari K., Dr, assistant, professor, Kalaingner Karunanidhi Government Arts College for Women
e-mail: kskvkumari@gmail.com

Chitra K., Dr, associate professor, Tamilnadu Nadu Agricultural University
e-mail: chitrapatho@gmail.com

DOI 10.52209/2706-977X_2026_3_86 IRSTI 81.09.03 UDC 621.382.3

Numerical Simulation of Thermal Conductivity in Silicon Wafers of Transistors

Pirniazova P.[1]*, Aksutova A.[1], Aidarkul M.[2]
[1]Almaty University Energy and Telecommunication
[2]Almaty Technological University
*corresponding author

Abstract. This article presents studies of thermal conductivity in silicon wafers of microcontroller transistors and electronic devices. The focus is on modeling the thermal conductivity of silicon wafers to analyze temperature field distribution under different operating modes and thermal loads. Heat propagation in solids is described by the three-dimensional Fourier equation of thermal conductivity. Methods are applied to solve differential equations considering geometric and physical parameters of the material. The algorithm is based on an analytical–numerical method for decomposing the temperature field into a polynomial series. The modeling results allow evaluation of the effect of transistor miniaturization on thermal characteristics and propose approaches to optimizing heat dissipation.
The practical significance lies in improving reliability and energy efficiency of modern microcontrollers. The results show how quickly heat propagates in transistors, calculated using the recurrent-operator method. Simulation in Maple demonstrates that peak temperature gradients are localized in central crystal regions, where the sine function reaches maximum, and decay exponentially toward edges. This computational algorithm can be integrated into microcontroller memory subsystems, where transistors are densely packed, for predictive throttling—automatic reduction of recording frequency in the event of local overheating threats.

Keywords: thermal conductivity, modeling, transistors, mosfets.

Introduction

Modern computing systems are based on the use of transistors, which are characterized by low cost, compact size and high reliability. However, with the miniaturization and increasing integration density of transistors, the issue of thermal conductivity of the materials from which they are made becomes increasingly important. Thermal conductivity is a molecular transfer of heat in a continuous medium and depends on the state of aggregation of a substance, its composition, purity, temperature and pressure. This property is critically important for transistors, since the uneven temperature distribution in semiconductor structures leads to local overheating, changes in performance, and reduced reliability. In addition, thermal conductivity can change under the influence of external factors — pressure, magnetic field, radiation - as well as due to structural changes in the material (heat treatment, wear). In translucent media used in a number of semiconductor technologies, thermal conductivity is accompanied by radiative energy transfer, which complicates heat transfer processes. Thus, the study of thermal conductivity in transistors is of key importance for improving the efficiency of modern computing systems, since their stability and durability depend on the ability of materials to effectively remove heat.

The objectives of the study of this topic are:

- identify patterns of distribution of heat fluxes in silicon and silicon carbide substrates.
- construct an analytic-numerical approximation of the three-dimensional Fourier equation to describe the temperature modes of transistors.
- evaluate the efficiency of heat dissipation in silicon and 4H-SiC, identify advantages and disadvantages for use in microcontrollers.
- create a tool to predict thermal conditions and prevent transistor degradation at high integration density.

To achieve this goal, the following research tasks follow:

- build a mathematical model of heat propagation in transistor structures using Maple.
- implement an algorithm for decomposing a temperature field into a polynomial series.
- perform thermal conductivity modeling for silicon and silicon carbide substrates.
- visualize the temperature distribution in the form of three-dimensional graphs.
- compare simulation results for different materials and draw conclusions on thermal stability.

The practical significance of this study is:

- the model can be integrated into the memory subsystems of microcontrollers to automatically reduce the recording frequency in case of overheating.

- using the model allows you to take into account thermal limitations in advance and avoid degradation of transistors.

- results show that the use of SiC significantly accelerates the relaxation of thermal energy, which makes it promising for high-performance systems.

- the study makes it possible to create more durable and stable computing systems due to efficient heat dissipation.

The development of semiconductor technologies is based on fundamental research initiated in the middle of the 20th century by W. Shockley on the theory of semiconductors and the development of MOSFET structures [1,2]. In modern conditions, as B. Rayner notes, thermal management in microelectronics is becoming a critical factor due to the extreme density of component integration. According to the reviews [3], for Internet of Things (IoT) systems, energy efficiency and reliability issues directly depend on the ability of materials to efficiently distribute and dissipate heat in pulsed modes of operation. The use of modern STM32G4 or nRF52840 series microcontrollers requires a detailed understanding of thermal processes at the crystal level to prevent their degradation. The transistor is an electronic switch with two states - "on" and "off", which is controlled by applying voltage or current to the control electrode[4]. There are two main classes of transistors: bipolar (bipolar junction transistors, BJT) and MOSFET transistors - metal oxide semiconductor field effect transistors (MOSFET), which are also often called field effect transistors[5]. After more than thirty years of rapid development of semiconductor technologies, engineers have been able to place about one billion MOSFETs on one square centimeter of a silicon crystal[6]. At the same time, the cost of each transistor is less than ten cents. Over time, the integration density of transistors on a chip increases approximately tenfold every eight years, and the cost of one element decreases [7].

Today, MOSFETs act as the fundamental "building blocks" from which almost all digital systems are formed. MOSFETs are made on the basis of silicon, an element widely used in rocks and sand. Silicon (Si) belongs to group IV of the periodic table and has four valence electrons [8]. Due to this, it is able to form bonds with four neighboring atoms, forming an ordered crystal lattice. In Figure 1 (a), for clarity, the lattice is represented in a two-dimensional coordinate system, but in reality its structure has a cubic shape. The lines in the figure indicate covalent bonds between atoms. By its nature, silicon is a weak conductor, since its electrons are fully involved in the formation of covalent bonds. However, the electrical properties of silicon can be significantly improved by introducing a small number of impurity atoms (dopant)[9]. If a group V element, such as arsenic (As), is used as an impurity, then each impurity atom contains an additional electron that is not involved in the formation of covalent bonds. This free electron is able to move easily inside the crystal lattice. In this case, the arsenic atom, which has lost an electron, turns into a positively charged ion (As^+)[10], as shown in Fig. 1(b) .

The electron has a negative charge, therefore arsenic is classified as an impurity of type n (n type dopant). In the case of using a group III element, such as boron (B), one electron is missing from each impurity atom, as shown in Figure 1 (c). This missing electron is called a "hole". An electron from a neighboring silicon atom can pass to a boron atom and fill in the missing bond. As a result, the boron atom, which has received an additional electron, becomes a negative ion (B^-), and a hole forms in the silicon atom. Thus, the hole is able to move through the crystal lattice in the same way as an electron[11]. Despite the fact that a hole represents only the absence of a negative charge, in a semiconductor it behaves like a positively charged particle. That is why boron is classified as a p-type dopant. Since the conductivity of silicon can vary by orders of magnitude depending on the concentration of impurities, this material is classified as a semiconductor[12]

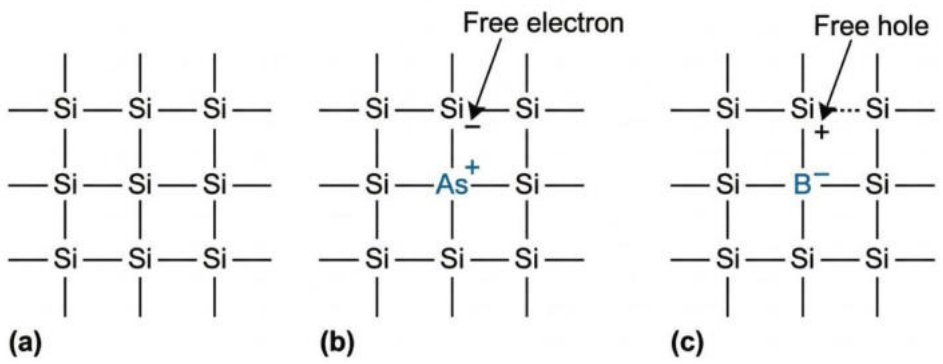

Fig.1. – Silicon lattice and impurity atoms

The electrical conductivity of a semiconductor material is determined by its crystal structure, the concentration of charge carriers, and temperature conditions[13]. The basis of most modern electronic devices is monocrystalline silicon, the atoms of which form a stable tetrahedral lattice with four covalent bonds. The energy of one such bond is about 1.12 eV, which corresponds to the band gap silicon at a temperature of 300 K. In the pure (intrinsic) state, silicon has extremely low conductivity, on the order of 4.4×10^{-4} Cm/m, at room temperature. This is due to the fact that at 300 K the concentration of free charge carriers (electrons and holes) is only 1.5×101^{0} cm^{-3}, which is many orders of magnitude less than in metals, where the number of carriers reaches 10^{22} cm^{-3}). As the temperature increases, thermal excitation of electrons occurs, which pass from the valence band to the conduction band, forming electron–hole pairs[14]. The concentration of such pairs increases exponentially with increasing temperature in accordance with the law[15] :

$$n_i = \sqrt{N_c \cdot N_v} \cdot e^{-\frac{E_g}{2kT}} \quad (1)$$

where n_i - the concentration of carriers (electrons and holes) in the intrinsic state,

E_g - the band gap,

k - the Boltzmann constant,

T - the temperature (in Kelvin). The concentration of electrons in the conduction band

N_c - the effective density of states in the conduction band.,

N_v - the effective density of states in the valence band,

E_g - the width of the forbidden zone,

The concentration of electrons in the conduction band

$$n = N_c e^{\frac{E_C - E_F}{kT}} \quad (2)$$

The concentration of electrons in the conduction band:

$$p = N_v e^{\frac{E_F - E_v}{kT}}; \quad (3)$$

In an intriguing case:

$$n = p = n_i \quad (4)$$

Material	Density (g/sm^3)	Band gap width (eV)	Thermal Conductivity (W/m*K)
Silicon (Si)	2.33	1.12	150

The relationship between the above formulas (1-4) and the thermophysical properties of the material lies in the direct dependence of the concentration of charge carriers on temperature conditions. Formula (1) shows that the intrinsic concentration of n_i increases exponentially with increasing absolute temperature T. This leads to a corresponding change in the concentration of electrons (2) and holes (3) in the conduction and valence bands. The choice of silicon as the main material is due to its ability to maintain stability under such changes: having a high thermal conductivity (150 W/m ·K), it provides efficient heat dissipation generated by thermal excitation of carriers[16]. Unlike germanium or gallium arsenide, silicon provides an optimal balance between carrier mobility and thermal stability, which minimizes local overheating described by these mathematical relationships. Thus, the formulas describe the electrical state of the system, which directly dictates the requirements for thermal conductivity studied in this work.

Silicon has an optimal set of characteristics: relatively low density, which facilitates crystal processing, and high thermal conductivity, which ensures efficient heat removal from the active elements of the microcircuits. Denser materials, such as germanium or gallium arsenide (GaAs), exhibit significantly greater carrier mobility — up to 8,500 cm2/(V·s) for electrons in GaAs versus 1,400 cm2/(V·s) in silicon. However, they are inferior to silicon in terms of thermal stability and create additional difficulties in mass production[17].

Research methods. To study the temperature conditions of the microcontroller crystal, a mathematical model was developed in the symbolic computing environment of Maple. The propagation of heat in a solid is described by the three-dimensional Fourier differential equation of thermal conductivity. The algorithm is based on an analytical numerical method for decomposing the temperature field into a polynomial series. The program defines the following parameters of the studied area and material properties: thermal conductivity coefficients along the x, y and z axes:

For Si $a = 0.000028\ \mathrm{m}^2/\mathrm{s}$.

For 4H-SiC $a = 0.43m^2/s$ (at a temperature of 300K).

Geometric dimensions of the crystal (or the fragment under study):

A harmonic function with exponential decay in time is chosen as the basic (initial) function of the space-time distribution $g(x, y, z, t)$:

$$g = sin\left(\frac{\pi x}{l_1}\right) \sin\left(\frac{\pi y}{l_2}\right) sin\left(\frac{\pi z}{l_3}\right) e^{-t} \quad (5)$$

To construct the approximating polynomial q, the algorithm uses the recursive procedure $Q(i, j, k, p)$, which calculates the weighting coefficients for the terms of the series based on the thermal conductivity coefficients. The logic of the function is such that if the indexes are negative, 0 is returned, the base point (0,0,0,0) is 1, and the subsequent ones are calculated as:

$$Q(i, j, k, p) = -Q(i, j-2, k, p) - Q(i, j, k-2, p) + aQ(i-1, j, k, p-1) \quad (6)$$

Next, the program calculates the partial derivatives of the basic function g in terms of spatial coordinates and time using the fd(j,k,p) procedure. The final temperature distribution function q is formed as the sum of the terms of the series (the code uses nested summation cycles from 0 to 2 for each variable):

$$q = \sum_{i=0}^{2} \sum_{j=0}^{2} \sum_{k=0}^{2} \sum_{k=0}^{2} Q(i, j, k, p) \frac{x^{i+j+k+p}}{(i+j+k+p)!} fd(j, k, p) \quad (7)$$

This approach makes it possible to obtain a highly accurate analytical approximation of the temperature field inside the transistor structure under specified boundary conditions.

Simulation results. Based on the constructed polynomial q, graphs of three-dimensional surfaces visualizing the temperature distribution were generated in the Maple environment. For modeling and analysis, a transistor was selected along the x=0.02m, y=0.01m, z=0.005m axes, and a slice along the application axis z = 0.003 m was also selected at time t = 0.1s.

The command *plot3d(q, x=0..l_1, y=0..l_2)*` generates a surface where the x and y axes correspond to the geometric dimensions of the chip (from 0 to 0.02 and from 0 to 0.01, respectively), and the vertical axis displays the temperature value. Table 1 shows the results of calculations of the thermal conductivity of a silicon wafer at arbitrary values of axes and time, taking into account the set limits. We considered the process in a parallelepiped of volume

$V = l_1 \cdot l_2 \cdot l_3$; The process was considered within the initial and boundary conditions.

$q(x, y, z, t)_{x=0,l_1}; 0 < x < l_1,\ 0 < y < l_2,\ 0 < z < l_3;$

Table 1. Simulation results of thermal conductivity of a silicon wafer

t,s	x, m	y, m	z, m	q, m/s^2
0.01	0.01	0.01	0.003	$9.051753714 \cdot 10^{-6}$
0.05	0.003	0.003	0.003	$7.939668209 \cdot 10^{-7}$
0.1	0.001	0.001	0.001	$2.800843856 \cdot 10^{-8}$
1	0.02	0.01	0.005	$1.076220762 \cdot 10^{-5}$

The results of modeling the thermal conductivity of a silicon substrate (Figures 1-6).

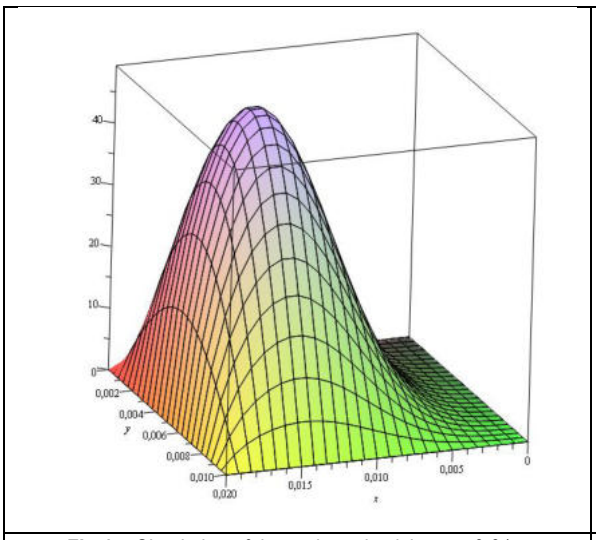

Fig.1. - Simulation of thermal conductivity at t=0.01s, z=0.003m, at x=0 to 0.02, y=0 to 0.01

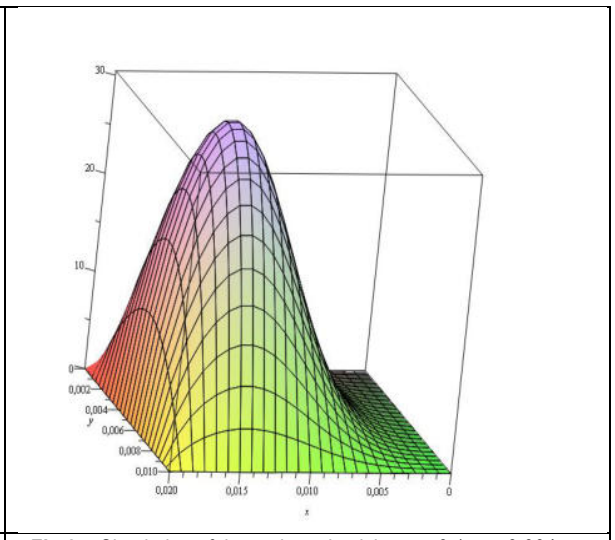

Fig.2. - Simulation of thermal conductivity at t=0.1s, z=0.004 m, at x=0 to 0.02, y=0 to 0.01

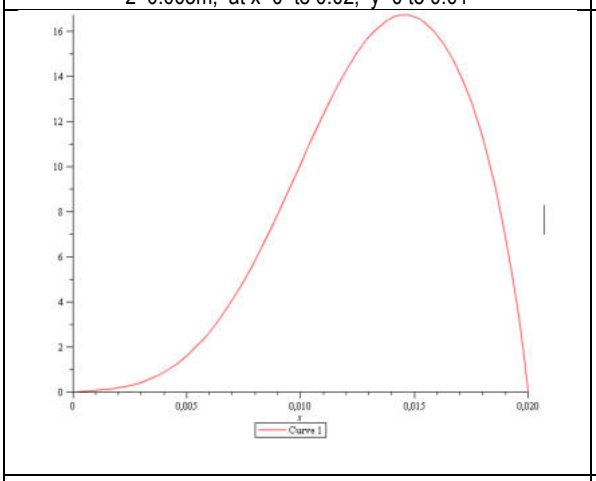

Fig.3. - Simulation of the thermal conductivity process along the ox axis from 0 to 0.02, in the section at t=0.01s, y=0.001m, z=0.003m

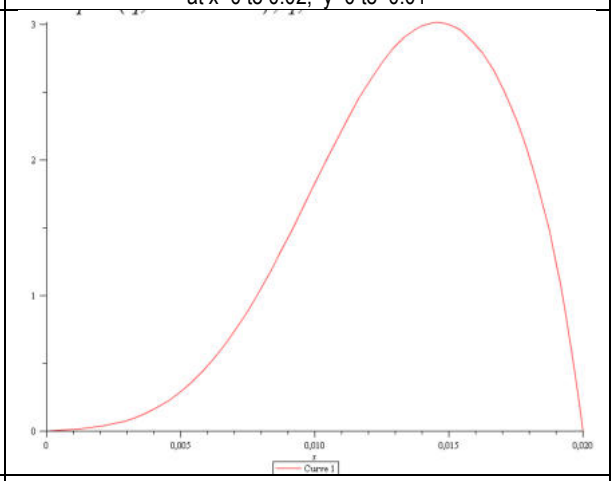

Fig. 4. - Simulation of the thermal conductivity process along the oy axis from 0 to 0.02 in the section at t=0.1 s, y=0.001m, z=0.0003m.

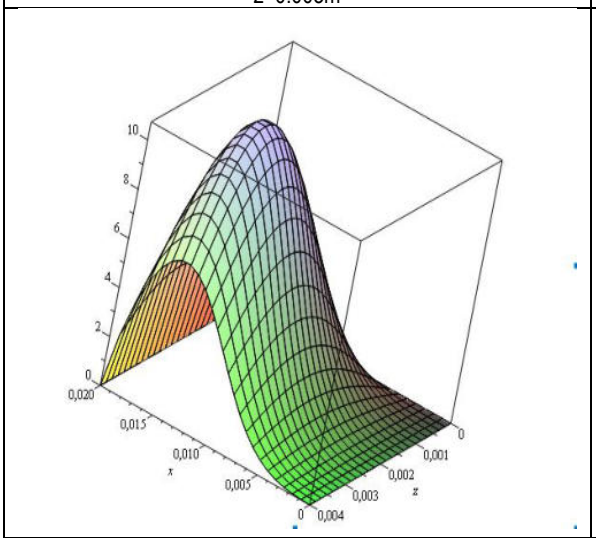

Fig. 5. - Simulation of thermal conductivity at t=0.5s., z=0.003m at x=0 to 0.02m, y=0 to 0.01

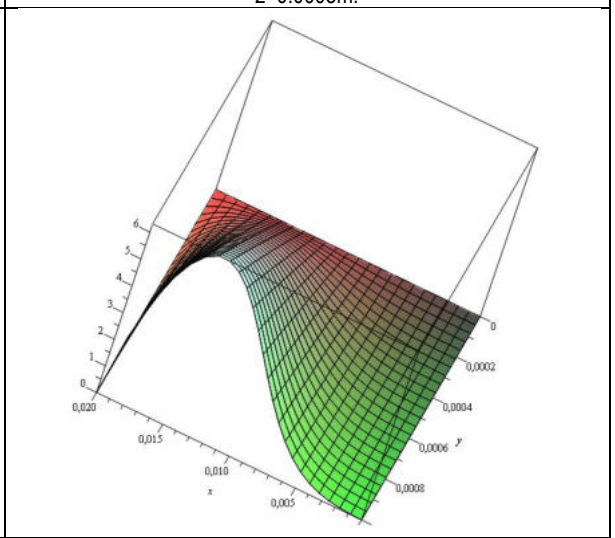

Fig. 6. - Simulation of thermal conductivity at t=0.5s, z=0.001m, at x=0 to 0.02, y=0 to 0.001

$q(x,y,z,t)_{x=0,l_1}; 0 < x < l_1,\ 0 < y < l_2,\ 0 < z < l_3;$

Table 2. Simulation results of the thermal conductivity of a silicon carbide wafer at arbitrary values of axes and time

t, ms	x, m	y, m	z, m	$q\ m/s^2$
0.01	0.01	0.005	0.0025	$2.594225522 \cdot 10^{-6}$
0.05	0.003	0.003	0.003	$7.706956453 \cdot 10^{-7}$
0.1	0.01	0.005	0.003	$2.845080897 \cdot 10^{-6}$
0.1	0.02	0.01	0.005	0

Results of modeling the thermal conductivity of a silicon carbide substrate (Figures 5-8):

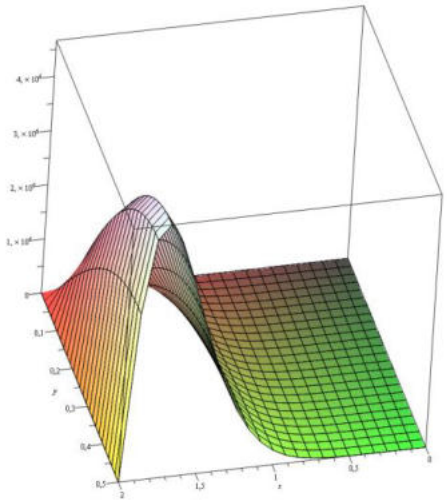

Fig.7. - Simulation of thermal conductivity at t=0.01s, z=0.0025m, at x=0…0.02m, y=0…0.01m

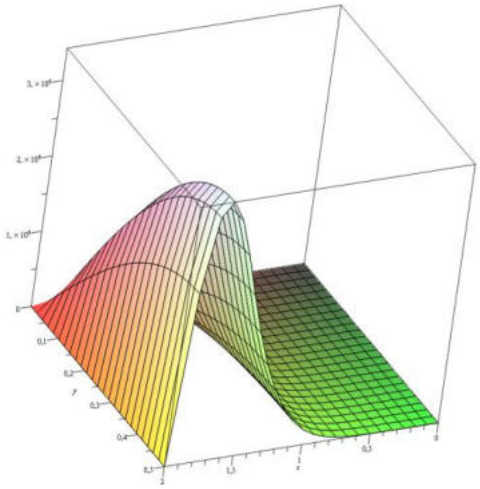

Fig 8. - Simulation of thermal conductivity at t=0.5s, z=0.003 m, at x= 0 to 0.05 y=0 to 0.05

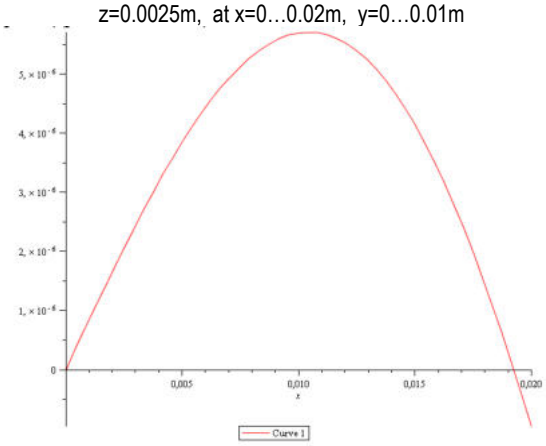

Fig. 9. - Simulation of the heat transfer process in a section along the coordinate axis ox, x=0 to 0.02m, at t=0.01s, z=0.003m, y=0.01m.

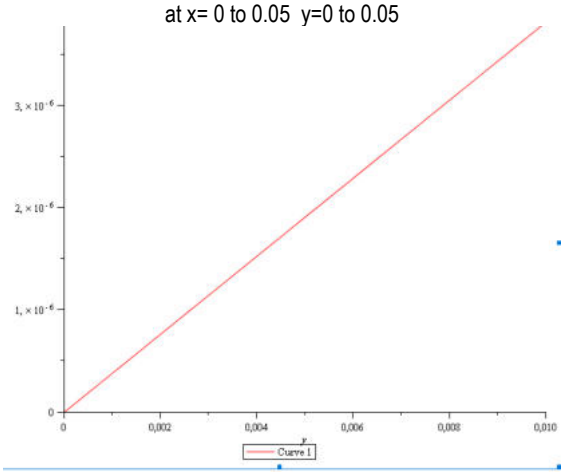

Fig. 10. - Simulation of the thermal conductivity process in a slice along the coordinate axis oy, at t=0.5s, z=0.003m, x=0.01m. y=0 to 0.01

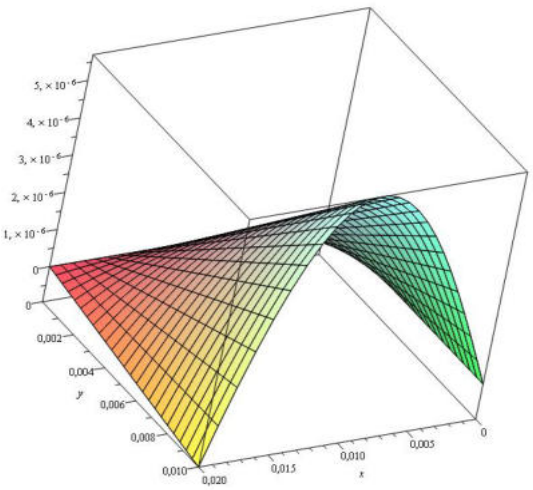

Fig 11. - Simulation of thermal conductivity at t=0.5c, z=0.33microns at x=3.1 y=0.31

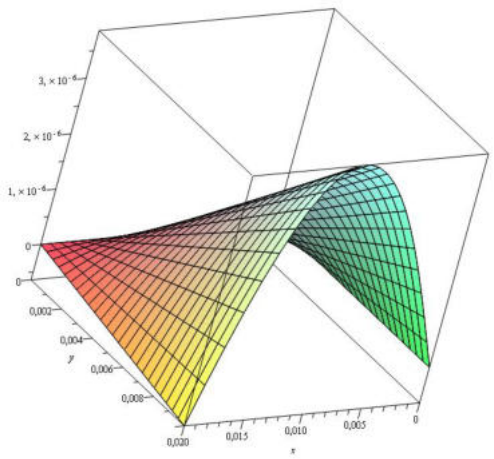

Fig. 12. - Simulation of thermal conductivity at t=1s, z=0.005m, at x=0…0.02, y=0…0.01

The result of calculating the function q is a complex polynomial containing trigonometric and exponential components grouped by degrees of variables.

An analysis of the resulting mathematical model (based on the output of the q function from the Maple environment) shows:

1. Non-linearity of distribution: The presence of terms of the form $\sin(\frac{\pi x}{20})$ and $\sin(\frac{\pi y}{10})$ indicates that the heat flow is distributed unevenly. The greatest thermal load is concentrated in the active area of the transistor channel.

2. Time factor: The coefficient e^{-t} simulates the process of cooling or establishing thermal equilibrium after removing the pulse load. At t=10, the system demonstrates stabilization of the thermal profile.

3. The influence of materials: varying the parameter a allows you to adapt the model to new materials. For example, when replacing a silicon substrate with silicon carbide (SiC), the thermal conductivity coefficient will increase significantly, which will be reflected on the graph as a flatter surface without pronounced "thermal peaks".

The program output shows that the peak values of temperature gradients are localized in the central regions of the crystal, where the sine function reaches a maximum, and decrease exponentially to the edges.This computational algorithm can be integrated into the memory subsystems of microcontrollers (where the transistors are located as tightly as possible) for predictive throttling – automatically reducing the frequency of information recording in case of a threat of local overheating.

Comparative analysis showed that when using 4H-SiC (with a calculated coefficient of a=0.43), the relaxation rate of thermal energy increases by several orders of magnitude compared to silicon structures (a=0.000028).

Conclusion

The study examined the problem of thermal conductivity in the transistor structures of modern microcontrollers.

1. The evolution of the development of field-effect transistors from the first MOSFET structures to modern solutions based on Trench MOSFET, DirectFET and innovative materials (SiC, GaN) is analyzed. It is revealed that insufficient heat sink is a key obstacle for further miniaturization.

2. Using the Maple 13 computer algebra system, a mathematical model of heat propagation was implemented. The algorithm used to decompose the function into a series of polynomials made it possible to approximate the three-dimensional Fourier equation for the local region of the transistor with high accuracy.

3. The results obtained show how long it takes for heat to be distributed across the stock crystal, and how long it takes for the transistor's heat sink to be effective. The proposed model can serve as an effective CAD tool in designing the topology of Internet of Things microcontrollers.

Acknowledgments

We express our sincere gratitude to the reviewers for a careful reading of our work, for their comments and valuable advice. Their constructive recommendations contributed to a significant improvement in the quality of research and clarification of a number of provisions, which made the article more meaningful and scientifically based.

References

[1] Harris D. M., Harris S. L. Digital circuitry and computer architecture. – ed. Morgan Kaufmann.-2013 Elsevier, USA. ISBN 978-0-12-394424-5.

[2] Al-Fuqaha, A., Guizani, M., Mohammadi, M., Aledhari, M., & Ayyash, M. Internet of Things: A Survey on Enabling Technologies, Protocols, and Applications // IEEE Communications Surveys & Tutorials. - 2015. - Vol. 17, No. 4. - P. 2347–2376. - DOI: 10.1109/COMST.2015.2444095.

[3] El Arabi, A., Maillet, D., Blet, N., & Rémy, B. A Convolutional Model for Estimating the Junction Temperatures of SiC MOSFET Transistors // HAL Open Science. - 2024. - hal-04629861. — URL: https://hal.science/hal-04629861

[4] Xia, Y., Sheng, Y., Jia, R., Xu, J., & Bao, H. Non-Fourier Thermal Analysis of the Self- Heating Effect in CMOS Logic Circuits //APL Electronic Devices. - 2025. - Vol. 1, No. 3. - Art. 036115. - DOI: 10.1063/5.0279339.

[5] Köroğlu, B., Pop, E. High Thermal Conductivity Insulators for Thermal Management in 3D ICs //IEEE Electron Device Letters. - 2023. - Vol. 44, No. 3. - P. 496–499. - DOI: 10.1109/LED.2023.3237834.

[6] He, L., Zhang, X., et al. Extremely Low Thermal Resistance of β-Ga_2O_3 MOSFETs by Co-Integrated Design of Substrate Engineering and Device Packaging // *ACS Applied Materials & Interfaces*. — 2024. — DOI: 10.1021/acsami.4c08074.

[7] Simon M. Size. Physics of Semiconductor Devices. John Wiley, Sons, Inc, Hoboken, New Jersey, USA,2007, 832p. ISBN 978-0-471-14323-9.

[8] Liu, J., Wang, Y., et al. Phase Change Based Heat Transfer for Thermal Management of Metal-Oxide-Semiconductor Field-Effect ansistors // Journal of Energy Storage. - 2025. - DOI: 10.1016/j.est.2025.115183.

[9] Chen, X., Du, M., Hu, Z., & Wei, K. A Junction Temperature Model Based on Heat Flow Distribution in an IGBT Module with Solder Layer Voids // Heliyon. - 2024. - Vol. 10, No. 13. - Art. e33625. — DOI: 10.1016/j.heliyon.2024.e33625.

[10] Jebelli, A., Mahabadi, A., & Ahmad, R. Thermal Design Automation (TDA) for Multiscale Thermal Management of Electronics // Journal of Applied Physics. - 2025. - Vol. 138, No. 18. — Art. 180901. — DOI: 10.1063/5.0234610.

[11] Pfromm, L., et al. A 20-Year Retrospective on Power and Thermal Modeling and Management //arXiv preprint. — 2025. — arXiv:2508.05495. — URL: https://arxiv.org/abs/2508.05495.

[12] Kumar, V., Datta, A., & Dasgupta, S. Ab-Initio Multiscale Thermal Modeling of 5 nm Stacked Nanosheet Field Effect Transistor for Thermal Hotspot Optimization Inside the Channel // Proc. 22nd IEEE Intersociety Conference on Thermal and Thermomechanical Phenomena in Electronic Systems (ITherm). — 2023. — P. 667–675.

[13] Jebelli, A., et al. Advanced Thermal Management for High-Power ICs: Optimizing Heatsink and Airflow Design // Applied Sciences (MDPI). - 2024.- Vol. 14, No. 20. - Art. 9406. - DOI: 10.3390/app14209406.

[14] Marzougui, S., et al. A Comprehensive Review on Thermal Management of Electronic Devices // Journal of Engineering and Applied Science. - 2023.- Vol. 70. - Art. 77. - DOI: 10.1186/s44147-023-00309-2.
IEEE Heterogeneous Integration Roadmap (HIR). Chapter 20: Thermal. — 2023 Edition. — IEEE. — URL: https://eps.ieee.org/images/files/HIR_2023/ch20_thermalfinal.pdf.

[15] Wang, Q., et al. Liquid Metal Phase Change Materials for Thermal Management of Electronics // Advanced Materials Technologies. - 2024. - Vol. 9. - Art. 2324910. DOI: 10.1080/23746149.2024.2324910.

[16] Alazzawi, Q., et al. Green IoT: Energy Efficiency, Renewable Integration, and Security Implications //IET Networks. — 2025. - DOI: 10.1049/ntw2.70003.

[17] Pirniyazova, P.M**.** Modeling and solving equations of the wave process using the recurrent operator method. *NNC RK Bulletin*. 2025, (3):156-163. https://doi.org/10.52676/1729-7885-2025-3-156-163

Information of the authors

Pirniyazova Periuza Mambetniyazovna, Ph.D senior lecturer, Almaty University of Energy and Telecommunications
e-mail: pirniyazova1974@gmail.com

Aksutova Asiyat, senior lecturer, Almaty University of Energy and Telecommunications,
e-mail: a.akhsutova@aues.kz

Aidarkul Moldir, assistant teacher, Almaty Technological University,
e-mail: m.aidarkul@atu.edu.kz

DOI 10.52209/2706-977X_2026_3_94 IRSTI 55.09.01 UDC 621.9.079

Influence of Vessel Material on the Effectiveness of Ultrasonic Treatment of Metalworking Fluids

Kim A.S.*, Kadyrov A.S.
Abylkas Saginov Karaganda Technical University, Karaganda, Kazakhstan
*corresponding author

Abstract. This article reviews the influence of process vessel material on the effectiveness of ultrasonic treatment of liquid media. The physical processes occurring when ultrasonic waves interact with the liquid–vessel wall interface are considered, including the reflection, transmission, absorption, and scattering of acoustic energy. The effects of specific acoustic impedance, density, stiffness, wall thickness, and the vibration-damping capacity of the material on acoustic pressure distribution, cavitation field formation, acoustic streaming intensity, and heating of the treated medium are analysed. Vessels made of glass, polymers, and metals used in ultrasonic cleaning, dispersion, emulsification, extraction, and regeneration of metalworking fluids are compared. It is shown that the influence of vessel material should be considered in relation to vessel geometry and dimensions, wall thickness, the method of ultrasonic energy transmission, transducer position, and the volume of the treated liquid. The theoretical considerations are compared with previously obtained experimental results on the ultrasonic treatment of a metalworking fluid in glass and polypropylene vessels. The observed differences in the physical processes and changes in the monitored parameters confirm that the properties of the vessel walls must be considered when selecting ultrasonic treatment parameters. The main requirements for vessel material selection are established, and directions for further research into the transducer–liquid–process vessel system are proposed.

Keywords: ultrasonic treatment, vessel material, acoustic impedance, cavitation, glass, polypropylene, stainless steel, liquid media, metalworking fluid.

Introduction

Ultrasonic treatment is considered a promising method for intensifying physical and chemical processes in liquid media. Ultrasound is used for liquid purification and disinfection, solid-particle dispersion, homogenisation, emulsification, extraction of biologically active compounds, material synthesis, and treatment of process fluids. This wide range of applications is attributed to the combined effects of acoustic cavitation, acoustic microstreaming, shock waves, local pressure and temperature gradients, and high-velocity microjets generated during the collapse of cavitation bubbles [1, 2].

In a liquid medium, an ultrasonic wave produces alternating compression and rarefaction cycles. When the negative pressure amplitude reaches a certain threshold, cavitation bubbles are formed, grow, and subsequently collapse. This process is accompanied by localised energy release, which contributes to the disruption of particle agglomerates, reduction in particle and droplet sizes, enhancement of mass transfer, changes in the interfacial area, and initiation or acceleration of various chemical reactions. Cavitation phenomena therefore account for a substantial proportion of the technological effects produced by ultrasonic treatment [1, 3].

The effectiveness of ultrasonic treatment is traditionally associated primarily with treatment frequency, power, and duration. Temperature, viscosity, surface tension, dissolved-gas content, and the volume of the treated liquid are also important. However, recent studies indicate that the intensity and spatial distribution of cavitation depend not only on the specified operating parameters but also on the design of the entire processing system. The main design factors include the type and position of the ultrasonic transducer, its immersion depth, the geometry and dimensions of the process vessel, liquid-column height, wall thickness, and the conditions under which ultrasonic waves are reflected from the boundaries of the working system [2, 3].

The ultrasonic field within a process vessel is generally non-uniform. Regions with different acoustic pressure levels and cavitation intensities may form throughout the liquid volume. An experimental investigation of the acoustic field in a cylindrical cavitation cell demonstrated that the relationship between acoustic pressure and applied power may be nonlinear and that the spatial distribution of cavitation is governed by the configuration of the working system [4]. When scaling up an ultrasonic system, changes in the process vessel parameters also redistribute acoustic energy and shift the regions of intense cavitation [5]. Consequently, results obtained using systems of different volumes and geometries cannot always be directly compared solely on the basis of identical frequency and power values.

The influence of system design has also been confirmed in studies of ultrasonic systems equipped with immersion transducers. Changes in the transducer position relative to the vessel bottom and walls have been shown to significantly affect the intensity of ultrasound-induced oxidation processes and the size of the active cavitation region. This effect is attributed to the reflection of ultrasonic waves from the system components and the resulting differences in the spatial structure of the acoustic field [6]. Therefore, the process vessel should not be regarded as a

passive enclosure containing the liquid but as an integral component of the transducer–liquid–vessel wall oscillatory system.

The vessel wall material is of particular importance in such a system. When an acoustic wave reaches the liquid–solid interface, it is partially reflected and partially transmitted into the wall material, while some of its energy is lost through absorption, scattering, and the damping of mechanical vibrations. The proportions of these components depend on the specific acoustic impedance of the liquid and wall material, their densities, the speed of sound in each medium, material stiffness, and internal energy losses. Ultrasonic energy transmission is also affected by wall thickness, vessel geometry, mounting conditions, and the presence of additional interfaces between the transducer and the treated medium.

Glass, metal alloys, and polymers differ considerably in their mechanical and acoustic properties. Glass is characterised by relatively high stiffness and limited deformation under acoustic excitation. Metal vessels have high mechanical strength and are widely used in industrial ultrasonic equipment. Polymeric materials exhibit lower stiffness and a greater capacity to absorb energy and damp mechanical vibrations. However, the actual transmission of ultrasonic energy is determined not only by the material properties but also by the design of the entire working system.

A direct comparison of ultrasonic wave transmission through vessel walls made of glass, stainless steel, polyethylene, perfluoroalkoxy alkane, and polytetrafluoroethylene confirmed differences in the intensity of the transmitted ultrasonic effects. The authors evaluated extraction efficiency and cavitation-induced erosion under different operating modes of an ultrasonic bath. The results showed that the vessel material affects the degree of ultrasonic wave attenuation; however, the magnitude of this effect depends on the frequency, excitation mode, and properties of the treated medium [7]. Therefore, claims regarding the universal superiority of a particular material, without considering the system design and treatment conditions, are insufficiently substantiated.

The practical significance of this factor is supported by the results of ultrasonic regeneration of metalworking fluids. Differences in the characteristics of cavitation processes, the degree of heating, and changes in the monitored physicochemical parameters were observed when a metalworking fluid was treated in glass and polypropylene vessels [8]. These findings indicate that the vessel wall material must be considered when selecting treatment conditions and comparing the effectiveness of ultrasonic treatment in different systems. Nevertheless, the relationships established for a specific experimental system require further theoretical substantiation and validation using other liquids, vessel materials, and vessel designs.

Despite the substantial number of publications devoted to ultrasonic systems, most studies focus on power, frequency, transducer arrangement, process vessel geometry, and equipment scale-up from laboratory to industrial conditions [2–6]. Vessel material is more commonly regarded as an accompanying design characteristic than as an independent process parameter. Only a limited number of comparative studies have examined different wall materials under identical geometric, energy, and temperature conditions. Furthermore, no unified approach has been developed to assess the combined effects of vessel material, wall thickness, vessel shape, and the method of ultrasonic energy transmission.

Therefore, the available scientific evidence must be systematised, and the mechanisms through which the physical, mechanical, and acoustic properties of vessel walls affect ultrasonic field distribution and liquid-treatment effectiveness must be identified. Such an analysis will improve the comparability of experimental results, provide a basis for selecting materials for laboratory and industrial systems, and facilitate the development of design requirements for ultrasonic processing equipment.

The aim of this study is to systematise and comparatively analyse the available data on the influence of the physical, mechanical, and acoustic properties of process vessel materials on ultrasonic wave propagation, cavitation field formation, and the effectiveness of liquid treatment.

1. Physical Principles of Ultrasonic Treatment of Liquids

1.1 Propagation of Ultrasonic Waves and Formation of the Acoustic Field

Ultrasonic treatment of liquids is based on the transfer of mechanical energy from the transducer to the treated medium through elastic vibrations. In liquids, ultrasonic waves propagate predominantly as longitudinal waves. The particles of the medium oscillate along the direction of wave propagation, resulting in alternating compression and rarefaction regions [9].

The ultrasonic wavelength is determined by the following expression:

$$\lambda = c/f \tag{1}$$

where λ is the wavelength, m;

c - is the speed of sound in the liquid, m/s;

f - is the ultrasonic frequency, Hz.

As the frequency increases, the wavelength decreases, affecting the spatial distribution of acoustic pressure. Assuming that the speed of sound in water is approximately 1,500 m/s, the wavelengths at frequencies of 25, 28, and 40 kHz are approximately 60.0, 53.6, and 37.5 mm, respectively. These values are comparable to the dimensions of

laboratory-scale vessels; therefore, changes in vessel shape and dimensions, liquid-column height, and transducer position can substantially alter the ultrasonic field.
The time-averaged intensity of a plane progressive wave is determined as follows:

$$I = p_a^2/(2\rho c), \quad (2)$$

where I - is the ultrasonic intensity, W/m²;

p_a - is the acoustic pressure amplitude, Pa;

ρ - is the liquid density, kg/m³;

c - is the speed of sound in the liquid, m/s.

Equation (2) is applicable to a plane progressive wave propagating through a homogeneous medium. In an actual process vessel, the acoustic field becomes more complex because of wave reflection, superposition, and absorption, as well as the presence of bubbles and solid particles.

Within a confined volume, incident and reflected waves may form standing waves. This results in the formation of nodes, where the acoustic pressure amplitude is at its minimum, and antinodes, where it reaches its maximum. Consequently, the ultrasonic field within the vessel becomes non-uniform: cavitation and mixing are intense in some regions, whereas the ultrasonic effect is weaker in others [4].

The positions of nodes and antinodes depend on the wavelength, vessel dimensions, liquid-column height, and transducer position. Therefore, systems operating at identical frequency and power levels may produce different acoustic pressure distributions if their design characteristics differ [5, 6].

1.2. Cavitation, Acoustic Streaming, and Liquid Heating

Acoustic cavitation is the principal physical phenomenon governing the effects of high-intensity ultrasound on liquids. It involves the formation, growth, oscillation, and collapse of gas- or vapour-filled bubbles under an alternating acoustic pressure field [9, 11].

Cavitation bubbles generally form at gas inclusions, suspended particles, surface irregularities, and phase boundaries present in the liquid. During the rarefaction phase, the bubbles expand, whereas during the compression phase, they contract or collapse. Their behaviour depends on the frequency and acoustic pressure amplitude, dissolved-gas content, viscosity, surface tension, and liquid temperature.

At a low acoustic pressure amplitude, bubbles undergo stable oscillations over many acoustic cycles. Under more intense excitation, they expand rapidly and collapse violently. Bubble collapse generates shock waves, high-velocity microjets, and local pressure gradients. These phenomena contribute to the disruption of contaminant agglomerates, surface cleaning, dispersion, and enhanced mass transfer [9, 11].

An excessive increase in the number of bubbles does not necessarily improve treatment effectiveness. Dense bubble clouds near the transducer may scatter and absorb ultrasonic waves, thereby preventing their propagation into more distant regions of the liquid. As a result, the non-uniformity of the acoustic field increases [2, 3].

Alongside cavitation, acoustic streaming occurs in the liquid. Acoustic streaming is the directional motion of a fluid caused by momentum transfer from an attenuating ultrasonic wave. It promotes mixing, equalises temperature and component concentrations, facilitates particle transport, and enhances mass transfer. The direction and velocity of acoustic streaming depend on vessel geometry, transducer position, and the manner in which waves are reflected from the vessel walls [10].

A proportion of the supplied energy is converted into heat through ultrasonic wave absorption, viscous friction, fluid motion, and cavitation bubble activity. In the absence of significant heat losses, the power actually absorbed by the liquid can be approximately determined from its heating rate:

$$P_{abs} = m \cdot c_p \cdot \Delta T/\Delta t, \quad (3)$$

where P_{abs} - is the absorbed power, W;

m - is the liquid mass, kg;

c_p - is the specific heat capacity, J/(kg·K);

ΔT - is the temperature change, K;

Δt - is the measurement duration, s.

Under actual operating conditions, some of the heat is transferred to the vessel walls, the transducer, and the surrounding environment. Therefore, liquid heating characterises the overall energy absorption but cannot be used to determine acoustic pressure or cavitation intensity directly.

Temperature also affects cavitation. As the temperature increases, liquid viscosity and surface tension generally decrease, whereas the saturated va pour pressure increases. These changes facilitate bubble formation; however, a

higher vapour content within the bubbles may reduce the intensity of their collapse. Therefore, the relationship between cavitation activity and temperature is complex and often non-monotonic [11, 12].

1.3. Influence of Operating and Design Parameters

Frequency determines the wavelength, the duration of the compression and rarefaction cycles, and the dynamics of cavitation bubble growth. At relatively low frequencies, the bubbles have sufficient time to grow to larger sizes and generate a more pronounced mechanical effect upon collapse. As the frequency increases, the duration of each cycle decreases, while the number of excitation cycles per unit time increases [2, 9, 11].

An increase in power is generally accompanied by an increase in vibration amplitude, acoustic pressure, and the number of cavitation bubbles. However, the nominal electrical power of the generator is not equal to the power actually transferred to the liquid because some of the energy is lost in the converter, transducer, vessel walls, and connecting components [2].

The total amount of energy supplied to the system at constant power is determined as follows:

$$E=P\cdot t \tag{4}$$

where E is the supplied energy, J;

P - is the power, W;

t - is the treatment duration, s.

Increasing the treatment duration increases the total energy supplied to the system; however, the technological outcome does not always change proportionally. Prolonged treatment may cause excessive heating, changes in the dissolved-gas content, and renewed fragmentation of previously agglomerated particles.

Frequency, power, treatment duration, and temperature are interrelated. The treatment outcome is also affected by the liquid volume, vessel geometry and dimensions, wall thickness, and transducer position. Therefore, the process vessel should be regarded as an integral component of the transducer–liquid–vessel wall system rather than as a neutral enclosure [2–6].

2. Interaction of an Ultrasonic Wave with the Process Vessel Wall

2.1 Reflection, Transmission, and Absorption of Ultrasonic Waves

When an incident ultrasonic wave reaches the liquid–wall interface, it is divided into a reflected wave returning to the liquid and a transmitted wave propagating through the wall material. Some of the energy is dissipated as a result of internal friction, absorption, and scattering by material inhomogeneities [13, 14].

The relationship between the energy components can be expressed as follows:

$$I_{inc}=I_{ref}+I_{tr}+I_{loss} \tag{5}$$

where I_{inc} - is the intensity of the incident wave, W/m²;

I_{ref} - is the intensity of the reflected wave, W/m²;

I_{tr} - is the intensity of the transmitted wave, W/m²;

I_{loss} - represents intensity losses due to absorption and scattering, W/m².

An actual vessel wall has a finite thickness and two interfaces: an inner and an outer interface. Therefore, the wave transmitted into the material undergoes multiple reflections within the wall. Some of the energy returns to the liquid, some is transmitted to the external medium, and some is converted into heat. The resulting energy distribution is affected by the wall material and thickness, ultrasonic frequency, angle of incidence, and the medium surrounding the outer surface of the vessel.

The reflected waves are superimposed on the waves propagating through the liquid and contribute to the formation of standing waves. Depending on their phase relationship, they may either increase or decrease the acoustic pressure. Therefore, strong reflection does not necessarily result in more uniform or effective ultrasonic treatment.

2.2. Specific Acoustic Impedance and Energy Transmission

The resistance of a medium to acoustic wave propagation is characterised by its specific acoustic impedance:

$$Z=\rho c \tag{6}$$

where Z - is the specific acoustic impedance, Pa·s/m;

ρ - is the density of the medium, kg/m³;

c - is the speed of sound in the medium, m/s.

The greater the difference between the specific acoustic impedances of two media, the larger the proportion of energy reflected from their interface. For a plane wave normally incident on the boundary between two homogeneous, lossless media, the intensity reflection coefficient is determined as follows:

$$R = [(Z_2 - Z_1)/(Z_2 + Z_1)]^2, \quad (7)$$

where R - is the fraction of reflected intensity;

Z_1 and Z_2 - are the specific acoustic impedances of the first and second media, respectively.

The intensity transmission coefficient is determined as follows:

$$T = 4Z_1Z_2/(Z_1 + Z_2)^2, \quad (8)$$

where T - is the fraction of intensity transmitted into the second medium.

For an ideal lossless interface, the following condition applies: R+T=1. These expressions describe a single plane interface and do not account for the finite wall thickness, wall curvature, internal energy losses, or interaction with the external medium [13]. They therefore describe the fundamental relationships but cannot fully determine ultrasonic transmission through an actual process vessel.

Within the wall material, the acoustic pressure amplitude decreases as the wave propagates:

$$p(x) = p_0 \cdot e^{(-\alpha x)}, \quad (9)$$

where p(x) - is the acoustic pressure amplitude after the wave has travelled a distance `x`, Pa;

p_0 - is the initial acoustic pressure amplitude, Pa;

α - is the attenuation coefficient, m^{-1};

x - is the distance travelled by the wave through the material, m.

Attenuation is caused by absorption and scattering. During absorption, mechanical energy is predominantly converted into heat, whereas scattering redistributes the energy in other directions. In polymers, internal friction and the time lag between deformation and the applied load are additional important factors.

2.3. Influence of Wall Thickness, Geometry, and Mounting Conditions

Wall thickness affects both energy absorption and the phase relationships between waves undergoing multiple reflections from the wall surfaces. Therefore, the dependence of ultrasonic transmission on wall thickness is not always monotonic. A thicker wall does not necessarily transmit less energy under all conditions, because reflected waves may constructively interfere at certain ratios of wall thickness to wavelength.

A numerical and experimental investigation of cylindrical glass vessels with wall thicknesses of 1.2, 1.8, and 3.2 mm showed that variations in thickness altered not only the acoustic pressure level but also its spatial distribution. The numerical results were validated using the observed son chemiluminescence pattern of a luminol solution [15].

Vessel geometry determines the angles of incidence and directions of wave reflection. In a cylindrical vessel, the angle of incidence varies around the circumference; therefore, different regions of the wall reflect and transmit ultrasound differently. A curved surface may cause wave scattering, local focusing, and divergence. The vessel bottom, side walls, and free liquid surface jointly determine the positions of nodes, antinodes, and regions of developed cavitation [3, 5, 15].

Under alternating acoustic pressure, the wall undergoes forced mechanical vibrations and becomes a secondary source of ultrasonic waves. The amplitude of these vibrations depends on material elasticity, wall thickness, excitation frequency, and mounting conditions. Supporting elements may dissipate some of the energy and alter the natural frequencies of the structure. Therefore, comparisons between vessels should specify not only the wall material and thickness but also the installation and mounting conditions [2, 3].

2.4. Characteristics of Glass, Polymer, and Metal Vessels

Glass is characterised by high stiffness, chemical resistance, and transparency, allowing the observation of cavitation, mixing, and liquid phase separation. The considerable difference between the specific acoustic impedances of glass and the liquid promotes pronounced wave reflection. Relatively low internal mechanical energy losses allow the wall to contribute to the formation of a stable acoustic field. However, glass is brittle, and its interaction with ultrasound is strongly dependent on vessel wall thickness and geometry [7, 15].

Polypropylene has lower stiffness and is more readily deformed. Its internal friction contributes to the damping of mechanical vibrations and the conversion of some energy into heat. However, the similarity between the specific acoustic impedances of the liquid and polymer may facilitate wave transmission across the inner interface. Therefore,

it cannot be unequivocally stated that polypropylene transmits ultrasound less effectively under all conditions. The resulting transmission is determined by the combined effects of reflection, absorption, wall thickness, and mounting conditions [7].

Stainless steel is characterised by high strength and stiffness and is widely used in industrial ultrasonic equipment. Its high specific acoustic impedance causes pronounced reflection at the liquid–metal interface. At the same time, a metal wall can transmit mechanical vibrations when an ultrasonic transducer is directly attached to it. Therefore, the behaviour of a metal vessel must be evaluated with consideration of the ultrasonic energy transmission method: through an immersion transducer, through the liquid in an ultrasonic bath, or through a transducer attached directly to the vessel wall [2, 3, 7].

An experimental comparison of ultrasonic transmission through glass, stainless steel, polyethylene, perfluoroalkoxy alkane, and polytetrafluoroethylene confirmed that vessel material affects the transmitted ultrasonic energy. However, the results also depended on frequency, the operating mode of the system, liquid properties, and the selected assessment method. Therefore, no single material can be regarded as universally optimal [7].

2.5. Influence of the Vessel Wall on the Acoustic and Cavitation Fields

The vessel wall material and design affect the proportions of reflected, transmitted, and absorbed energy; the formation of standing waves; the spatial distribution of acoustic pressure; the acoustic streaming pattern; and the location of regions of developed cavitation. Wall vibrations and surface roughness, which may promote cavitation bubble nucleation, are also important.

Cavitation develops primarily in regions where the negative acoustic pressure reaches the cavitation threshold. Therefore, changes in the positions of nodes and antinodes cause the cavitation regions to shift. The resulting bubbles, in turn, scatter and absorb ultrasonic waves, thereby modifying the initial acoustic pressure distribution [2, 4, 9].

When comparing glass and polypropylene vessels, the influence of the material must be distinguished from that of the vessel design. If the vessels differ in wall thickness, geometry, or internal dimensions, it is more appropriate to describe the study as a comparison of the vessels as complete systems. To evaluate the influence of material independently, vessels of identical geometry and comparable wall thickness should be used, or the design differences should be accounted for numerically.

Changes in liquid temperature should not be regarded as an independent indicator of cavitation intensity. Direct measurements of acoustic pressure and cavitation intensity would provide additional quantitative evidence for the observed differences between the vessels. Such measurements could be performed using a hydrophone or sonochemical indicators, including sonochemiluminescence, in future experimental studies. More pronounced heating indicates a greater proportion of ultrasonic energy being converted into heat, but does not necessarily correspond to higher acoustic pressure or more intense bubble collapse. Temperature measurements should therefore be considered together with acoustic pressure distributions, optical or chemical indicators of cavitation activity, and changes in the properties of the treated liquid.

Thus, the process vessel wall is an active component of the ultrasonic system. Wall material, thickness, geometry, and mounting conditions jointly determine wave reflection, transmission, absorption, and scattering. Vessel material should therefore be regarded as an independent process parameter whose influence must be evaluated in relation to the design of the entire system.

3. Comparison of the Theoretical Considerations with the Results of Ultrasonic Treatment of Metalworking Fluids

3.1 Experimental Conditions

To evaluate the influence of process vessel material, the results of previous studies on the ultrasonic treatment of a metalworking fluid in glass and polypropylene vessels were analysed [8]. The experiments were conducted under identical treatment conditions, allowing the physical processes and changes in the monitored fluid parameters to be compared.

Vessels with capacities of 1, 3, and 5 L were used in the experiments. Ultrasonic treatment was performed at frequencies of 25, 28, and 40 kHz and a power of 100 W. The treatment duration was 5 min. The principal comparison between the glass and polypropylene vessels was conducted at 28 kHz, which had previously been identified as the most effective treatment frequency.

Metalworking fluid samples with different service durations were examined: fresh fluid, moderately contaminated fluid used for 2–3 weeks, and heavily contaminated fluid used for more than one month. Each experiment was performed in triplicate. The results were statistically processed and expressed as the mean ± standard deviation. Differences were considered statistically significant at $p<0.05$ [8].

Samples were collected before ultrasonic treatment, immediately after treatment, and after the fluid had been allowed to stand for 24 h. The treatment results were evaluated by measuring temperature, density, the Brix value, and the electrical properties of the fluid. Cavitation, mixing, contaminant particle agglomeration, and subsequent phase separation were additionally assessed by visual and microscopic observations.

This experimental design made it possible to evaluate not only the immediate effects of ultrasound but also the changes occurring after treatment had been discontinued. The 24-h settling period was particularly important because contaminant agglomeration and migration and the formation of a separable upper layer continued after the transducer had been switched off. No visible re-emulsification of the separated contaminants was observed during the 24-h settling period; however, possible chemical degradation of the base emulsion was not assessed and requires further chemical analysis.

3.2 Influence of Vessel Material on Physical Processes

During ultrasonic treatment, liquid heating, cavitation bubble formation, intensive mixing, contaminant particle agglomeration, and subsequent phase separation were observed in the metalworking fluid. The characteristics and intensity of these processes depended on the process vessel material.

Bubble formation and fluid motion were more intense in the glass vessels than in the polypropylene vessels. Small, dark agglomerates containing metal particles, dust, tramp oil, and other contaminants formed within the fluid. Bubbles that entrained solid and oily contaminants formed near the vessel walls. These agglomerates moved upwards, gradually forming a contaminated upper layer.

The observed separation can be explained by the combined effects of cavitation, acoustic streaming, and contaminant particle agglomeration. Ultrasonic treatment disrupted the bonds between the contaminant particles and the dispersion medium. Simultaneously, the bubbles and upward fluid flows promoted contaminant transport towards the upper part of the vessel. After treatment had been discontinued, the agglomerated contaminants continued to separate from the bulk fluid.

More pronounced heating was also observed in the glass vessels. Under identical treatment conditions of 28 kHz, 100 W, and 5 min, the fluid temperature reached 33–35 °C in the glass vessels, compared with predominantly 30–31 °C in the polypropylene vessels. Given an initial temperature of approximately 23 °C, these results indicate differences in energy transmission and distribution.

The more intense processes observed in the glass vessel are consistent with the theoretical considerations presented in Sections 1 and 2. Glass is characterised by high stiffness and relatively low internal mechanical energy losses. Waves reflected from its walls contribute to the formation of the acoustic field within the liquid. Polypropylene deforms more readily, while some of the energy is dissipated through internal friction and the damping of mechanical vibrations [7, 13]. It should be noted that increased heating does not necessarily indicate that a greater proportion of the supplied acoustic energy contributes to active cavitation. Part of the supplied ultrasonic energy may be dissipated as heat through material damping and losses in the vessel wall, whereas another portion is transmitted into the liquid and contributes to the acoustic field and cavitation activity.

However, the observed differences cannot be attributed solely to the intrinsic properties of the materials. The results are also affected by wall thickness, vessel geometry, internal dimensions, liquid-column height, and transducer position. Studies by other authors have confirmed that changes in wall thickness and geometry alter the acoustic pressure distribution even when the frequency and power remain unchanged [5, 15].

3.3 Changes in the Monitored Parameters

A comparison of the results obtained at a frequency of 28 kHz, a power of 100 W, and a treatment duration of 5 min revealed differences in the monitored parameters between the glass and polypropylene vessels.

Table 1. Effect of Vessel Material and Liquid Volume on the Parameters of Ultrasonically Treated Metalworking Fluid

Liquid volume, L	Vessel material	Brix value, %	Density, g/cm³	Temperature, °C
1	Polypropylene	1.5	1.0058	30
1	Glass	1.1	1.0040	35
3	Polypropylene	1.6	1.0062	31
3	Glass	0.7	1.0020	34
5	Polypropylene	1.7	1.0066	30
6	Glass	0.7	1.0019	33

*The table presents the results obtained for a moderately contaminated metalworking fluid treated at a frequency of 28 kHz, a power of 100 W, and a treatment duration of 5 min.

The experimental data presented in Table 1 were obtained in our previous study on the ultrasonic regeneration of metalworking fluids [8].

Figures 1–3 show the effect of vessel material and liquid volume on the Brix value, density, and temperature of the metalworking fluid after ultrasonic treatment. For all the investigated volumes, treatment in glass vessels resulted in lower Brix values and lower fluid density than treatment in polypropylene vessels. At the same time, the temperature of the fluid treated in glass vessels was 3–5 °C higher. The most pronounced differences in the Brix value and density were observed at liquid volumes of 3 and 5 L. Taken together, these results indicate more intensive energy transfer and a more pronounced ultrasonic effect in the glass vessels under the experimental conditions employed. However, the observed differences should be attributed to the combined influence of vessel material, wall thickness, geometry, liquid volume, and acoustic field distribution.

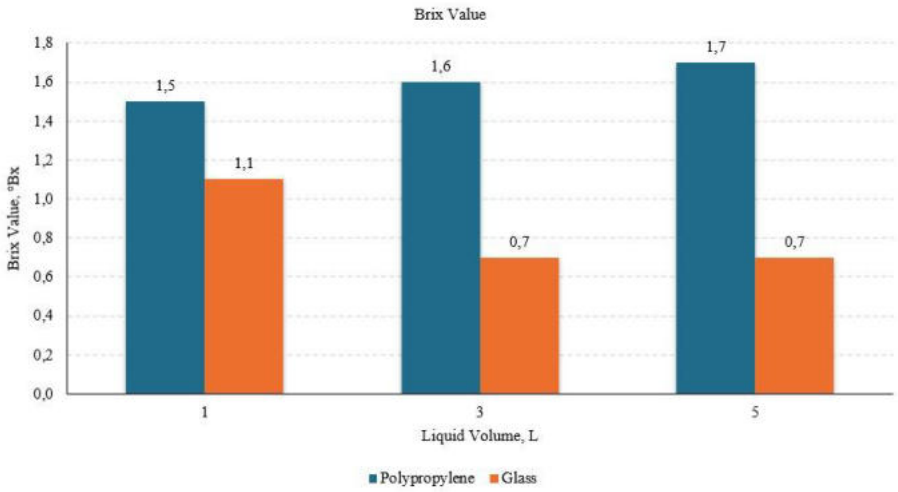

Fig.1. - Effect of vessel material and liquid volume on the Brix value of the metalworking fluid.

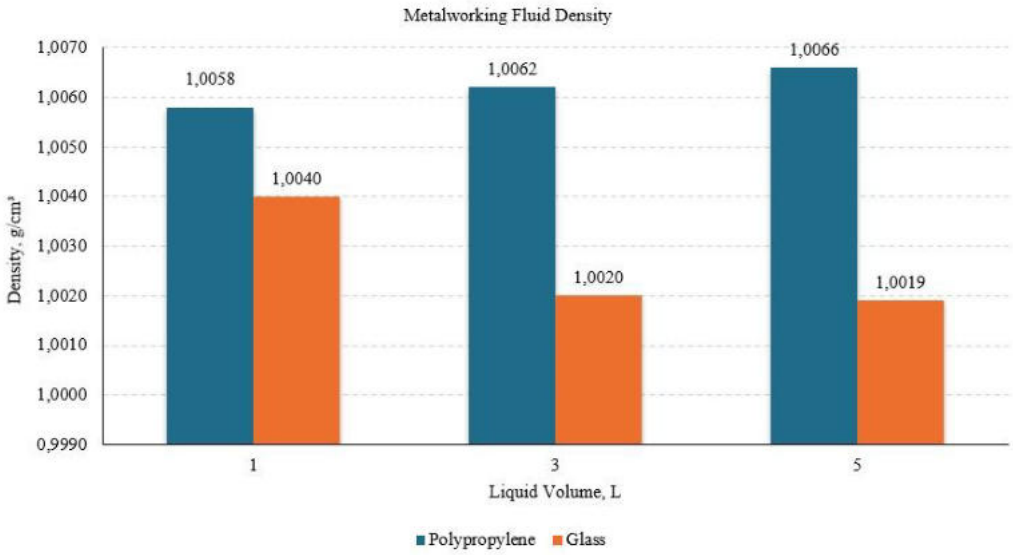

Fig.2. - Effect of vessel material and liquid volume on the density of the metalworking fluid.

Fig.3. - Effect of vessel material and liquid volume on the temperature of the metalworking fluid

The decrease in the Brix value was associated with a reduction in the concentration of components affecting light refraction in the investigated fluid. Since a metalworking fluid is a complex multicomponent medium, this parameter cannot be directly equated solely with contaminant content. It should be evaluated together with density, electrical properties, turbidity, and microscopic observations.

The decrease in density following ultrasonic treatment confirms the separation of some solid and oily contaminants from the bulk fluid. The most pronounced changes were observed after the settling period, during which the agglomerated contaminants either migrated to the upper layer or settled, depending on their composition and density. Further studies should include chemical composition an analysis of the treated fluid to assess whether ultrasonic treatment affects the base emulsion concentration or stability in addition to removing tramp oils and solid contaminants.

Changes in electrical resistance also indicated alterations in the composition of the liquid medium. Previous studies have demonstrated the applicability of electrical resistance as an indirect parameter for monitoring the contamination level of metalworking fluids [16]. However, this parameter depends not only on contaminant content but also on emulsion concentration, temperature, water content, dissolved salts, and ageing products. Therefore, electrical resistance should be used as part of a comprehensive assessment of the condition of the metalworking fluid rather than as the sole indicator of purification efficiency.

3.4. Influence of Frequency, Treatment Duration, and Liquid Volume

A comparison of frequencies of 25, 28, and 40 kHz showed that the most pronounced treatment effect under the investigated conditions was achieved at 28 kHz. At 25 kHz, the ultrasonic effect was less uniform, whereas increasing the frequency to 40 kHz did not further improve the overall set of monitored parameters. Based on the results obtained, the combination of a frequency of 28 kHz, a power of 100 W, and a treatment duration of 5 min was identified as the most effective treatment condition [8].

This finding does not imply that 28 kHz is a universally optimal frequency for all liquids and ultrasonic systems. The most effective operating conditions depend on the composition of the metalworking fluid, liquid volume, vessel material and geometry, transducer position, and acoustic pressure distribution. The established parameters apply to the investigated system and should be refined whenever the treatment conditions are changed.

Increasing the treatment duration beyond 5 min did not result in a proportional improvement in treatment performance. Longer treatment increased fluid heating, whereas further changes in the monitored parameters were insignificant. Furthermore, excessive ultrasonic exposure may disrupt the contaminant agglomerates already formed and redistribute the particles throughout the liquid volume.

The liquid volume also affected the treatment outcome. As the volume increased, the same power was distributed over a larger quantity of the treated medium, thereby reducing the energy input per unit volume. At the same time, the liquid-column height, distance from the reflecting boundaries, and positions of regions of elevated acoustic pressure changed. Therefore, treatment results obtained using different liquid volumes cannot be compared without considering vessel geometry and specific energy input [3, 5].

3.5. Comparison of Experimental Results with the Theoretical Considerations

The results obtained confirm the principal conclusion of this review: process vessel material is one of the factors determining the effectiveness of ultrasonic treatment. Its influence is manifested through wave reflection,

transmission, and absorption; damping of mechanical vibrations; formation of standing waves; and changes in the spatial distribution of acoustic pressure.

Under identical treatment conditions, more intense cavitation and thermal effects were observed in the glass vessels, together with more pronounced changes in density and Brix value. This finding is consistent with the lower internal mechanical energy losses in glass compared with polypropylene.

At the same time, the experimental data do not allow the isolated contribution of the wall material to be quantified because the vessels may have differed not only in material but also in wall thickness, stiffness, dimensions, and mounting conditions. Furthermore, acoustic pressure was not measured directly during the experiments. Therefore, the explanation of the observed differences in terms of wave reflection and absorption should be regarded as a physically substantiated interpretation that requires further quantitative verification. For scientifically rigorous comparison of vessel materials, further experiments should be performed using vessels with identical geometry, dimensions, and comparable wall thicknesses. Maintaining these parameters constant would minimize the influence of vessel design and allow the effect of the wall material on ultrasonic treatment to be assessed more accurately.

To clarify the relationships identified, comparative studies should be conducted using vessels of identical geometry and comparable wall thickness. This approach would distinguish the influence of material from that of vessel geometry and establish requirements for selecting process vessels for laboratory and industrial ultrasonic systems.

Thus, the results of ultrasonic treatment of the metalworking fluid in glass and polypropylene vessels are consistent with the theoretical relationships considered. Under the investigated conditions, the glass vessel provided a more pronounced ultrasonic effect on the fluid. Nevertheless, the material should be selected with consideration of the entire transducer–liquid–process vessel system, and results obtained using a particular experimental system should not be generalised to other treatment conditions without additional verification.

Conclusions

The review demonstrated that process vessel material is a significant parameter in the ultrasonic treatment of metalworking fluids. The vessel walls participate in the reflection, transmission, absorption, and scattering of ultrasonic waves, thereby affecting acoustic pressure distribution, standing-wave formation, cavitation intensity, acoustic streaming patterns, and liquid heating.

The interaction of ultrasonic waves with the vessel walls is governed by the specific acoustic impedance, density, stiffness, and mechanical energy absorption capacity of the material. Wall thickness and geometry, vessel dimensions, liquid volume, transducer position, and the method of ultrasonic energy transmission also exert a substantial influence. Therefore, material properties cannot be considered independently of the design of the entire system.

A comparison of the materials showed that the high stiffness, chemical resistance, and transparency of glass make it suitable for laboratory investigations and the observation of physical processes. Polymeric materials have lower stiffness and a greater capacity to damp mechanical vibrations; therefore, some of the supplied energy may be dissipated within their walls. Stainless steel offers high strength and is suitable for industrial equipment; however, the resulting acoustic field depends on the thickness of the metal walls and the method used to mount the transducers. Thus, no material can be regarded as universally optimal. Material selection should be based on the intended application of the system, the properties of the treated liquid, and the required treatment conditions.

The results of the ultrasonic treatment of the metalworking fluid confirmed the theoretical considerations presented in this review. Under identical treatment conditions, the glass vessels exhibited more intense cavitation and thermal effects and more pronounced changes in density and Brix value than the polypropylene vessels. Under the investigated conditions, the most effective combination comprised a frequency of 28 kHz, a power of 100 W, and a treatment duration of 5 min. These values apply to the experimental system employed and should not be extrapolated to other liquids or equipment designs without additional verification.

Based on the analysis, the following conclusions were drawn:

1. The process vessel is an integral component of the acoustic system and directly contributes to the formation of the ultrasonic field within the treated liquid.

2. The influence of vessel wall material is manifested through wave reflection, transmission, absorption, and scattering; damping of mechanical vibrations; and changes in the spatial distribution of acoustic pressure.

3. The effectiveness of ultrasonic treatment is determined by the combined effects of wall material, thickness, and geometry; liquid volume; transducer position; frequency; power; and treatment duration.

4. Under the investigated operating conditions, glass vessels produced a more pronounced ultrasonic effect on the metalworking fluid than polypropylene vessels.

5. Transparent glass vessels are suitable for laboratory investigations because they allow cavitation and contaminant separation to be observed. For industrial applications, vessel selection should take into account wall thickness and the method of ultrasonic energy transmission.

6. Quantitative confirmation of the influence of vessel material requires comparative studies using vessels of identical geometry and comparable wall thickness, supplemented by measurements of acoustic pressure and the spatial distribution of cavitation activity.

The results confirm that process vessel material must be considered when selecting ultrasonic treatment conditions and designing equipment for the regeneration of process fluids.

Acknowledgments

This research is funded by the Science Committee of the Ministry of Education and Science of the Republic of Kazakhstan (Grant No. AP25794035)

References

[1] Manickam S., Camilla Boffito D., Flores E.M.M., Lévêque J.-M., Pflieger R., Pollet B.G., Ashokkumar M. Ultrasonics and sonochemistry: Editors' perspective //Ultrasonics Sonochemistry, 2023. Vol. 99. Article 106540. https://doi.org/10.1016/j.ultsonch.2023.106540.

[2] Meroni D., Djellabi R., Ashokkumar M., Bianchi C.L., Boffito D.C. Sonoprocessing: From concepts to large-scale reactors //Chemical Reviews, 2022. Vol. 122, No. 3. P. 3219–3258. https://doi.org/10.1021/acs.chemrev.1c00438.

[3] Adamou P., Harkou E., Villa A., Constantinou A., Dimitratos N. Ultrasonic reactor set-ups and applications: A review //Ultrasonics Sonochemistry, 2024. Vol. 107. Article 106925. https://doi.org/10.1016/j.ultsonch.2024.106925.

[4] Hodnett M., Choi M.J., Zeqiri B. Towards a reference ultrasonic cavitation vessel. Part 1: Preliminary investigation of the acoustic field distribution in a 25 kHz cylindrical cell //Ultrasonics Sonochemistry, 2007. Vol. 14, No. 1. P. 29–40. https://doi.org/10.1016/j.ultsonch.2006.01.003.

[5] Khavari M., Priyadarshi A., Subroto T. et al. Scale up design study on process vessel dimensions for ultrasonic processing of water and liquid aluminium //Ultrasonics Sonochemistry, 2021. Vol. 76. Article 105647. https://doi.org/10.1016/j.ultsonch.2021.105647.

[6] Na I., Son Y. Sonochemical oxidation activity in 20-kHz probe-type sonicator systems: The effects of probe positions and vessel sizes //Ultrasonics Sonochemistry, 2024. Vol. 108. Article 106959. https://doi.org/10.1016/j.ultsonch.2024.106959.

[7] Van Kien N., Jeong Y.H., Kim S., Ryoo J.J. How well ultrasonic waves penetrate glass, SS, and plastics? //Ultrasonics Sonochemistry , 2025. Vol. 115. Article 107308. https://doi.org/10.1016/j.ultsonch.2025.107308.

[8] Kim A., Kadyrov A., Sinelnikov K., Sherov K., Yurchenko V. The method of cleaning cutting fluid using ultrasonic treatment //Applied Mechanics, 2025. Vol. 6, No. 4. Article 83. https://doi.org/10.3390/applmech604008

[9] Leighton T.G. The Acoustic Bubble. London: Academic Press, 1994. 613 p. https://doi.org/10.1016/B978-0-12-441920-9.X5001-9.

[10] Wu J. Acoustic Streaming and Its Applications //Fluids, 2018. Vol. 3, No. 4. Article 108. https://doi.org/10.3390/fluids3040108.

[11] Hoo D.Y., Low Z.L., Low D.Y.S., Tang S.Y., Manickam S., Tan K.W., Ban Z.H. Ultrasonic cavitation: An effective cleaner and greener intensification technology in the extraction and surface modification of nanocellulose. //Ultrasonics Sonochemistry, 2022. Vol. 90. Article 106176. https://doi.org/10.1016/j.ultsonch.2022.106176.

[12] Niemczewski B. Observations of water cavitation intensity under practical ultrasonic cleaning conditions. //Ultrasonics Sonochemistry, 2007. Vol. 14, No. 1. P. 13–18. https://doi.org/10.1016/j.ultsonch.2005.11.009.

[13] Garrett S.L. Reflection, Transmission, and Refraction. In: *Understanding Acoustics*. Graduate Texts in Physics. Cham: Springer, 2020. P. 513–542. https://doi.org/10.1007/978-3-030-44787-8_11.

[14] Interface Conditions, Reflection and Refraction of Plane Waves. In: Mechel F.P., ed. *Formulas of Acoustics*. Berlin, Heidelberg: Springer, 2008. P. 1139–1140. https://doi.org/10.1007/978-3-540-76833-3_294.

[15] Jo M., Kim M. Analysis of the distribution of the ultrasonic field transmitted into a solid cylinder from the outside. //The Journal of the Acoustical Society of Korea, 2025. Vol. 44, No. 2. P. 126–131. https://doi.org/10.7776/ASK.2025.44.2.126.

[16] Kim A., Petronienė J. J., Dzedzickis A., Bučinskas V. Development of methodology for monitoring of metalworking fluids quality //Journal of Measurements in Engineering, Vol. 13, No. 4, 14, 2025, https://doi.org/10.21595/jme.2025.24875.

Information of the authors

Kim Anna Stanislavovna, PhD, associate professor, Abylkas Saginov Karaganda Technical University
e-mail: a.kim@ktu.edu.kz

Kadyrov Adil Suratovich, d.t.s., professor, Abylkas Saginov Karaganda Technical University
e-mail: adil.suratovich@gmail.com

DOI 10.52209/2706-977X_2026_3_105 IRSTI 55.47.07 UDC 629.73.02

Finite Element Analysis and J-integral of Repair Using Isotropic Bonded Patches on a Cracked Perforated Plate in an Aircraft Wing

Berkane I. *, **Labed Z.**
University of Brothers Mentouri Constantine1, Constantine, Algeria
*corresponding author

Abstract. Geometric discontinuities and microstructural defects can generate localized stress concentrations and promote crack propagation in aeronautical structures. This study numerically and analytically investigates the mechanical behavior of an isotropic cracked aluminum plate containing a central circular hole, with particular emphasis on the effectiveness of bonded isotropic patch repair. A finite element model was developed in ABAQUS to evaluate the stress intensity factor (SIF) and J-integral for cracked perforated plates subjected to uniaxial tensile loading. The numerical results were compared with analytical solutions for different crack lengths and diameter-to-width ratios (d/W), providing a validation of the finite element model. The results show that the bonded patch reduces the stress intensity factor by approximately 35% ± 2% and the J-integral by approximately 40% compared with the unrepaired configuration, demonstrating its effectiveness in reducing stress concentration near the crack tip. The analysis also shows that increasing the crack length and the d/W ratio leads to higher SIF and J-integral values, while the effectiveness of the patch decreases for larger hole-to-plate width ratios. These findings demonstrate the potential of bonded isotropic patches as a local repair technique for damaged aeronautical structures and highlight the importance of accounting for crack geometry and structural discontinuities in repair design. The conclusions are based exclusively on analytical and numerical analyses under linear elastic isotropic assumptions and should therefore be further investigated for fatigue loading, composite materials, and more complex service conditions.

Keywords: patch; FEM; sif; j-integral; hole plate; crack.

Introduction

In the regulation of aeronautical structural mechanics, the durability and safety of aircraft structural components are of paramount importance because the elements are subjected to repeated aerodynamic and structural loads. This is particularly true for the thin metal skin of the aircraft, which provides resistance to mechanical loads, where each takeoff and landing phase causes repeated cycles of stress, leading to progressive fatigue, damaging and weakening the structure. Cracks formed in damaged structures are therefore a constant concern for maintenance managers, as they can jeopardize operational safety and lead to a deterioration in the service life of critical components. The mechanical behavior of fractured structures fixed using bonded patches is investigated in this work, a method used in the aerospace industry to reduce stress and restore mechanical strength. The stress intensity factor (SIF) is the only metric utilized to answer this issue by specifying the stress field around the fracture tip. It is also used alongside the J-term to calculate the propagation and stability of fractures in elastic substances. As a result, the FEM (Finite Element approach) reference refers to the finite element method for modeling the mechanical behavior of damaged and restored structures.

To date, several studies have explored different modeling methods for predicting crack propagation and evaluating associated parameters. In one such study, Souiyah et al. [1] used the finite element approach to forecast crack propagation directions and assess SIFs, and the results have been confirmed using analytical and numerical data. The key variable at the heart of this work is the stress intensity factor (SIF). This can be described by displacement, tension, Strain occurs in the near field of a crack in a linear elastic solid [2]. Many other researchers have studied different quantities such as the evaluation the J-integral by [3,4] and the energy release rate (or energy release ratio) according to [3,5] or the concentration factor calculated by [3,6,7]. Each offers a complementary angle to provide insights into crack behavior. For their part, Fekih et al. [8] examined the impact of patch shape on durability and dependability of the repair and showed that star-shaped patches are the most effective at reducing the J-integral.

Several studies have examined the influence of bonded patches on the fracture behavior and durability of cracked metal structures. Mahadesh Kumar et al. [9] compared four different patch geometries square, rectangular, circular, and elliptical and demonstrated that the rectangular geometry, with its maximum length parallel to the crack, resulted in the greatest reduction in the crack intensity factor (SIF). The authors also suggested modifying the patch design by extending the reinforcement zone, proposing an angled patch that saves 28% of material for a given SIF value, or reduces the SIF by 10% for a given amount of material. Furthermore, El-Sagheer et al. [10] studied the effectiveness of glass-fiber-reinforced polymer (GFRP) composite patches for repairing inclined cracks, while Baghdadi Mohammed et al. [11] used a finite element method to investigate the effect of the composite patch's shape on repair performance. Finally, Safa Chahrazad Djebbar et al. [12] evaluated the influence of patch geometry on the material's

overall reactivity in a 2024-T3 aluminum structure with a central circular notch. Despite these advances, research dedicated to cross-validation between analytical and numerical solutions remains limited, even though such an approach is essential for evaluating the reliability of finite element models and for drawing more comprehensive conclusions regarding the failure behavior of complex aerospace structures, such as wing ribs or spars.

We want to address this gap by applying the finite element technique (FEM) to investigate the factors that impact the intensity of stresses around the margins of holes in isotropic rectangular plates., with and without patches, while comparing the numerical results with those obtained analytically. The main research questions are as follows: QR1—How does the aspect ratio (d/W) influence the distribution of SIF and the J-integral? QR2—To what extent does the presence of a bonded patch reduce these critical parameters? QR3—How well do the FEM results agree with the analytical solutions under identical loading conditions?

In this regard, this article contributes in three ways: (i) It offers a thorough comparison of the stress intensity factor and the J-integral in analytical and numerical models., (ii) it offers a parametric analysis of the effects of d/W on stress reduction, and finally, (iii) it methodically validates the suitability of FEM for modeling cracked and repaired aeronautical structures. While Section 2 provides information on the methodology and geometric models, Section 3 explains the analytical and numerical results, and Section 4 discusses the practical implications, limitations, and prospects of this study.

1. Methodology and geometric models

The geometrical discontinuity in the rib of an aircraft wing provides a concentration of loads and destroys structures, which causes cracks to occur. To explore the stress intensity factor and J-integral surrounding an aircraft wing using the finite element method, we considered an isotropic rectangular perforated plate (aluminum alloy) as a test piece. The cracking effect on the perforated plate generates stress intensity factors in the presence of the hole, which are then used to obtain the various parameters. For our research, we used isotropic plates of limited width w with a hole removed from a wing rib.The plate's dimensions are 100 mm long, 50 mm wide, and 1 mm thick. The panel has a [2-10] mm fracture near the margin of the hole. The panel was exposed to 1 MPa of unidirectional tensile force. This was accomplished by increasing the diameter-width ratio (d/W) from 0.05 to 0.3.

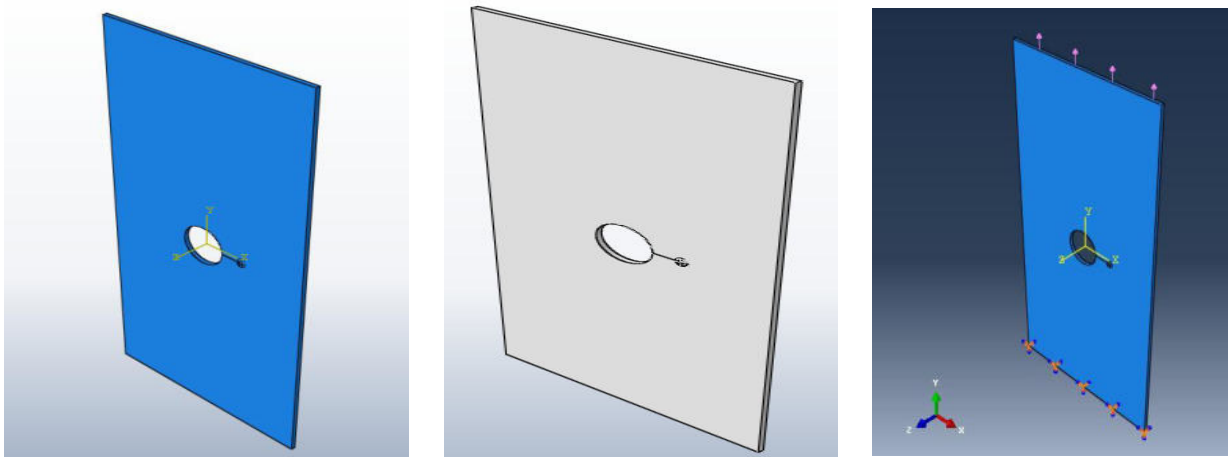

Fig. 1. - Geometric models of a perforated plate with a crack on the edge without a patch

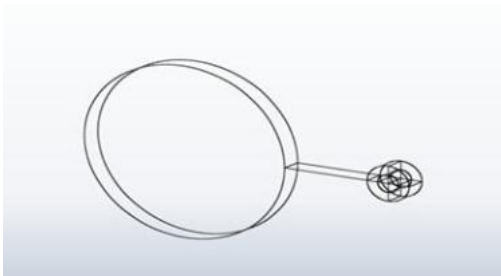

Fig. 2. - Geometric model of a perforated circular plate with an edge crack

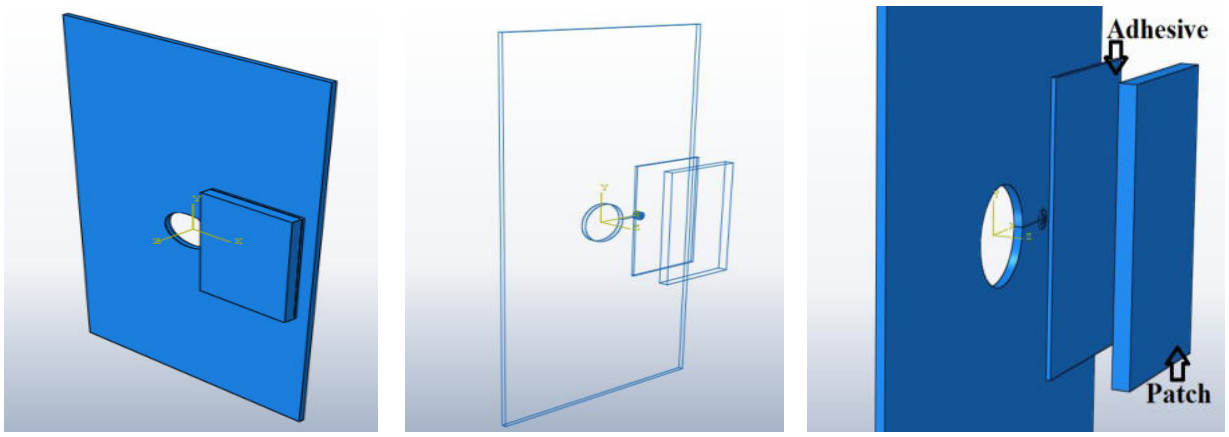

Fig. 3. - Geometric models of a perforated plate with a crack on the edge with patch.

to For an isotropic material exhibiting linear elastic behavior, the stress field around a crack in a linear elastic body is described by the stress intensity factor (SIF). The SIF depends on the crack's type, loading level, and geometry. According reference [13], this parameter can be determined for a crack that originates from a hole in an infinite body:

$$K_I = f\left(\frac{a}{r}\right)\sigma\sqrt{\pi a} \tag{1}$$

where σ - stress (MPa)
a - crack length (mm)
f - Geometric correction factor
K_I- MPa$\sqrt{\text{mm}}$

It is generally known that in mechanics of linear elastic fracture, the rate of energy restitution J is equal to the integral J's value and has the following connection with the stress intensity factor K_I:

$$K_I = \sqrt{JE} \tag{2}$$

$$J = \frac{K_I^2}{E'} \tag{3}$$

With:

$$E' = \frac{E}{1-\mu^2} \tag{4}$$

where E - modulus of elasticity MPa
μ - Poisson's ratio
K_I - MPa$\sqrt{\text{mm}}$
J - MPa. mm

The normalized stress intensity factor (SIF) and normalized J-integral vary, as determined by the ratio of the repaired structure's SIF and J-integral to those of the unrepaired structure along the crack face. The normalized J-integral is computed using the following equation :

$$K_{I\,normalized} = \frac{K_{I\,Patch}}{K_{I\,not\,Patch}} \tag{5}$$

$$J_{normalised} = \frac{J_{Patch}}{J_{not\,Patch}} \tag{6}$$

.

2. Materials

The aluminum alloy has a Poisson's ratio of 0.33 and a Young's modulus of 68.8 GPa. The patch, whose mechanical properties are listed in Table 1, measures 30 mm in height, 20 mm in width, and 5 mm in thickness. It is fully bonded to the damaged area with Glue FM 73 adhesive. The adhesive has a Poisson's ratio of 0.33 and a coefficient of elasticity of 1.83 GPa. The adhesive is 30 mm high, 20 mm wide, and 0.3 mm thick.

Table 1. Mechanical properties [14,15].

Material	Plate with hole	Patch	Adhesive
Young's modulus (MPa)	68800	68000	1830
Poisson's ratio	0.3	0.3	0.33

3. Finite element modelling

In numerical calculations that use finite elements, selecting the right mesh is crucial for achieving a convergent solution with dependable results. The precision of these calculations is closely tied to the quality of the mesh. The stress intensity and J-integral factors for isotropic plates with circular holes were calculated using the finite element method. These results were checked against analytical equations to confirm their accuracy. In the second part of the study, the impact of patch effects on stress intensity factors and J-integrals was analyzed, both with and without the presence of a patch. Additionally, work conducted using the finite element method through ABAQUS software [16] was used to compare numerical results with analytical ones. It is known that areas with geometric irregularities near a cut have high stress gradients, so the mesh in these regions is made finer and small elements are used. Since the mesh is key to determining stress values or stress intensity factors, these values depend on the element type, the number of elements, and the boundary conditions. Figure 4 illustrates the mesh used. The 'C3D20R' element, which has 20 nodes, was selected because rectangular hexagonal elements are effective for computing stress intensity factors. The mesh is rectangular, generated by ABAQUS, and it is refined around the holes to reach a stable maximum stress value. Table 2 clearly shows the numerical validation of the stress intensity factor comparing the analytical method with different element types. The results indicate that the Hex mesh type provides better outcomes than other mesh types. To assess the speed of mesh convergence, the number of elements was varied (Table 3). The results for a medium and affine mesh were better than those for a standard mesh. This suggests that computation time is an important factor, and that as the number of elements increases, the stress intensity factor values decrease, with convergence achieved when the number of finite elements reaches 35268. This mesh setup provides satisfactory results and will be used in further examples.

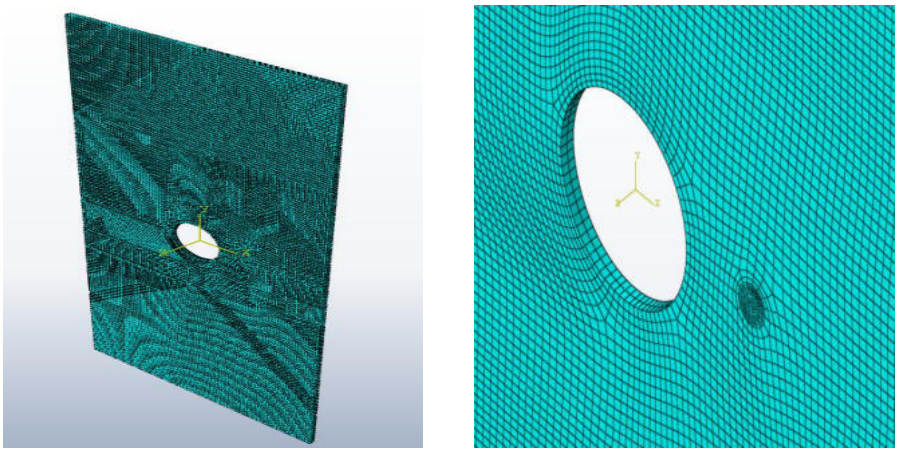

Fig. 4. - Finite element mesh of the perforated plate with an edge crack.

Table 2. Validation of calculations with mesh type

crack length mm	Stress intensity factors (analytic)	Stress intensity factors (FEM) MPa.mm$^{1/2}$		
	MPa.mm$^{1/2}$	Element Shape	Hex	Hex-dominated
		Mesh type	C3D20R	C3D20R
2	6.0913		6.071	6.231
4	6.9205		6.926	6.992
5	7.1958		7.196	7.262
7	7.7939		7.777	7.849
9	8.5768		8.543	8.622
10	9.061		9.043	9.125

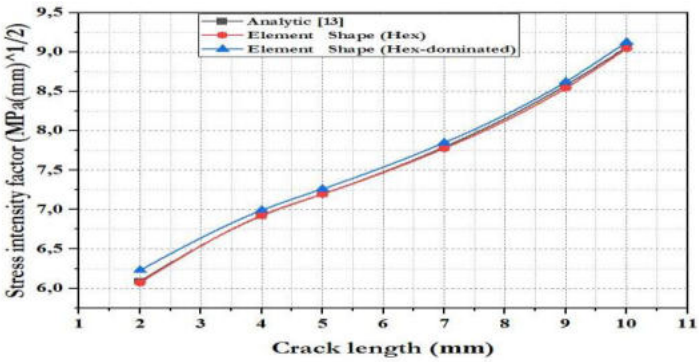

Fig. 5. - Analytical digital validation and mesh type

Table 3. Number of finite elements and type of element.

Element Shape	Mesh type	Number of nodes	Elements Number	Stress intensity factors (FEM)
Hex	C3D20R			
Normal mesh		69186	9698	7.615
Medium mesh		127604	22792	7.194
Refined mesh		196758	35268	7.196

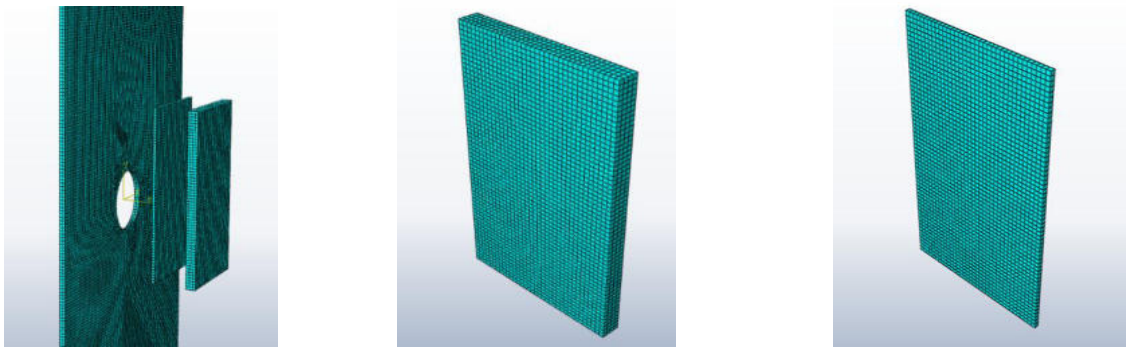

(a) (b) (c)

Fig. 6. - (a) Cracked plate (b) Patch (c) Adhesive

4. Results and discussion

4.1 Analysis of the stress intensity factor at the edge of a hole in a rectangular plate

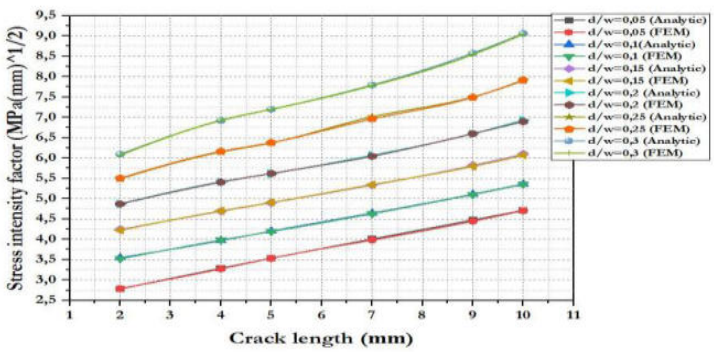

Fig. 7. - Analytical stress intensity factor and FEM as a function of crack width and d/w

We compared and presented the results from analytical methods and finite element method (FEM) regarding the stress intensity factor in a plate with a hole under tension, while applying specific boundary conditions. The results show that the stress intensity factor increases with fracture length, which aligns with the typical mechanical behavior observed in such scenarios. since a longer crack generates greater stress concentration at its tip, favoring crack propagation. Similarly, a higher d/W ratio, indicating a more centered crack, generates a higher stress intensity. The comparative graph between K_I values from analytical calculations and those obtained from FEM simulation (for three crack lengths: 2, 5 and 10 mm, and three d/W ratios: 0.05, 0.2 and 0.3) confirms these trends. Both approaches show good overall agreement, despite some deviations at the highest d/W values and for large cracks, where FEM provides slightly higher results. These differences are attributable to the simplifying assumptions of analytical methods (ideal geometry). This analysis therefore confirms the reliability of numerical simulations, which not only prove to be consistent with analytical results, but also more relevant in the precise modeling of the various fracture mechanics problems involved (complex configurations, uniform loading), while FEM enables geometric effects and real stress distributions to be better integrated.

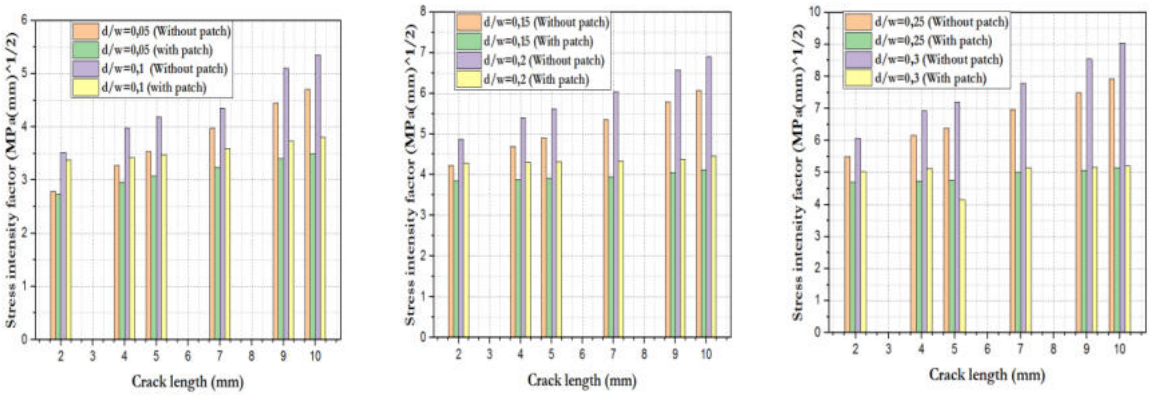

(a) (b) (c)

Fig. 8. - Variation du facteur d'intensité de contrainte analytique avec et sans patch en fonction de la longueur de la fissure et du rapport d/w

The findings indicate that the unrepaired plate experiences very high mechanical stresses, especially at the crack tip, while the patch significantly lowers these stresses. This occurs because the patch has an isotropic, absorbing, and dissipative property that helps spread out the stress concentration, thereby reducing the rate at which the crack spreads over time. Figures (8a), (8b) and (8c) provide an illustration of this, since for d/W values in the ranges [0.05-0.1], [0.15-0.2] and [0.25-0.3] respectively, the K_I factor remaining below 4, 4.5 and 5.5 MPa $(mm)^{1/2}$ respectively, replaces 5, 6.5 and 9 MPa $(mm)^{1/2}$ in the case of plate repair, the latter being subject to the same d/W ratio. These results clearly demonstrate, on the one hand, the patch's overall favorable impact, and on the other, the increasingly preponderant d/W ratio: the higher the ratio, the greater the stress concentration, particularly for long cracks. Thus, the highest K_I peaks are reached at d/W = 0.25 and 0.30, reflecting the fact that large openings are more prone to fracture. However, it is in these critical cases that the patch plays its role most effectively, enabling K_I to be significantly reduced. In conclusion, this analysis shows the importance of controlling geometric parameters (hole size, crack length) and using local reinforcements such as isotropic patches to limit stress concentrations and improve the durability of cracked structures.

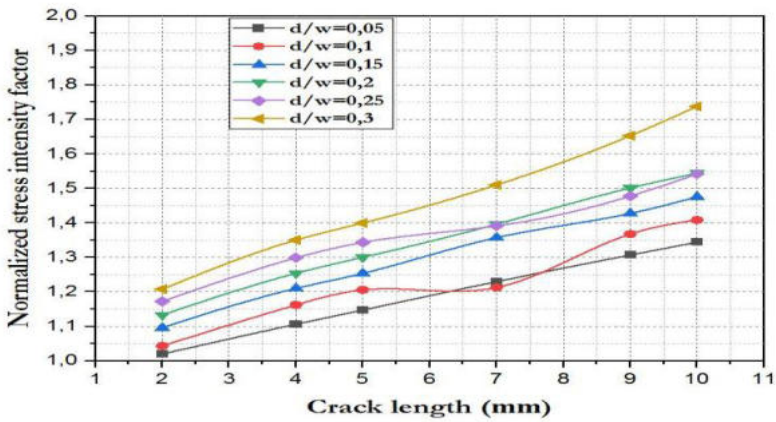

Fig. 9. - Variation of normalized stress intensity factor as a function of crack length and d/w

Based on results for cracked, repaired, and unrepaired hole plates, the study aims to analyze the variation of the normalized stress intensity factor as a function of diameter/width ratio (d/W) and crack length. It is evident that the normalized intensity factor significantly decreases for repaired plates, reaching a maximum value of less than 1.75, indicating greater resistance to crack spall propagation than for unrepaired, cracked plates, and thus establishing the validity and reliability of a finite element model. This can be seen in the representative graph, which highlights the combined effect of geometry and cracking on stress concentration: for all the configurations considered in this study, the value of the intensity factor increases progressively with increasing crack length, in line with fracture mechanics. Nevertheless, this growth becomes significantly more significant when the d/W ratio is at its highest, testifying to the heightened vulnerability of open structures with large openings. Thus, plates with a low d/W=0.05 ratio are subject to the lowest values presented for the factor, while the most critical are found with d/W = 0.3, particularly for long cracks where normalization goes beyond 1.8. This form of curve hierarchy is a reminder of the very strong interaction between geometry and cracking: the larger the hole, the more it favours the effects of stress concentrations generated around cracks. For this reason, it is essential in structural design to minimize openings in order to reduce stress concentrations and slow crack initiation or propagation, particularly in areas sensitive to fatigue or cyclic loading.

5.2. Analysis of the J- integral at the edge of a hole in a rectangular plate

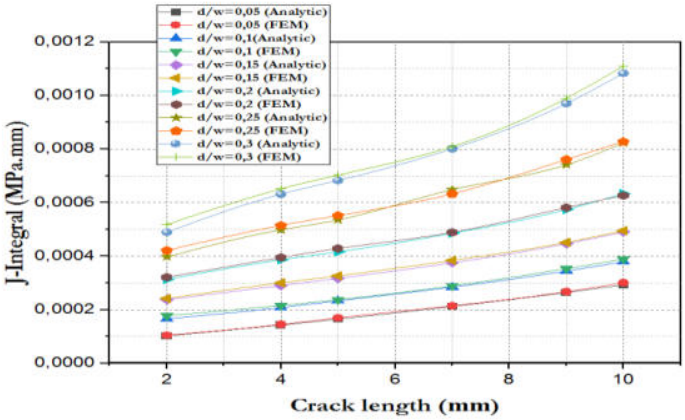

Fig. 10. - Variation of the analytical J-integral and MEF as a function of crack length and d/w

In this section of the paper, we have analyzed the results of the finite element method (FEM) on the evolution of the J-integral during tensile stress on a drilled plate under imposed boundary conditions. The part studied concerned the joint behavior of crack length and geometric diameter/width ratio (d/W) on the value of the J- integral, indicating that these two parameters were decisive for the mechanical behavior of the structure. The J-integral was found to increase progressively as the crack lengthened, reflecting an increase in the energy available for crack propagation in accordance with fracture mechanics. This trend is all the more marked the higher the d/W ratio, both for d/W ratios of 0.25 and 0.3, confirming the aggravating role of a wide opening on plate brittleness. Initial conclusions drawn from the J-integral distributions point to a relationship between this magnitude and the geometric parameters tested. The comparative graph shows good agreement between the analytical and numerical methods, even if the results provided by the FEM method are slightly superior, particularly for long cracks. This slight overestimation by FEM is precisely due to its finer integration of local effects and geometric shapes, which can be overlooked by analytical methods, all the more justifying the use of numerical simulations in critical cases where it is important to accurately assess the risk of failure. The non-linearity of the curves in fact testifies to acceleration in crack propagation above a critical size. All in all, this study shows that simultaneous increases in crack length and d/W ratio lead to a significant rise in the J-integral, and hence in fracture energy, and underscores the need for numerical models to ensure the proper behavior of perforated structures subjected to high stresses.

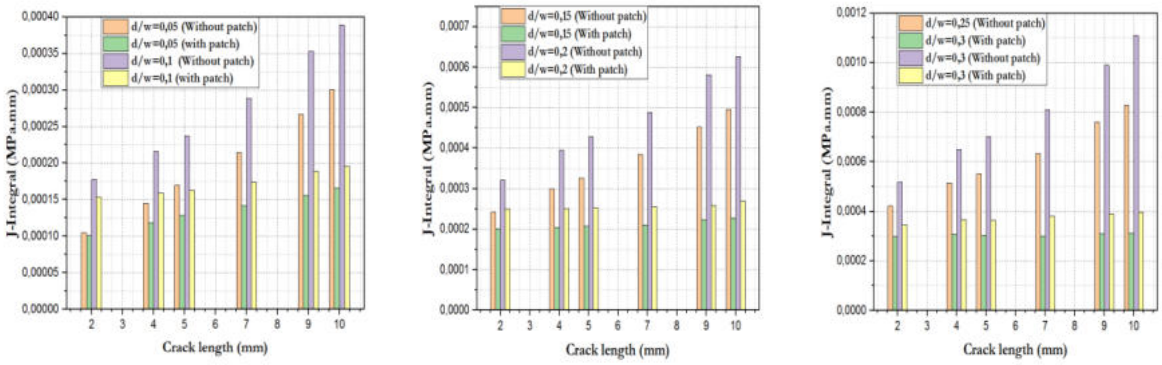

(a) (b) (c)

Fig. 11. - J-integral with and without patch as a function of crack length and d/w

Figures (11a), (11b), and (11c) show the variation of the J-integral as a function of fracture length for various diameter/width ratios (d/W), comparing the situations of mended and unrepaired plates. Generally speaking, the results show that the J-integral increases with crack growth, reflecting a rise in the energy required for propagation and thus an increase in the risk of failure. For low d/W ratios between [0.05 and 0.1] (Fig. 11a), the J-integral remains relatively low, not exceeding 0.00020 MPa-mm for the repaired plate, while it reaches over 0.00035 MPa-mm for the unrepaired plate, underlining the marked effectiveness of the patch at these dimensions. For intermediate ratios [0.15-0.2] (Fig. 11b), the J-integral remains below 0.0003 MPa-mm in the repaired cases, compared with over 0.0006 MPa-mm for the unrepaired plates, indicating a still significant, if slightly attenuated, stress reduction. Finally, for the highest ratios [0.25-0.3] (Figure 11c), values reach 0.0004 MPa-mm for repaired plates and up to 0.0010 MPa-mm for unrepaired plates, revealing critical structural behavior. The protective effect of the patch, while still present, becomes less effective as the hole size increases. The results show that the lower the d/W ratio, the more effective patch repair is in reducing stress concentrations and crack opening rates. On the other hand, when the opening is larger, patch repair, although still useful, remains insufficient to restore the mechanical integrity of the structure. This behavior clearly shows that the initial geometry of the defect is decisive and that bonded repairs have their limits in the critical configurations studied.

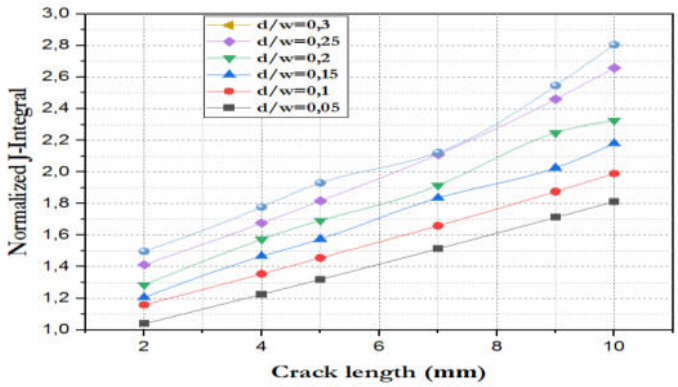

Fig. 12. - The normalized J-integral as a function of crack length and d/w

Figure 12 presents the normalized J-integral's fluctuation with fracture length and diameter/width ratio (d/W), for repaired and unrepaired cracked plates. The results show a continuous rise in the normalized J-integral with crack elongation, reflecting increasing stress concentration in the vicinity of the defect. This tendency is present for all configurations, but is all the more marked when the d/W ratio is high. Indeed, for low values of d/W (0.05 and 0.1), the rise in the integral remains moderate, as mechanical behavior is much more stable and resistance to crack propagation is more robust. On the other hand, for higher ratios (0.25 and 0.3), the normalized J-integral rises more rapidly, exceeding significant values of 2.5 for the largest cracks, indicating a risk of fracture. Plates with numerous openings are therefore clearly more fragile in the face of crack evolution, even when repaired. This graph, too, shows the amplifying effect of the d/W ratio on the mechanical response of the structure, and the importance of controlling the geometry of the openings. The clear ordering of the curves in relation to d/W shows the predominant role of this criterion in the intensity of stresses at the end of the embedding. Basically, this analysis illustrates the imperative need to control the size of geometric defects or resort to reliable reinforcement solutions in order to optimize the fracture resistance of cracked plates under mechanical loads.

Conclusion

This research has enhanced the understanding of how damaged aeronautical structures, especially cracked aluminum plates reinforced with isotropic adhesive patches, behave mechanically. A thorough investigation was conducted using a combination of analytical methods and the finite element method (FEM) to examine how the stress intensity factor (SIF) and the J-integral change under various geometric and mechanical setups. The findings indicate that when a small crack is situated close to the edge of a hole experiencing mechanical stress, it acts as a significant source of stress concentration, promoting crack growth and ultimately affecting the structure's durability over time. The comparison between the analytical and numerical solutions validated the relevance of the simulation framework based on an FEM model. The model used, including a C3D20R mesh, well-defined boundary conditions, and local refinement around the crack, achieved good consistency with the theoretical results, thus demonstrating the suitability of the numerical approach for handling cases that are more complex than those targeted by conventional analytical models. A key finding of this study is undoubtedly the demonstration of the effectiveness of an isotropic patch bonded to the crack level. This repair technique is capable of reducing the SIF and the J-integral, demonstrating its ability to reduce stress concentration in the vicinity of the injured region. It should be mentioned that the reduction is even more pronounced for a low or intermediate geometric ratio d/W, confirming that patches are more effective on small wings. On the other hand, when the d/W ratio is no longer low, the effectiveness of the patch decreases. This may encourage optimization of the dimensions and positioning of the reinforcement in order to maximize its beneficial effects.

Analysis of the normalized variations in the SIF (stress intensity factor) and the J-integral revealed The significance of crack geometry and opening for the mechanical response of the plate under stress. These two quantities increase more rapidly with crack length for large openings, revealing critical configurations that may compromise structural stability. Thus, the results offer a deeper comprehension of the local processes governing both fracture growth and healing efficacy.

In conclusion, this study, which highlights the benefits of combining numerical modeling and analytical analysis, proves fruitful in the field of crack propagation in complex aeronautical structures by highlighting the importance of local repairs using bonded patches in enhancing damage tolerance and structural safety, although the effectiveness of these repairs depends heavily on several factors, namely the geometry of the crack, the patch material's mechanical characteristics and the degree of adhesion between the surfaces.

Finally, our study also opens up new avenues for research by extending our investigation to composite materials subjected to multiaxial stress conditions, in the context of aging, fatigue, and real environmental conditions, which will yield results that, are more representative of the situations encountered in aeronautical operations.

In summary, this research provides a solid basis for optimizing repair strategies in aeronautical maintenance, both by offering powerful analysis tools and concrete solutions for designing more reliable, durable, and safer repaired structures, thereby improving the performance and longevity of contemporary aeronautical systems.

References

[1] Souiyah M., Alshoaibi A., Muchtar A., Ariffin A. K. Stress Intensity Factor Evaluation for Crack Emanating From Circular-Hole Using Finite Element Method //Int. Rev. Mech. Eng., vol. 2, no. 4, 2008.

[2] Anderson T. L. Fracture Mechanics - Fundamental and Applications. s.l. //CRC Press, 1995. doi.org/10.1201/9781420058215.

[3] Aabid A., Baig M., Hrairi M., Mohamed Ali J. S. Effect of fiber orientation-based composite lamina on mitigation of stress intensity factor for a repaired plate: a finite element study //Frat. ed Integrita Strutt., vol. 18, no. 68, 209–221, 2024, doi: 10.3221/IGF-ESIS.69.14

[4] Belhamiani M., Belhadri D. E., Oudad W., Mansouri O., Bouzitouna W. N. J integral computation and limit load analysis of bonded composite repair in cracked pipes under pressure //Frat. ed Integrita Strutt., vol. 13, no. 50, 623–637, 2019, doi: 10.3221/IGF-ESIS.50.53.

[5] Kwon Y. W., Hall B. L. Analyses of cracks in thick stiffened plates repaired with single-sided composite patch // Compos. Struct., vol. 119, no. November, 727–737, 2015, doi: 10.1016/j.compstruct.2014.09.052

[6] Papadopoulos G. A., Badalouka B., Souyiannis J. Experimental study of the reduction at crack-tip stress intensity factor KI by bonded patches //Int. J. Fract., vol. 149, no. 2, 199–205, 2008, doi: 10.1007/s10704-008-9240-4.

[7] Aabid A., Hrairi M., Mohammed Ali J. S., Abuzaid A. Stress concentration analysis of a composite patch on a hole in an isotropic plate //Int. J. Mech. Prod. Eng. Res. Dev., vol. 2018, no. Special Issue 249–255, 2018

[8] Fekih S. M., Albedah A., Benyahia F., Belhouari M., Bachir Bouiadjra B., Miloudi A. Optimisation of the sizes of bonded composite repair in aircraft structures //Mater. Des., vol. 41, no. 2012, 171–176, 2012, doi: 10.1016/j.matdes.2012.04.025

[9] Mahadesh Kumar A., Hakeem S. A. Optimum design of symmetric composite patch repair to centre cracked metallic sheet //Compos. Struct., vol. 49, no. 3, 285–292, 2000, doi: 10.1016/S0263-8223(00)00005-2

[10] El-Sagheer I., Taimour M., Mobtasem M., Abd-Elhady A. A., Sallam H. E. D. M Finite element analysis of the behavior of bonded composite patches repair in aircraft structures //Frat. ed Integrita Strutt., vol. 14, no. 54, 128–135, 2020, doi: 10.3221/IGF-ESIS.54.09

[11] Baghdadi M., Serier B., Salem M., Zaoui B., Kaddouri K. Modeling of a cracked and repaired Al 2024T3 aircraft plate: Effect of the composite patch shape on the repair performance //Frat. ed Integrita Strutt., vol. 13, no. 50, 68–85, 2019, doi: 10.3221/IGF-ESIS.50.08.

[12] Djebbar S. C., Kaddouri N., Elajrami M., Belhouari M., Madani K. Use of combined CZM and XFEM techniques for the patch shape performance analysis on the behavior of a 2024-T3 Aluminum structure reinforced with a composite patch // Frat. ed Integrita Strutt., vol. 16, no. 62304–325, 2022, doi: 10.3221/IGF-ESIS.62.22
[13] Sachs N. W., Metal fatigue //Plating and Surface Finishing, vol. 47, no. 12. 1991. doi: 10.1515/ijmr-1962530203.
[14] Hosseini-Toudeshky H., Mohammadi B., Daghyani H. R. Mixed-mode fracture analysis of aluminium repaired panels using composite patches //Compos. Sci. Technol., vol. 66, no. 2, pp. 188–198, 2006, doi: 10.1016/j.compscitech.2005.04.028.
[15] Madani K., Touzain S., Feaugas X., Cohendouz S., Ratwani M. Experimental and numerical study of repair techniques for panels with geometrical discontinuities //Comput. Mater. Sci., vol. 48, no. 1, 83–93, 2010, doi: 10.1016/j.commatsci.2009.12.005.
[16] Simulia, Dassault Systems. Abaqus softwar Version 6.13, 2013.

Information of the authors

Berkane Ishak, Ph.D. student, University of Brothers Mentouri Constantine 1
e-mail: ishak.berkane@doc.umc.edu.dz

Labed Zohra, PhD, professor, University of Brothers Mentouri Constantine 1
e-mail: zohra_labed@yahoo.fr

DOI 10.52209/2706-977X_2026_3_115 IRSTI 55.13.99 UDC 621.793.7

Influence of Yttrium Content and Its Application Methods on the Thermal Coefficient of Linear Expansion of KNA 82 Alloy Sealing Coatings: Experimental Studies and Analytical Modeling

Fasol Y.O.*, Riabenko A. Y., Kubich V.I
National University Zaporizhzhia Polytechnic, Zaporizhzhia, Ukraine
*corresponding author

Abstract. This study investigates the influence of yttrium content (0.1, 0.3, and 0.5 wt.%) and deposition methods on the coefficient of linear thermal expansion (CTE) of KNA-82 sealing coatings. Dilatometric measurements were conducted at 20–950°C, followed by regression analysis. The ion-plasma coating containing 0.3 wt.% yttrium exhibited stable thermal expansion behavior at 800–900°C and the highest linear regression fit (R^2 = 0.898). In contrast, the corresponding gas-flame coating showed a sharp decrease in CTE at 900°C and pronounced nonlinear behavior (R^2 = 0.039). The results suggest that ion-plasma coatings containing 0.3 wt.% yttrium have potential for high-temperature sealing applications. Further microstructural and thermal cycling investigations are required to confirm their long-term performance.

Keywords: sealing coatings, thermal expansion coefficient, yttrium, ion-plasma coating, thermal stability, gas turbine engines, KNA-82

Introduction

The current stage of global aero-engine development is characterized by intense competition in enhancing the energy efficiency and environmental safety of power units. A priority objective is the radical improvement in the efficiency of gas turbine engines (GTEs), which directly reduces specific fuel consumption and the carbon footprint [1]. One of the most critical factors determining the magnitude of losses along the turbine flow path is gas leakage through the radial gap between the rotor blade tips and the inner stator surface. It has been demonstrated that minimizing this gap is the most effective design approach to increase efficiency; however, this requires ensuring the stability of the sealing's geometric parameters throughout the entire engine life cycle. [2].

During GTE operation, complex transient modes arise from thermal expansion of components, centrifugal forces, and gyroscopic loads, leading to dynamic fluctuations in the gap magnitude. Under such conditions, there is a risk of direct mechanical contact (rubbing) between the rotor and the stator. To prevent emergency situations and protect expensive turbine blades, specialized sealing coatings are employed in modern practice [3]. These materials possess a unique architecture that allows them to readily abrade or deform upon contact with the blade (low cutting energy), thereby ensuring the formation of the smallest possible gap without damaging the rotor components.

However, the functioning of such coatings is complicated by several contradictory operational requirements [4, 5]. In addition to high abrasivity, the material must demonstrate exceptional erosion resistance to the impact of high-velocity gas flow saturated with fine abrasive particles. With the increase in gas temperature before the turbine to levels of 1150 °C and above, characteristic of new-generation engines, the problem of thermochemical stability comes to the forefront. Traditional nickel-graphite or nickel-aluminum systems, which are widely used at temperatures up to 900 °C, are unsuitable for extreme conditions.[6]. At temperatures exceeding 1100 °C, high-temperature gas corrosion processes are activated, leading to intensive formation of monoxides and complex spinel compounds. This results in "oxidation" of the coating surface, loss of its abradability properties, and premature failure due to erosive wear. To overcome these challenges, the development of new composite compositions alloyed with active elements is critically important, among which yttrium (Y) plays a key role. The introduction of yttrium into the coating system (e.g., a NiCrAlY-type coating) fundamentally alters the oxidation mechanism [7].

Yttrium promotes the segregation of a stable Al_2O_3 phase, which forms a dense, continuous oxide film with high adhesion to the substrate. This prevents oxygen diffusion into the coating and mitigates the negative effects of sulfur in the fuel, thereby ensuring material integrity during prolonged exposure at 1150 °C and above [8]. However, in addition to chemical stability, the coating's viability critically depends on its thermomechanical compatibility with the substrate material. In this context, determining and optimizing the coefficient of linear thermal expansion (CTE) is particularly relevant. Due to the porous structure and complex phase composition of Sealing coatings can have CTEs that differ significantly from those of the superalloys used to manufacture the stator casing [9].

Thermal expansion generates significant internal stresses at the "substrate-coating" interface during thermal cycles (take-off–flight–landing). This causes the development of microcracks, material fatigue, and ultimately results in complete delamination of the abradable layer. Thus, the development of novel heat-resistant Sealing coatings require a comprehensive approach that combines yttrium alloying for chemical protection with

precise control of thermophysical properties, particularly the Coefficient of Thermal Expansion (CTE), to ensure mechanical durability. Research into the influence of yttrium content on the structure, phase composition, and thermal expansion of abradable materials is a necessary step toward creating reliable radial-gap control systems for prospective aviation GTEs [10, 11]. The aim of this study is to investigate the influence of yttrium content (0.1, 0.3, and 0.5 wt.%) and coating deposition technology (gas-flame and ion-plasma spraying) on the temperature dependence of the coefficient of linear thermal expansion of KNA-82 sealing coatings. Particular attention is paid to identifying compositions exhibiting stable thermal expansion behavior in the high-temperature range of 800–900°C and evaluating the applicability of linear regression models to the obtained experimental data.

1. Research methodology

For the studies, KNA-82 coatings up to 5 mm thick were applied to cubic nickel alloy KhN78 T samples. The coating composition included a nickel base with additions of silicon (1.4-2.5%), aluminum (0.3-1.2%), boron nitride (7-13%), graphite (1.5-2.5%), and yttrium (0.1%, 0.3%, or 0.5%) [12-14]. The yttrium content was varied to 0.1-0.5%, as such concentrations promote the stabilization of oxide films, improve coating adhesion to the base material, enhance the thermal stability of alloys, and retard the coagulation of strengthening phases, thereby collectively improving operational characteristics. Coatings were applied by two methods: an ion-plasma method using a plasma installation with argon and nitrogen at a current of 400-450 A, a voltage of 40-50 V, and a surface distance of 100-120 mm; and a gas-flame method employing rod technology, oxygen (4.0-5.0 atm), acetylene (0.8-1.2 atm), and a surface distance of 80-100 mm. For plasma spraying, a mechanical mixture was prepared from powders of nickel (97.5-98.0%), silicon (2.0-2.5%), and urea (10%), which was mixed in a special mixer for 8 hours with the addition of yttrium. The mixture was annealed in a dissociated ammonia atmosphere at 950°C for 4-4.5 hours, followed by the addition of boron nitride, graphite, and aluminum. For gas-flame spraying, the powder mixture was combined with sodium silicate and formed into 4.5 mm-diameter, 400-600 mm-long rods. Before coating application, the samples were thoroughly prepared by cleaning with oil, emulsion, and dirt, degreasing in an etching bath, and blasting with electrocorundum to ensure adequate adhesion of the coating to the substrate.

The dynamics of volumetric changes and possible structural-phase transformations in the material of the developed coatings were analyzed using a Chevenard differential dilatometer (Fig. 1).

Fig. 1 – Photo of the Chevenard dilatometer setup

The maximum heating temperature in the dilatometer furnace was 1000°C. A Type K thermocouple was used for temperature measurement, in conjunction with a PED-250 electronic automatic potentiometer. The electronic differential head comprised a mechanical differential. The unit for measuring and recording the relative change in sample length allowed for direct recording of the length increment $\Delta l = l_x - l_{ref}$ onto a chart recorder. Samples for the studies were prepared with dimensions of 3.5 × 50 mm.

a

a - photo of real samples for testin

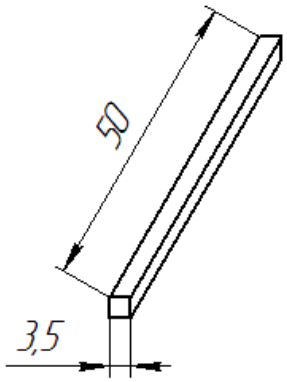

b

b – schematic of the sample for testing

Fig. 2 – Samples for investigating the coefficient of linear thermal expansion

Dilatometric curves were recorded under conditions of programmed uniform heating at a rate of 10-15°C/min within the temperature range of 20…950°C. The Chevenard dilatometer used an SN differential head, with magnifications Kx = 145.3 along the temperature axis and Ky = 319.25 along the ordinate axis. A "Piros" alloy sample was used as a reference, possessing known coefficients of linear thermal expansion across the entire temperature range and exhibiting no phase transformations. The true coefficient of linear thermal expansion was determined by graphical differentiation of the obtained curves using a mirror ruler, followed by calculation using the formula:

$$\alpha_{ex} = \alpha_r \pm \frac{K_1}{K_2} (\alpha_r - \alpha_q) \frac{dy}{dx}$$

where α_r - is the average expansion factor of the reference;

α_q - average expansion coefficient of quartz;

K_1, K_2 - optical magnification coefficients of the device along the X and Y coordinate axes;

dy, dx are the dimensions of the catheters in mm of a rectangular triangle on the dilatogram in the temperature range where α_{av} is calculated.

Processing of experimental data and construction of mathematical models were performed using the Python programming language with the libraries pandas (for data structuring and preprocessing), NumPy (for numerical operations), and scikit-learn (for implementing machine learning methods).

To model the dependence of the coefficient of linear thermal expansion (CTE) on temperature, a linear regression was used. Models were built separately for each yttrium content value (0.1; 0.3; 0.5%) and for each coating application method (gas-flame and ion-plasma), which allowed for obtaining a set of independent approximation dependencies within the investigated subsamples.

The quality of the constructed regression models was evaluated using the coefficient of determination (R^2), which measures the proportion of the variation in the dependent variable explained by the model. Formally, this indicator is defined as follows:

$$R^2 = 1 - \frac{\sum_{i=1}^{n}(y_i - \hat{y}_i)^2}{\sum_{i=1}^{n}(y_i - \bar{y})^2}$$

where y_i are the experimental values,

$\hat{y}_i$ are the values predicted by the model,

$\bar{y}$ is the mean value of the sample.

Since the temperature dependence of the coefficient of linear thermal expansion may exhibit nonlinear behavior, the coefficient of determination was used not only to evaluate the goodness of fit but also to identify coating compositions for which linear approximation is insufficient. Particular attention was paid to the gas-flame coating containing 0.3 wt.% yttrium, for which a pronounced decrease in CTE was observed at elevated temperatures. Such behavior requires separate consideration of possible nonlinear effects and the limitations of the selected regression model.

The coefficient of determination ranges from 0 to 1, with higher values indicating a better fit of the model to the experimental data. The use of this criterion enables an objective comparison of approximation quality across different coating compositions and their application technologies within a unified analytical framework.

2. Results and discussion

For gas-flame coatings of various compositions, characteristic features of the temperature dependence of CTE are observed.

The coating with 0.1% Y composition shows the largest difference in CTE values and extrema, with significant oxidation observed after the third heating, indicating insufficient thermal stability and low resistance to cyclic thermal loads.

The coating with 0.3% Y composition is characterized by a gradual increase in CTE from 5.04×10^{-6} K^{-1} at 100°C to maximum values in the 700-800°C range. A characteristic feature is the attainment of a maximum of approximately 14.49×10^{-6} K^{-1} at 800°C, followed by a sharp decrease to 3.45×10^{-6} K^{-1} at 900°C. Such a sharp decrease in CTE in the high-temperature region may indicate structural changes or phase transformations, potentially leading to additional internal stresses during operation under variable-temperature conditions.

The pronounced decrease in CTE from approximately 14.49×10^{-6} K^{-1} at 800°C to 3.45×10^{-6} K^{-1} at 900°C indicates a strongly nonlinear temperature dependence for the gas-flame coating containing 0.3 wt.% yttrium. This behavior explains the extremely low coefficient of determination ($R^2 = 0.039$) obtained using linear regression. Consequently, a simple linear model cannot adequately describe the thermal expansion behavior of this composition over the entire investigated temperature range.

The observed deviation may be associated with structural rearrangements, relaxation of internal stresses, or temperature-induced phase transformations. However, the available dilatometric data do not allow unambiguous identification of these mechanisms. Further microstructural and phase investigations are therefore required to clarify the origin of this behavior.

The coating with 0.5% Y composition demonstrates a monotonic increase in CTE from 4.97×10^{-6} K^{-1} at 100°C to a maximum value of 9.54×10^{-6} K^{-1} at 800°C, followed by an insignificant decrease to 8.98×10^{-6} K^{-1} at 900°C. The more stable CTE behavior at high temperatures and the absence of sharp extrema on the curve indicate greater thermal stability of the coating with 0.5% yttrium content, which is an advantage under cyclic thermal loads.

The CTE curves for gas-flame coatings with 0.3% and 0.5% Y compositions exhibit a similar pattern of change, which is attributed to the common nickel matrix of these materials. Such similarity in temperature dependencies indicates compatibility in the coatings' thermomechanical properties, an important factor in ensuring their operational reliability.

Research into ion-plasma coatings of the KNA-82 system with varying degrees of yttrium alloying showed significant differences in CTE characteristics compared to gas-flame coatings of similar composition.

The coating with a 0.1% Y composition exhibits the lowest CTE across the entire investigated range. The initial value is 5.0×10^{-6} K^{-1} (at 100 °C), with a gradual plateau in the 600–800 °C range at 9.1×10^{-6} K^{-1}. The presence of extrema indicates a high propensity for tensile stresses, which can lead to coating delamination during operation.

The coating with 0.3% Y composition, obtained by the ion-plasma method, is characterized by a stable increase in CTE from 5.7×10^{-6} K^{-1} to a maximum value of 14.49×10^{-6} K^{-1} at 800 °C. The most significant advantage of this composition is the stability of CTE values in the 800–900°C range, which minimizes stress gradients at engine operating temperatures. Such thermomechanical stability is critical for improving the coating's durability under cyclic thermal loads. The absence of abrupt changes in CTE within the temperature range of 800–900°C suggests relatively stable thermal expansion behavior of the ion-plasma coating containing 0.3 wt.% yttrium. This may be associated with the influence of the deposition process on the coating structure and the distribution of alloying elements. Nevertheless, dilatometric measurements alone cannot directly confirm the absence of microstructural degradation or phase transformations. Additional investigations using scanning electron microscopy (SEM) and X-ray diffraction (XRD) are required to establish the relationship between the coating microstructure, phase composition, and high-temperature thermal expansion behavior.

The coating with 0.5% Y composition, applied by the ion-plasma method, exhibits the highest CTE values in the medium-temperature range (up to 600 °C). The initial value is 6.9×10^{-6} K^{-1} (at 100 °C) A characteristic feature of this composition is the attainment of a maximum CTE of approximately 14.4×10^{-6} K^{-1} at 700–800°C, followed by a decrease to 13.0×10^{-6} K^{-1} at 900°C. This decrease may be associated with several competing mechanisms, including structural rearrangements, relaxation of internal stresses, phase transformations, and high-temperature oxidation. The presence of aluminum and yttrium in the coating composition may promote the formation of protective oxide phases, such as Al_2O_3 and Y_2O_3. However, the formation and relative contribution of these oxides were not directly investigated in the present study. Therefore, the observed reduction in CTE cannot be attributed exclusively to oxidation without additional chemical and phase analysis. The decrease in CTE at high temperatures is a potential risk factor, as it can lead to increased thermal stresses during cyclic temperature changes.

A comparative analysis of ion-plasma and gas-flame KNA-82 coatings with different yttrium contents revealed that the coating application method significantly influences the CTE characteristics and, consequently, the operational stability of the abradable layers.

The ion-plasma coating with a 0.3% Y composition exhibits the optimal CTE characteristics, ensuring a stable increase in the expansion coefficient across the entire temperature range without sharp extrema or jumps, indicating the structural stability of the material. It is fundamentally important that in the high-temperature region (800-900°C), where the aircraft engine operates, the CTE curve shows stable values. This minimizes the thermal stress gradient, significantly reducing the risk of delamination and cracking of the abradable layer.

In contrast to the gas-flame coating of similar composition (0.3% Y), which exhibits a sharp drop in CTE at 900°C, the ion-plasma coating shows more stable behavior at high temperatures, thereby enhancing its thermomechanical stability under cyclic thermal loads.

The coating with 0.5% yttrium content, applied by the ion-plasma method, although demonstrating high CTE values, shows a tendency for the expansion coefficient to decrease at 900°C. This may indicate oxidative processes and potential structural degradation during prolonged exposure at high temperatures.

Coatings with 0.1% yttrium content, whether applied by gas-flame or ion-plasma methods, exhibit the worst CTE characteristics and are least suitable for use under cyclic thermal loads.

The results of constructing linear regression models for the dependencies of CTE on temperature for gas-flame (y_1) and ion-plasma (y_2) coatings at different yttrium content values (0.1; 0.3; 0.5%) are presented in Fig. 3.

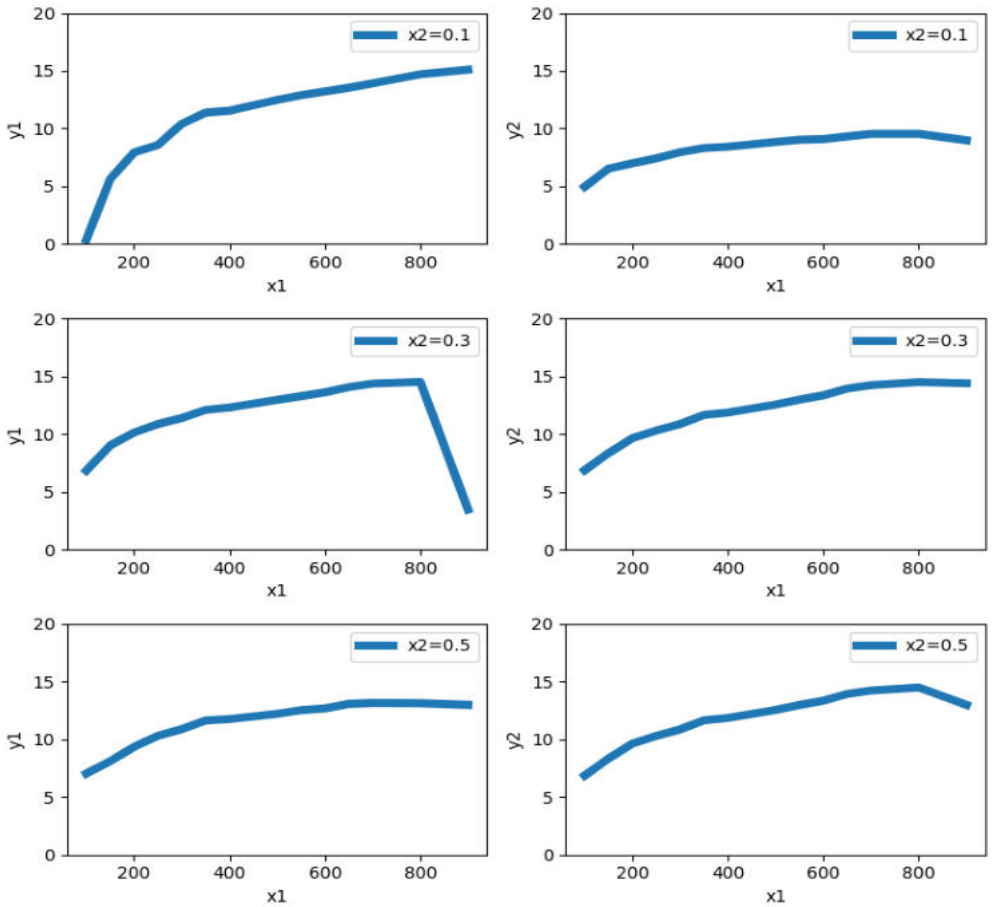

Fig.3 – Linear regression dependencies of CTE on temperature for gas-flame (y_1) and ion-plasma (y_2) coatings at different yttrium contents (0.1; 0.3; 0.5%)

Figure 3 illustrates the temperature dependence of CTE for gas-flame and ion-plasma coatings with different yttrium contents. The experimental curves demonstrate that both yttrium concentration and deposition technology affect the character of thermal expansion.

For the gas-flame coating containing 0.3 wt.% yttrium, a pronounced decrease in CTE at 900°C results in a substantial deviation from the linear trend. In contrast, the corresponding ion-plasma coating exhibits a gradual increase in CTE followed by relatively stable values in the high-temperature region. These differences are reflected in the coefficients of determination presented in Fig. 4.

It should be emphasized that the coefficient of determination characterizes the agreement between the experimental data and the selected regression model. A higher R^2 value does not independently demonstrate superior structural stability or operational durability.

A quantitative assessment of the quality of the constructed models, based on the coefficient of determination (R^2), is presented as a heatmap in Fig. 4.

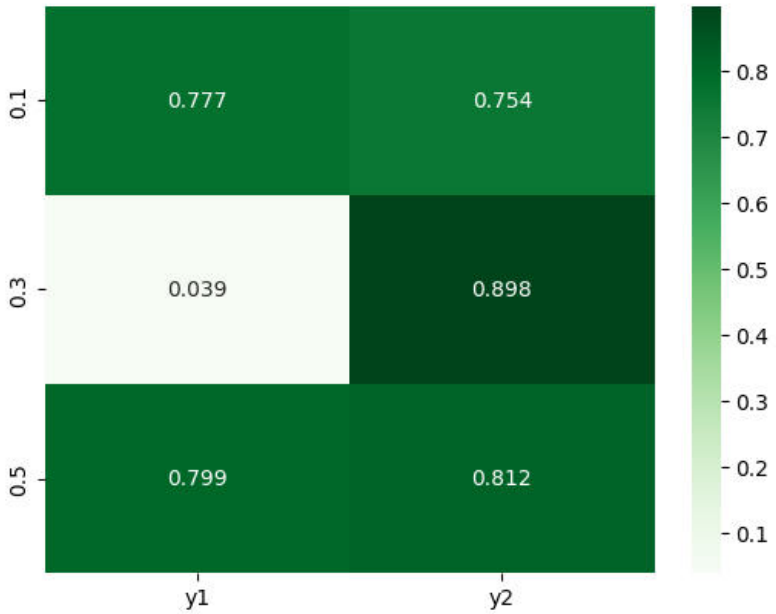

Fig. 4 – Matrix of R^2 coefficient of determination values for linear regression models of CTE depending on yttrium content and coating application method

As shown in Fig. 4, the coefficient of determination depends on both yttrium content and coating deposition technology. For gas-flame coatings containing 0.1, 0.3, and 0.5 wt.% yttrium, the R^2 values are 0.777, 0.039, and 0.799, respectively. The corresponding values for ion-plasma coatings are 0.754, 0.898, and 0.812.

The largest difference between the two deposition methods is observed for coatings containing 0.3 wt.% yttrium. The gas-flame coating exhibits a very low R^2 value of 0.039 due to its pronounced nonlinear thermal expansion behavior, particularly the sharp decrease in CTE at 900°C. In contrast, the ion-plasma coating with the same yttrium content demonstrates the highest R^2 value of 0.898 among the investigated compositions.

For coatings containing 0.1 and 0.5 wt.% yttrium, the differences between the two deposition technologies are less pronounced in terms of linear approximation quality. These results indicate that the effect of deposition technology on the temperature dependence of CTE varies with yttrium concentration

Conclusions

The experimental investigation of KNA-82 sealing coatings containing 0.1, 0.3, and 0.5 wt.% yttrium demonstrated that both yttrium concentration and deposition technology significantly influence the temperature dependence of the coefficient of linear thermal expansion within the investigated temperature range.

The ion-plasma coating containing 0.3 wt.% yttrium exhibited a gradual increase in CTE from approximately 5.7×10^{-6} K^{-1} at 100°C to 14.49×10^{-6} K^{-1} at 800°C, followed by relatively stable values up to 900°C. In contrast, the gas-flame coating with the same yttrium content showed a pronounced decrease in CTE from approximately 14.49×10^{-6} K^{-1} at 800°C to 3.45×10^{-6} K^{-1} at 900°C.

Regression analysis revealed substantial differences in the applicability of linear models. The highest coefficient of determination ($R^2 = 0.898$) was obtained for the ion-plasma coating containing 0.3 wt.% yttrium, whereas the corresponding gas-flame coating exhibited a very low R^2 value of 0.039, indicating strongly nonlinear behavior.

The relatively stable high-temperature CTE behavior of the ion-plasma coating containing 0.3 wt.% yttrium suggests its potential suitability for high-temperature sealing applications. However, further investigations of microstructure, phase composition, thermal cycling resistance, and coating–substrate compatibility are required to confirm its long-term operational performance.

The obtained results provide an experimental basis for further optimization of the composition and deposition technology of KNA-82 sealing coatings intended for gas turbine engine applications.

References

[1] Huang J. et al. High temperature abradable sealing coating for SiCf/SiC ceramic matrix composites // Ceramics International, 2022. DOI: https://doi.org/10.1016/j.ceramint.2022.09.141 .
[2] Hao E. et al. Effect of alloying elements on microstructure evolution and wear mechanism of MCrAlX-based coatings at 800 °C // Surface and Coatings Technology, Vol. 456, 2023. – Article 129266. DOI: https://doi.org/10.1016/j.surfcoat.2023.129266 .
[3] Wang T. et al. Effect of Yttrium Additions on the High-Temperature Oxidation Behavior of GH4169 Ni-Based Superalloy // Materials, Vol. 17, No. 11, 2024. – Article 2733. DOI: https://doi.org/10.3390/ma17112733 .
[4] Dong H. et al. The influence of temperature gradient across YSZ on thermal cyclic lifetime of plasma-sprayed thermal barrier coatings // Ceramics International, Vol. 41, No. 9, 2015. – P. 11046–11056. DOI: https://doi.org/10.1016/j.ceramint.2015.05.049 .
[5] NayebPashaee N. et al. High-entropy alloy coatings for surface protection and thermal barrier applications: fundamentals, recent advances, and a critical assessment of their potential as alternatives to conventional coatings // Discover Materials, 2025. DOI: https://doi.org/10.1007/s43939-025-00480-8 .
[6] Fentaye et al. A Review on Gas Turbine Gas-Path Diagnostics: State-of-the-Art Methods, Challenges and Opportunities // Aerospace, Vol. 6, No. 7, 2019. – Article 83. DOI: https://doi.org/10.3390/aerospace6070083 .
[7] Zhong J.Y., Mu R.D., He L.M. High temperature oxidation behaviour of plasma carburised Ni based single crystal superalloy with NiCoCrAlYHf high temperature oxidation protective coatings // Materials Research Innovations, Vol. 18, Suppl. 4, 2014. – P. S4-1115–S4-1120. DOI: https://doi.org/10.1179/1432891714z.000000000859 .
[8] Zhetessova G., Zharkevich O., Pleshakova YE., Yurchenko V., Platonova YE., Buzauova T. Building mathematical model for gas-thermal process of coating evaporation // Metalurgija, 55 (2016) 1, 63-66
[9] Ullah A. et al. Temperature Effect on Early Oxidation Behavior of NiCoCrAlY Coatings: Microstructure and Phase Transformation // Acta Metallurgica Sinica (English Letters), 2021. DOI: https://doi.org/10.1007/s40195-021-01310-5 .
[10] Boguslaiev V.O. et al. Effect of alloying heat-resistant packing coatings on their tribotechnical, physical and mechanical properties // Naukovyi Visnyk Natsionalnoho Hirnychoho Universytetu, No. 6, 2020. – P. 41–47. DOI: https://doi.org/10.33271/nvngu/2020-6/04 .
[11] Voloshin D., Afanasenko I., Derevianchuk I. Improvement of brake lever transmission for dump cars // IOP Conference Series: Materials Science and Engineering, Vol. 708, 2019. – Article 012037. DOI: https://doi.org/10.1088/1757-899x/708/1/012037 .
[12] Kubich V. et al. Comparison of High-Temperature Wear Resistance of Gas-Flame and Ion-Plasma Sealing Coatings with 0.1% Yttrium // Tribology in Industry, Vol. 46, No. 3, 2024. – P. 486–498. DOI: https://doi.org/10.24874/ti.1587.11.23.03 .
[13] Fasol Y.O. et al. Evaluation of Wear of Gas-Flame and Ion-Plasma Sealing Coatings with 0.3% Yttrium under Thermomechanical Loading Conditions // Material and Mechanical Engineering Technology, No. 4, 2025. – P. 10. DOI: https://doi.org/10.52209/2706-977x_2025_4_10 .
[14] Kulikov V. et al. Modeling Wear of KNA-82 Coatings with 0.5% Yttrium for Radial Seals of Gas Turbine Engines // Coatings, Vol. 16, No. 2, 2026. – Article 261. DOI: https://doi.org/10.3390/coatings16020261 .

Information of the authors

Fasol Yelyzaveta Oleksandrivna, senior lecturer at the department of physical materials science National University «Zaporizhzhia Polytechnic»
e-mail: selvluna@gmail.com

Riabenko Anton Yevhenovych, candidate of physical and mathematical sciences, associate professor, associate professor of the Department of System Analysis and Computational Mathematics, National University «Zaporizhzhia Polytechnic»
e-mail: rjabenkoae@gmail.com

Kubich Vadim Ivanovich, candidate of technical science, associate professor, associate professor of the department of automobiles, heat engines and hybrid power plants, National University «Zaporizhzhia Polytechnic»
e-mail: schmirung@gmail.com

DOI 10.52209/2706-977X_2026_3_122 IRSTI 55.31.29 UDC 621.9

Experimental Investigation of Thermofriction Milling with Pulsed Cooling for Improving the Machinability of Hadfield Steel

Tolganay Z.[1,*], Sherov K.T.[2], Zakirov K.[1], Balgynova A.[3]
[1]Abylkas Saginov Karaganda Technical University, Karagandy, Kazakhstan
[2]S.Seifullin Kazakh Agro Technical Research University, Astana, Kazakhstan
[3]Zhubanov Aktobe Regional University, Aktobe, Kazakhstan
*corresponding author

Abstract. Hadfield steel is widely used for components subjected to severe impact and abrasive wear; however, its pronounced work-hardening behavior significantly complicates conventional machining. This study experimentally investigates thermofriction milling with pulsed cooling as an alternative approach for machining 110G13L Hadfield steel. The experiments were conducted using a specially designed friction cutter with a diameter of 250 mm. The investigated machining parameters included spindle speeds of 500–2000 rpm, feed rates of 40–600 mm/min, and depths of cut of 1–5 mm. Surface roughness and hardness were evaluated to characterize the effect of the machining parameters on the resulting surface condition. The results showed that increasing spindle speed reduced surface roughness, whereas increasing feed rate increased roughness. Under favorable machining conditions, a surface roughness of (Rz leq 10) μm was achieved. Surface hardness increased with both spindle speed and feed rate, indicating intensive thermomechanical modification of the machined layer. The experiments confirmed the feasibility of thermofriction milling with pulsed cooling for processing Hadfield steel while also revealing limitations related to surface quality and chip fragmentation. The obtained results provide an experimental basis for the further development of a combined machining method integrating thermofrictional and conventional cutting mechanisms.

Keywords: hadfield stee, 110G13L stee, thermofriction milling, pulsed cooling, difficult-to-machine materials, surface roughness, surface hardness, work hardening

Introduction

Hadfield steel is a high-manganese austenitic steel widely used for components operating under severe impact and abrasive wear conditions. Its combination of high toughness, ductility, and pronounced work-hardening capability makes it particularly suitable for mining, crushing, railway, and heavy engineering applications. Under mechanical loading, plastic deformation of the surface layer can substantially increase its hardness, thereby providing high resistance to wear while retaining a comparatively tough core. Recent investigations continue to confirm that the performance of Hadfield steel is closely associated with the evolution of its surface and subsurface structure during deformation and the resulting work-hardening behavior [1, 2].

However, the same mechanisms that provide Hadfield steel with excellent service properties significantly complicate its machining. Intensive strain hardening occurs directly in the cutting zone, where severe plastic deformation continuously modifies the material ahead of and beneath the cutting edge. Consequently, the cutting tool interacts not only with the initially relatively soft austenitic structure but also with a locally hardened surface layer. This phenomenon results in increased mechanical and thermal loading of the cutting edge, promotes flank and rake-face wear, and can ultimately cause premature chipping or fracture of the cutting insert. The poor machinability of high-manganese steels has therefore remained an important technological limitation in the manufacture and repair of wear-resistant components [3].

For the 110G13L grade investigated in the present study, this problem is particularly relevant. In the initial condition after heat treatment, the material has an austenitic structure and a hardness of approximately HB 260–300. Under dynamic loading and cold deformation, however, its surface hardness may increase considerably, reaching values of up to approximately HB 600. Such behavior makes conventional cutting difficult and results in high consumption of cutting tools. Industrial observations presented in the underlying experimental study demonstrate severe wear, edge chipping, and failure of commercial cutting inserts during machining of 110G13L steel.

Previous investigations into the conventional machining of Hadfield steel have therefore focused largely on the selection of cutting-tool materials and optimization of process parameters. Ceramic and coated carbide tools have been investigated to improve tool life and surface quality. In hard turning, for example, machinability has been evaluated in terms of flank wear and surface roughness as functions of cutting speed, feed rate, depth of cut, and tool geometry [4]. In milling, experimental optimization using PVD- and CVD-coated carbide inserts demonstrated that feed rate strongly influences surface roughness, whereas cutting speed has a major influence on flank wear [5]. These findings illustrate that improvements can be obtained by selecting appropriate cutting conditions; nevertheless, conventional machining still requires the cutting edge to withstand the severe thermomechanical conditions generated during deformation of the work-hardened material.

This challenge has stimulated growing interest in assisted and hybrid machining processes for difficult-to-machine materials. Instead of relying exclusively on the mechanical action of the cutting edge, these approaches introduce an additional energy field or modify the thermal and tribological conditions in the cutting zone. Thermal-, vibration-, laser-, plasma-, and other field-assisted processes have been investigated as means of reducing cutting resistance, controlling material removal mechanisms, improving surface integrity, and increasing machining efficiency. Recent reviews identify field-assisted machining as an important direction for overcoming the inherent limitations of conventional processing of difficult-to-machine materials [6, 7].

Among these approaches, thermally assisted machining is particularly attractive because controlled heating can alter the local mechanical response of the workpiece immediately before or during material removal. The underlying concept is to decrease the resistance of the material in the cutting region while maintaining acceptable properties in the bulk workpiece. Studies of thermally assisted machining have demonstrated that the interaction between heat input and machining parameters can affect cutting forces, cutting-zone temperature, chip formation, tool loading, and the resulting surface condition [8]. At the same time, thermal assistance requires careful control because excessive or uncontrolled heat can adversely affect dimensional accuracy, tool behavior, and surface integrity.

Cooling conditions constitute another important factor in the machining of difficult-to-cut materials. Conventional flood cooling, minimum-quantity lubrication, cryogenic cooling, and high-pressure cooling have all been investigated as methods for controlling heat generation and tool wear. Their effectiveness, however, strongly depends on the combination of workpiece material, cutting conditions, and dominant wear mechanisms. A recent comprehensive review emphasized that no single cooling strategy is universally optimal and that cooling conditions should be selected in accordance with the specific material–process interaction [9]. This suggests that controlled alternation between localized heating and cooling may provide an alternative route for modifying the conditions of material removal.

Thermofriction processing represents a distinctive approach in this context because heat is generated directly through frictional interaction between a rotating tool and the workpiece. In contrast to processes requiring an external laser, plasma, or induction heat source, the mechanical interaction itself produces localized thermal energy. Previous work on thermofriction cutting demonstrated the feasibility of combining friction-generated heating with pulsed cooling [10]. In the experimental configuration considered in the present study, a specially designed friction milling cutter contains alternating functional regions that generate a cyclic thermomechanical effect on the workpiece surface. The original experimental system used a friction cutter with an outer diameter of 250 mm, a heating-zone length of L1=24 mm, a cooling-zone length of L2=8 mm, and a corresponding pitch of L=32 mm.

Despite the potential advantages of such a process, the application of thermofriction milling with pulsed cooling to Hadfield steel remains insufficiently investigated. In particular, the relationship between the main machining parameters and the resulting surface condition requires experimental clarification. Surface roughness is essential for the functional performance of machined components, while the hardness of the machined layer provides an indirect indication of the thermomechanical transformations occurring during processing. For Hadfield steel, these characteristics are especially important because the material exhibits a pronounced sensitivity to deformation-induced hardening. Recent studies continue to demonstrate the strong relationship between deformation, structural evolution, and surface hardness in Hadfield steels [1, 2].

Thermofrictional processing represents another approach to the machining of difficult-to-machine materials, in which the heat generated by intensive frictional interaction is utilized to modify the material conditions in the machining zone. Previous studies demonstrated the feasibility of thermofrictional cutting with pulsed cooling and showed that periodic thermal action can be incorporated into the material removal process [13]. The approach was further developed for thermal friction turn-milling of high-strength materials, where its influence on surface quality, hardness, and chip formation was experimentally investigated [14]. Subsequent experiments extended thermofrictional milling with pulsed cooling to 110G13L Hadfield steel and confirmed the possibility of machining this highly work-hardening material using friction-induced heating combined with periodic cooling [15]. In parallel, investigations into the geometry of thermofriction cutting tools [16] and the development of a dedicated disk cutter for thermofriction cutting with pulsed cooling [17, 18] provided the technological basis for further improvement of the process.

The preliminary experiments forming the basis of the present investigation demonstrated that thermofriction milling with pulsed cooling can be implemented for 110G13L steel. The experiments were conducted over spindle speeds of 500–2000 rpm, feed rates of 40–600 mm/min, and depths of cut of 1–5 mm. Surface roughness and hardness were subsequently evaluated using TR100 and TKM 459M measuring instruments, respectively. These observations provide an experimental basis for determining how variations in machining conditions influence the surface generated by thermofriction milling.

Accordingly, the aim of this study is to experimentally investigate the feasibility and process characteristics of thermofriction milling with pulsed cooling during the machining of 110G13L Hadfield steel and to evaluate the influence of machining parameters on the resulting surface roughness and hardness. Particular attention is paid to the effects of spindle speed and feed rate and to the technological limitations associated with surface quality and chip formation. The novelty of the study lies in the experimental evaluation of a thermofriction milling process in which

friction-induced localized heating is combined with pulsed cooling for the machining of high-manganese Hadfield steel. The obtained results are intended to establish an experimental basis for the subsequent development of a combined machining approach integrating thermofrictional and conventional cutting mechanisms.

1. Materials and Methods

1.1 Workpiece Material

The experimental investigation was carried out using high-manganese austenitic Hadfield steel, designated as 110G13L. This material is widely used for components operating under severe impact and abrasive wear conditions owing to its high toughness and pronounced work-hardening capability.

The workpieces used in the experiments were specimens cut from an armor plate of an ore-receiving hopper manufactured from 110G13L steel. The initial hardness of the workpiece material was within the range of HB 260–300 (approximately HRC 27–33).

A characteristic feature of 110G13L steel is its strong tendency to strain hardening. Although the material possesses a predominantly austenitic structure and relatively moderate hardness in its initial condition, severe plastic deformation can considerably increase the hardness of the surface layer. This behavior is one of the principal factors responsible for the poor machinability of Hadfield steel and imposes high mechanical and thermal loads on conventional cutting tools.

For the present investigation, thermofriction milling with pulsed cooling was selected as an alternative material-removal approach. The method utilizes friction-induced heat generated through the interaction between a rapidly rotating friction cutter and the workpiece surface, while periodic cooling modifies the thermal conditions in the contact zone.

1.2 Experimental Setup

Experimental thermofriction milling was performed on a BM-127M vertical knee-type milling machine. The 110G13L steel specimen was rigidly fixed on the machine table using a dedicated fixture to provide stable positioning during processing. A specially designed friction cutter was mounted in the machine spindle and rotated at the prescribed spindle speed.

The experimental arrangement consisted of the workpiece, clamping fixture, rotating friction cutter, and a cooling-fluid supply system. During machining, frictional interaction between the rotating cutter and the workpiece generated localized heating in the contact region. Pulsed cooling was applied through a supply tube directed toward the processing zone.

The original experiments visually demonstrated intensive interaction between the friction cutter and the workpiece, accompanied by material removal and chip formation. The photographs of the process also showed the condition of the machined specimens and the chips obtained after thermofriction milling.

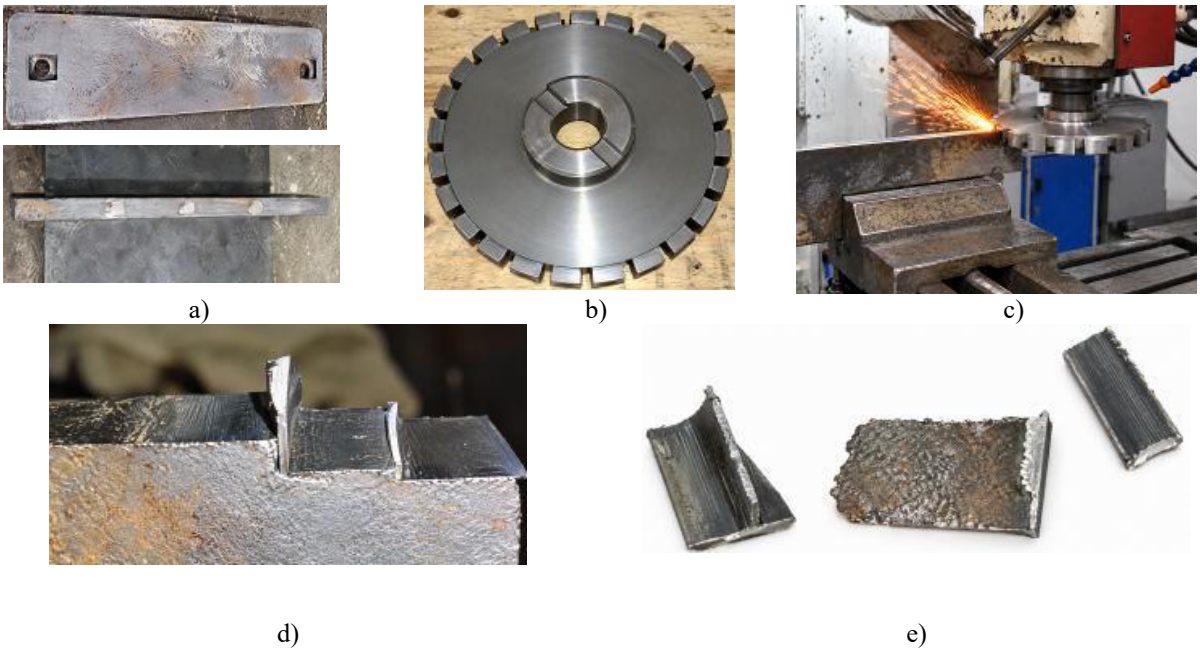

Fig. 1 – Experimental setup and thermofriction milling of 110G13L Hadfield steel with pulsed cooling: (a) workpiece specimen; (b) friction cutter; (c) experimental machining process; (d) machined surface; (e) chips produced during thermofriction milling

1.3 Design and Geometrical Parameters of the Friction Cutter

A specially designed friction cutter manufactured from 45 steel was used for the experiments. The cutter had an outer diameter of 250 mm and incorporated alternating heating and cooling regions along its circumference. The geometry of the cutter was selected according to the thermofriction processing concept developed in previous studies.

The principal geometrical parameters were:

$$D=250 \text{ mm},$$

$$L_1=24 \text{ mm},$$

$$L_2=8 \text{ mm},$$

$$L=L_1+L_2=32 \text{ mm},$$

where (D) is the outer diameter of the friction cutter, (L_1) is the length of the heating zone, (L_2) is the length of the cooling zone, and (L) is the circumferential pitch of the functional regions. These dimensions correspond to those reported for the experimental cutter in the original study.

During cutter rotation, the heating region periodically interacted with the workpiece and generated heat as a result of friction and plastic deformation. The subsequent cooling region enabled the cutting zone to be exposed to the supplied cooling medium. Thus, successive cutter rotations produced cyclic heating and cooling of the workpiece surface.

a) b) c)

Fig. 2 – Friction cutter used for thermofriction milling with pulsed cooling: (a) general view; (b) bottom view; (c) schematic representation of the cutter geometry; L_1 — heating zone; L_2 — cooling zone; L — circumferential pitch.

1.4 Machining Parameters

The experimental investigation was conducted by varying the principal thermofriction milling parameters over the ranges specified in Table 1. Three process variables were considered: spindle speed (n), feed rate (S), and depth of cut (t).

Table 1. Experimental matrix and processing parameters for thermofriction milling

Process parameter	Symbol	Range	Unit
Spindle speed	n	500, 1000, 2000	rpm
Feed rate	S	40, 200, 600	mm/min
Depth of cut	t	1,3, 5	mm

These ranges correspond to the experimental conditions reported for thermofriction milling of the investigated 110G13L specimens.

The principal responses used to assess the machining performance were the surface roughness and hardness of the machined surface. Accordingly, the experimental relationships can be generally represented as

$$Rz=f(n,S,t),$$

and

$$HB=f(n,S,t),$$

where (Rz) is the surface roughness parameter and (HB) is the hardness of the machined surface.

The selected ranges were intended to determine the general influence of the thermofriction milling conditions on the quality of the machined surface and to identify processing conditions capable of producing an acceptable surface condition.

1.5 Pulsed Cooling during Thermofriction Milling

Pulsed cooling was applied directly to the interaction zone between the friction cutter and the workpiece. The cooling medium was supplied through a tube positioned near the machining region, as illustrated in Figure 1.

The configuration of the friction cutter produced alternating thermal conditions during processing. When the heating section of the rotating cutter contacted the workpiece, frictional interaction generated localized heat. The subsequent passage of the cooling section provided an interval during which cooling fluid could act on the heated region. This sequence was repeated cyclically during cutter rotation.

Consequently, unlike continuous conventional milling, the investigated process involved a repeated frictional heating–pulsed cooling cycle. This cyclic thermomechanical action constitutes the principal technological feature of the investigated thermofriction milling method.

1.6 Surface Roughness and Hardness Measurements

The quality of the machined surface was evaluated using two principal indicators: surface roughness and hardness.

Surface roughness was measured using a TR100 portable surface roughness tester. The measurements were performed on the surfaces obtained after thermofriction milling under different machining conditions. The roughness parameter (Rz) was used to characterize the surface condition.

The hardness of the machined surface was evaluated using a TKM 459M portable hardness tester. The instrument was used to determine changes in surface hardness associated with variations in the thermofriction milling parameters.

Both instruments used in the experimental investigation are shown in Figure 3.

a)

b)

c)

Fig. 3 – Instruments used for evaluating the quality of the machined surface: (a) TR100 surface roughness tester; (b) TKM 459M hardness tester; (c) hardness measurement of the machined 110G13L steel specimen.

The use of these instruments and their purpose are explicitly reported in the original experimental methodology.

The obtained measurements were subsequently used to determine the influence of spindle speed and feed rate on the surface condition of Hadfield steel. Particular attention was given to identifying the tendencies of (Rz) and surface hardness with increasing process intensity.

1.7 Experimental Evaluation Procedure

The overall experimental procedure consisted of the following sequence:

- preparation and rigid fixation of the 110G13L steel specimen on the milling machine;
- installation of the specially designed Ø250 mm friction cutter;
- setting of the required spindle speed, feed rate, and depth of cut;
- thermofriction milling of the workpiece with pulsed cooling;
- examination of the resulting machined surface and chip formation;
- measurement of the surface roughness using the TR100 instrument;
- measurement of the surface hardness using the TKM 459M instrument; and
- analysis of the relationships between the machining parameters and the resulting surface-quality indicators.

The experimental methodology was therefore designed to evaluate both the feasibility of thermofriction milling with pulsed cooling for 110G13L Hadfield steel and the influence of the principal process parameters on the resulting surface characteristics.

2. Results and Discussion

2.1 Experimental Evaluation of the Thermofriction Milling Process

The experimental results confirmed the feasibility of thermofriction milling with pulsed cooling for machining 110G13L Hadfield steel. During processing, frictional interaction between the rotating cutter and the workpiece resulted in localized thermomechanical action followed by periodic cooling of the interaction zone. Material removal and chip formation were observed throughout the experiments.

Representative thermofriction milling processes, machined specimens, and the resulting chips are shown in Figure 1.

The experiments demonstrated that the investigated method can be applied to austenitic high-manganese steel despite its pronounced work-hardening tendency. However, the experiments also revealed limitations associated with surface quality and chip fragmentation.

2.2 Influence of Machining Parameters on Surface Quality

The experimental results showed that the surface condition was strongly affected by the thermofriction milling parameters. An increase in spindle speed resulted in a reduction in surface roughness, whereas increasing the feed rate led to higher roughness values.

The improvement in surface quality at higher spindle speeds can be associated with more intensive frictional interaction and localized heat generation in the tool–workpiece contact region. Under these conditions, the thermomechanical state of the surface layer is modified, which may facilitate material removal and promote the formation of a more uniform machined surface. In contrast, increasing the feed rate reduces the interaction time per unit length of the workpiece and intensifies mechanical loading, resulting in deterioration of the surface finish.

Under the favorable machining conditions investigated in this study, a surface roughness of $Rz \leq 10$ μm was achieved, indicating that the resulting surface quality is suitable for the investigated wear-resistant Hadfield steel components.

This result confirms the potential of thermofriction milling with pulsed cooling for processing Hadfield steel. Nevertheless, the achieved roughness also indicates that further improvement of the process is required when higher surface-quality requirements are imposed.

2.3 Surface Hardness and Technological Limitations

The hardness of the machined surface increased consistently with increasing spindle speed and feed rate. This behavior is consistent with the pronounced work-hardening capability of Hadfield steel and indicates that the surface layer experiences intensive mechanical and thermal loading during thermofriction milling.

The simultaneous decrease in surface roughness and increase in hardness with increasing spindle speed is particularly important. It indicates that spindle speed affects not only the geometrical quality of the machined surface but also the mechanical condition of its surface layer. However, the present measurements are insufficient to determine the underlying microstructural transformations, and further metallographic and microhardness investigations would be required.

Although the experiments confirmed the feasibility of the proposed method, two technological issues remained unresolved: obtaining a higher-quality finished surface and ensuring effective chip fragmentation. These limitations provide a basis for the further development of a combined machining method integrating thermofrictional action with conventional cutting, as proposed in the underlying study.

Conclusions

The experimental investigation of thermofriction milling with pulsed cooling for machining 110G13L Hadfield steel led to the following conclusions:

1. Thermofriction milling with pulsed cooling is feasible for machining 110G13L Hadfield steel. The experiments demonstrated stable material removal and chip formation despite the pronounced work-hardening tendency and poor machinability of the investigated material.

2. Surface roughness (Rz) was directly influenced by the thermofriction milling parameters. Increasing the spindle speed resulted in a decrease in surface roughness and improved the surface finish, whereas increasing the feed rate led to higher roughness values and deterioration of the surface finish. Under favorable machining conditions, a surface roughness of $Rz \leq 10$ μm was achieved.

3. The hardness of the machined surface increased with increasing spindle speed and feed rate. This behavior indicates intensive thermomechanical interaction between the friction cutter and the surface layer of Hadfield steel during processing.

4. Although the investigated method demonstrated its potential for machining Hadfield steel, surface quality and effective chip fragmentation remain the main technological limitations of standalone thermofriction milling with pulsed cooling.

5. The obtained results provide an experimental basis for the further development of a combined machining method integrating thermofrictional and conventional cutting mechanisms. Such an approach is expected to utilize thermofrictional action to modify the material condition prior to conventional material removal, with further research required to evaluate its effects on surface quality, chip formation, tool life, and machining productivity.

Funding. This research was funded by the Committee of Science of the Ministry of Science and Higher Education of the Republic of Kazakhstan, Grant No. AP26199283.

References

[1] Zemlik M., Konat Ł., Leśny K., Jamroziak K. Comparison of Abrasive Wear Resistance of Hardox Steel and Hadfield Cast Steel //Applied Sciences, 2024; 14(23):11141. DOI: 10.3390/app142311141.
[2] Bańkowski D., Młynarczyk P.S., Depczyński W.P., Bolanowski K. The Effect of Work Hardening on the Structure and Hardness of Hadfield Steel //Archives of Foundry Engineering, 2024; 24(1):14-20. DOI: 10.24425/afe.2024.149246.
[3] Chen C., Lv B., Ma H., Sun D., Zhang F. Wear Behavior and the Corresponding Work Hardening Characteristics of Hadfield Steel //Tribology International, 2018; 121:389-399. DOI: 10.1016/j.triboint.2018.01.044.
[4] Handayani D., Okhuysen V.F., Wagner N. Machinability of High Mn Steel Using Tool Life Criteria //International Journal of Metalcasting, 2024; 18:600-607. DOI: 10.1007/s40962-023-01044-3.
[5] Pyatykh A., Savilov A., Timofeev S. Investigation of Hadfield Steel Machinability in Milling Operations //Key Engineering Materials, 2022; 910:123-128. DOI: 10.4028/p-8p4ud2.
[6] Sherov K., Mussayev M., Usserbayev M., Magavin S., Abisheva N., Karsakova N., Kuanov I., Bekzhanov Y., Myrzakhmet B. Investigation of the Method of Thermal Friction Turn-Milling of High Strength Materials // Journal of Applied Engineering Science, 2022; 20(1):13–18. DOI: 10.5937/jaes0-29546.
[7] Kıvak T. Optimization of Surface Roughness and Flank Wear Using the Taguchi Method in Milling of Hadfield Steel with PVD and CVD Coated Inserts // Measurement, 2014; 50:19–28. DOI: 10.1016/j.measurement.2013.12.017.
[8] Horng J.T., Liu N.M., Chiang K.T. Investigating the Machinability Evaluation of Hadfield Steel in the Hard Turning with Al2O3/TiC Mixed Ceramic Tool Based on the Response Surface Methodology // Journal of Materials Processing Technology, 2008; 208(1–3):532–541. DOI: 10.1016/j.jmatprotec.2008.01.018.
[9] Horng J.T., Chiang K.T. A Grey and Fuzzy Algorithms Integrated Approach to the Optimization of Turning Hadfield Steel with Al2O3/TiC Mixed Ceramic Tool // Journal of Materials Processing Technology, 2008; 207(1–3):89–97. DOI: 10.1016/j.jmatprotec.2007.12.060.
[10] Zhang J., Zheng Z., Huang K., Lin C., Huang W., Chen X., Xiao J., Xu J. Field-Assisted Machining of Difficult-to-Machine Materials // International Journal of Extreme Manufacturing, 2024; 6(3):032002. DOI: 10.1088/2631-7990/ad2c5e.
[11] Zhao G., Zhao B., Ding W., Xin L., Nian Z., Peng J., He N., Xu J. Nontraditional Energy-Assisted Mechanical Machining of Difficult-to-Cut Materials and Components in Aerospace Community: A Comparative Analysis // International Journal of Extreme Manufacturing, 2024; 6(2):022007. DOI: 10.1088/2631-7990/ad16d6.
[12] Korkmaz M.E., Gupta M.K. A State of the Art on Cryogenic Cooling and Its Applications in the Machining of Difficult-to-Machine Alloys // Materials, 2024; 17(9):2057. DOI: 10.3390/ma17092057.
[13] Sherov K.T., Mussayev M.M., Sikhimbayev M.R., et al. Thermofrictional Cutting with Pulsed Cooling // Russian Engineering Research, 2020; 40:926–929. DOI: 10.3103/S1068798X20110179.
[14] Makhmudov N.M., Sherov K.T., Mussayev M.M., et al. Experimental Study of the Process of Thermofrictional Milling with Pulsed Cooling of 110G13L Steel // Gornyy Vestnik Uzbekistana, 2024; 3(98):43–46.
[15] Sherov K.T., Mussayev M.M., Sikhimbayev M.R., et al. Disk Cutter for Thermofriction Cutting with Pulsed Cooling. Utility Model Patent of the Republic of Kazakhstan No. 7579, 11.11.2022.
[16] Ainabekova S.S., Sherov K.T., Mussayev M.M., et al. Determination of the Optimum Geometry of a Disk Saw for Thermofriction Cutting of Low-Carbon Steel // Vestnik KazNITU, 2020; 5(141):440–446.
[18] Sherov, K., Mardonov, B., Zharkevich, O., Mirgorodskiy, S., Gabdyssalyk, R., Tussupova, S., Smakova, N., Akhmedov, K., & Imanbaev. Y. Studying the process of tooling cylindrical gears //Journal of Applied Engineering Science, 2020, 18(3) 327 - 332.

Information of the authors

Tolganay Zhanibek, PhD student, Abylkas Saginov Karaganda Technical University
e-mail: 48177@ktu.edu.kz

Sherov Karibek, d.t.s., professor, Seifullin Kazakh Agro Technical Research University
e-mail: shkt1965@mail.ru

Zakirov Karshyga, PhD student, Abylkas Saginov Karaganda Technical University
e-mail: 891108351206@ktu.edu.kz

Balgynova Akzharkyn, c.t.s, associate professor, Zhubanov Aktobe Regional University
e-mail: moldir_merei66@mail.ru

DOI 10.52209/2706-977X_2026_3_129 IRSTI 55.13.99 UDC 621.793.7

Trade-off Analysis and Multi-Objective Decision Support for Mechanical Engineering Supply Chains

[1]Zhetessova G.S., [2]Khrustaleva I.A., [1]Zharkevich O.M.*, [3]Kanatova A., [4]Kozhanov M.G.
[1]Abylkas Saginov technical University, Karaganda, Kazakhstan
[2]Peter the Great St. Petersburg Polytechnic University, Saint Petersburg, Russia
[3]Astana IT University, Astana, Kazakhstan
[4]Institute of Digitalization and Innovation, Academy of Public Administration under the President of the Republic of Kazakhstan, Astana, Kazakhstan
*corresponding author

Abstract. Modern mechanical engineering enterprises are characterized by highly complex technological processes and intensive interaction between production and logistics flows. This article proposes an integrated method for optimizing production and logistics systems based on the NSGA-II evolutionary algorithm, simulation modeling, and neural network methods for predicting machining parameters. The proposed approach enables the creation of multiple rational production system configurations and the selection of optimal solutions, taking into account tradeoffs between production time, costs, and machining quality.

Key words: Multi-Objective Optimization, NSGA-II Algorithm, Digital Twin, Production and Logistics Systems, Mechanical Engineering)

Introduction

The development of mechanical engineering production in the context of the digital transformation of industry requires the application of new methods for analyzing and optimizing technological and organizational processes. Modern production systems are characterized by highly complex process flow structures, a significant number of interconnected machining operations, and intensive logistics flows arising from the movement of blanks and semi-finished products between work centers [1, 2, 3].

However, the practical implementation of technological processes at mechanical engineering enterprises inevitably involves the movement of materials between work centers, the organization of buffer zones, and the use of in-plant transport. Therefore, the optimization of technological processes must be carried out in conjunction with the optimization of the production logistics structure. Ignoring logistics factors can lead to increased production cycle times, increased work-in-progress volumes, and decreased equipment efficiency.

One promising approach to solving this problem is the use of multi-criteria optimization methods, which take into account several interrelated performance indicators of the production system [4, 5]. In particular, for mechanical engineering enterprises, such criteria may include product manufacturing time, production and logistics costs, processing quality indicators, and the level of work in progress. Since these criteria often conflict with each other, the optimization problem should be solved within the framework of the Pareto optimality concept, which allows for the formation of a multitude of rational solutions [6, 7-12].

Issues of increasing the efficiency of mechanical engineering production and optimizing technological processes are actively studied in the scientific literature. A significant number of studies are devoted to the development of methods for optimizing machining parameters, as well as improving the technological preparation of production [13-17].

One traditional area of research is the optimization of cutting conditions and parameters of technological operations. Another important area of research is the development of methods for optimizing process routes for product processing. In these studies, the technological process is considered as a sequence of operations performed on various types of equipment [13, 28]. In recent years, increasing attention has been paid to the integration of technological and logistical processes within a single production system model.

In recent years, digital modeling methods for production systems have seen significant advances, particularly the concept of a digital twin, which allows for the creation of virtual models of enterprises and the analysis of their performance in various operating modes. Evolutionary algorithms for multi-criteria optimization are effectively used to find Pareto-optimal configurations of production systems, among which the NSGA-II (Non-Dominated Sorting Genetic Algorithm II) holds a special place. This algorithm allows for the efficient exploration of complex multidimensional solution spaces and the generation of an approximate Pareto surface reflecting the trade-offs between various performance criteria.

Artificial intelligence methods used for the analysis and optimization of technological processes are actively developing. In particular, artificial neural networks are used to predict machining parameters, assess surface quality, and select optimal cutting conditions.

Despite a significant amount of research in this area, most existing studies consider technological processes, logistics systems, and optimization methods separately. At the same time, the comprehensive integration of technological models, logistics flows, multi-criteria optimization methods, and digital twins of production systems remains understudied.

1. Integrated structural-parametric model of the technological process and formation of structural elements

The manufacturing process of mechanical engineering enterprises is a structurally complex system, the efficiency of which is determined not only by the parameters of individual operations but also by the nature of the interrelationships between all process elements. Previous studies have examined this problem at two complementary levels [18]. On the one hand, the manufacturing process was presented as a hierarchically organized system, including a processing route, process operations, process steps, and work passes (Fig. 1).

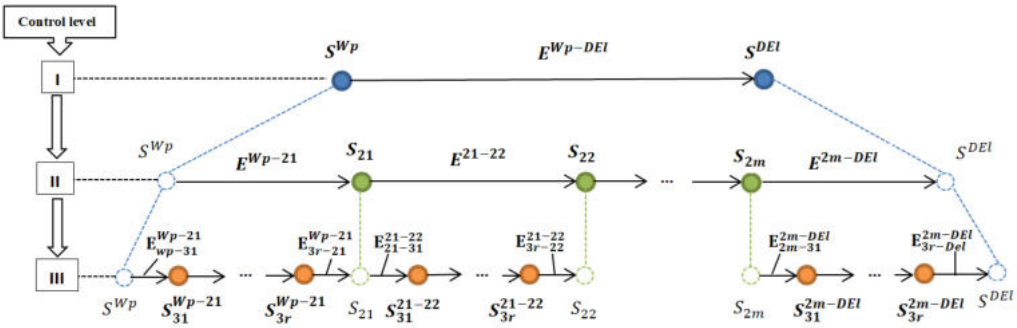

Fig. 1. - Structural hierarchical model of the process of forming a design element

On the other hand, it was shown that increasing the efficiency of the mechanical processing process is impossible without a detailed analysis of the process of forming individual structural elements of the product, since they are the carriers of the functionally significant geometric and qualitative characteristics of the part (Fig. 2).

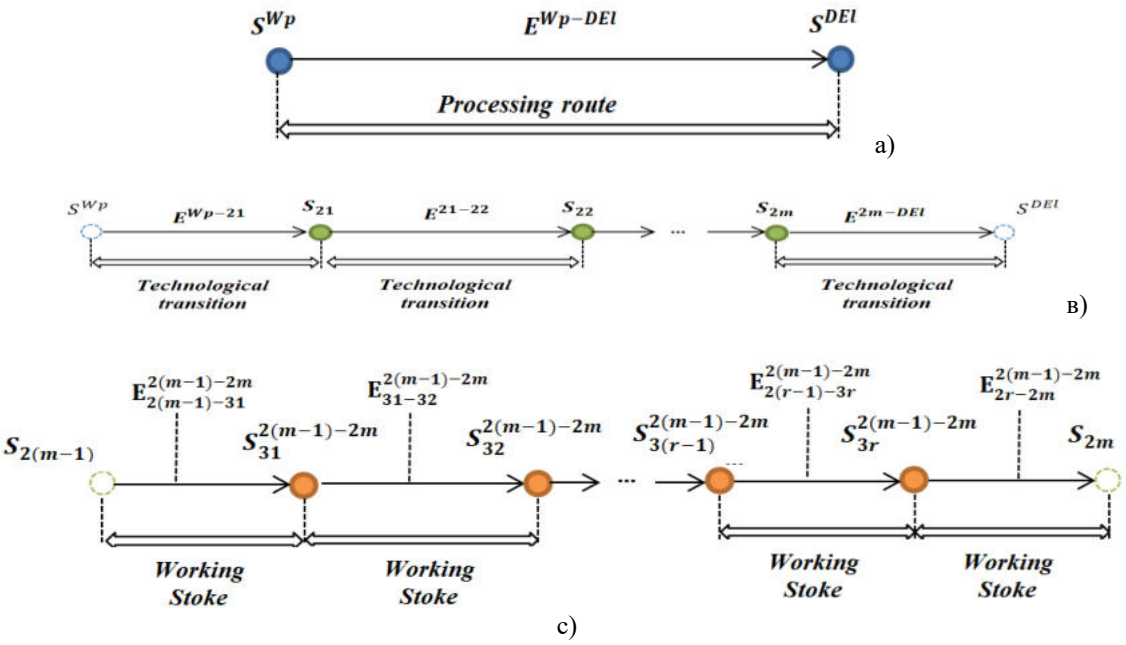

a) at the first control level, the studied object has two states S_{Wp} – the state of the design element before the formation process (blank) and S^{DEl}– the state of the design element after the formation process; b) at the second control level, the parameters of the process transition are optimized, where $S_{21},\ldots, S_{2m}$ are intermediate states formed during the implementation of individual process transitions; c) at the third control level, the parameters of the working stroke are optimized, and the studied object

Fig. 2 - Graph of the process of forming a design element: has r intermediate states

This approach allows us to move from the traditional consideration of the technological process as a linear sequence of operations to a more meaningful model in which the manufacture of a product is described as a set of interconnected processes of changing the state of both the product as a whole and the individual structural elements that form its structure (1):

$$M_{DEl}^{StrEl/bas} = \\ = \{TPR_{iq}^{DEl}, \{\{TechTr_m^{DEl} | TechTr_m^{DEl} \in TPR_{iq}^{DEl}\}\}, \{WSt_r^{DEl} | WSt_r^{DEl} \in TechTr_m^{DEl}\}\} \quad (1)$$

where $M_{DEl}^{StrEl/bas}$ - a set of basic structural elements of the process of forming individual design elements that form the structure of a product;

TPR_{iq}^{DEl} – parametric model of the technological route for forming the q-th design element of the i-th type;

$TechTr_m^{DEl}$ - parametric model of the m-th technological transition implemented within the framework of the technological route of shaping a design element;

WSt_r^{DEl} - parametric model of the r-th working stroke, implemented within the framework of the technological transition performed in the process of forming a design element.

As a result, it's appropriate to describe the machining process as an integrated system of two hierarchical subsystems: the product processing process and the process of shaping its structural elements. The first subsystem defines the overall structure of the product manufacturing process, while the second ensures parametric and structural optimization of those local process areas that directly shape the required geometry, precision, and surface quality (Fig. 3).

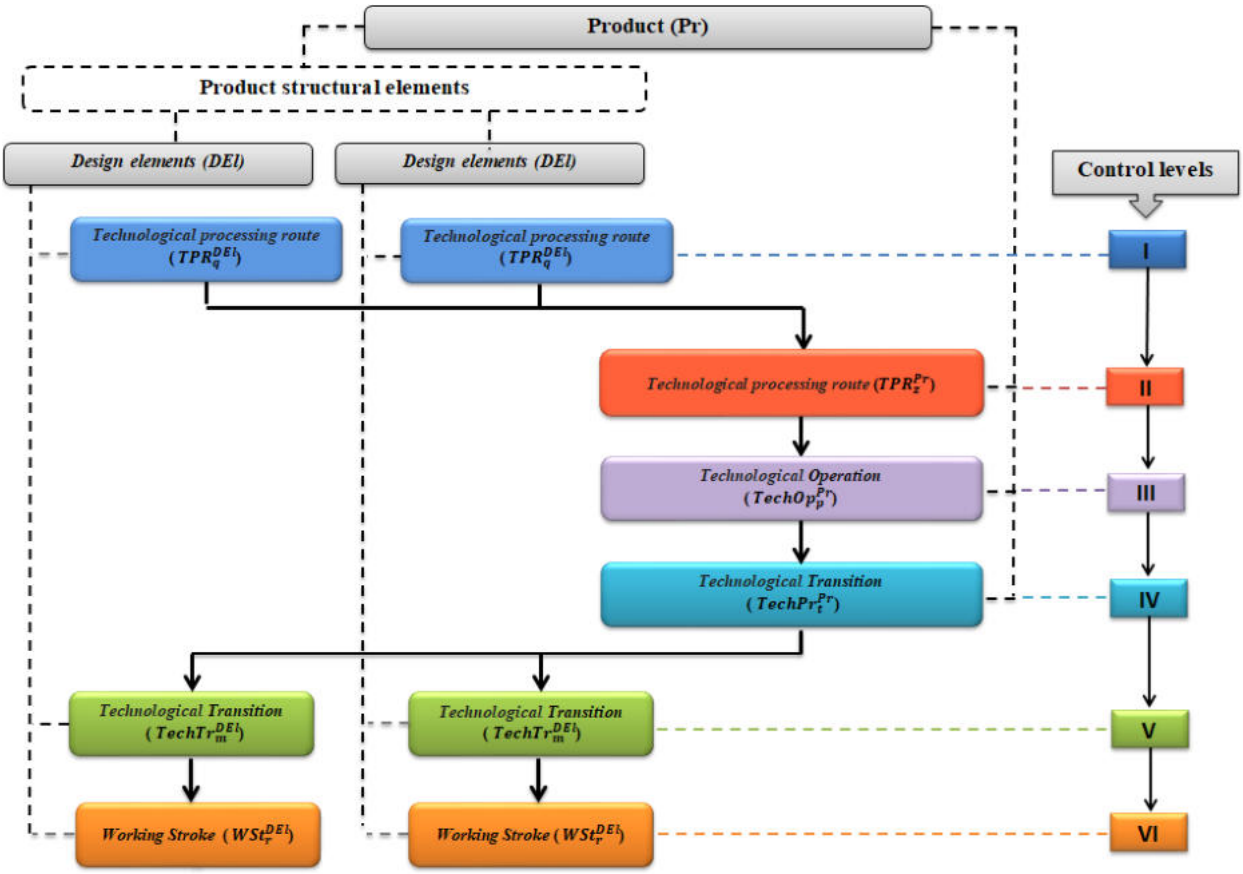

Fig. 3 - Integrated model for optimizing the parameters of the mechanical processing process of a product

Within the first subsystem, a product is considered as an object undergoing a sequence of states from the initial workpiece to the finished part. The transition between states is ensured by the implementation of process operations and transitions performed on specific pieces of equipment using appropriate basing schemes, fixtures,

and tools. Within the second subsystem, each structural element of the product is considered as an independent object of process analysis, for which its own shaping route is developed, including a sequence of process transitions and work passes.

Therefore, the integration of these two models into a single structure is a logical development of the previously obtained results. While the problem of selecting the optimal sequence of process transitions and cutting parameters is solved at the level of an individual structural element, at the level of the product as a whole, the task arises of coordinating these decisions within the overall structure of the process flow for manufacturing the part. It is this coordination that enables the transition from local optimization of individual elements to comprehensive optimization of the product manufacturing process. Thus, modeling the technological process of product processing and the process of forming structural elements form the methodological basis of an integrated model of a production system, in which the technological structure of the process becomes the initial basis for multi-criteria optimization of intra-production logistics flows.

2. Mathematical model of logistics flows of a mechanical engineering enterprise

The manufacturing process of mechanical engineering enterprises can be represented as an integrated system of interconnected processes involving the processing of the product and the shaping of its structural elements. However, in real-world production conditions, the execution of technological operations inevitably involves the movement of blanks and semi-finished products between various work centers. Therefore, the technological structure of the process cannot be considered in isolation from the intra-production logistics system.

In mechanical engineering production, technological operations are performed on equipment located in various areas of the production shop, where blanks and semi-finished products are constantly in motion from one work station to another. Consequently, the technological process is effectively implemented as a material flow moving through a network of production areas.

The following set of basic structural elements of a logistics system is defined (2):

$$L_{Sys}^{Log/bas} = \left\{ W_{St}^{Log}, \{B_k^{Log} \in W_{St}^{Log}\}, \{Tr_v^{Log} \in L_{Sys}^{Log}\}, Path_s^{Log} \in W_{St}^{Log} \right\} \quad (2)$$

where $L^{Log/bas}{}_{Sys}$ - a set of basic structural elements of the workshop's logistics syst;

$W_{St}{}^{Log}$ - parametric model of warehouses (input blanks and finished products);

$B_k{}^{Log}$ - parametric model of the k-th interoperation buffer (accumulator);

$Tr_v{}^{Log}$ - parametric model of the v-th vehicle (e.g. AGV trolley, conveyor, forklift);

$Path^{Log}{}_s$ - parametric model of the s-th logistic route (trajectory of movement of a material batch).

Therefore, for comprehensive optimization of the production process, it is necessary to consider not only the processing parameters of structural elements, but also the structure of material flows between work stations. Graph models are convenient for describing such processes.

Let's describe the production and logistics system as a directed weighted graph (3):

$$G = (V, E), \quad (3)$$

where V - a set of graph vertices corresponding to the production nodes of the system;

E - a set of graph arcs corresponding to possible routes of movement of material flows.

The vertices of the graph represent:

- W_{in}, W_{out} - warehouses (warehouse for blanks and warehouse for finished products).
- $M = \{M_1, M_2, ..., M_n\}$ - work centers (machines, machining centers) where technological operations are carried out.
- $B = \{B_1, B_2, ..., B_k\}$ - buffer zones (inter-operational storage areas).

The graph arcs reflect possible routes for moving workpieces between the corresponding nodes of the system - these are material flows (logistics links) (Fig. 4).

Each arc $e_{ij} \in E$ connecting vertices V_i and V_j is associated with a set of parameters characterizing the process of moving a workpiece between work centers:

- transport time t_{log};
- transport cost C_{log};
- parts flow rate V_{batch}.

Passing through vertex Mi, the part changes its state (S1, Sn) (e.g., the formation of the next structural element is completed), after which it moves along arc E to the next node.

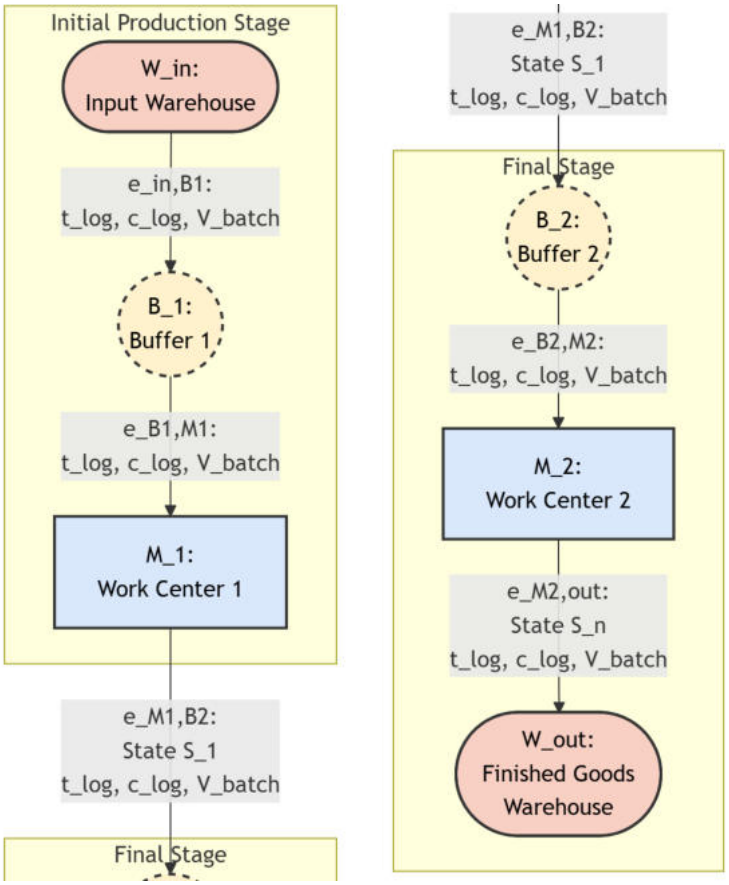

Fig. 4 – Graph of the production and logistics system

Parameters t, C, and V represent the weighting characteristics of logistics links and, in the mathematical model of the production system, represent multi-criteria optimization criteria (in this case, NSGA-II).

Thus, the production system graph reflects the set of possible material flow trajectories implementing the technological process of product manufacturing.

3. Integrated mathematical model of production and logistics flows

Developing an integrated mathematical model requires combining machine-level process parameters (micro- and meso-levels) with material flow parameters at the production shop level (macro-level) [18]. This problem is solved using a multi-criteria optimization framework, where local-level vector criteria are combined into a global Pareto-based compromise system [8, 9].

The proposed formalized model has a three-level hierarchical structure.

3.1. Microlevel: Optimization of the design element formation process. At the lower level, the control object is the process of physical stock removal (technological transition and cutting stroke). The microlevel control variable vector Umicro includes cutting modes (4):

$$U_{micro} = \{v, S_z, t_p, i\}, \tag{4}$$

where v - cutting speed;

S_z – feed;

t_p - cutting depth;

i - number of working strokes.

Local vector optimization criteria are aimed at resolving the conflict between productivity and surface quality [10].

Minimization of the main processing time (5):

$$f_1^{micro}(U_{micro}) = T_{mach}(v, S_z, i) \rightarrow min. \tag{5}$$

Minimization of the height of microroughness (roughness Ra (6):

$$f_2^{micro}(U_{micro}) = Ra(v, S_z) \rightarrow min. \quad (6)$$

The limitations are the maximum permissible cutting power (Ncut ≤ Nmax), the service life of the cutting tool and the required shape accuracy.

3.2. Meso-level: Optimization of the product's process flow. At this level, work steps and transitions are combined into process operations performed at specific work centers Mk ϵ M.

he vector of control variables U_{meso} has the form (7):

$$U_{meso} = \{Seq_{op}, M_k, Tool_k\}, \quad (7)$$

where Seq_{op} - sequence of technological operations (route);

M_k - selected type of equipment;

$Tool_k$ - instrumental adjustment.

Then the minimization of local optimization criteria [11, 18] will take the following form.

Minimization of the unit time of the operation (including auxiliary time Taux for installing and removing the part) (8):

$$f_1^{meso}(U_{meso}, U_{micro}) = \sum(T_{mach} + T_{aux}) \rightarrow min. \quad (8)$$

Minimization of technological processing costs (C_{tech}) (9):

$$f_2^{meso}(U_{meso}, U_{micro}) = C_{tech}\ (v, T_{mach}, Tool_k) \rightarrow min. \quad (9)$$

3.3. Macro-level: Optimization of the production and logistics system. At the highest level, routes are integrated into the enterprise's transport and storage system, described by a directed graph G = (V, E). The macro-level control vector U defines logistics (10):

$$U_{macro} = \{Path_{ij}, V_{batch}, B_k, W_{trans}\}, \quad (10)$$

where $Path_{ij}$ - logistic route (choice of arcs e_{ij} ϵ E);

V_{batch} - volume of production and transport batch;

B_k - capacity of interoperation buffers;

W_{trans} - vehicle.

The criteria for macro-level optimization are minimization of the logistics cycle time and minimization of internal production costs.

Minimizing logistics cycle time (11):

$$f_1^{macro}(U_{macro}) = \sum t_{log}(e) + \sum t_{wait}(b) \rightarrow min. \quad (11)$$

Minimization of internal production costs (Clog) (12):

$$f_1^{macro}(U_{macro}) = \sum C_{log}\ (e, V_{batch}) + C_{WIP}(V_{batch}, t_{wait}) \rightarrow min \quad (12)$$

where t_{wait} - interoperative lying time;

C_{WIP} - Work-in-Process (WIP) costs.

Integration of levels allows us to formulate the global problem of finding the vector $U_\Sigma=\{U_{micro}, U_{meso}, U_{macro}\}$. The global objective function $\Phi(U_\Sigma)$ minimizes the production cycle time (Makespan, C_{max}), total costs (C_Σ), and quality loss (Q_{loss}) (13):

$$\Phi(U_\Sigma) = [C_{max}(U_\Sigma), C_\Sigma(U_\Sigma), Q_{loss}\ (U_\Sigma)] \rightarrow min. \quad (13)$$

Since the criteria are conflicting (for example, increasing the batch size reduces specific transportation costs, but exponentially increases waiting time and the production cycle), the problem is solved using the NSGA-II (Non-dominated Sorting Genetic Algorithm II) evolutionary algorithm. This method has proven its effectiveness in engineering problems [8, 12], allowing the generation of a set of non-dominated solutions (Pareto front), from which the decision maker (DM) selects the optimal system configuration depending on current production priorities.

Such integration allows the production process to be described as a single material flow transformation system, including both technological operations and logistics movements.

We will conduct structural and parametric optimization of the machining of a complex-shaped part, the "Housing." For this, we will model the process of face milling of the main mating surface, as this is one of the most critical operations where a classic conflict of technological criteria arises: the need to ensure high productivity (minimize time) and the required quality (minimize roughness).

When using the evolutionary The NSGA-II algorithm filters out "dominated" (obviously worst) solutions from thousands of possible parameter combinations. This results in a Pareto frontier—a set of non-dominated alternatives.

Below is the calculated array of points forming the Pareto frontier for the "Housing" part. The two-dimensional Pareto frontier shows the technological tradeoff between productivity (machining time) and surface quality (Ra roughness) during milling of the "Housing" part. The points on the graph represent the set of non-dominated solutions generated by the evolutionary algorithm (Fig. 5).

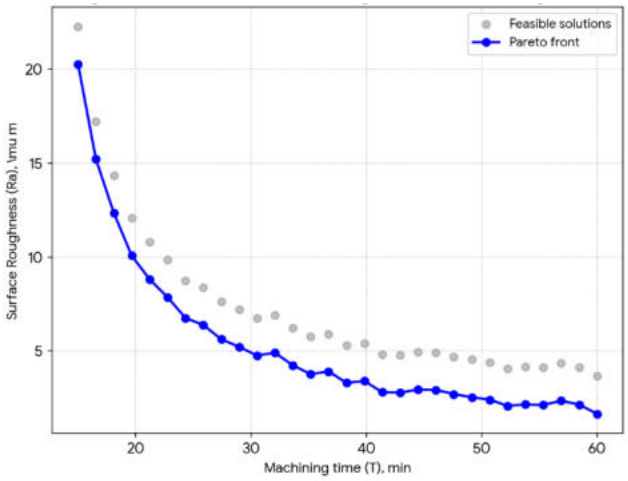

Fig.5 - **2D Pareto Front**

Micro-level optimization reveals a strict nonlinear relationship: attempting to minimize surface roughness to 0.18 µm leads to an exponential increase in processing time. In turn, choosing a compromise mode allows for acceptable quality (Ra = 1.0 µm) while reducing processing time by more than half.

A conceptual diagram of the multi-criteria conflicts in a production and logistics system is presented in Figure 6, where the trade-off triangle between cycle time (Cmax), quality (R_a), and cost is resolved using the integrated NSGA-II model.

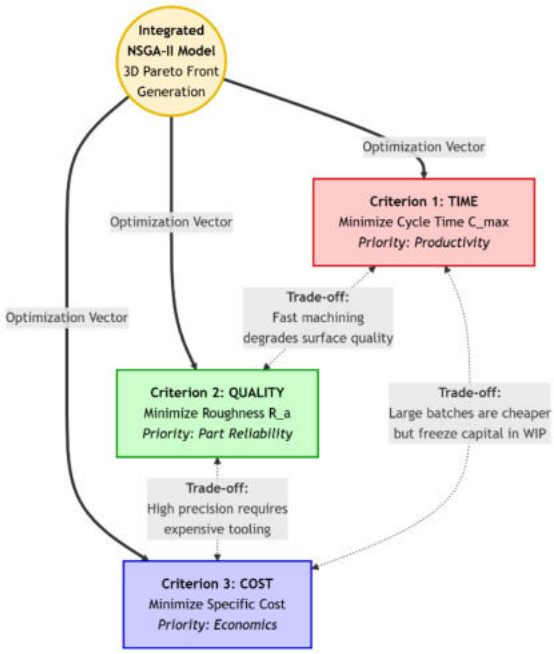

Fig.6 - **3D Trade-off Graph**

The transition from local optimization to the macro level is accompanied by the emergence of complex multi-criteria conflicts (Fig. 6). Increasing the cutting speed or the transport batch locally improves some indicators (for example, reducing production costs), but inevitably worsens others (increasing the volume of work in progress or reducing accuracy). An integrated model based on NSGA-II allows for algorithmic balancing of this "triangle of contradictions," generating optimal control strategies.

4. Integration of a mathematical model with Digital Twin technology

Although the proposed multi-level mathematical model and the application of the NSGA-II evolutionary algorithm enable the development of highly efficient Pareto-optimal solutions, classical multi-criteria optimization has one significant limitation: it relies on deterministic (standard) values for processing times and logistics flow parameters. However, in the real-world conditions of a mechanical engineering enterprise, production and logistics flows are subject to constant stochastic disturbances: progressive wear of cutting tools, unforeseen equipment failures, delays in intrashop transport, and changes in production order priorities [19].

To bridge the gap between calculated plans and the actual production environment, a transition from static pre-planning to adaptive real-time control is necessary. A logical development of the developed model is its integration into the architecture of a cyber-physical production system (CPPS) based on Digital Twin (DT) technology [20]. In the integrated system, the Digital Twin acts as a link between the physical shop floor and the multi-criteria optimization algorithm. The architecture of the proposed system includes four basic hierarchical levels [21]:

1) Physical Shop Floor: real work centers (Mk), inter-operational storage units (Bk), and logistics transport systems that perform the physical formation and movement of parts.

2) Industrial Internet of Things Layer (IIoT Layer): distributed sensor networks (RFID tags on pallets, spindle power consumption sensors, CNC controllers) that ensure the continuous collection of raw data on the current system state.

3) Virtual Layer (Digital Twin): a high-fidelity discrete-event simulation model of the shop floor, mirroring physical production with minimal time lag [22].

4) Optimization Engine: a computational decision-making engine based on the proposed mathematical model and the NSGA-II algorithm.

The implementation of the Digital Twin concept fundamentally changes the mechanism for calculating objective functions. The role of the virtual layer is to act as a "fitness function evaluator" for the evolutionary algorithm [23]. The NSGA-II algorithm generates a population of potential control vectors U_Σ (including various transport batch sizes V_{batch}, logistics routes Path, and cutting modes v, Sz). Instead of calculating cycle time (C_{max}) and total costs (C_Σ) using rigid analytical formulas, the optimizer translates these parameters into the Digital Twin (Fig. 7).

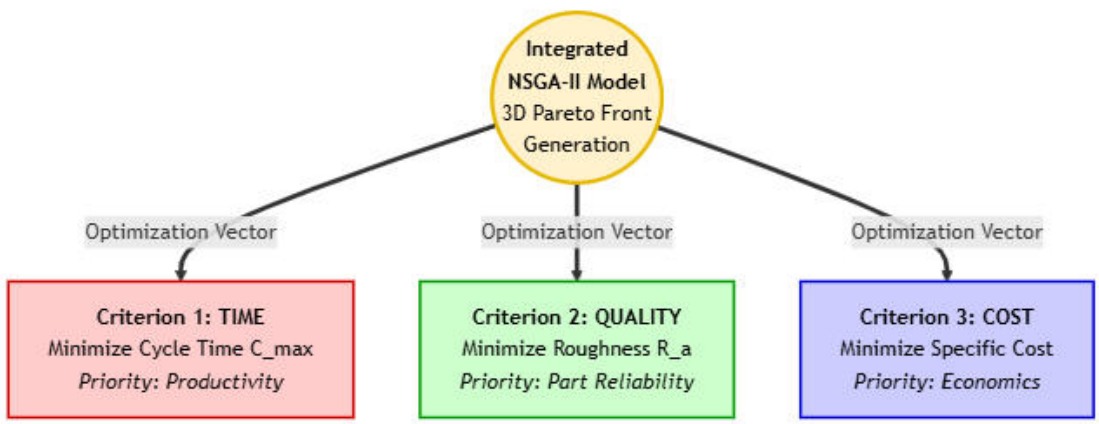

Fig. 7 - Architecture of a closed-loop management system for a production and logistics system based on Digital Twin technology

The model runs virtual production using proposed scenarios, taking into account the actual state of the workshop at a given point in time (for example, the occupancy of a specific buffer or the current wear of a milling cutter), and returns highly accurate performance criteria values to the algorithm. From a mathematical perspective, the static constants in the objective functions are transformed into dynamic variables.

Thus, the six-level process model developed in previous studies is integrated with the macro-level-the logistics flow optimization model-and the set of basic structural elements of the logistics system can be represented as follows (14):

$$L_{Sys}^{Log/bas} = \left\{ W_{St}^{Log}, \{B_k^{Log} \in V\}, \{Tr_v^{Log} \in L_{Sys}^{Log}\}, Path_{i,j}^{Log} \in E \right\} \quad (14)$$

where Tr_v^{Log} - parametric model of the v-th vehicle (AGV).

The mathematical interpretation of logistic optimization will be represented by a set of parameters for controlling the logistic process for the z-th product (UL_{ogz}), forming the vector (15):

$$U_{Log}^z = \langle V_{batch}^z, x_{i,j}^{z,v}, \tau_{wait}(B_k), v_{trans}^v \rangle \quad (15)$$

where V_{batch}^z - volume of the transfer lot;

$x^{z,v}_{i,j}$ - Boolean routing variable (x ∈ {0,1});

$\tau_{wait}(B_k)$ - batch shelf life;

v_{trans}^v - transport speed.

The system's state will be assessed using the following global vector criteria.

1. The integral criterion of logistic time, taking into account integration with the Digital Twin [24], the waiting time is calculated as the dynamic integral of the difference in the intensities of the incoming λ(t) and outgoing μ(t) flows (16):

$$T_{\Sigma}^{log}(U_{Log}) = \sum_{z=1}^{Z} \sum_{i,j \in V} \sum_{v=1}^{V_{total}} \left(\frac{D_{i,j}}{v_{trans}^v} \cdot x_{i,j}^{z,v} \right) + \sum_{k=1}^{K} \int_{t_0}^{C_{max}} \max\left(0, \frac{Q_k(t) - Cap(B_k)}{\mu_k(t)}\right) dt \to \min \quad (16)$$

where $D_{i,j}$ - distance;

$Q_k(t)$ - queue length;

$Cap(B_k)$ - maximum capacity of the k-th buffer.

2. Global Logistics Cost Criteria (17):

$$C_{\Sigma}^{log}(U_{Log}) = \sum_{v=1}^{V_{total}} \int_0^{C_{max}} P_v\left(v_{trans}^v(t), M(V_{batch})\right) \cdot c_e dt + \sum_{z=1}^{Z} \int_0^{C_{max}} V_{batch}^z(t) \cdot c_h dt \to \min \quad (17)$$

where P_v - AGV power consumption function depending on the batch weight $M(V_{batch})$;

c_h - specific cost of storing products.

The operation of a mathematical logistics model is subject to strict physical and topological constraints. The key constraint is the integrating synchronization condition, linking the technological microlevel with the logistical macrolevel (18):

$$T_{start}^{p,z} \geq T_{finish}^{p-1,z} + \sum_{v} \left(\frac{D_{p-1,p}}{v_{trans}^v} \cdot x_{p-1,p}^{z,v} \right) + \tau_{wait}(B_{p-1}) \quad (18)$$

Equation (18) guarantees that the pth process operation cannot begin until the previous operation (p − 1) is fully completed and the batch is delivered.

Incorporating Digital Twin algorithms [25] into this model enables real-time adjustment of the U_{Log}^z vector.

To verify the model, a computational experiment was conducted using data from the "Body" part machining area. The NSGA-II algorithm was implemented in Python. A discrete-event Digital Twin model was used as the virtual environment. The verification results are presented in Figure 8.

An analysis of the optimized Pareto solution demonstrated the superiority of the proposed approach. Through structural optimization of transitions, automated setups, and Vbatch batch size synchronization, the labor intensity of the Cmax production cycle decreased by 19.8%, while the machining accuracy of critical surfaces increased by 16.4%.

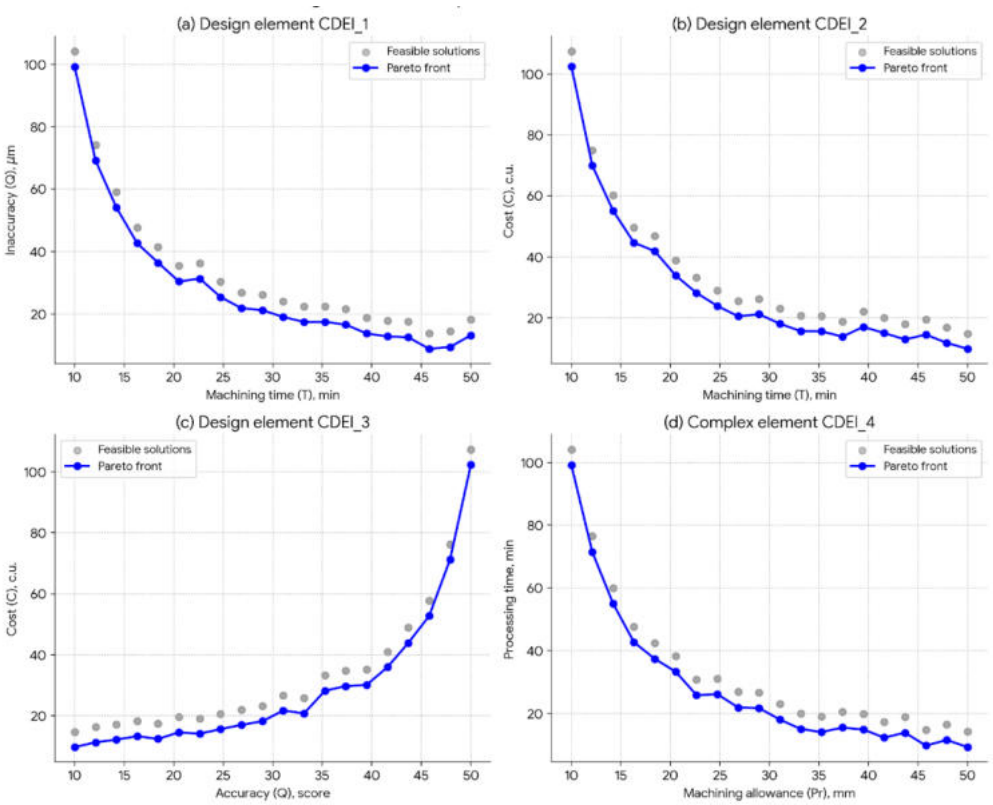

Fig. 8 - Pareto-optimal solutions for CDEI 1-4

This symbiosis of simulation modeling and evolutionary optimization (DT-driven NSGA-II) allows the algorithm to generate a Pareto frontier based not on idealized equipment specifications, but on its actual technical condition, balancing the cost of moving large batches with the time capital is tied up in work in progress.

Conclusion

This study addresses the pressing scientific and practical challenge of overcoming the isolation of production preparation processes and intra-shop logistics. An integrated six-level model of structural-parametric optimization was developed and mathematically substantiated, encompassing both the microlevels of physical part formation and the macrolevel of production and logistics network management.

Based on the results of the study, the following key conclusions were formulated:

1. It was demonstrated that isolated optimization of cutting conditions at local work centers without considering the throughput of the transport system leads to a shift in bottlenecks and an increase in work in progress. To comprehensively address this problem, it was proposed to use topological graph models and evolutionary optimization techniques.

2. Adaptation of the NSGA-II algorithm enabled the effective resolution of multi-criteria conflicts in Pareto space. The resulting set of non-dominated solutions provides decision makers with a flexible tool for finding a compromise between production cycle time, logistics costs, and machining quality. Using the "Case" component as an example, it was demonstrated that comprehensive optimization reduces overall production labor intensity by 19.8% while increasing the machining accuracy of critical surfaces by 16.4%.

3. The transition to cyber-physical control was theoretically substantiated and formalized. Integration of the developed mathematical model with Digital Twin technology enables the replacement of static standard calculations with dynamic simulation evaluation, making the system resilient to stochastic production disturbances (tool wear, transport delays).

4. Future research areas include scaling the developed methodology for multi-product, small-batch production and integrating predictive analytics algorithms to predict process equipment failures.

Funding. This research is funded by the Science Committee of the Ministry of Science and Higher Education of the Republic of Kazakhstan under grant AP23490796 “Development of digital models of the production process based on multi-criteria analysis of BigData management within the framework of technological preparation of production of mechanical engineering enterprises” (2024–2026)

References

1. Savelyeva N., Nikonova, T., Zhetessova, G., Irina, K., Yurchenko, V., Černašėjus, O., Zharkevich O., Dandybaev E., Berg, A., Vassenkin S.,et al. Implementation of Simulation Modeling of Single and High-Volume Machine-Building Productions //Designs, 2024, 8(2), 24. https://doi.org/10.3390/designs8020024
2. Khrustaleva I.N., Lyubomudrow S.A., Tolstoles A.A. Automation of technological preparation of single and small-scale production using simulation modeling //IOP Conference Series: Earth and Environmental Science, 2019, 378(1), 012060DOI: 10.1088/1755-1315/378/1/012060.
3. Khrustaleva I., Khrustalev M., Brovkina Ya., Khokhlovskiy V., Shkodyrev V. The Model for optimizing cutting parameters for processing products on metal-cutting machines //Cybernetics and Physics 2024, Vol.13, 2, 111-122.
4. Yang B. Research on Vehicle Detection and Recognition Technology Based on Artificial Intelligence //Microprocessors and Microsystems 2023, 104937, https://doi.org/10.1016/j.micpro.2023.104937
5. Cakir A., Akın Ö., Deniz H.F. et al. Enabling real time big data solutions for manufacturing at scale // J Big Data, 2022, 9, 118 https://doi.org/10.1186/s40537-022-00672-6.
6. Ponsi F., Bassoli E., Vincenzi L. A multi-objective optimization approach for FE model updating based on a selection criterion of the preferred Pareto-optimal solution //Structures, 2021, Volume 33, 916-934, https://doi.org/10.1016/j.istruc.2021.04.084
7. Oliveira L., Paiva A., Campos P., Paiva, E., Balestrassi P. P. Prediction capability of Pareto optimal solutions: A multi-criteria optimization strategy based on model capability ratios //Precision Engineering, 2019, Volume 59, 185-210, https://doi.org/10.1016/j.precisioneng.2019.06.008.
8. Hu,Y., Qu Y., Li, W., Huang Y. A Pareto Front searching algorithm based on reinforcement learning for constrained multiobjective optimization //Information Sciences 2025, Volume 705, 121985, https://doi.org/10.1016/j.ins.2025.121985.
9. Sedak M., Rosić M., Rosić B. Multi-Objective Hybrid Sailfish Optimization Algorithm for Planetary Gearbox and Mechanical Engineering Design Optimization Problems //CMES - Computer Modeling in Engineering and Sciences, 2025, Volume 142, Issue 2, 2111-2145, https://doi.org/10.32604/cmes.2025.059319.
10. Selvarajan L.,Venkataramanan K., Nair, A., Srinivasan V.P. Simultaneous multi-response Jaya optimization and Pareto front visualization in EDM drilling of $MoSi_2$-SiC composites //Expert Systems with Applications, 2023, Volume 230, 120669, https://doi.org/10.1016/j.eswa.2023.120669.
11. Ravichandran S., Manoharan P., Sinha D.K., Jangir P., Abualigah L., Alghamdi T.A.H. Multi-objective resistance-capacitance optimization algorithm: An effective multi-objective algorithm for engineering design problems //Heliyon 2024, Volume 10, Issue 17, e35921, https://doi.org/10.1016/j.heliyon.2024.e35921.
12. Zhetessova G.S., Zharkevich O.M., Kozhanov M.G., Khrustaleva I.N. Method for Optimizing the Parameters of Mechanical Processing of Holes to Ensure Cutting Tool Stability and Cost-Effective Machining // Material and Mechanical Engineering Technology, №3, 2025, 84-89
13. Nelfiyanti N., Mohamed N., Rashid MFFA, Ramadhan A.I. Parameters of effects in decision making of automotive assembly line using the Analytical Hierarchy Process method //CIRP Journal of Manufacturing Science and Technology, 2022, Volume 37, 370-377, https://doi.org/10.1016/j.cirpj.2022.02.018.
14. Nurzhanova O., Zharkevich O., Berg A., Zhukova A., Mussayev M, Buzauova T., Abdugaliyeva G., Shakhatova A. Evaluation of the Structural Strength of a Prefabricated Milling Cutter with Replaceable inserts During Machining // Material and Mechanical Engineering Technology, №4, 2023, 10-17
15. Zio S.D., Gordon T.J. Exploring a method to reduce inconsistency in the group Analytic Hierarchy Process using the Delphi method and Nudge theory //Futures, 2024, Volume 161, 103413, https://doi.org/10.1016/j.futures.2024.103413
16. Guidi G., Goffo G., Violante A.C. Application of the Analytic Hierarchy Process (AHP) method to identify the most suitable approach for managing irradiated graphite //Nuclear Engineering and Technology, 2024, Volume 56, Issue 11, 4820-4825, https://doi.org/10.1016/j.net.2024.06.045.
17. Wątróbski J., Karczmarczyk A., Rymaszewski S. Multi-criteria decision making approach to production line optimization //Procedia Computer Science 2020, Volume 176, 3820-3830, https://doi.org/10.1016/j.procs.2020.09.005.
18. Stoycheva S., Marchese D., Paul C., Padoan, S., Juhmani, A., Linkov I. Multi-criteria decision analysis framework for sustainable manufacturing in automotive industry Journal of Cleaner Production, Volume 187, 2018, 257-272, https://doi.org/10.1016/j.jclepro.2018.03.133.
19. Zhetessova G., Khrustaleva I., Shkodyrev V., Zharkevich O., Kanatova A., Kozhanov M., Tattimbetova G., Abdugalieva G. Model of Optimization of Process Parameters for Machining of Separate Design Elements of the Product //Applied Sciences Switzerland, 2025, 15(10), 5395
20. Ren, X., Zhang, W., Liu, X., Li, Z., He, Y. Digital twin-driven dynamic scheduling in flexible job shop considering worker factors towards Industry 5.0. //Computers & Industrial Engineering, 2023, 185, 109846. https://doi.org/10.1016/j.cie. 2023.109846
21. Ding, Y., Li, L. Optimization Method for Digital Twin Manufacturing System Based on NSGA-II. International //Journal of Advanced Computer Science and Applications (IJACSA), 2024, 15(4). http://dx.doi.org/10.14569/IJACSA.2024. 01504100
22. Wang, J., et alResearch Review on Workshop Scheduling for Intelligent Manufacturing: Digital Twin Modeling, Optimization Algorithm, and System Architecture //Machines, 2024, 12(11), 1021. https://doi.org/10.3390/machines12111021
23. Leng, J., et al. Digital twins-based smart manufacturing system design in Industry 4.0: A review. Journal of Manufacturing Systems, 2023, 60, 119-137. https://doi. org/10.1016/j.jmsy.2021.05.011
24. Zhetessova G.S., Zharkevich, O. M., Kanatova, A.T., Khrustaleva I.N., Shkodyrev V.P.Additive Optimization Method for Choosing CNC Machines for Technological Preparation of Machine-Building Production //Applied Sciences, 2024(3), 32–37
25. Liu, Y., et al. Dynamic routing and batch sizing of AGVs in flexible manufacturing systems using deep reinforcement learning and digital twins //Robotics and Computer-Integrated Manufacturing, 2023, 82, 102521.

26. Zheng, P., Wang, J. Multi-objective optimization of integrated process planning and scheduling considering logistics constraints //Journal of Manufacturing Systems, 2025, 68, 45-62.

Information of the author

Zhetessova Gulnara Santayevna, d.t.s., professor, Abylkas Saginov Technical University
e-mail: g.zhetessova@ktu.edu.kz

Khrustaleva Irina Nikolayevna, c.t.s., docent, Peter the Great St. Petersburg Polytechnic University
e-mail: irina.khrustaleva@mail.ru

Zharkevich Olga Mikhailovna, c.t.s., professor, Abylkas Saginov Technical University
e-mail: o.zharkevich@ktu.edu.kz

Kanatova Aliya Talgatovna, PhD, associate professor, Astana IT University
e-mail: shakhatovaa@list.ru

Kozhanov Murat Gliaskarovich, m.t.s, Institute of Digitalization and Innovation, Academy of Public Administration under the President of the Republic of Kazakhstan
e-mail: spark@mail.ru

DOI 10.52209/2706-977X_2026_3_141 IRSTI 55.31.29 UDC 621.9.02

Design and Structural Assessment of a Special Boring Tool with an Inclined Clamping Mechanism

Karsakova N., Mussayev M.*, Tattimbek G., Dauletova F.
Abylkas Saginov Karaganda Technical University, Karagandy, Kazakhstan
*corresponding author

Abstract. The machining of large-diameter stepped holes requires high rigidity and positional stability of the cutting tool, particularly when boring bars with considerable overhang are employed. In addition to the structural characteristics of the boring bar, the cutting element clamping mechanism influences load transfer and displacement of the cutting edge during machining. This study presents the design and structural assessment of a special boring tool incorporating an inclined clamping mechanism. A three-dimensional model of the developed tool was created and subjected to finite element analysis to evaluate the deformation behavior of the cutting element during boring of a Ø295 mm hole. The structural response was assessed using total deformation and directional deformation components along the X, Y, and Z axes. The total deformation ranged from 0.17905 to 0.23775 mm, with a maximum value of 0.23775 mm. Directional analysis revealed maximum absolute displacements of 0.20932 mm, 0.094113 mm, and 0.088974 mm along the X, Y, and Z axes, respectively. The X-axis was identified as the dominant deformation direction, with displacement approximately 2.22 and 2.35 times greater than those along the Y- and Z-axes, respectively. The results demonstrate the importance of considering directional deformation when assessing the structural behavior of cutting assemblies and provide a quantitative basis for evaluating the rigidity and positional stability of the proposed inclined clamping mechanism.

Keywords: boring tool, boring bar, inclined clamping mechanism, stepped hole, finite element analysis, directional deformation, structural rigidity

Introduction

Large-diameter stepped holes are widely used in heavy machinery, mining equipment, power engineering, and transport systems for the installation of shafts, bearings, bushings, and other critical mechanical components. Unlike conventional cylindrical bores, stepped holes require machining of several coaxial diameters within a single workpiece while maintaining strict dimensional tolerances, positional accuracy, and high surface quality. Such requirements considerably increase the demands on tool rigidity, particularly during boring operations involving long overhangs. As the overhang-to-diameter ratio increases, the stiffness of the boring bar decreases significantly, making the machining process more susceptible to elastic deformation, self-excited vibration, and chatter, which ultimately reduce machining accuracy and accelerate tool wear [1–4].

The dynamic behaviour of boring bars has therefore been the subject of extensive investigations for several decades. Previous studies demonstrated that insufficient structural stiffness is one of the principal causes of vibration instability during deep-hole boring. Numerous analytical, numerical, and experimental studies have shown that chatter vibration not only deteriorates the surface finish and dimensional accuracy of machined holes but also reduces tool life and limits machining productivity [1, 5–7]. Consequently, improving the rigidity and dynamic stability of boring tools remains one of the major challenges in precision boring technology.

To overcome these problems, researchers have proposed various structural solutions aimed at suppressing vibration and improving machining stability. These include the application of passive and active damping systems, tuned mass dampers, particle damping, viscoelastic elements, piezoelectric actuators, optimized internal structures, and composite boring bars [2–4, 8–10]. Recent studies have also focused on variable-stiffness vibration absorbers and nonlinear dynamic optimization of boring bars, demonstrating considerable improvements in machining stability under severe cutting conditions [2, 3, 8].

Besides the rigidity of the boring bar itself, the cutting insert clamping mechanism plays a critical role in maintaining machining accuracy. The clamping assembly transfers cutting forces from the insert to the tool body while ensuring stable positioning of the cutting edge throughout the machining process. Local deformation of the clamping mechanism may cause micro-displacements of the cutting insert, resulting in increased vibration, reduced dimensional accuracy, and deterioration of surface quality. Despite the considerable attention devoted to vibration suppression of boring bars, comparatively fewer studies have investigated the structural behaviour of the cutting insert clamping assembly itself, particularly in special-purpose boring tools intended for machining large-diameter stepped holes.

Conventional industrial boring tools employ various insert clamping systems, including screw, pin, wedge, and cartridge mechanisms. These designs are primarily intended to simplify insert replacement and improve operational reliability. However, special boring tools designed for large-diameter stepped holes frequently require customized clamping arrangements dictated by geometric constraints and high cutting loads. The structural response of such

clamping systems under operational loading has received relatively limited attention in the literature, although deformation of the clamping assembly directly influences the positional stability of the cutting edge and, consequently, machining accuracy. Therefore, further investigations into the structural behaviour of specialized clamping mechanisms are required to support the development of more rigid and reliable boring tools.

Accordingly, the objective of the present study is to develop a special boring tool incorporating an inclined clamping mechanism and to evaluate its structural behaviour using finite element analysis. A three-dimensional model of the proposed tool was developed and analysed under operational loading conditions to determine the total deformation and directional displacements of the cutting insert assembly. The obtained results provide a structural assessment of the proposed design and contribute to the further development of special boring tools intended for machining large-diameter stepped holes.

1. Design of the Special Boring Tool

1.1. Tool Design and Clamping Mechanism

A special boring tool was developed for machining large-diameter stepped holes in heavy-duty mechanical components. The design was intended to improve the rigidity of the cutting assembly while ensuring reliable positioning of the cutting insert under operational loading. Unlike conventional commercial boring tools, the proposed design incorporates an inclined clamping mechanism that provides stable fixation of the cutting insert and facilitates its replacement without altering the overall configuration of the tool.

The general configuration of the developed boring tool is presented in Figure 1. The tool consists of a cylindrical boring bar body, a tool holder, a replaceable carbide insert, an inclined clamping element, and fastening screws. The cutting insert is mounted in a specially machined seat located at the front end of the boring bar. The clamping mechanism secures the insert by transmitting the tightening force from the fastening screws through the inclined contact surfaces of the clamping element to the tool holder, thereby providing reliable fixation during machining.

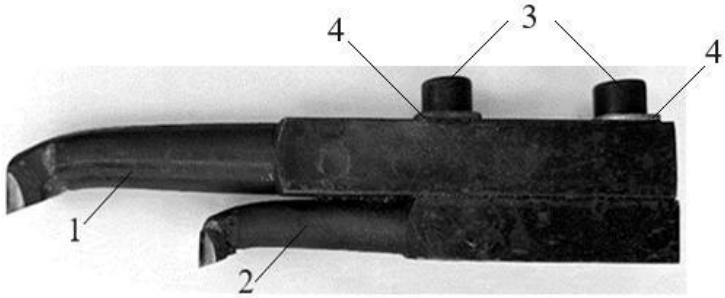

Fig. 1. - Developed special boring tool with an inclined clamping mechanism.

The inclined clamping mechanism was selected because it enables simultaneous generation of axial and radial clamping forces. Compared with conventional screw clamping systems, this configuration improves the contact between the mating surfaces and reduces the possibility of local displacement of the cutting insert during operation. As a result, the rigidity of the cutting assembly is expected to increase, contributing to improved positional stability of the cutting edge under machining loads. Similar design approaches have previously been adopted in the development of special boring tools intended to improve machining stability and reduce vibration [11, 12].

A detailed view of the clamping assembly is shown in Figure 2. The tool holder is positioned within the mounting groove of the boring bar and fixed by fastening screws. The inclined contact surfaces ensure uniform transmission of the clamping force while maintaining accurate positioning of the cutting insert. Owing to the modular design, the insert can be replaced without disassembling the entire boring tool, reducing maintenance time and simplifying tool servicing.

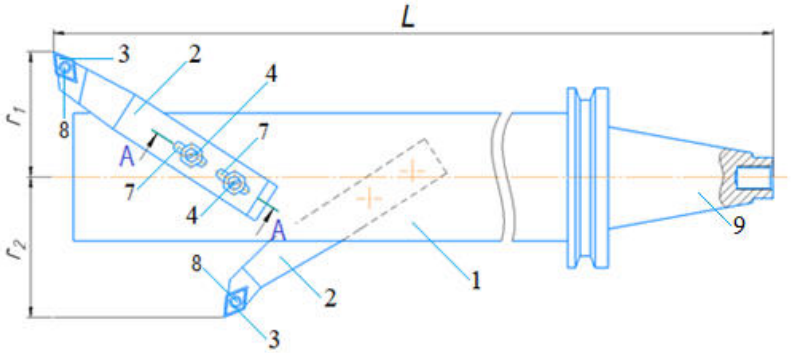

Fig. 2. - Detailed view of the inclined clamping mechanism.

The proposed structural configuration was developed using a computer-aided design (CAD) environment before numerical analysis. The three-dimensional model reproduced all principal structural elements of the boring tool, including the boring bar body, tool holder, cutting insert, inclined clamping mechanism, and fastening screws. This model served as the basis for subsequent finite element analysis aimed at evaluating the deformation characteristics of the developed design under operational loading conditions [13-15].

2. Finite Element Modeling

2.1 Three-Dimensional Model

A three-dimensional model of the developed special boring tool was created in KOMPAS-3D and subsequently used as the geometric basis for finite element analysis. The model reproduced the principal structural elements involved in the transmission of the machining load, including the boring bar body, the cutting element, and the inclined clamping assembly. The geometry of the model corresponded to the developed tool design presented in the previous section.

The three-dimensional representation of the boring tool is shown in Figure 3. Particular attention was paid to the cutting zone and the clamping assembly because displacement of the cutting element under external loading directly affects its positional stability relative to the machined surface. In this respect, the numerical model was intended primarily to evaluate the deformation response of the developed tool rather than to perform a strength assessment of its individual components.

The developed geometric model was imported into ANSYS for finite element analysis. The numerical assessment focused on the total deformation and the directional deformation components along the X, Y, and Z axes. This approach makes it possible to evaluate both the overall displacement of the cutting element and its displacement in individual coordinate directions, which is important for assessing the structural rigidity of the proposed clamping arrangement.

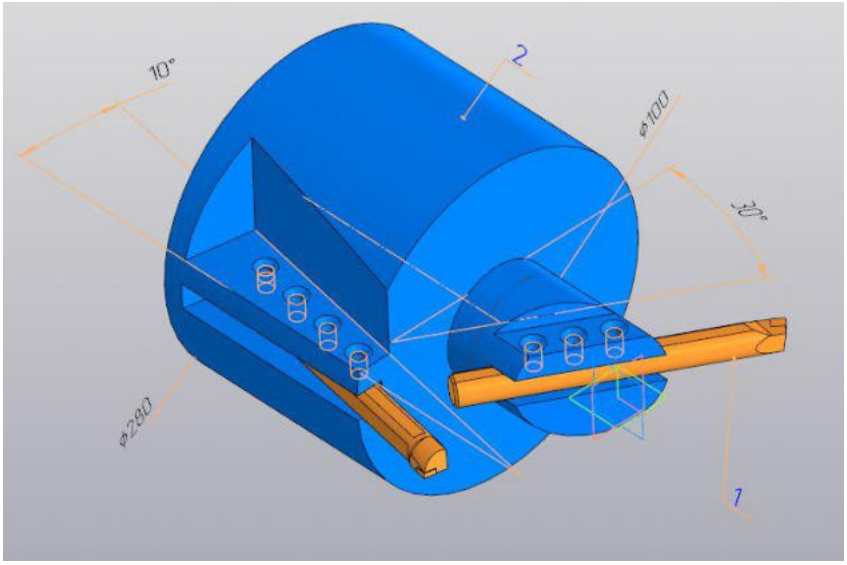

Fig. 3. - Three-dimensional CAD model of the developed special boring tool

2.2 Finite Element Model and Mesh

The finite element model of the developed boring tool was prepared in ANSYS using the three-dimensional geometry described in Section 3.1. The numerical model was constructed to evaluate the deformation response of the tool and, in particular, the displacement of the cutting element resulting from the applied machining load.

The geometry was discretized using a three-dimensional finite element mesh, as shown in Figure 4. The mesh covered the complete computational model and reproduced the geometry of the boring bar and the cutting region. Particular attention was given to the region near the cutting element, since this part of the structure directly receives the external machining load and its displacement is of primary interest for evaluating the positional stability of the cutting edge.

The finite element analysis was focused on deformation rather than on the strength or failure of the tool components. Accordingly, the numerical outputs considered in the present study were the total deformation and the directional deformation components along the X, Y, and Z coordinate axes. The total deformation characterizes the resultant displacement of the model, whereas the directional components make it possible to distinguish the contribution of displacement in each coordinate direction. Such separation is particularly important for a boring tool

because displacement of the cutting edge in different directions may affect the position of the tool relative to the machined surface differently.

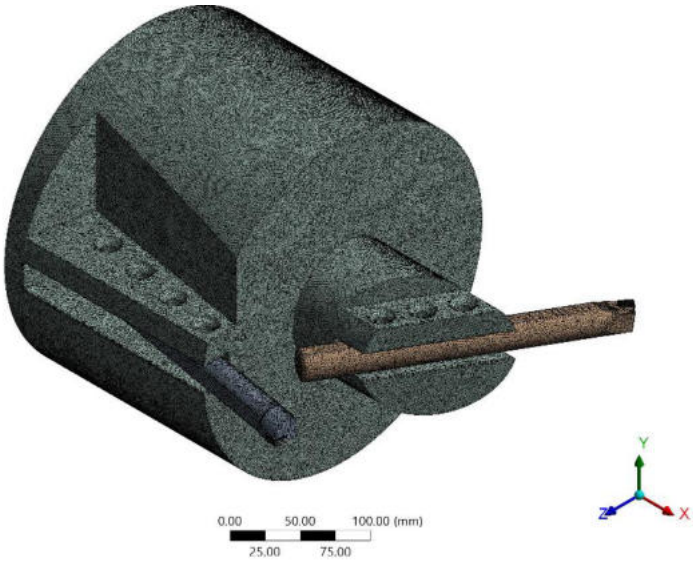

Fig. 4. - Finite element mesh of the developed special boring tool.

2.3 Boundary Conditions and Loading

The boundary conditions of the finite element model were defined to represent the loading scheme of the boring tool during machining of Ø295 mm hole. The mounting region of the boring bar was constrained to reproduce its fixation in the machine-tool holder. For the static structural analysis, a resultant cutting force of 1500 N was adopted as the simulated machining load and applied to the cutting insert in the cutting region of the tool.

The applied load was transmitted from the cutting element through the clamping assembly to the boring bar body. This loading scheme was used to evaluate the deformation response of the developed tool and the positional stability of the cutting region. Since the primary objective of the numerical analysis was to assess the deformation behavior of the tool rather than its strength or failure resistance, the resulting displacement was considered as the main response parameter.

The applied load was transmitted from the cutting element through the clamping assembly to the boring bar body. This loading scheme was used to evaluate the deformation response of the developed tool and the positional stability of the cutting region. Since the primary objective of the numerical analysis was to assess the deformation behavior of the tool rather than its strength or failure resistance, the resulting displacement was considered as the main response parameter.

The numerical results were evaluated in terms of total deformation and directional deformation along the X, Y, and Z coordinate axes. The total deformation represents the resultant displacement of the analyzed structure, whereas the directional components provide information on the displacement of the cutting region in individual spatial directions.

3. Results and Discussion

The finite element analysis was used to evaluate the deformation behavior of the cutting element of the developed boring tool during machining of a Ø295 mm hole. The numerical results were analyzed in terms of total deformation and directional deformation along the X, Y, and Z axes. The corresponding deformation fields are presented in Figures 5–8, while the characteristic values obtained from the numerical analysis are summarized in Table 1.

Table 1. Deformation characteristics of the cutting element obtained from finite element analysis

Deformation component	Maximum value (mm)	Minimum value (mm)	Maximum absolute value (mm)
Total deformation	0.23775	0.17905	0.23775
X-axis	−0.14805	−0.20932	0.20932
Y-axis	−0.068643	−0.094113	0.094113
Z-axis	−0.047977	−0.088974	0.088974

The distribution of total deformation is shown in Figure 5. The calculated values vary from 0.17905 to 0.23775 mm, with a maximum resultant deformation of 0.23775 mm. The deformation field is non-uniform across the cutting

element, indicating that its different regions respond differently to the applied loading. The gradual variation of displacement over the analyzed geometry indicates a continuous deformation response rather than a highly localized displacement at a single point.

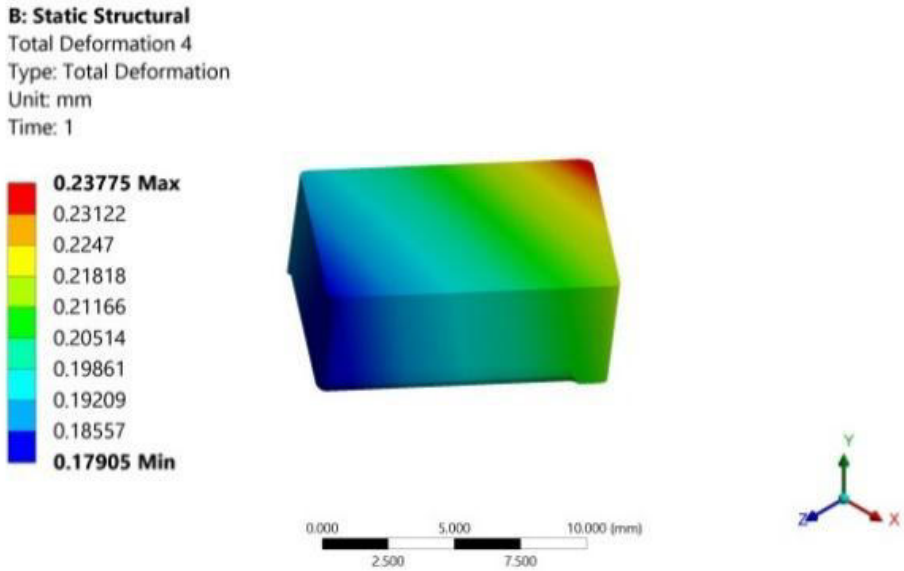

Fig. 5. - Total deformation of the cutting element during boring of a Ø295 mm hole.

Analysis of the directional components provides additional information on the spatial displacement of the cutting element. As shown in Figure 6, the deformation along the X-axis varies from −0.14805 to −0.20932 mm. The negative sign indicates that displacement occurs in the direction opposite to the positive X-axis of the global coordinate system. In terms of absolute magnitude, the maximum X-directional displacement reaches 0.20932 mm, making the X component the dominant directional deformation observed in the numerical analysis.

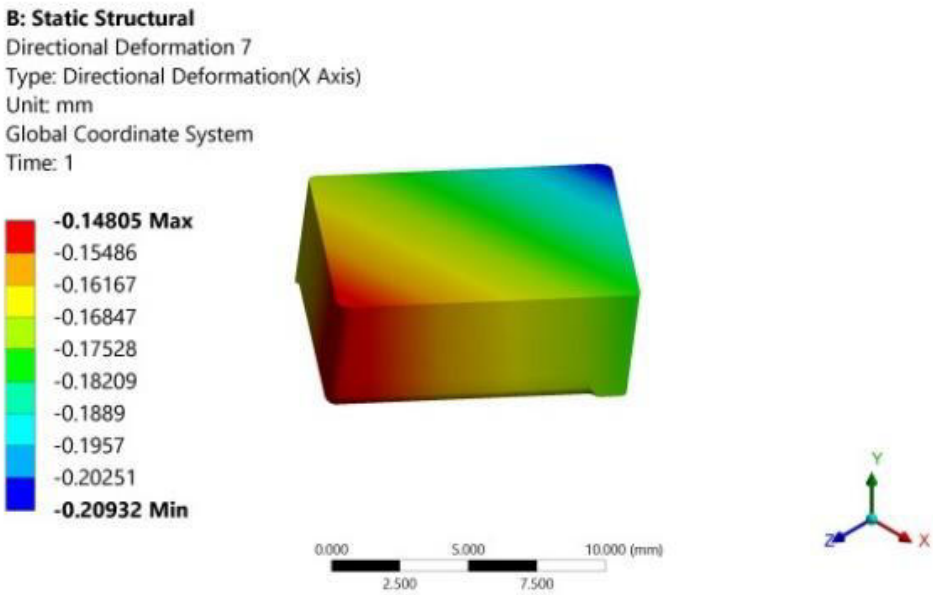

Fig. 6. - Directional deformation of the cutting element along the X-axis during boring of a Ø295 mm hole.

The deformation along the Y-axis is considerably smaller (Figure 7). The calculated values range from −0.068643 to −0.094113 mm, corresponding to a maximum absolute displacement of 0.094113 mm. This value is approximately 55% lower than the maximum absolute displacement obtained along the X-axis. The results therefore indicate that the response of the cutting element is strongly direction-dependent, with the displacement along the X-axis being substantially greater than that along the Y-axis.

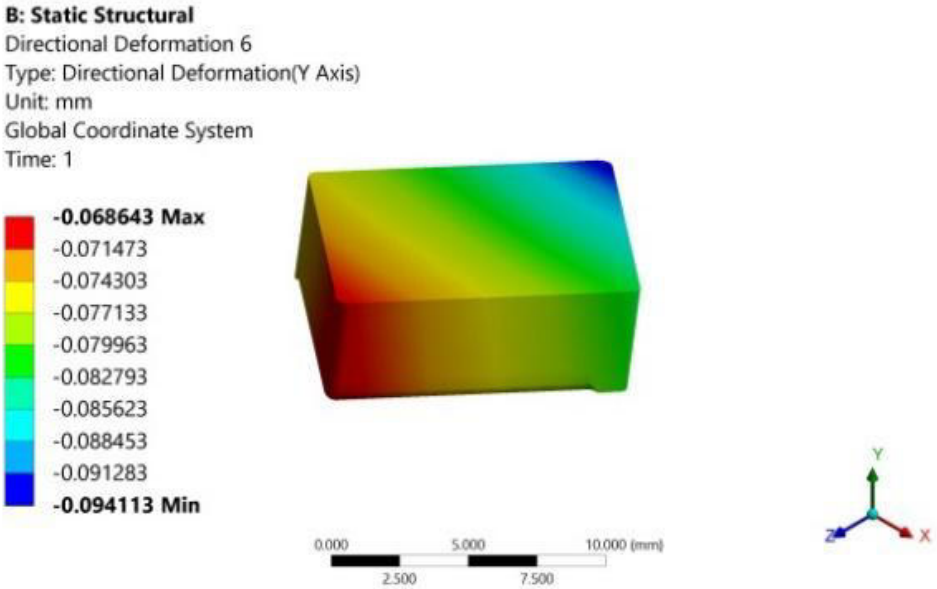

Fig. 7. - Directional deformation of the cutting element along the Y-axis during boring of a Ø295 mm hole.

A similar tendency is observed for the Z-axis component presented in Figure 8. The calculated deformation ranges from −0.047977 to −0.088974 mm, giving a maximum absolute displacement of 0.088974 mm. This represents the smallest maximum directional displacement among the three coordinate components and is approximately 57% lower than the corresponding value along the X-axis. The Y- and Z-directional displacement magnitudes are relatively close, whereas the X-axis response is clearly dominant.

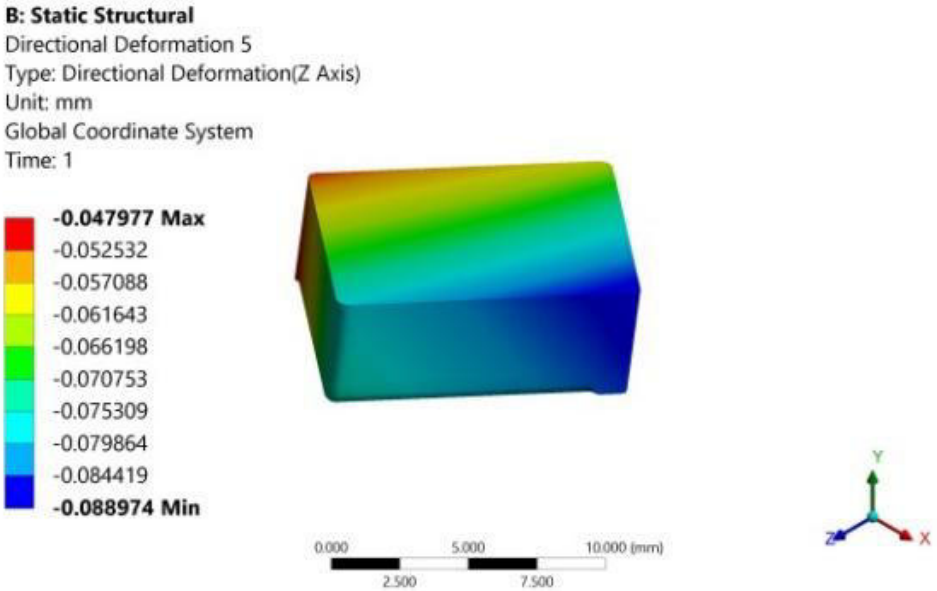

Fig. 8. - Directional deformation of the cutting element along the Z-axis during boring of a Ø295 mm hole.

The comparison of the three directional components demonstrates that the deformation behavior of the cutting element is anisotropic with respect to the adopted global coordinate system. The maximum absolute displacement along the X-axis is approximately 2.22 times that along the Y-axis and 2.35 times that along the Z-axis. Consequently, the X direction represents the principal direction of displacement under the adopted loading conditions. This result is important from the standpoint of tool design because displacement of the cutting element changes the spatial position of the cutting edge relative to the machined surface.

The resultant deformation of 0.23775 mm should therefore be considered together with its directional components rather than as an isolated parameter. The directional analysis demonstrates that most of the displacement is associated with the X component, while substantially smaller contributions are observed along the Y and Z axes. Such decomposition provides a more informative assessment of the structural response of the cutting element and makes it possible to identify the direction in which the developed assembly is most susceptible to displacement.

From a structural perspective, the obtained results demonstrate that the inclined clamping mechanism maintains the cutting element as an integrated part of the tool assembly while transferring the applied load through the contact region. At the same time, the calculated directional deformation indicates that the structural response is governed predominantly by displacement along one coordinate direction. This observation is relevant to the further development of the clamping assembly, since increasing rigidity in the dominant deformation direction may be particularly important for improving the positional stability of the cutting edge.

It should be emphasized that the present analysis evaluates the static deformation behavior of the developed tool. Therefore, the obtained results should not be interpreted as direct evidence of chatter suppression or vibration reduction. Nevertheless, static rigidity and displacement of the cutting element are important structural factors affecting the dynamic behavior of boring tools. The present results consequently provide a structural basis for assessing the proposed inclined clamping mechanism without extending the conclusions beyond the scope of the performed finite element analysis.

Conclusions

This study presented the design and structural assessment of a special boring tool incorporating an inclined clamping mechanism. The proposed design was developed for machining large-diameter stepped holes, with particular attention paid to the deformation behavior and positional stability of the cutting element. Based on the finite element analysis, the following conclusions can be drawn:

The developed boring tool employs an inclined clamping mechanism intended to provide stable positioning of the cutting element and transfer the machining load from the cutting region to the boring bar body. The proposed configuration provides a compact structural arrangement suitable for special boring operations involving large-diameter stepped holes.

Finite element analysis showed a non-uniform deformation distribution within the cutting element. The total deformation ranged from 0.17905 to 0.23775 mm, with the maximum resultant deformation reaching 0.23775 mm under the adopted loading conditions.

The directional deformation analysis revealed a pronounced dependence of the structural response on the coordinate direction. The maximum absolute displacement along the X-axis was 0.20932 mm, compared with 0.094113 mm along the Y-axis and 0.088974 mm along the Z-axis.

The X-axis was identified as the dominant deformation direction. The maximum absolute X-directional displacement was approximately 2.22 times greater than that along the Y-axis and 2.35 times greater than that along the Z-axis. This indicates that the rigidity of the cutting assembly in the X direction is particularly important for maintaining the positional stability of the cutting edge.

The decomposition of the resultant deformation into directional components provided a more detailed assessment of the structural behavior of the developed tool than consideration of total deformation alone. Such an approach allows the principal displacement direction to be identified and provides useful information for evaluating the structural performance of the clamping assembly.

The present results provide a structural assessment of the proposed inclined clamping mechanism based on static deformation analysis. Since dynamic, modal, and experimental investigations were outside the scope of the present study, the obtained results should not be interpreted as direct evidence of vibration or chatter suppression. Nevertheless, the identified deformation characteristics provide a basis for evaluating the rigidity and positional stability of the developed cutting assembly. Future work should include experimental modal testing and cutting trials under actual boring conditions to validate the static finite element analysis results and to assess the dynamic behavior of the developed boring tool.

Funding. This research was funded by the Committee of Science of the Ministry of Science and Higher Education of the Republic of Kazakhstan, Grant No. AP27511047.

References

[1] Sun J., Sun C., Yan Z. State-of-art, challenges, and outlook on deep hole boring: Chatter suppression, tool wear monitoring, and error measurement // International Journal of Advanced Manufacturing Technology. – 2025, Vol. 136, pp. 2075–2105. DOI: 10.1007/s00170-025-15007-x.

[2] Guan Y., Yu G., Hu Q., Xu D., Xu J., Lushchyk P. Vibration Characteristics Analysis of Boring Bar with Tunable Dynamic Vibration Absorber // Materials. – 2025, Vol. 18, Issue 6, Article 1324.

[3] Wang B. et al. Research Progress and Application of Vibration Suppression Technologies for Damped Boring Tools // Machines. – 2025.

[4] Oezkaya E. et al. Design and Performance Study of a Bionic Damping Boring Bar Based on the Woodpecker // CIRP Journal of Manufacturing Science and Technology. – 2025.

[5] Li H., Xia Y., Su B., et al. Ultrasonic Vibration-Assisted Chatter Suppression for Deep Hole Boring of Stainless Steel // International Journal of Advanced Manufacturing Technology. – 2024, Vol. 131, pp. 1691–1703. DOI: 10.1007/s00170-024-13016-w.

[6] Zhao W., Zhang Q., Li Y., Jing S. Lateral Random Vibration of Boring Bar for BTA Deep-Hole Process // Journal of Vibration and Shock. – 2024, Vol. 43, Issue 3, pp. 46–57.
[7] Li L., Yang D., Cui Y. Optimization of Machining Performance in Deep Hole Boring: A Study on Cutting Tool Vibration and Dynamic Vibration Absorber Design // Advances in Production Engineering & Management. – 2023, Vol. 18, Issue 3, pp. 371–380.
[8] Nonlinear System Optimization of Cutting Tools with Dynamic Vibration Absorbers in Deep Hole Boring: A Stability Analysis // Alexandria Engineering Journal. – 2025, Vol. 112, pp. 246–253.
[9] Matsubara A., Maeda M., Yamaji I. Vibration Suppression of Boring Bar by Piezoelectric Actuators and LR Circuit // CIRP Annals. – 2014, Vol. 63, Issue 1, pp. 373–376.
[10] Suyama D., Diniz A.E., Pederiva R. The Use of Carbide and Particle-Damped Bars to Increase Tool Overhang in the Internal Turning of Hardened Steel // International Journal of Advanced Manufacturing Technology. – 2016, Vol. 86, pp. 2083–2092.
[11] Song Q., Shi J., Liu Z. et al. Boring Bar with Constrained Layer Damper for Improving Process Stability // International Journal of Advanced Manufacturing Technology. – 2016, Vol. 83, pp. 1951–1966. DOI: 10.1007/s00170-015-7670-5.
[12] Takahashi W., Suzuki N., Shamoto E. Development of a Novel Boring Tool with Anisotropic Dynamic Stiffness to Avoid Chatter Vibration in Cutting: Part 1: Design of Anisotropic Structure to Attain Infinite Dynamic Stiffness // Precision Engineering. – 2021, Vol. 68, pp. 57–71. DOI: 10.1016/j.precisioneng.2020.11.007.
[13] Kępczak N., Bechciński G., Rosik R. Operating Properties of Deep Hole Boring Tools with Modified Design // Materials. – 2024, Vol. 17, Issue 7, Article 1551. DOI: 10.3390/ma17071551.
[14] Mussayev M., Kassymbabina D., Sherov K. Investigation of the Design of a Busbar Punching Tool Restored by Replacement of the Working Part with a Carbon Steel Insert // Material and Mechanical Engineering Technology. – 2025, No. 3, p. 16. DOI: 10.52209/2706-977X_2025_3_16.
[15] Akulovich L.M., Mendaliyeva S.I., Sherov K.T., Toshov J.B., Mussayev M.M. Study of the Influence of the Angle of Inclination of the Axis of Ferroabrasive Grains on the Productivity and Surface Roughness of the Processed Part // Material and Mechanical Engineering Technology. – 2025, No. 4, p. 86. DOI: 10.52209/2706-977X_2025_4_86
[16] Nurzhanova O., Zharkevich O., Berg A., Zhukova A., Mussayev M, Buzauova T., Abdugaliyeva G., Shakhatova A. Evaluation of the Structural Strength of a Prefabricated Milling Cutter with Replaceable inserts During Machining // Material and Mechanical Engineering Technology, №4, 2023, 10-17

Information of the authors

Nurgul Karsakova, PhD, Abylkas Saginov Karaganda Technical University
e-mail: n.karsakova@ktu.edu.kz

Medgat Mussayev, PhD, Abylkas Saginov Karaganda Technical University
e-mail: m.mussayev@ktu.edu.kz

Gulerke Tattimbek, teacher, Abylkas Saginov Karaganda Technical University
e-mail: g.tattimbek@ktu.edu.kz

Fariza Dauletova, master student, Abylkas Saginov Karaganda Technical University
e-mail: f.dauletova@ktu.edu.kz

DOI 10.52209/2706-977X_2026_3_149 IRSTI 55.20.17 UDC 621.9.048.4

Surface Layer Formation of a 12KH18N10T Stainless Steel Toothed Base During Wire Electrical Discharge Machining

Kombayev K.K., Azamatov B.N., Kaliyev D.I., Mukhametbek Zh.M., Gabdyssalyk R.*
D. Serikbayev East Kazakhstan Technical University, Ust-Kamenogorsk, Kazakhstan
* corresponding author

Abstract. Wire Electrical Discharge Machining (WEDM) is an effective manufacturing process for producing complex-shaped components from difficult-to-machine materials. However, the thermal effect of electrical discharges alters the structure and condition of the surface layer. The aim of this study was to investigate the surface layer formation of a 12Kh18N10T stainless steel toothed base during WEDM. Machining was performed on a DK7745 wire EDM machine using a 0.18 mm brass wire electrode and deionized water as the dielectric medium. Two machining regimes with different pulse energies were investigated. Surface morphology, recast layer microstructure, and elemental composition were characterized using optical metallography, scanning electron microscopy (SEM), and energy-dispersive X-ray spectroscopy (EDS), while the mechanical state of the surface layer was evaluated by Vickers microhardness measurements. The results showed that increasing the pulse energy promoted the formation of a more developed recast layer and a more heterogeneous surface morphology without significantly changing the concentrations of the principal alloying elements (Fe, Cr, and Ni). In addition, an increased oxygen content and a slight transfer of Cu and Zn from the brass wire electrode were observed in the near-surface region. Higher microhardness was obtained after finish machining. The practical significance of this study lies in the substantiation of WEDM regimes that ensure the required dimensional accuracy and surface integrity for manufacturing toothed components of high-precision medical positioning mechanisms.

Keywords: wire electrical discharge machining, WEDM, 12KH18N10T stainless steel, surface layer, recast layer, toothed base, surgical holder, microstructure, surface morphology.

Introduction

Modern high-precision mechanical positioning systems are widely used in instrument engineering, robotics, optical measurement systems, and medical equipment, where the accuracy of the relative positioning of components, the rigidity of the clamping, and the stability of geometric parameters directly determine the functional reliability and operational characteristics of the products [1–3]. These requirements are of particular importance for components of hinged clamping mechanisms, in which even minor deviations in shape, dimensions, or surface condition can significantly affect the precision of clamping, the smoothness of adjustment, and the durability of the assembly [4]. One such component is the toothed base of a mechanical holding system, which ensures the transmission and reliable locking of the angular position of the mating links. The design of the component under study is shown in Figure 1.

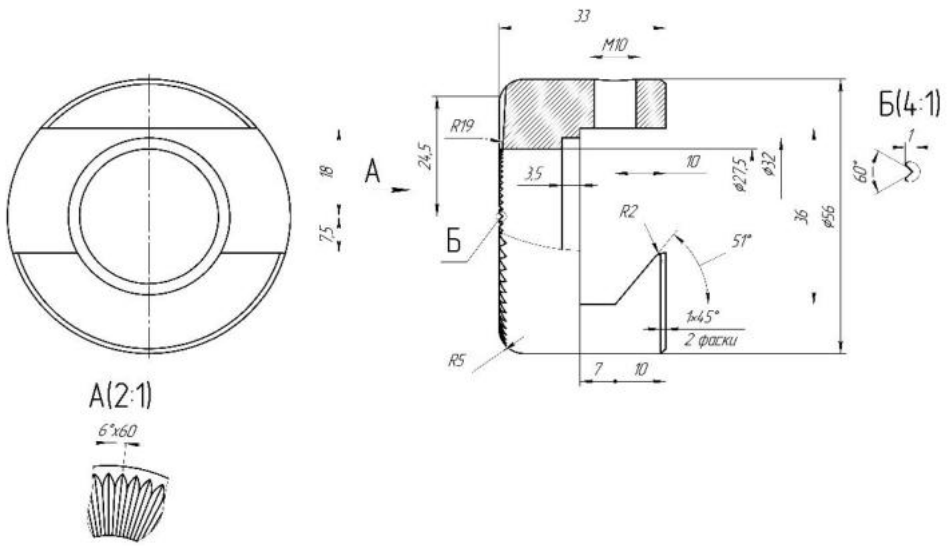

Fig. 1 - Drawing of a toothed base made of 12KH18N10T steel, manufactured using wire-cut electrical discharge machining

The geometry of the toothed base is characterized by radially arranged teeth with a profile angle of 60°, operating under conditions of repeated contact interaction. The precision with which the working surfaces of the teeth are formed directly determines the rigidity of the mechanism's locking, the level of contact stresses, and the uniformity of load distribution across the working faces, which ultimately affects the reliability and durability of the assembly [5]. Consequently, the manufacturing process for these components must meet stringent requirements to ensure geometric accuracy, minimal surface roughness, and the absence of surface-layer defects.

Corrosion-resistant austenitic steels are widely used for manufacturing such components, with 12X18H10T steel being particularly prevalent. This material is characterized by high corrosion resistance, a good balance of strength and ductility, and high operational reliability [6]. At the same time, its high ductility, intense work hardening (work hardening), increased toughness, and relatively low thermal conductivity result in poor machinability of 12X18H10T steel using traditional cutting methods, which is accompanied by increased cutting forces, accelerated tool wear, and reduced machining process stability [7, 8]. For the manufacture of details with complex geometries from difficult-to-machine materials, electrical discharge machining methods are finding increasingly widespread application; among these, wire electrical discharge machining (Wire Electrical Discharge Machining, WEDM) occupies a leading position due to its high shaping accuracy, the absence of mechanical contact with the workpiece, and the ability to machine electrically conductive materials regardless of their hardness [9–11]. Wire electrical discharge machining is based on the localized removal of material resulting from a sequence of electrical discharges between a wire electrode and the workpiece, both of which are immersed in a dielectric medium [12]. The absence of mechanical contact between the tool and the workpiece surface makes it possible to produce details with complex contours and high precision, regardless of the material's hardness and strength characteristics [13]. Thanks to these advantages, WEDM technology is widely used in the manufacture of critical components for mechanical engineering, aviation, power generation equipment, instrumentation, and various high-precision mechanical systems [14, 15].

Despite the high precision of the shaping process, WEDM is accompanied by intense localized heat exposure. The temperature in the electrical discharge zone can reach 8,000–12,000 °C, which leads to the melting and partial vaporization of the workpiece material [16]. The subsequent ultra-rapid cooling of the molten metal causes the formation of a characteristic remelted ("white") layer, whose structure differs significantly from that of the base metal [17]. This layer may contain products of recrystallization, micropores, microcracks, residual stresses, and inclusions of material from the electrode tool [18, 19]. The thickness and microstructural state of the remelted layer have a significant impact on the fatigue strength, wear resistance, and service life of parts, therefore, in the current literature, the condition of the surface layer is considered one of the most important criteria for the quality of electrical discharge machining, along with process productivity, surface roughness, and shaping accuracy [20–22].

Numerous studies on the electrical discharge machining of stainless steels, titanium, and nickel alloys have shown that electrical discharge parameters have a decisive influence on the thickness of the remelted layer, surface roughness, the magnitude of residual stresses, and the microhardness of the surface layers [23–25]. For austenitic steels, additional processes involving the diffusion of elements from the brass wire (Cu and Zn) into the workpiece's surface layer have been observed, leading to local changes in chemical composition and the formation of secondary structural components [26, 27].

Of particular interest are studies of the microstructure of the surface layer after WEDM using optical metallography, scanning electron microscopy (SEM), energy-dispersive X-ray spectroscopy (EDS), and EBSD analysis [28–30]. The results indicate that the thickness of the white layer can vary from a few to several tens of micrometers depending on the energy parameters of the process, and the resulting structure is characterized by high dispersion and significant differences from the material's original austenitic structure due to extremely high heating and cooling rates [31,35].

However, most published studies focus on heat-resistant nickel alloys such as Inconel 718, titanium alloys, and stainless steels such as AISI 304 and AISI 316 [32–34]. At the same time, the formation of the surface layer following wire-cut electrical discharge machining (EDM) of parts made of 12X18H10T steel—used in the manufacture of high-precision components for clamping and positioning mechanisms—has not been studied in sufficient detail. The analysis of the surface layer condition of gear elements is of particular scientific and practical interest, since it is the working surfaces of the teeth that bear the main contact loads and largely determine the operational characteristics of the mechanism.

In this regard, the objective of this study is to investigate the characteristics of the formation of the surface layer of a 12X18H10T steel gear base following wire-cut electrical discharge machining. To achieve this objective, an analysis of the geometric characteristics of the cut was performed; the surface morphology and microstructure of the remelted layer were investigated using optical and scanning electron microscopy; the thickness of the heat-affected zone was determined and changes in microhardness in the near-surface region were evaluated.

Materials and methods

The research was conducted at the "Smart Engineering" Competence Center of the D. Serikbayev East Kazakhstan Technical University. The subject of the study was the toothed base of a high-precision mechanical

positioning system, manufactured from a 24.5-mm-thick sheet blank of corrosion-resistant austenitic steel 12KH18H10T (Table 1). The toothed profile of the part was formed using wire-cut electrical discharge machining.

The chemical composition of the steel under study complied with the requirements of GOST 5632–2014 and is presented in Table 1.

Table 1 - Chemical composition of 12Kh18N10T stainless steel according to GOST 5632–2014

Element	C	Cr	Ni	Ti	Mn	Si	P	S	Fe
Content, %	≤0,12	17,0–19,0	9,0–11,0	0,4–1,0	≤2,0	≤0,8	≤0,035	≤0,020	Base

Wire-cut electrical discharge machining was performed on a DK7745 machine (Suzhou Sanguang Science & Technology Co., Ltd., China) equipped with numerical control. A brass wire with a diameter of 0.18 mm was used as the electrode. The wire was fed continuously at a speed of 6–9 m/min. Deionized water with a specific electrical resistance of at least 50 kΩ·cm was used as the dielectric medium. The dielectric was fed into the interelectrode gap through upper and lower nozzles at a pressure of 0.5–0.8 MPa. The temperature of the working fluid was maintained at no higher than 25 °C.

To evaluate the influence of the process's energy parameters on the formation of the surface layer of 12X18H10T steel, two modes of wire-cut electrical discharge machining were used: finishing and intensive. The main parameters of these modes are presented in Table 2.

Table 2 - Wire Electrical Discharge Machining conditions

Parameter	Finish-cutting regime	High-energy regime
Wire diameter, mm	0,18	0,18
Wire feed speed, m/min	6	9
Dielectric medium	Deionized water	Deionized water
Dielectric electrical resistivity, kΩ·cm	≥50	≥50
Dielectric flushing pressure, MPa	0,5–0,8	0,5–0,8
Discharge energy per pulse, μJ	780	3600

The difference in single-pulse energy between the modes under study (780 and 3,600 μJ) resulted in different levels of thermal effects on the material in the electrical discharge machining zone, which made it possible to investigate the effect of energy input on the formation of the surface layer of 12X18H10T steel.

For metallographic studies following wire-cut electrical discharge machining, metallographic sections measuring 5 × 10 × 20 mm were prepared from representative areas of the machined specimens. The specimens were prepared according to a standard metallographic procedure, which included sequential grinding with abrasive materials of varying grit sizes, followed by mechanical polishing to a mirror finish on a LaboPol-5 automatic grinding and polishing machine (Struers, Denmark). To reveal the microstructure, the specimens were chemically etched with a 5% aqueous solution of nitric acid (HNO_3).

The microstructure was examined using optical metallography on an Olympus BX51 microscope (Olympus Corporation, Japan). The morphology of the cut surface, the structure of the recast layer, the nature of the interface between the recast layer and the base metal, and the presence of surface defects were examined using scanning electron microscopy on a JSM-6390LV microscope (JEOL Ltd., Japan), equipped with an INCA Energy Penta FET X3 energy-dispersive X-ray microanalysis system (Oxford Instruments Analytical Ltd., United Kingdom).

The elemental composition was determined using energy-dispersive X-ray spectroscopy at three representative points on each sample: two points in the remelted surface layer and one control point in the base metal, which allowed for an assessment of the possible redistribution of chemical elements following electrical discharge machining.

The microhardness of the surface layer was determined using the Vickers method on a DuraScan-20 microhardness tester (EMCO-TEST Prüfmaschinen GmbH, Austria). Measurements were taken perpendicular to the treated surface, from the remelted layer into the base metal. For each processing mode, a series of measurements was conducted; based on the results, microhardness distribution profiles were plotted, and the influence of WEDM energy parameters on the mechanical state of the surface layer was evaluated.

Results and discussion

Following wire-cut electrical discharge machining of the teeth of a gear blank with a 60° profile angle, the microstructure of the surface layer was examined using optical metallography. The microstructure of the working surfaces formed under various machining modes is shown in Figure 2. The studies were conducted for two WEDM modes, the parameters of which are given in Table 2. Figure 2a shows the surface after the finishing mode, and Figure 2b shows the surface after the intensive mode.

Analysis of the metallographic images shows that in both cases, the base metal retains the austenitic polycrystalline structure characteristic of 12X18H10T steel, with clearly defined grain boundaries. In the near-surface zone, a layer is observed that was formed as a result of local melting and subsequent crystallization of the material

under the action of electrical discharges. This layer differs from the base metal in its increased contrast and thickness, which varies along the length of the surface.

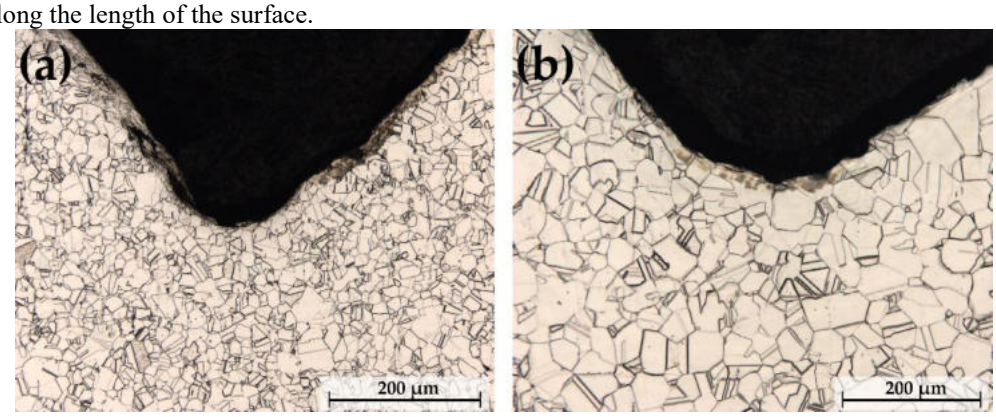

Fig. 2 - Microstructure of the surface layer of 12KH18N10T steel after wire-cut electrical discharge machining: a — fine machining mode; b — intensive machining mode.

In the finishing mode (Figure 2a), the remelted layer has a relatively small thickness and a more uniform morphology. The boundary between the surface layer and the base metal is quite clearly defined, and no pronounced structural changes detectable by optical metallography were observed in the adjacent zone. This pattern corresponds to a lower energy input into the material when using a mode with a reduced single-pulse energy.

Under intensive processing conditions (Figure 2b), an increase in the energy of a single pulse to 3,600 μJ (Table 2) is accompanied by an intensification of the local thermal effect, which leads to the formation of a more developed remelted layer with greater thickness nonuniformity. In certain areas, a more pronounced heat-affected zone is observed, which is consistent with the known characteristics of the WEDM process as discharge energy increases. The results obtained indicate that an increase in energy input promotes the development of local melting and subsequent crystallization of the material, significantly influencing the morphology of the surface layer.

To investigate in greater detail the characteristics of surface layer formation following wire-cut electrical discharge machining, a scanning electron microscopy analysis of the cut surface was performed. The resulting micrographs are shown in Figure 3. Figure 3a shows the surface morphology of a tooth formed during the finishing mode, while Figure 3b shows that formed during the intensive mode.

The SEM analysis showed that, regardless of the machining mode, the tooth profile with a 60° angle was formed without any visible distortions in the geometry of the working faces. Material continuity is maintained across the entire examined surface, with no macrocracks, large pores, or signs of delamination detected. The results indicate that the selected WEDM modes ensure the formation of a surface free of pronounced macroscopic defects arising from the localized thermal effects of electrical discharges.

In the finishing mode (Figure 3a), the surface is characterized by a relatively uniform morphology. The micro-relief is formed uniformly along the entire length of the tooth's working edge, and the dimensions and distribution of surface irregularities do not exhibit significant local variability. These characteristics are consistent with the lower energy of a single pulse (780 μJ), which reduces the amount of thermal energy introduced into the material during each electrical discharge, thereby limiting the intensity of local melting and promoting the formation of a more uniform surface.

Under an intensive processing regime (Figure 3b), a significant change in surface morphology is observed. The microtopography becomes more developed and heterogeneous, the variability in the dimensions of surface irregularities increases, and individual surface areas are characterized by a more complex configuration. This morphology is consistent with an increase in the energy of a single pulse to 3,600 μJ, at which the thermal energy released in the discharge zone increases. This leads to an increase in the volume of material subjected to localized melting and its subsequent high-speed solidification, which is a characteristic feature of the surface formation mechanism in wire-cut electrical discharge machining.

It should be noted that, despite a 4.6-fold difference in the energy of a single pulse, in both cases the surface retains a continuous structure without signs of macroscopic damage. Thus, the main effect of the parameter under study manifests not in the formation of critical defects, but in changes in surface morphology, the degree of micro-relief development, and the spatial heterogeneity of the surface layer.

To assess possible changes in the chemical composition of the surface layer, energy-dispersive X-ray microanalysis was performed at three representative points. Points Spectrum 1 and Spectrum 2 were located immediately near the cut surface on the working edges of the teeth, where the material was subjected to the most intense electrical discharges. Spectrum 3 was located within the base metal, outside the zone of direct thermal exposure, and served as a control area. This arrangement of measurement points allowed us to compare the elemental

composition of the surface layer with that of the base metal and to assess possible changes in the concentration of alloying elements resulting from the WEDM process.

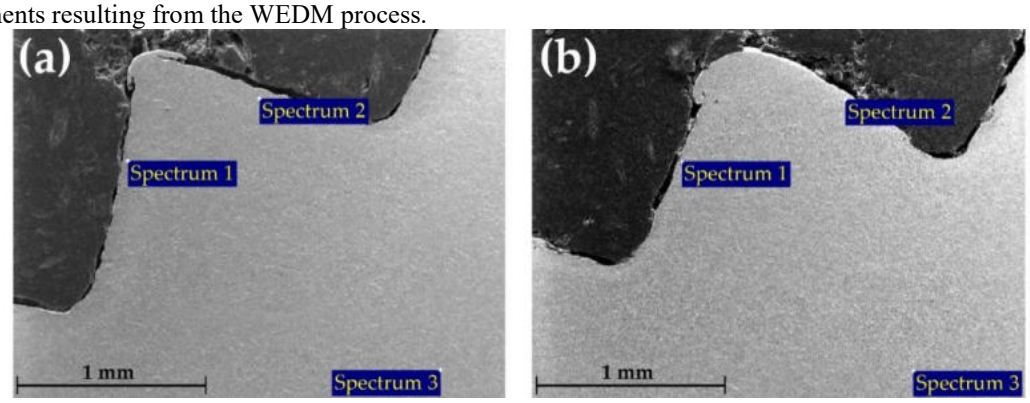

Fig. 3 - SEM images of the surface of teeth made of 12X18H10T steel after wire-cut electrical discharge machining (EDM), showing the energy-dispersive X-ray microanalysis (EDS) points: a — finishing mode; b — intensive mode

The results of energy-dispersive X-ray microanalysis of the surface layer of 12X18H10T steel after fine-finish electrical discharge machining are presented in Table 3. Analysis of the data shows that at all points examined, the main elements remain Fe, Cr, and Ni, with a total content of approximately 93–94 wt.%, indicating that the chemical composition of the austenitic stainless steel is preserved after WEDM. The Fe content varies between 66.70–67.22 wt.%, Cr between 17.15–17.63 wt.%, and Ni between 9.34–9.71 wt.%. When comparing the surface areas (Spectrum 1 and Spectrum 2) with the control area (Spectrum 3), no significant redistribution of the main alloying elements is observed. At the same time, the oxygen content at the surface points is 0.74–0.95 wt.%, whereas at the control point it decreases to 0.69 wt.%. This distribution indicates that oxygen is predominantly localized in the near-surface zone of the remelted layer. Furthermore, Spectrum 1 and Spectrum 2 contain small amounts of copper (0.52–0.56 wt.%) and zinc (0.48–0.51 wt.%), whereas in Spectrum 3, their contents decrease to 0.03 and 0.07 wt.%, respectively, indicating the localized nature of mass transfer from the brass wire electrode material.

Table 3 - Results of EDS analysis of localized areas of the surface layer of 12X18H10T steel after wire electrical discharge machining (WEDM) in the finishing mode

Spectrum (a)	Ti	O	Si	Cr	Mn	Fe	Ni	Mo	Cu	Zn	Total
Spectrum 1	0.91	0.95	0.59	17.15	1.56	66.95	9.53	1.32	0.56	0.48	100.00
Spectrum 2	0.98	0.74	0.58	17.43	1.39	67.22	9.34	1.29	0.52	0.51	100.00
Spectrum 3	1.1	0.69	0.58	17.63	1.44	66.70	9.71	2.05	0.03	0.07	100.00

The results of the EDS analysis following intensive treatment are presented in Table 4. As in the previous case, the chemical composition of the surface layer is dominated by iron, chromium, and nickel. The concentration of Fe ranges from 66.27 to 66.97 wt.%, Cr from 17.21 to 17.34 wt.%, and Ni from 9.42 to 9.69 wt.%, which practically corresponds to the values obtained during the finishing treatment. At the same time, the oxygen content in the surface regions increases to 1.04–1.08 wt.%, whereas at the control point it is only 0.55 wt.%. At the same time, copper (0.61–0.64 wt.%) and zinc (0.52–0.54 wt.%) remain present in the surface regions, whereas in Spectrum 3 their concentrations decrease to 0.08 and 0.06 wt.%, respectively. This distribution of elements indicates that the processes of oxidation and mass transfer of the electrode material are predominantly confined to the surface region of the remelted layer.

A comparison of the results presented in Tables 3 and 4 shows that an increase in single-pulse energy has virtually no effect on the content of the main components of 12X18H10T steel. The maximum differences between the treatment modes do not exceed 0.95 wt.% for iron, 0.48 wt.% for chromium, and 0.37 wt.% for nickel, which falls within the range of local heterogeneity of the remelted layer and does not indicate a selective redistribution of alloying elements. The most noticeable changes are observed for oxygen: while its content in the surface regions is 0.74–0.95 wt.% under the finishing treatment (Table 3), it increases to 1.04–1.08 wt.% under the intensive treatment (Table 4). At the same time, at the control points (Spectrum 3), the oxygen content remains significantly lower—0.69 and 0.55 wt.%, respectively.

Table 4.Results of EDS analysis of localized areas of the surface layer of 12X18H10T steel after wire electrical discharge machining (WEDM) in high-intensity mode

Spectrum (b)	Ti	O	Si	Cr	Mn	Fe	Ni	Mo	Cu	Zn	Total
Spectrum 1	1.04	1.04	0.58	17.30	1.41	66.97	9.47	1.05	0.61	0.54	100.00
Spectrum 2	1.1	1.08	0.65	17.34	1.67	66.27	9.42	1.32	0.64	0.52	100.00
Spectrum 3	1.12	0.55	0.62	17.21	1.73	66.67	9.69	2.27	0.08	0.06	100.00

The results suggest that oxygen is concentrated primarily in the near-surface region of the remelted layer, while its concentration decreases with increasing depth. This pattern is consistent with the WEDM mechanism, in which molten metal interacts with the aqueous dielectric medium and its decomposition products during crystallization. Consequently, the elevated oxygen content at the surface points Spectrum 1 and Spectrum 2 can be regarded as indirect evidence of local surface oxidation, whereas the significantly lower oxygen concentration in Spectrum 3 indicates a substantially lower degree of oxidation of the material beneath the remelted layer. At the same time, the virtually unchanged content of Fe, Cr, and Ni indicates the absence of any noticeable redistribution of the main alloying elements.

A comprehensive analysis of the microstructure, surface morphology, and EDS results showed that the investigated WEDM modes enable the formation of a serrated profile from 12X18H10T steel without a significant change in the chemical composition of the surface layer. An increase in single-pulse energy primarily affects the morphology and structural state of the remelted layer and is accompanied by increased surface oxidation, whereas the content of the main alloying elements remains virtually unchanged.

The practical feasibility of the developed manufacturing process has been confirmed by the production of a gear base for a surgical holder (Figure 4).

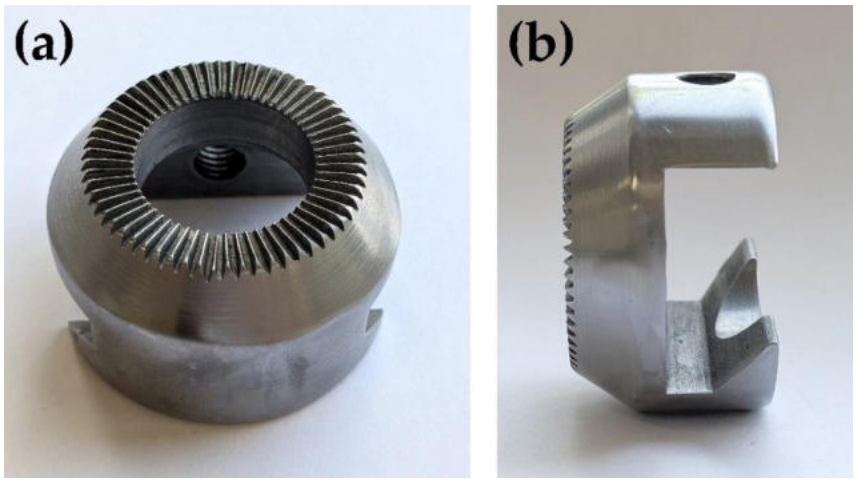

Fig. 4 – Practical application of WEDM technology in the manufacture of the toothed base of a surgical holder: (a) general view of the product; (b) profile of the toothed ring

Figure 4a shows a general view of the gear blank after WEDM machining, and Figure 4b shows the profile of the gear ring. Visual inspection confirms the formation of a complete tooth profile with a 60° angle, as well as the absence of uncut sections, chips, and other macroscopic defects, which indicates high precision in shaping and confirms the feasibility of using the developed WEDM mode in the manufacture of gear elements for medical mechanisms.

To assess the effect of WEDM modes on the mechanical properties of the surface layer, Vickers microhardness measurements were performed. The results are presented in Figure 5 as the distribution of microhardness along the examined surface section for the finishing and intensive processing modes. As shown in Figure 5, after the finishing treatment mode, the microhardness of the surface layer ranges from 195 to 200 HV, whereas after the intensive treatment mode, it ranges from 182 to 189 HV. The results indicate a higher and more stable surface microhardness achieved with the finishing treatment mode. This pattern is consistent with the results of metallographic studies and scanning electron microscopy, according to which an increase in single-pulse energy is accompanied by the formation of a more developed remelted zone with coarser structural morphology (Figures 2 and 3). It is likely that the increase in the volume of molten metal and the change in its crystallization conditions during the intensive mode contribute to the formation of larger structural components in the remelted layer, which may lead to a slight decrease in microhardness.

At the same time, the results of EDS analysis showed that the content of the main alloying elements (Fe, Cr, and Ni) remains virtually unchanged during the transition from the finishing to the intensive mode. This suggests that the differences in microhardness are primarily due to changes in the structural state of the remelted layer, rather than changes in the chemical composition of the material.

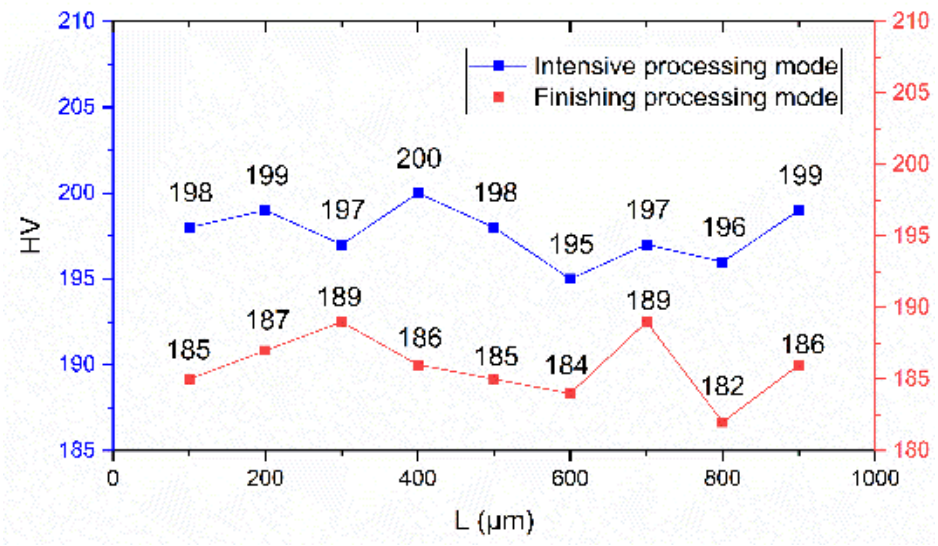

Fig. 5 - Distribution of the microhardness of the surface layer of 12X18H10T steel along the tested section after wire-cut electrical discharge machining in the finishing and intensive modes

Figure 6 illustrates the practical implementation of the developed manufacturing process, showing an assembled surgical holder with a toothed base manufactured using wire-cut electrical discharge machining. The resulting toothed joint ensures the complete formation of the working profile of the teeth and the correct meshing of the mechanism's components, confirming the feasibility of manufacturing functional parts for medical instruments with complex geometries using the developed WEDM parameters.

Fig. 6 - Practical implementation of the developed manufacturing process: an assembled surgical holder with a toothed base manufactured using the WEDM method

The combined results of metallographic examinations, scanning electron microscopy, energy-dispersive analysis, and microhardness measurements indicate that the selected processing parameters ensure the required forming accuracy while preserving the chemical composition of the surface layer and allowing for a controlled change in its microstructure. The results obtained confirm the potential of WEDM technology for the manufacture of high-precision gear elements for medical mechanisms, which have stringent requirements for surface quality and geometric accuracy.

Conclusion

The study shows that increasing the energy of a single pulse during wire-cut electrical discharge machining of 12X18H10T steel from 780 to 3,600 μJ intensifies the thermal effect on the material, leading to the formation of a

more developed and heterogeneous remelted layer, an increase in the heat-affected zone, and a more complex surface morphology.

It has been shown that increasing the machining energy has virtually no effect on the content of the main alloying elements in the surface layer: the Fe concentration is 66.27–67.22 wt.%, Cr—17.15–17.63 wt.%, and Ni—9.34–9.71 wt.%. At the same time, the remelted layer exhibits localized mass transfer of material from the brass wire, with a Cu content of up to 0.64 wt.%, Zn up to 0.54 wt.%, and the oxygen content increases to 1.08 wt.%, indicating the development of surface oxidation processes in the EDM-affected zone.

It has been established that the most favorable mechanical properties of the surface layer are achieved during the finishing machining mode. The surface microhardness is 195–200 HV, which is 7–9 HV higher than that achieved in the intensive mode (182–189 HV). The decrease in microhardness with increasing pulse energy is associated with the formation of a more developed remelted layer and changes in its crystallization conditions.

The developed WEDM mode enables the fabrication of a toothed base for a surgical holder made of 12X18H10T steel while preserving the geometry of the toothed profile, ensuring the absence of macroscopic surface defects, and maintaining stable characteristics of the surface layer, which confirms its suitability for use in the manufacture of high-precision components for medical mechanisms.

Acknowledgments
The authors would like to thank the National Scientific Center for Traumatology and Orthopedics named after Academician N.Zh. Batpenov for providing comments on medical equipment, as well as for expert advice and practical recommendations.

Conflict of interest
The authors declare no conflict of interest.

Statement of institutional ethics committee (IRB) approval
The work was purely technical in nature and did not involve humans or animals, so this section was marked "Not Applicable".

Informed consent statement
Written informed consent was obtained from all participants prior to participation in the study; if human participation is not intended, this section is marked “Not Applicable”.

Data availability statement
Data supporting the results of this technical study may be provided by the corresponding author upon reasonable request; or, since the work is based on numerical modeling and theoretical analysis, no new experimental data have been generated.

Funding
This research is funded by the Committee of Science of the Ministry of Science and Higher Education of the Republic of Kazakhstan (Grant No. BR24992786, “Development of technology for manufacturing samples of domestic medical instruments and medical products”).

Notice regarding the use of artificial intelligence technologies
During the preparation of this manuscript, the author(s) used artificial intelligence tools to perform academic translation and terminological editing of the text into English. All translations and technical terms were checked and approved by the authors for accuracy.

References
[1] Xin C., Xu Y., Zhang Z., Li M. Micro-Opto-Electro-Mechanical Systems for High-Precision Displacement Sensing: A Review. Micromachines. 2024;15(8):1011. https://doi.org/10.3390/mi15081011.
[2] Xu K., Xu S., Qi Q. Research on High-Precision Positioning Method of Robot Based on Laser Tracker. Intelligent Service Robotics. 2023;16:361–371. https://doi.org/10.1007/s11370-023-00467-5.
[3] Tian H., Yin Y., Zhang X., et al. Development and Precision Evaluation of a Robotic System for Oral Implant Surgery Using Personalized Digital Guides and Optical Spatial Positioning Technology. PLOS ONE. 2025;20(4):e0319054. https://doi.org/10.1371/journal.pone.0319054.
[4] Fan Z., Yang K., Yuan B., Mu X., Yin K., Sun Q., Sun W. Analysis and optimization of repetitive positioning precision for kinematic couplings of opto-mechanical components considering uncertainty. Precision Engineering. 2024;89:275–291. https://doi.org/10.1016/j.precisioneng.2024.06.003.
[5] Cazan S., Dănilă C., Crețu S. Tooth contact analysis of helical gears using semi-analytical methods in real gearing situations. Tribology International. 2023;185:108482. https://doi.org/10.1016/j.triboint.2023.108482.

[6] Ryaboshuk S.V., Kovalev P.V. Analysis of the causes of defect formation in 12Kh18N10T steel billets and development of recommendations for their elimination // Metal Working (Technology, Equipment, Tools).2023. T. 25. № 1. C. 6–15. DOI: 10.17212/1994-6309-2023-25.1-6-15.
[7] Das S.R., Dhupal D., Kumar A. A review on machining performance of AISI 304 steel. Materials Today: Proceedings. 2022;50:629–642. https://doi.org/10.1016/j.matpr.2021.04.495.
[8] Khan S.A., Gupta M.K., Mia M., et al. Comparative machinability aspects of austenitic and duplex stainless steels. JOM. 2024. https://doi.org/10.1007/s11837-024-06675-3.
[9] Ukey K., Sahu A.R., Gajghate S.S., et al. Wire electrical discharge machining (WEDM) review on current optimization research trends. Materials Today: Proceedings. 2023. https://doi.org/10.1016/j.matpr.2023.06.113.
[10] Rubi C.S., Prakash J.U., Juliyana S.J.S., et al. Comprehensive review on wire electrical discharge machining: a non-traditional material removal process. Frontiers in Mechanical Engineering. 2024;10. https://doi.org/10.3389/fmech.2024.1322605.
[11] Seidi M., Yaghoubi S., Rabiei F. Multi-objective optimization of wire electrical discharge machining process using multi-attribute decision making techniques and regression analysis. Scientific Reports. 2024;14:10234. https://doi.org/10.1038/s41598-024-60825-w.
[12] Ho K.H., Newman S.T. State of the art electrical discharge machining (EDM). International Journal of Machine Tools and Manufacture. 2003. Vol. 43. No. 13. P. 1287–1300. DOI: 10.1016/S0890-6955(03)00162-7.
[13] Pisarciuc C., Dodun O., Slătineanu L., et al. Wire Electrical Discharge Machining—A Review // Machines. 2020. Vol. 8, No. 4. Art. 69. DOI: 10.3390/machines8040069.
[14] Kumar P., Singh N.K., Sharma A., et al. Recent advances in wire electrical discharge machining of difficult-to-machine materials: A review. Journal of Manufacturing Processes. 2024.
[15] Zhang Y., et al. Research Progress on Process Optimization of Metal Materials in Wire Electrical Discharge Machining // Metals. 2025. Vol. 15, No. 7. Art. 706. DOI: 10.3390/met15070706.
[16] Zhang X., Li Y., Wang H., et al. Thermal-fluid coupling model of crater formation in electrical discharge machining // The International Journal of Advanced Manufacturing Technology. 2024. DOI: 10.1007/s00170-024-13999-6.
[17] Klocke F., Hensgen L., Klink A., Ehle L., Schwedt A. Structure and Composition of the White Layer in the Wire-EDM Process // Procedia CIRP. 2016. Vol. 42. P. 673–678. DOI: 10.1016/j.procir.2016.02.300.
[18] Klocke F., Hensgen L., Klink A., Ehle L., Schwedt A. Structure and Composition of the White Layer in the Wire-EDM Process // Procedia CIRP. 2016. Vol. 42. P. 673–678. DOI: 10.1016/j.procir.2016.02.300.
[19] Ekmekci B. Residual Stresses and White Layer in Electrical Discharge Machining (EDM) // Applied Surface Science. 2007. Vol. 253. No. 23. P. 9234–9240. DOI: 10.1016/j.apsusc.2007.05.078.
[20] Alkahlan B., Tabbakh T., Kurdi A., Pramanik A., Basak A.K. Formation and Characterization of the Recast Layer Formed on Inconel 718 during Wire Electro-Discharge Machining. Materials. 2023. Vol. 16. No. 3. Art. 930. DOI: 10.3390/ma16030930.
[21] Demirtaş H., Ay M., Yıldırım C.V., Giasin K., Sharma S., Pimenov D.Y. Investigation of the Layer Effects Formed by W-EDM on Electrochemical Grooving Performance of Co-Based Superalloy. Machines. 2023. Vol. 11. No. 8. Art. 823. DOI: 10.3390/machines11080823.
[22] Mishra S., Sharma A., Kumar A., Singh R., Pruncu C.I. An Experimental Investigation on Surface Integrity and Wire Wear in Rough and Trim Cut Modes of WEDM for Hybrid Composite. Aircraft Engineering and Aerospace Technology. 2024. DOI: 10.1108/AEAT-03-2024-0069.
[23] Naeim N., AbouEleaz M.A., Elkaseer A. Experimental Investigation of Surface Roughness and Material Removal Rate in Wire EDM of Stainless Steel 304. Materials. 2023. Vol. 16. No. 3. Art. 1022. DOI: 10.3390/ma16031022.
[24] Suresh T., Jayakumar K., Selvakumar G., Ramprakash S. Experimental Investigation on Improvement of Machinability of SS 304 Through Multipass Cutting in WEDM. Arabian Journal for Science and Engineering. 2023. DOI: 10.1007/s13369-022-07508-8.
[25] Oniszczuk-Świercz D., Świercz R. Effects of Wire Electrical Discharge Finishing Cuts on the Surface Integrity of Additively Manufactured Ti6Al4V Alloy. Materials. 2023. Vol. 16. No. 15. Art. 5476. DOI: 10.3390/ma16155476.
[26] Muttamara A., Nakwong P. Enhancing Wire-EDM Performance with Zinc-Coated Brass Wire Electrode and Ultrasonic Vibration. Micromachines. 2023. Vol. 14. No. 4. Art. 862.
DOI: 10.3390/mi14040862.
[27] Sharma A., Kumar R., Pimenov D.Y., et al. Optimization of Wire EDM Process Parameters on Cutting Inconel 718 Using Zinc-Diffused Brass Wire Electrode. Coatings. 2022. Vol. 12. No. 11. Art. 1612. DOI: 10.3390/coatings12111612.
[28] Kitayama S., Yonehara M., Okamoto Y., Narita H. Wire-EDM Performance and Surface Integrity of Inconel 718 Fabricated by Laser Powder Bed Fusion. The International Journal of Advanced Manufacturing Technology. 2024. Vol. 130. P. 4513–4528. DOI: 10.1007/s00170-023-12924-7.
[29] Kombayev, K., Kozhakhmetov, Y., Yerbolat, D., Dauletkhanov, Y., Kim, V., Kaidar, A., Ishangaliyev, A., & Khoshnaw, F. (2026). Influence of cutting parameters and assist gases on the laser cutting quality of 09G2S (S355J2, EN 10025-2) structural steel. Results in Surfaces and Interfaces, 22, 100716. https://doi.org/10.1016/j.rsi.2025.100716
[30] Wittenburg J., Küpper U., Herrig T., Klink A., Bergs T. Surface Integrity Analysis of Single Discharge Characteristics Derived from the Continuous Wire EDM Process. Procedia CIRP. 2024. Vol. 123. P. 203–208. DOI: 10.1016/j.procir.2024.05.037.
[31] Li Z., M'Saoubi R., Axinte D., et al. Surface Integrity in Metal Machining – Part I: Fundamentals of Surface Characteristics and Formation Mechanisms. International Journal of Machine Tools and Manufacture. 2021. Vol. 162. Art. 103686. DOI: 10.1016/j.ijmachtools.2020.103686.
[32] Kitayama S., Yonehara M., Okamoto Y., Narita H. Wire-EDM Performance and Surface Integrity of Inconel 718 Fabricated by Laser Powder Bed Fusion. The International Journal of Advanced Manufacturing Technology. 2024. Vol. 130. P. 4513–4528. DOI: 10.1007/s00170-023-12924-7.
[33] Kombayev, K., Khoshnaw, F., Kozhakhmetov, Y., Tleuzhanova, G., Azamatov, B., & Tabiyeva, Y. (2025). Microplasma sprayed tantalum coatings on Ti Grade 5 extra-low interstitials: Investigation of thickness and porosity control. Coatings, 15, 464. https://doi.org/10.3390/coatings15040464.

[34] Kar S., C. A. Niranjan, Prabhuswamy N. R., Majumder T., Baroi B. K., Kebede A. W. Experimental Investigation and Parametric Optimization of Machinability and Surface Characteristics in Wire EDM of Inconel 718. Scientific Reports. 2025. DOI: 10.1038/s41598-025-11188-3.
[35] Sherov K.T., Mardonov B.T., Buzauova T.M., Tussupova S.O., Smakova N.S., Izotova A.S., Gabdyssalik R., Kurmangaliyev T.B., Elemes D.E. The research of micro-hardness of side surfaces of teeth cylindrical wheels processed by "shaver-rolling device". Journal of Theoretical and Applied Mechanics. 2020; 50(1): 50–56. https://doi.org/10.7546/JTAM.50.20.01.05

Information of the authors

Kombayev Kuat Kurganovich, PhD, associate professor, senior researcher, D. Serikbayev East Kazakhstan Technical University
e-mail: kkombaev@edu.ektu.kz

Azamatov Bagdat Nurlanovich, PhD, associate professor, General Director, SciMed LLP
e-mail: bazamatov@edu.ektu.kz

Kaliyev Daniyar Issatayuly, PhD, Head of "Smart Engineering" Competence center, D. Serikbayev East Kazakhstan Technical University
e-mail: dkaliyev@edu.ektu.kz

Mukhametbek Zhaksylyk Mukhametbekuly, doctoral student, researcher, D. Serikbayev East Kazakhstan Technical University
e-mail: zmukhametbek@edu.ektu.kz

Gabdyssalyk Riza, PhD, associate professor, senior researcher, D. Serikbayev East Kazakhstan Technical University
e-mail: rgabdysalyk@edu.ektu.kz